FEDERAL UNIVERSITY OF SANTA CATARINA
SCHOOL OF TECHNOLOGY
GRADUATE PROGRAM IN CHEMICAL ENGINEERING

Tatiana Matiazzo

Reactive Flow and Photon Fate in a Mesoscale Reactor Applied to the Photocatalytic Abatement of Pollutants in Gas Phase: A Theoretical Investigation

Florianópolis
2022

Tatiana Matiazzo

Reactive Flow and Photon Fate in a Mesoscale Reactor Applied to the Photocatalytic Abatement of Pollutants in Gas Phase: A Theoretical Investigation

Doctorate Thesis submitted to the Graduate Program in Chemical Engineering of the Federal University of Santa Catarina in partial fulfillment of the requirements for the degree of Doctor in Chemical Engineering.
Supervisor: Prof. Cíntia Soares, Dr.
Co-supervisor: Prof. Natan Padoin, Dr.
Prof. Vítor J. P. Vilar, Dr.

Florianópolis
2022

Ficha de identificação da obra elaborada pelo autor,
através do Programa de Geração Automática da Biblioteca Universitária da UFSC.

Matiazzo, Tatiana
Reactive flow and photon fate in a mesoscale reactor applied to the photocatalytic abatement of pollutants in gas phase : a theoretical investigation / Tatiana Matiazzo ; orientadora, Cíntia Soares, coorientador, Natan Padoin, coorientador, Vítor J. P. Vilar, 2022.
167 p.

Tese (doutorado) - Universidade Federal de Santa Catarina, Centro Tecnológico, Programa de Pós-Graduação em Engenharia Química, Florianópolis, 2022.

Inclui referências.

1. Engenharia Química. 2. Process Intensification. 3. Computational Fluid Dynamics. 4. n-decane degradation. 5. NETmix. I. Soares, Cíntia. II. Padoin, Natan. III. Vilar, Vítor J. P. IV. Universidade Federal de Santa Catarina. Programa de Pós-Graduação em Engenharia Química. V. Título.

Tatiana Matiazzo

Reactive Flow and Photon Fate in a Mesoscale Reactor Applied to the Photocatalytic Abatement of Pollutants in Gas Phase: A Theoretical Investigation

The present work at Doctoral level was evaluated and approved by an examining board composed of the following members:

Prof. Dirceu Noriler, Dr.
State University of Campinas

Prof. Ricardo Jorge Nogueira dos Santos, Dr.
University of Porto

Maria Alice Prado Cechinel, Dr.
Hydroinformatics Solutions Ltda

We certify that this is the **original and final version** of the conclusion work that was considered suitable for obtaining the title of Doctor in Chemical Engineering.

ICP-Edu
Documento assinado digitalmente
Debora de Oliveira
Data: 04/06/2022 13:01:30-0300
CPF: 728.453.929-15
Verifique as assinaturas em https://v.ufsc.br

Prof. Débora de Oliveira
Coordinator of PósENQ

ICP-Edu
Documento assinado digitalmente
Cintia Soares
Data: 03/06/2022 09:51:42-0300
CPF: 020.401.629-09
Verifique as assinaturas em https://v.ufsc.br

Prof. Cíntia Soares, Dr.
Supervisor

Florianópolis, 2022.

ACKNOWLEDGEMENTS

First of all, I would like to thank my family that throughout my academic career have encouraged, sustained, inspired and tolerated me in this journey.

I would like to express my sincere gratitude to my supervisors Drª. Cíntia Soares (UFSC), Dr. Natan Padoin (UFSC) and Dr. Vítor J.P. Vilar, for the guidance, continuous support, constructive criticism, and encouragement throughout this project.

I would like to thank my friends and colleagues, the entire LabMAC (Laboratory of Materials and Scientific Computing) team for the moral and technical support, for their assistance, contributions and efforts in helping me throughout the course of this research.

My sincere appreciation to all the professors and collaborators of the Chemical and Food Engineering Department of the Federal University of Santa Catarina (UFSC).

I would like to specially express my gratitude towards Ansys Inc. and ESSS and their teams for their support and software license lease.

Lastly, I would like to thank the Coordination for the Improvement of Higher-Level Personnel (CAPES) and the National Council for Scientific and Technological Development (CNPq) for the financial support.

“If you want to find the secrets of the universe, think in terms of energy, frequency and vibration.”
(Nikola Tesla)

RESUMO

A fotocatálise heterogênea tem ganhado crescente interesse desde os anos de 1970. Desde então, diversas aplicações estão associadas com a fotocatálise heterogênea, tais como a busca por fontes alternativas de energia, síntese orgânica e tratamento de correntes líquidas e gasosas. Ao longo das últimas décadas, misturadores estáticos e reatores em escala milimétrica ou inferior têm ganhado atenção. Mili- e microdispositivos têm sido empregados em processos químicos pelo fato de otimizarem as trocas de calor e massa. Associados a fotocatálise, mili- e microreatores podem ser uma vantajosa alternativa para a degradação de poluentes orgânicos contidos em correntes gasosas. Os reatores fotocatalíticos enfrentam duas limitações principais: transferência de massa e transferência de fótons. Essas limitações podem ser superadas por meio de mudanças no sistema de iluminação do reator e por meio de melhorias na geometria do mesmo. Neste trabalho, a transferência de fótons no milireator fotocatalítico denominado NETmix é avaliada usando um algoritmo baseado na técnica conhecida como *ray tracing*. Este tipo de algoritmo é capaz de simular o comportamento da luz utilizando os princípios da óptica geométrica associada à técnicas de Monte Carlo. A radiação sobre uma superfície fina de catalisador de TiO_2 é avaliada para vários sistemas de iluminação, considerando a posição e um número distinto de LEDs. O impacto que o sistema de iluminação tem sobre a degradação fotocatalítica de uma corrente de ar contendo *n*-decano é investigada e permite a determinação de um número ideal / econômico de LEDs no sistema de iluminação, bem como uma distância ideal entre os LEDs e o reator. Neste trabalho avalia-se também, através de números adimensionais, a performance do sistema fotocatalítico, determinando qual é a etapa limitante do sistema - transferência de massa ou taxa de reação - para distintas condições operacionais.

Palavras-chave: Intensificação de Processos. Fluidodinâmica Computacional. Degradação *n*-decano. NETmix.

ABSTRACT

Heterogeneous photocatalysis has gained increasing interest since the 1970s. Since then, several applications have been associated with heterogeneous photocatalysis, such as the search for alternative energy sources, organic syntheses and the treatment of liquid and gas streams. Over the past few decades, static mixers and reactors on a millimeter scale or less have gained attention. Milli- and microdevices have been used in chemical processes due to the fact that they optimize heat and mass transfer. Associated with photocatalysis, milli- and micro-reactors can be an advantageous alternative for the degradation of organic pollutants contained in gas streams. Photocatalytic reactors face two main limitations: mass transfer and photon transfer. These limitations can be overcome through changes in the illumination system of reactor and through improvements on the reactor's geometry. In this work, the photon transfer in the NETmix milli-photoreactor is evaluated using a ray tracing algorithm. This type of algorithm is capable to simulate the behavior of light using the principals of geometrical optics associated with Monte Carlo techniques. The radiation field over a TiO_2 thin catalyst surface is evaluated for several illumination systems, considering the position and a distinct number of LEDs. The impact that the illumination system has over the photocatalytic degradation of an air stream containing *n*-decane is investigated and allows the determination of an ideal/economical number of LEDs in the illumination system, as well as an ideal LEDs-to-reactor distance. In the current work, it is also evaluated through dimensionless numbers the performance of the photocatalytic system to determine the system bottleneck phenomena - mass transfer or reaction rate - under distinct operational conditions.

Keywords: Process Intensification. Computational Fluid Dynamics. *n*-decane degradation. NETmix.

RESUMO EXPANDIDO

Introdução

A qualidade do ar exerce significativo impacto na saúde pública. Dessa forma, técnicas para mitigação de poluentes são de extrema importância. A qualidade do ar sofre influência de uma série de substâncias, tais como pólen, microrganismos, material particulado e fibras, além de gases como monóxido de carbono, ozônio, radônio e compostos orgânicos voláteis (COVs). COVs são substâncias orgânicas presentes em diversos materiais, com ponto de ebulição inferior a 250 °C. Dessa forma, diversas técnicas de mitigação de poluentes de correntes gasosas estão em uso, tais como precipitação eletrostática, adsorção, ozonização, fotólise, plasma não térmico e fotocatálise. A oxidação fotocatalítica é a técnica na qual poluentes gasosos podem ser degradados na presença de um material semicondutor, por exemplo dióxido de titânio, exposto à radiação ultravioleta. O desempenho da fotocatálise heterogênea é função de parâmetros operacionais (concentração de poluente, umidade, vazão), além do design do reator, tipo e intensidade das fontes de iluminação. Dentre as geometrias de reatores mais comuns estão os reatores de placas planas, anulares, monolíticos, leito fluidizado, chicanados, micro- e milireatores. Os micro- e milireatores são particularmente vantajosos para a intensificação de processos. Além disso, a crescente disponibilização de LEDs como fontes luminosas também contribui para a miniaturização de sistemas fotocatalíticos. Técnicas de fluidodinâmica computacional (CFD) e *ray tracing* são ferramentas de alta relevância para a avaliação e melhoramento de processos fotocatalíticos. Neste trabalho, o sistema de iluminação do milireator fotocatalítico denominado NETmix é analisado para a remoção de um composto orgânico volátil de correntes gasosas utilizando simulações de CFD e *ray tracing*. As técnicas de CFD são baseadas na resolução das equações da continuidade e conservação de momento, acopladas aos termos de reação. Para avaliar a transferência de fótons do sistema de iluminação, a técnica utilizada, *ray tracing*, é baseada nos princípios de conservação de energia e ótica geométrica.

Objetivos

O principal objetivo deste trabalho é avaliar o sistema de iluminação de um milireator fotocatalítico para a oxidação fotocatalítica de compostos orgânicos voláteis presentes em correntes gasosas. A análise do sistema de iluminação é realizada através de ferramentas de fluidodinâmica computacional e *ray tracing*. Para a validação das simulações a degradação fotocatalítica de *n*-decano no milireator NETmix é considerada. As simulações numéricas realizadas possuem dois objetivos principais: i) simular a transferência de fótons das fontes luminosas até a superfície do catalisador usando *ray tracing*; e ii) simular o fluxo reativo dentro do reator usando técnicas de fluidodinâmica computacional. Dentre os objetivos específicos estão a avalição do impacto da posição geométrica de cada LED que compõe o sistema de iluminação, levando em consideração a distância entre os LEDs e o reator e a distância entre cada LED. São também considerados diferentes disposições

para o catalisador dentro do reator, além da variação do número de LEDs que compõem o sistema de iluminação e o formato do arranjo geométrico utilizado.

Metodologia

Para a análise do sistema de iluminação do reator fotocatalítico a metodologia foi dividida em dois tópicos: i) simulações da transferência de fótons (*ray tracing*); e ii) simulações do fluxo reativo (CFD). As simulações da transferência de fótons foram conduzidas no *software* Ansys Speos®, que utiliza um algoritmo de *ray tracing* não sequencial baseado no método de Monte Carlo. Para simular a interação da luz com os diversos materiais que compõem o reator, os materiais e as fontes luminosas devem ser completamente descritos. Para representar os LEDs do sistema de iluminação foram criadas superfícies de dimensões equivalentes aos LEDs e foram especificadas a potência emitida por cada LED, o espectro de emissão e a distribuição de intensidade. Para descrever os materiais que compõem o sistema, a geometria de cada material foi associada a suas propriedades óticas. Foram descritos os índices de refração, número de Abbe e a proporcionalidade de luz que é refletida, transmitida e absorvida por cada material em função do ângulo de incidência. Para quantificar os valores de irradiância registrados na superfície do catalisador sensores são criados sobre tais superfícies. Os resultados numéricos foram validados com dados experimentais para, então, procederem-se os testes de posicionamento, arranjo e número de LEDs no sistema. O segundo tópico compreende as simulações fluidodinâmicas do reator. Para essas simulações o *software* Ansys Fluent® foi utilizado. Um teste de independência de malha é conduzido e os resultados de degradação do poluente são validados com dados experimentais. As condições de contorno utilizadas nas simulações CFD compreendem a velocidade prescrita na entrada do reator, informando também as frações de poluente e vapor d'água na entrada do mesmo e pressão atmosférica prescrita na saída do reator. Para a superfície do catalisador são utilizados os perfis de irradiação registrados pelos sensores das simulações de *ray tracing* além de uma função definida pelo usuário para representar a equação de oxidação do poluente em função da concentração do poluente, umidade e irradiação.

Resultados e Discussão

As simulações do transporte de luz foram validadas para um sistema composto por 18 LEDs e apresentaram erros relativos aos valores experimentais inferiores a 7%. A irradiação gerada pelo sistema foi validada para duas disposições distintas de catalisador, sendo estas denominadas: i) BSI (*back side illumination*), onde o filme de catalisador recebe a iluminação através da face oposta àquela em contato com o fluxo reativo; e ii) FSI (*front side illumination*), na qual a face de catalisador iluminada é a mesma que está em direto contato com o fluxo gasoso. Para o catalisador BSI um valor médio para a irradiância equivalente a 1018 W/m^2 foi obtido tendo uma eficiência de absorção de 33,5% e um coeficiente de variância de 31,6%. Para a configuração FSI a irradiância média é de 285 W/m^2, com eficiência de absorção de 35% e coeficiente de variância equivalente a 70,6%. Subsequentemente, a posição geométrica dos 18 LEDs foi variada em termos da distância entre um LED e outro e entre os LEDs e o reator. As variações

geométricas deram origem a 27 novos sistemas de iluminação que foram simulados para as configurações BSI e FSI. Para ambas as disposições de catalisador, percebe-se que o aumento do distanciamento entre os LEDs e entre os LEDs e o reator reduz o coeficiente de variância, porém estão associados a valores mais baixos de irradiância e eficiência de absorção. O posicionamento dos LEDs se mostrou determinante para a eficiência do sistema de iluminação. As mudanças na posição dos LEDs levam a eficiência de absorção a variar entre 29,2% e 42,8% para o BSI e entre 31,3% e 40,5% para a configuração FSI. Os coeficientes de variância são ainda mais impactados, situando-se entre 25%-238% e 68%-306% para BSI e FSI, respectivamente. As simulações permitem encontrar posições ideais para os 18 LEDs, de modo a manterem alta absorção da luz pelo catalisador e, ao mesmo tempo, menores valores de coeficiente de variância para encontrar um campo mais homogêneo. Em uma nova análise são considerados diferentes números de LEDs no sistema de iluminação, sendo esses distribuídos de acordo com duas distribuições: i) LEDs alinhados; e ii) LEDs alternados. Para o arranjo alinhado foram simulados sistemas com 6, 15 e 28 LEDs, enquanto que para o arranjo alternado foram considerados 5, 12, 18 e 30 LEDs. Os LEDs foram posicionados em cada sistema de modo a manter a maior distância possível entre cada LED. A distância entre os LEDs e o reator foi variada, considerando 6 mm, 12 mm, 24 mm e 48 mm e o catalisador foi depositado considerando o esquema FSI. Os perfis de irradiância obtidos pelas simulações de *ray tracing* foram acopladas às simulações fluidodinâmicas. Para cada uma das 28 configurações de iluminação, foram analisadas a eficiência de absorção da luz, a homogeneidade do campo gerado, a eficiência global de iluminação e a conversão do poluente. Os sistemas alternados apresentaram valores de irradiância ligeiramente maiores que as configurações alinhadas. No entanto, sistemas alinhados apresentaram maior homogeneidade de iluminação da superfície de catalisador. Como esperado, independentemente do alinhamento do sistema, quanto maior for a distância entre os LEDs e o reator menor são os valores de irradiação encontrados e sistemas com maiores números de LEDs resultam em maiores valores de irradiância. A irradiância média obtida em cada simulação foi plotada junto à conversão de poluente obtida em cada caso. Essa análise permite encontrar a distância ideal dos LEDs até o reator, que equivale a 12 mm, independente de quantos LEDs compõem o sistema. É também possível identificar qual dos sistemas fornece energia o suficiente para degradar o poluente com o menor custo energético e reduzido número de LEDs.

Considerações Finais

A degradação de poluentes gasosos é um importante processo e requer atenção, visto que a qualidade do ar tem influência direta na saúde humana. O uso de reatores fotocatalíticos para a degradação de compostos orgânicos voláteis é uma das possíveis técnicas para tratamento de gases. Nesse trabalho, o sistema de iluminação de um milireator fotocatalítico foi analisado. A radiação que incide sobre a superfície do catalisador foi simulada através de um algoritmo estocástico baseado na técnica de Monte Carlo. A posição geométrica dos LEDs, o número de LEDs que compõem o sistema e arranjo dos mesmos foi avaliado. A irradiância registrada em cada ponto da superfície do catalisador é considerada em simulações CFD. A homogeneidade do campo de radiação bem como os valores

da irradiância registrada são fatores determinantes sobre a conversão do poluente. As principais contribuições do trabalho são resumidas a seguir:

- as simulações da transferência de fótons e da fluidodinâmica computacional foram validadas com dados experimentais e os erros relativos encontrados foram inferiores a 7%;
- a posição geométrica de 18 LEDs que compõem o sistema de iluminação do reator fotocatalítico foi avaliada de acordo com 3 parâmetros adimensionais que representam a proximidade entre os LEDs e entre os LEDs e o reator. Nessa etapa 27 posições diferentes para os LEDs foram investigadas duas disposições de catalisador, BSI e FSI. A eficiência de absorção foi similar nas duas disposições, porém, a homogeneidade do campo de radiação foi menor para o FSI. Os testes demonstraram que a proximidade entre os LEDs e entre os LEDs e o reator resulta no aumento da eficiência de absorção em detrimento da homogeneidade do campo;
- sistemas de iluminação compostos por 5, 12, 18 e 30 LEDs alternados foram comparados com sistemas contendo 6, 15 e 28 LEDs alinhados. Para cada sistema a distância entre os LEDs e o reator foi variada e o campo de radiação obtido sobre a superfície do catalisador foi avaliada. Os níveis de irradiação obtidos variaram entre 57 W/m^2 e 589 W/m^2. A eficiência de absorção chegou a 44% e o índice de uniformidade atingiu até 76%. A eficiência global de iluminação variou entre 14% e 31%;
- os perfis de irradiação foram incorporados a simulações de fluidodinâmica computacional e a oxidação do poluente *n*-decano foi observada. Independentemente do arranjo e do número de LEDs a melhor conversão do poluente foi encontrada para os sistemas com distância equivalente a 12 mm entre os LEDs e o reator;
- a comparação entre o emprego de um valor médio para a irradiância e o uso do perfil de radiação sobre a superfície do catalisador nas simulações fluidodinâmicas foi conduzido, e diferenças consideráveis foram registradas para casos com baixo índice de homogeneidade;
- os fenômenos que controlam o sistema fotocatalítico foram avaliados de acordo com a metodologia do número de unidades de transferências (NTUm). Foi determinado qual dos fenômenos, transferência de massa ou reação química, que controla o sistema. A oxidação do poluente foi simulada para números de Reynolds variando entre 0,5 e 530. O método demonstrou que para baixos números de Reynolds o sistema é controlado pela transferência de massa e com o aumento do número de Reynolds o fenômeno limitante fica relacionado com a taxa de reação.

Palavras-chave: Intensificação de Processos. Fluidodinâmica Computacional. Degradação *n*-decano. NETmix.

LIST OF FIGURES

LIST OF TABLES

CONTENTS

1 INTRODUCTION

The quality of air is an important standard for human health and the discussion of its importance dates far back as the times of ancient Greece (SEGUEL et al., 2017). In the modern world, the majority of the population spends about 90% of their time in indoor environments and it has been estimated that pollutant levels are commonly 2-5 times higher indoors than outdoor. In some cases, the levels can be up to 100 times greater (STAFFORD, 2015).

The quality of indoor air has a significant impact in public health. Besides respiratory infections, asthma, rhinitis and skin rashes, poor air quality is linked to eye and nose irritations, nausea, fatigue, dizziness and also cognitive effects (GENNARO et al., 2014). However, the problem of air pollution goes way beyond the respiratory system. Around 20% of cardiovascular and stroke deaths are linked to air pollution. Several types of cancer, autoimmune afflictions, osteoporosis, diabetes and anemia are also related to air quality problems (KELLY; FUSSELL, 2019; SCHRAUFNAGEL et al., 2019).

Air quality is affected by a series of substances including biological particles (bacteria, fungi and pollen), particulate matter and fibers, gases such as carbon monoxide, ozone and radon, and volatile organic compounds (VOCs) (CINCINELLI; MARTELLINI, 2017). VOCs are organic substances with boiling point equal or inferior to 250 °C at atmospheric pressure. VOCs are naturally occurring compounds; however, the pollution problems are linked to human activities, such as fossil fuels usage, biomass burning and solvent utilization (JING et al., 2019; HE et al., 2019).

Besides industrial operations, the indoor air quality is affected by the construction and furnishing materials that are slowly emitters of VOCs (WEIGL et al., 2014). Formaldehyde, for example, is one of the most commons VOCs, and is an indoor pollutant commonly found in wood building materials, mainly in the resins that bind together wood products like plywood and fiberboard. It is also found in plastics, textiles, carpet, pesticides, paint and cleaning products (SEGUEL et al., 2017).

In this work, the evaluated pollutant is *n*-decane ($C_{10}H_{22}$). This VOC is an alkane that consists of a straight chain of 10 carbon atoms. According to a report from the National Toxicology Program (NTP) from the United State Department of Health and Human Services, the majority of *n*-decane manufactured came from the petroleum refining, along with coal liquefaction through Fisher-Tropsch synthesis and hydrogenation of 1-decene. This compound is part of jet and engine fuels and has applicability as a solvent besides taking part in organic synthesis, manufacturing of paraffin products, rubber, paint and paper-processing industries, among others. The $C_{10}H_{22}$ is a common indoor pollutant that originates from building materials (TRI, 2003; KJÆRGAARD; MØLHAVE; PEDERSEN,

1989).

There are several techniques available to recover or destroy VOCs from air streams, including physical, chemical and biological treatments (BERENJIAN; CHAN; MALMIRI, 2012). Biological treatments employ microorganisms or plants to eliminate pollutants. Biological techniques such as botanical biofiltration, phytoremediation, bioscrubbers, biotrickling filters besides membrane and capillary bioreactors can be applied to air treatment (GONZÁLEZ-MARTÍN et al., 2021).

Biofiltration consists of the transfer of pollutants from air to a support medium followed by the biocatalysis of these contaminants. A biofiltration system can be described as a fixed-bed bioreactor, in which the catalyst is a microorganism that is immobilized in an inert support, forming what is known as biofilm (BERENJIAN; CHAN; MALMIRI, 2012). In biotrickling filters, the packed bed is irrigated by a trickling liquid that contains essential nutrients for the microorganisms. Therefore, the pollutants are absorbed into the liquid, adsorbed onto biofilm particles and then are biodegraded by the microorganism (RYBARCZYK et al., 2019).

Botanical biofiltration combines biofiltration with phytoremediation, that means that the structure of a biofilter is integrated with green plants. This technique benefits from the natural microorganisms that live near or inside the roots of plants, since these microorganisms will remove the contaminants of an air stream (SOREANU; DIXON; DARLINGTON, 2013). Bioscrubbers are composed of two units: first the contaminated air flows through a packed-bed or mist absorption unit where the pollutants are partially transferred to an aqueous current. Subsequently, the remaining pollutants are degraded by the microorganisms that are suspended in the second unit (GONZÁLEZ-MARTÍN et al., 2021).

In membrane reactors, the gaseous pollutants diffuse through the membrane and are biodegraded at the other side, where a liquid solution containing nutrients and microorganisms exist. The degradation can occur in a biofilm formed in the liquid side of the membrane or in the bulk solution (GONZÁLEZ-MARTÍN et al., 2021). The main advantage of this reactor is the easy scale-up, large gas-liquid interface, and the gas and water flows can be varied independently, without flooding, loading and foaming issues (MUDLIAR et al., 2010). Another possibility for the biodegradation of pollutants is the use of capillary bioreactors. This kind of reactor is composed by parallel straight microchannels, with no more than 5 mm in diameter, where a Taylor flow is desired (segmented sections of air bubbles and liquid slug). This configuration improves significantly the gas-liquid mass transfer while keeping low pressure drop (GONZÁLEZ-MARTÍN et al., 2021).

Among the physical-chemical processes that can be used for air treatment are electrostatic precipitator, adsorption, ozonation, photolysis, non-thermal plasma and photocatalysis (GUIEYSSE et al., 2008). Adsorption consists of the retention of pollutants at the

surface of an adsorbent material, for example, activated carbon, zeolites, silica, activated alumina, mineral clay among others. This technique can be effective for the removal of VOCs and microorganisms of a gas stream; however, in this type of process the pollutants are not destructed, they simply are transferred from one phase to another producing hazardous waste that must be treated or disposed (LUENGAS et al., 2015).

Ozonation comprises the production of O_3 molecules from ambient O_2 using high voltage discharge or UV radiation. Ozone is a powerful oxidizer; however, ozonisers do not present superior efficiency in comparison to other techniques. Besides that, the levels of ozone must be highly controlled in indoor environment since this compound presents health risks (GONZÁLEZ-MARTÍN et al., 2021). Photolysis employs ultraviolet radiation to oxidize pollutants, but this technology might release toxic compounds under non-ideal conditions (GUIEYSSE et al., 2008).

The pollutant decomposition in non-thermal plasma technology occurs due to the excitance of electrons and other radicals that compose the generated plasma. The plasma is generated by high voltage discharges (SCHIAVON et al., 2017). The downside of this technology is the high energy consumption and the fact that toxic byproducts can be generated, ozone and nitrogen dioxide molecules for example (GONZÁLEZ-MARTÍN et al., 2021; CHEEK et al., 2021).

Photocatalytic oxidation (PCO) degrades contaminants via the radicals that are produced when a semiconductor material, such as TiO_2, is exposed to ultraviolet light (GUIEYSSE et al., 2008). This technology has a vast applicability, since several organic compounds and microorganisms can be decomposed via PCO. The performance of these photocatalytic reactors are connected to the humidity and pollutant levels, besides the light source type and intensity, and the photocatalytic reactor design (ZHONG; HAGHIGHAT, 2015). Among the reactors designs available for PCO reactions are: flat plate, honeycomb monolith, annular, packed bed, slurry, hollow fiber and microreactors (MALAYERI; HAGHIGHAT; CHANG-SEO, 2019).

In this work, the illumination system of a photocatalytic reactor is evaluated. The mesoscale reactor, known as NETmix, is employed for the oxidation of the n-decane contained in a gas stream. The class of reactors employed has similar process intensification qualities to the microreactors, but at the same time, the manufacturing costs are minimized since its scale lies upon the millimeter range.

Process intensification can be defined as a strategy to reduce a plant size while keeping a predefined production objective, meanwhile a significant optimization of energy consumption and waste generation is achieved (SANTANA et al., 2018; QIAN; QI; GROSSMANN, 2018; RAMSHAW, 1995). Due to the minimization of costs with simultaneous increase in raw materials and energy efficiency that process intensification proportionates,

the development of micro- and millireactor technology has gained a lot of attention in the last two decades (ABIEV, 2019; JESSY; HAYNES, 2017).

Abiev (2019) lists some of the industrial operations that benefit from the microstructuring of their process line. The examples include the Fisher-Tropsch reaction, the catalytic production of propene oxide, hydrogen and hydrogen peroxide, besides the synthesis of pigments and polymers. The oxidation and absorption of nitrous gases is another area that can benefit from the concepts of process intensification and microreaction systems. The effluent treatment is also a possible target area for the process intensification strategies.

The main differential of microscale systems are the high rates of interfacial heat and mass transfer. Besides, the micro- and milliscales of the plant make it safer and more environmental friendly (ABIEV, 2019; VANKAYALA et al., 2007).

According to Abiev (2019) the cross-section of such devices range between 10 μm and 3 mm. With intensification in mind, the term microfluidic arises, and refers to reactor devices with cross-sections inferior than 1 mm. Usually lithography or etching inside a clean room are the fabrication techniques employed. In order to mitigate manufacturing costs, researches have turned to millidevices. The denominated millifluidic is equivalent to microfluidic devices that are scaled-up to a millimeter range, but in this case the fabrication costs are lower if compared with the microdevices (YUEHAO, 2012).

The optimization of this micro- and millidevices is facilitated with the use of Computational Fluid Dynamics (CFD). The CFD tools can be described as a combination of physics, mathematics and computational sciences. In order to describe fluid flow behavior the CFD tools solve the continuity and momentum conservation equations for each control volume created to describe the hole geometry of the reactor. Both heat and mass transfer, besides homogeneous and/or heterogeneous reactions can be coupled with the conservation equations in the simulations (SANTANA et al., 2020; JÚNIOR, 2019).

1.1 RESEARCH AIM AND SCOPE

The main objective of this thesis is to comprehend the relevance that photon transfer simulations exert over the project of photocatalytic oxidation systems employed in air purification and describe numerically the photocatalytic oxidation of a model volatile organic compound, *n*-decane, in a milli-photocatalytic reactor denominated NETmix.

1.1.1 Specific objectives

As specific objectives this thesis project comprises the achievement of the following steps:

(a) validate the photon transfer, for the milli-photoreactor NETmix, employing ray tracing simulations;

(b) evaluate the geometrical position of an LED system, considering how LEDs-to-LEDs and LEDs-to-reactor distances influence the radiation field registered at the catalyst surface;

(c) evaluate the impact of distinct illuminations schemes, BSI and FSI, that directly change the position of catalyst deposition inside the reactor and consequently the photon-transfer;

(d) evaluate how the number of employed LEDs, in staggered or inline arrangements, impact the irradiance values and homogeneity of light distribution over the catalyst surface;

(e) couple radiation field data to CFD to simulate the reactive flow inside the NETmix photoreactor and evaluate the impact that distinct radiation fields have on the photocatalytic reaction;

(f) evaluate the impact of using radiation field data and averaged values in the reaction rate of CFD simulations;

(g) evaluate the performance of the reactor under distinct flow conditions to characterize if the process is controlled by reaction rate or mass transfer.

1.2 THESIS OUTLINE

To ensure a good understanding, the current thesis was organized as follows:

Chapter 2 presents a literature review and the background of this thesis. First, the principles of photocatalysis are discussed along with the most common photoreactors geometries. An overview of light simulation and modeling for photoreactors is also explored, briefly summarizing the principles of ray optics. Finally, the chapter covers the state of the art of photocatalytic reactors modeling.

In Chapter 3, entitled “Radiation Field Modeling of the NETmix Milli-Photocatalytic Reactor: Effect of LEDs Position over the Reactor Window”, the simulation of light for a photoreactor is addressed. The radiation field in the meso-scale NETmix photoreactor was evaluated employing a Monte Carlo-based algorithm through the use of the software Ansys Speos®. The chapter presents the validation of the light simulation and explores the impact of the geometrical position of the LEDs that compose the illumination system in the obtained radiation field.

Chapter 4, entitled “CFD and Radiation Field Modeling of the NETmix Milli-Photocatalytic Reactor for *n*-Decane Oxidation at Gas Phase: Effect of LEDs Number and Arrangement”, explores the union of ray tracing (simulation of light) and CFD (flow and reaction simulation). Several illumination systems were simulated using ray tracing and their results were coupled with CFD simulations for the degradation of a model VOC pollutant. The chapter discusses how the radiation field affects the oxidation of organic pollutants in the NETmix photoreactor.

In Chapter 5, a brief comparison was caried out between CFD coupled with radiation field data and CFD simulations using average irradiance values. The chapter discusses the relevance of employing the radiation field data alongside CFD simulations for a better accuracy in the pollutant degradation results.

Chapter 6 evaluates the behavior of the photoreactor operating under distinct Reynolds numbers. The regime flow is characterized, and dimensionless numbers were used to evaluate the performance of the photoreactor. A number of mass transfer units method was employed to calculate the reaction effectiveness and to determine if the process is controlled by the mass transfer or by the reaction rate.

Finally, Chapter 7 closes the present work with the concluding remarks and perspectives for future work. In the sequence, all references used in this document are listed.

Complementary, in Appendix A the regression of the reaction rate employed is presented. Appendix B shows the grid convergence test of the mesh employed in CFD simulations and the validation of the CFD model. The Appendixes C and D present supplementary information for Chapters 3 and 4, respectively.

2 RESEARCH BACKGROUND

2.1 PHOTOCATALYSIS

In the simplest terms, photocatalysis refers to chemical reactions that occur in the presence of a semiconductor material that is activated in the presence of light. This topic summarizes the main concepts of this technology aimed at air purification.

2.1.1 Principles

The oxidation of an organic compound can occur over the surface of a semiconductor photocatalyst material in the presence of light. This type of photocatalytic process is gaining attention in recent years due to the global efforts to eradicate hazardous materials from wastewater and air streams, besides the growing efforts to synthesize fine chemicals and generate alternative energy (GAYA, 2014b; DURAN; TAGHIPOUR; MOHSENI, 2010).

The basis of semiconductor photoelectrochemistry started in the 1960s. However, it gained interest with the demand for new energy technologies caused by the oil crisis of 1973 and the energy crisis of 1979. One of the most cited works of this period is the one of Fujishima and Honda (1972), in which they split water using a TiO_2 electrode (HORTELANO; LUIS DE LA FUENTE, 2019; BOYJOO et al., 2017; PETER, 2016).

The physics of the semiconductor has already been explored in many works (LE BAHERS; TAKANABE, 2019; AKERDI; BAHRAMI, 2019; XU et al., 2018; GAYA, 2014a; OHTANI, 2011). Fundamentally, electron transfer reactions can be initialized in semiconductors surfaces when such surfaces are irradiated by light with energy equal or greater than its band gap, which leads to the appearance of conduction band electrons (e^-) and valence band holes (h^+). The photogenerated electrons then react with O_2 resulting first in a superoxide radical and then in H_2O_2. The formed holes are then transferred to the target molecule and according to its oxidizing power ends up degrading the pollutant molecules (WANG et al., 2006; MENDIVE; CURTI; BAHNEMANN, 2016).

The overall photocatalytic reaction can be written according to Equation (1), that is theorized to occur according to the following steps: first the reactants must diffuse from the bulk through the boundary layer and reach the catalyst surface, in an external mass transfer process; then, the reactants must diffuse through the catalyst to reach the active surfaces sites (internal mass transfer); following, at least one of the reactants is adsorbed onto the active sites where the reaction then takes place; after reacting, the products/intermediates must desorb and diffuse to the bulk region (MOZIA, 2010; CHONG et al., 2010).

$$Pollutant \xrightarrow{TiO_2/h_v} Intermediates \rightarrow CO_2 + H_2O + Mineral\ Acids \quad (1)$$

Titanium oxide (TiO_2) is one of the most utilized semiconductors. That is justified by its low cost, high stability and due to its high efficient photoactivity. The compound has been widely used as a pigment in the past (ABDULLAH; KAMARUDIN, 2015; HASHIMOTO; IRIE; FUJISHIMA, 2005).

The mechanism of photocatalysis over TiO_2 has been thoroughly discussed in the literature (VISAN et al., 2019; MUÑOZ-BATISTA et al., 2019; FUJISHIMA; RAO; TRYK, 2000). In sum, when the TiO_2 is illuminated with a photon energy (h_v) equal or greater than its bandgap energy, normally around 3.2 eV, the lone electron of its outer orbital will be excited and this process leaves an empty unfilled valence band, that gives origin to the electron-hole pair ($e^- - h^+$). The positive hole could oxidize contaminants directly or produce very reactive hydroxyl radicals ($OH^{\cdot}$). The electron in the conduction band can recombine with the holes in the valance band producing heat (SHAYEGAN; LEE; HAGHIGHAT, 2018; YANGYANG, 2013; ZHONG et al., 2010; CHONG et al., 2010; MOZIA, 2010; KONSTANTINOU; ALBANIS, 2004). The chain series of photoinduced oxidative-reductive reactions can be postulated as in Equations (2) to (9) (SHAYEGAN; LEE; HAGHIGHAT, 2018).

$$\text{Photoexcitation}: \ \mathrm{TiO_2} + h_v \rightarrow h^+ + e^- \tag{2}$$

$$\text{Oxidation reaction}: \ \mathrm{OH^-} + h^+ \rightarrow \mathrm{OH^{\cdot}} \tag{3}$$

$$\text{Reduction reaction}: \ \mathrm{O_{2(ads)}} + e^- \rightarrow \mathrm{O^-_{2(ads)}} \tag{4}$$

$$\text{Ionization of water}: \ \mathrm{H_2O} \rightarrow \mathrm{OH^-} + \mathrm{H^+} \tag{5}$$

$$\text{Protonation of superoxide}: \ \mathrm{O_2^{\cdot -}} + \mathrm{H^+} \rightarrow \mathrm{HOO^{\cdot}} \tag{6}$$

$$\text{Electron scavenger}: \ \mathrm{HOO^{\cdot}} + e^- \rightarrow \mathrm{HOO^-} \tag{7}$$

$$\text{Formation of } \mathrm{H_2O_2}: \ \mathrm{HOO^-} + \mathrm{H^+} \rightarrow \mathrm{H_2O_2} \tag{8}$$

$$\mathrm{OH^-} + pollutant + \mathrm{O_2^-} \rightarrow products\,(\mathrm{CO_2}, \mathrm{H_2O}\ , etc.) \tag{9}$$

2.1.2 Photocatalysis for environmental applications

Photocatalytic processes present an easy operation, high efficiency, low energy consumption and minimal secondary pollution (DHANJAI et al., 2018). In general, this technology is efficient for the degradation of aromatic compounds, halocarbons, alcohols, alkenes and volatile organic compounds (OBENDORF, 2011).

Photocatalytic oxidation is also a viable alternative for air disinfection. Via photocatalysis a wide range of harmful microorganisms can be inactivated (JEONGHYUN; JANG, 2018; GAMAGE; ZHANG, 2010). The ability of photocatalysis using TiO_2 for viral inactivation is known since the 1990s and the COVID-19 pandemic brings focus into this type of technology (HABIBI-YANGJEH et al., 2020).

2.1.3 Parameters that influence photocatalytic reactions

The efficiency of the photocatalytic process is affected by the reactor's design, by the light source and intensity, contaminant concentration, humidity and flow rate. The following topics relate the most relevant factors that can alter a reactor's efficiency.

2.1.3.1 Light source and intensity

The activity of the catalyst is dependent on the system's illumination source type and intensity. For the TiO_2 the ultraviolet (UV) light activates its photocatalytic properties. The UV light corresponds to the wavelength of 10 nm - 400 nm. The visible light spectrum (400 nm - 750 nm) can be used with modified TiO_2, such as nitrogen doped TiO_2 (YANGYANG, 2013).

Both artificial and natural light can be employed as illumination sources. Conventional lamps, like the incandescent and gas discharge lamps can be utilized, however their low efficiency leads to the increase of LEDs utilization (SUNDAR; KANMANI, 2020).

2.1.3.2 Humidity

The adsorption of water on the catalyst surface has been found to increase the efficiency of recombination of photo-generated electrons and holes. The adsorption of O_2, however, suppress the electron hole recombination process, which results in higher efficacy photo-activity (LINSEBIGLER; LU; YATES, 1995).

According to Juan and Xudong (2003), for the degradation of some compounds the mineralization to CO_2 is decelerated or does not even occur. On the other hand, excess of water vapor causes a significant reduction in the reaction rate, due to the occupancy of

the active sites of the catalyst by water. Therefore, it is relevant to balance the humidity content in the system to achieve maximum efficiency.

2.1.3.3 Contaminant concentration

The reaction rate is obviously a function of the contaminant concentration at the inlet. Juan and Xudong (2003) have found that the enhancement of the reaction rate can be achieved increasing the initial concentration until a certain limit. With greater concentrations, the rate may not vary significantly with the increase in initial pollutant concentration.

2.1.4 Photocatalytic reactors

The efficacy of the photocatalytic reaction is dependent, among other parameters, on the reactor's design type. Sundar and Kanmani (2020) classified the photocatalytic reactors according to three main criteria: light source, catalyst type and reactor flow. For the light source, reactors can use conventional lamps, light emitting diodes (LEDs) or natural solar light. Depending on the catalyst used, photocatalytic reactors can be classified as TiO_2 and non-TiO_2 based. According to the catalyst, the reactors can use immobilized or suspended catalyst. The classification can be due to the catalyst size, micro or nanometer. Furthermore, the reactors are classified on batch, continuous or batch recirculation mode, and also by the hydrodynamic regime as completely stirred tank (CSTR) or plug flow reactor (PFR).

Sundar and Kanmani (2020) also list and describe 28 types of photocatalytic reactors. In laboratory scale, the most common are the flat plate and annular reactors, and these are usually used to investigate the kinetics of a particular reaction. Among the other designs, that intend to maximize the catalyst area, are the monolith, packed and fluidized bed, corrugated plate, multi-annular, multi-plate, honeycomb and optical fiber (BOYJOO et al., 2017; MO et al., 2009).

2.1.4.1 Slit reactor

The slit or plate reactors have a very simple construction. Basically, the flow chamber is formed by two sandwiched plates. The catalyst is deposited in one of the reactor's plates (Figure 1). This kind of reactor has a very easy operation and construction, and for that is particularly useful for kinetic data studies. Verbruggen, Lenaerts, and Denys (2015) used a slit reactor associated with analytical and CFD approaches to propose a kinetic model for the degradation of acetaldehyde from a gaseous stream.

Figure 1 – Slit reactor scheme.

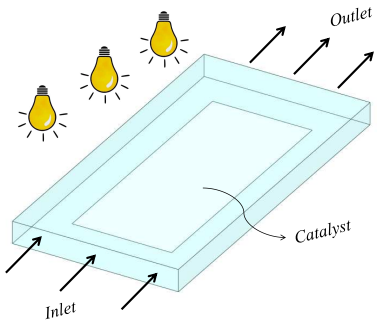

Source: elaborated by the author (2022).

2.1.4.2 Annular reactor

One of the simplest photocatalytic reactors is composed by two concentric glass cylinders (Figure 2). The illumination of this reactor is due to the placement of a cylindrical lamp in the empty cavity created in the center of the cylinders that compose the reactor. Light sources can also be located at the outside of the cylinders. Although simple and capable of processing high flow rates, these reactors can present issues related to lack of agitation and uneven illumination (SUNDAR; KANMANI, 2020).

Figure 2 – Annular reactor scheme.

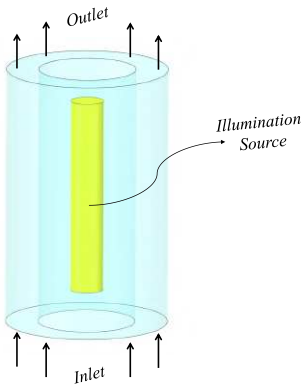

Source: elaborated by the author (2022).

2.1.4.3 Honeycomb monolith

Honeycomb monolith reactors, composed by a collective of small channels, are widely employed in automobiles for the regulation of NO_x emissions (HOSSAIN et al., 1999). This technology can be adapted for photocatalytic oxidation when combining honeycomb modules coated with TiO_2 and light sources (Figure 3). The main advantage of this reactor is the low pressure drop and the high surface-area-to-volume ratio (JUAN; XUDONG, 2003).

Figure 3 – Honeycomb monolith reactor.

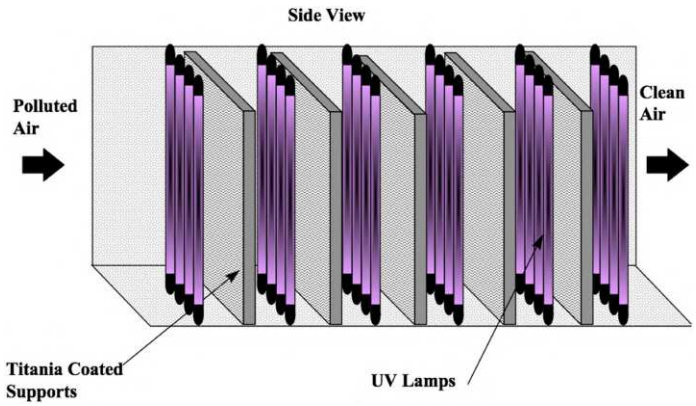

Source: Hay et al. (2015).

2.1.4.4 Fluidized-bed reactor

Fluidized-bed reactors can also be associated with light sources to conduct photocatalytic reactions. Lamps can be added to the interior of the reactor (Figure 4) or externally (Figure 5). In this kind of reactor, high gas flow rates can be treated with low pressure drop and efficient catalyst illumination (JUAN; XUDONG, 2003).

2.1.4.5 Microreactors

In the last three decades microreactors technology has been on crescent development (TANIMU; JAENICKE; ALHOOSHANI, 2017). This type of reactor is composed by a series of channels of various designs with cross section in the micrometer scale (Figure 6). The main advantages of this kind of reactor lies on short molecular diffusion distance and fast mixing, effective heat exchange, laminar flow and high surface-to-volume ratio, besides having high spatial illumination homogeneity and good light distribution through the entire reactor depth (MATSUSHITA et al., 2008).

Figure 4 – Annular fluidized-bed reactor.

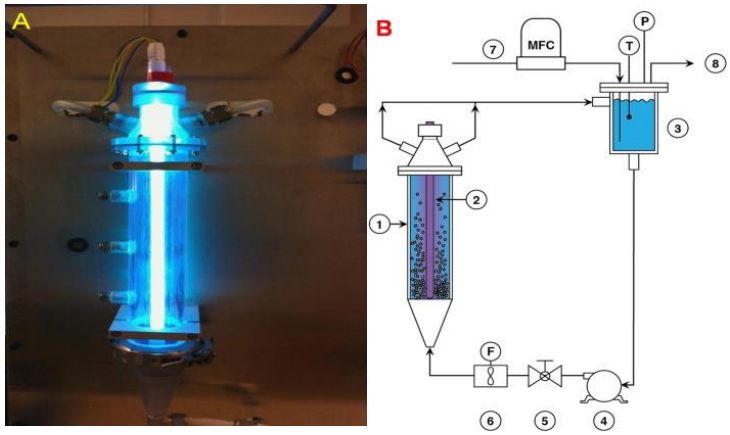

Source: Reilly et al. (2017).

Figure 5 – Fluidized-bed reactor with external illumination.

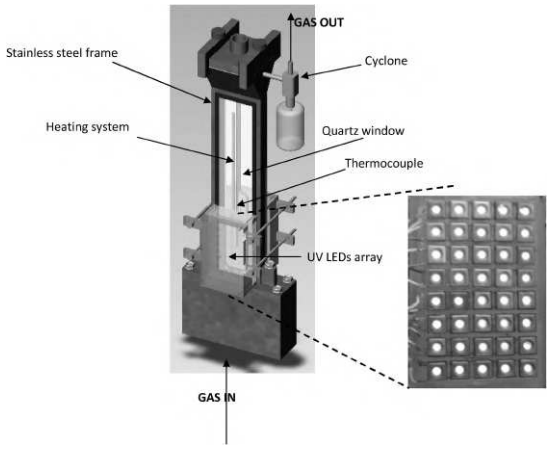

Source: Hajaghazadeh et al. (2014).

2.1.4.6 The NETmix, static mixer and reactor

The NETmix is a static mixer and millireactor characterized by the presence of several circular chambers interconnected through a series of prismatic channels. This reactor was developed by the researchers of the Laboratory of Separation and Reaction Engineering and Laboratory of Catalysis and Materials (LSRE-LCM) from University of Porto - Portugal (LOPES et al., 2005).

The reactor is composed by a metallic slab, Figure (7), where the patterns of chambers and channels are engraved. The reactor is sealed with a flat borosilicate glass slab

Figure 6 – Example of microreactor.

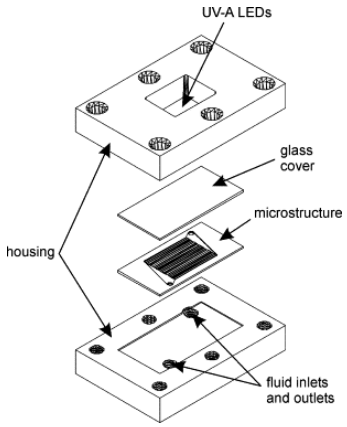

Source: Gorges, Meyer, and Kreisel (2004).

Figure 7 – NETmix photoreactor metallic slab.

Source: adapted from Da Costa Filho et al. (2019).

with high light transmission. Figure (8a) illustrates the NETmix reactor components, and Figures (8b) and (8c) show two variations in the illumination sources, where LEDs with distinct viewing angles and power are employed. The reactor dimensions are summarized in Table (1).

The catalyst TiO_2 can be disposed in the glass slab, or it can be immobilized on the imprinted pattern engraved at the metallic slab. Therefore, two illumination mechanisms can be employed: back-side illumination (BSI) or front-side illumination (FSI). When the catalyst is immobilized at the metallic plate, the mechanism employed is the FSI. Therefore, the light has to go through the fluid before reaching the catalyst surface. When the catalyst is supported at the glass window, the catalyst is illuminated in one side, and is in contact with the fluid flow at the other side, so the charge carriers are generated far from fluid interface, and because of this the carriers are more susceptible to recombination loss.

Table 1 – Geometrical parameters.

NETmix Photoreactor	
Window:	
Length (mm)	136.0
Width (mm)	76.0
Chambers:	
Diameter (mm)	6.5
Channels:	
Length (mm)	2.0
Width (mm)	1.0
Borosilicate glass slab thickness (mm)	4.0
Geometry depht (mm)	3.0

Source: Da Costa Filho et al. (2017).

Figure 8 – NETmix photoreactor.

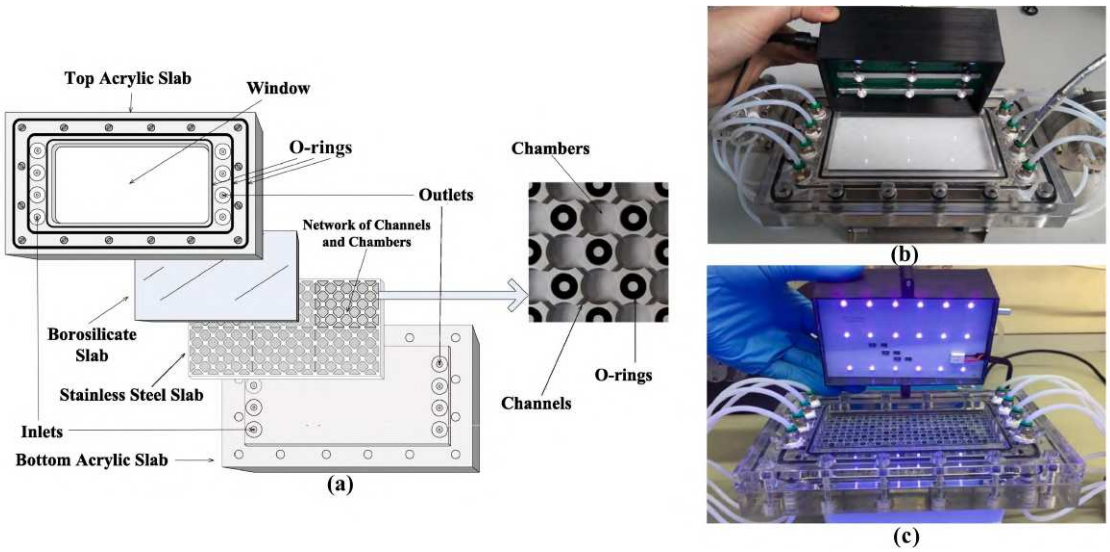

Source: adapted from Da Costa Filho et al. (2019).

Figure (9) shows a schematic of both FSI and BSI mechanisms (DA COSTA FILHO et al., 2019).

Da Costa Filho et al. (2017, 2019) studied the impact of the illumination mechanism and different light sources at the gas phase oxidation of *n*-decane. The authors evaluated the influence of the catalyst film thickness under a BSI illumination configuration and found that an increment on the thickness from 1.4 to 4.2 micrometers can increase the degradation velocity in 22%; however, due to the illumination configuration, greater thickness could lower the conversion since charge carriers are generated far from fluid interface, and the carriers are more susceptible to recombination loss. The study also evaluated distinct light sources. A simulated solar light was compared with a system with 9 LEDs and the LED system was found to have greater conversions rate, which is justified by the increase of

the energy that reaches the reactants.

The FSI mechanism was also investigated, and this configuration has three times more catalyst surface than the BSI set. However, under a simulated solar light, the degradation velocity does not increase in the same proportion, which implies that the light does not reach all of the catalyst surface. To get around this issue, the authors also analyzed the use of conventional UVA light and LED systems. The conventional UVA lights showed a slight improvement, while a setting with 9 LEDs had no expressive increase on conversion. A system with 18 LEDs was also developed in order to minimize shadow zones and improve light distribution. Although the system allowed an increase of about 3.6 times on the catalyst area, the authors found analogous reaction rates between the FSI and BSI mechanisms.

2.2 PHOTON FATE

One of the main limitations of photocatalytic reactors is the photon transfer (VAN GERVEN et al., 2007). Therefore, the evaluation of the illumination system is of extreme importance and the capability of simulating distinct configurations for this system can be of crucial importance. There are several software and codes available that employ distinct techniques to simulate the behavior of light (JENSEN et al., 2007).

In general terms, light transport algorithms can be classified as stochastic or deterministic methods. More commonly, they are referred to as either Monte Carlo algorithms or finite element-based methods (FEM), although most of the available light algorithms incorporate more than one technique in its core, which makes the classification of certain codes a difficult task (VEACH, 1997).

Figure 9 – Illumination schemes.

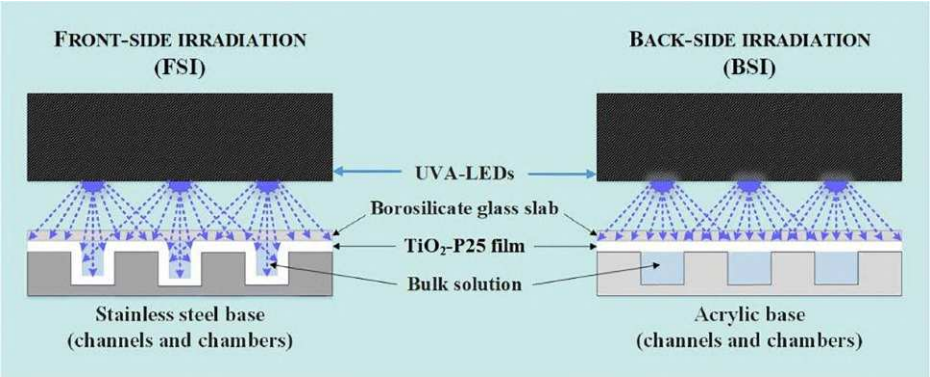

Source: Santos et al. (2019).

The finite-based algorithms are also classified as view-independent, which means that the light flow will be calculated throughout the entire domain at once (LESEV, 2010). The initial FEM techniques were adapted from radiative heat transfer methods. The initial algorithms to employ the technique forced all surfaces to be lambertian reflectors (JAKICA, 2018).

One of the most employed FEM techniques is the discrete ordinate method (DOM) that is implemented in the most common CFD software, such as Ansys Fluent®, OpenFOAM and COMSOL® (MORENO; CASADO; MARUGÁN, 2019). It consists of the solution of the radiative transport equation (RTE) (Equation 10 (VISAN et al., 2019)) via a finite element method. However, this class of codes can face limitations regarding the variation of radiative properties in the presence of scattering and reflecting walls, resulting in slow convergence (MODEST, 2003b,a).

$$\begin{aligned} &\frac{\mathrm{d}I_{\lambda,\Omega}(s,t)}{\mathrm{d}s} + \underbrace{\alpha_\lambda(s,t)I_{\lambda,\Omega}(s,t)}_{\text{absorption}} + \underbrace{\sigma_\lambda(s,t)I_{\lambda,\Omega}(s,t)}_{\text{out-scattering}} \\ &= \underbrace{j^e_\lambda(s,t)}_{\text{emission}} + \underbrace{\frac{\sigma_\lambda(s,t)}{4\pi}\int_{\Omega'=4\pi} p\left(\Omega' \rightarrow \Omega\right) I_{\lambda,\Omega'}(s,t)\mathrm{d}\Omega'}_{\text{in-scattering}} \end{aligned} \tag{10}$$

where α_λ is the spectral volumetric absorption coefficient, σ_λ is the scattering coefficient, $p\left(\Omega' \rightarrow \Omega\right)$ is the scattering phase function, $I_{\lambda,\Omega}(s,t)$ represents the spectral radiation intensity, s is a spatial parameter, Ω is the direction of propagation and λ is the wavelength.

An alternative method to determine what happens to the photons emitted by the reactor's illumination system is ray tracing. This methodology is capable to easily simulate the interactions of light with complex geometries (TSANGRASSOULIS; BOURDAKIS, 2003); and has applicability at several areas such as acoustics (MAK; ZHEN, 2015), gravitational waves (KOTAKE et al., 2009), optics (ROIBU et al., 2018; LIU et al., 2008), missile detection (ZHU; FANG, 2020), agriculture (SHIN et al., 2021), architecture (AYOUB, 2020) and animation (LIANG et al., 2016).

Ray tracing algorithms are classified as view-dependent, since the light flow will be calculated at specific areas of the geometry domain; it emulates the natural behavior of light, tracing rays through a viewing plane (sensor) at the receiving surfaces (AYOUB, 2020). Ray tracing algorithms employ a Monte Carlo-based method to simulate the behavior of light in a system. Detailed information of the geometry and the optical properties of all materials are required. In this approach light is represented though rays that follow a series of geometrical laws (LALAU KERALY et al., 2017).

Figure 10 shows the most basic steps of ray tracing simulation. First a high number of rays are emitted from a source and transported over a medium. If this medium is

homogeneous the law of rectilinear propagation is employed; this means that rays travel in straight lines. However, if the medium is inhomogeneous the integration of the eikonal equation is required (GROSS, 2005). The next step is to determine the interception point of a ray and the interface between two media and subsequently determine the change in a ray direction. The energy conservation principles are followed at every ray bounce, which means that at every interaction the ray tracing algorithm can split rays into parcels for reflection, transmission, absorption and emission (JAKICA, 2018).

Figure 10 – Basic steps of ray tracing approach.

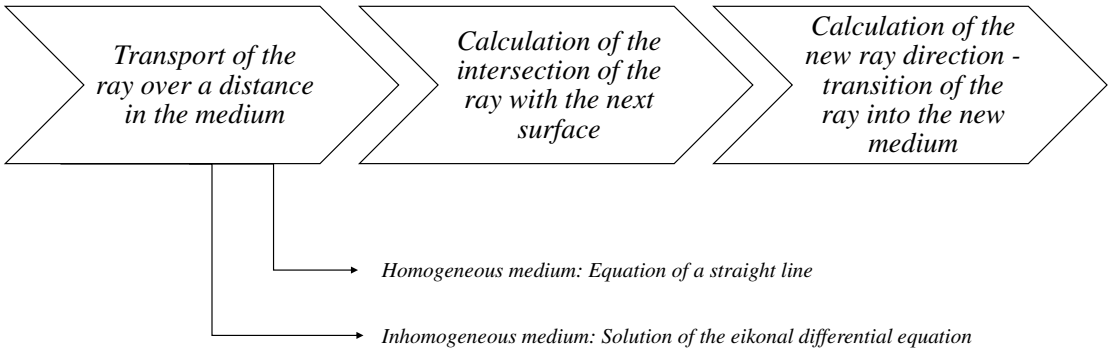

Source: adapted from Gross (2005).

To evaluate the photon transfer in a system, radiance values must be computed for a selection of points in the interest area. The light transport can be expressed in different forms according to application. The rendering equation is usually used to represent the principles of conservation applied to light. The equation can be written in terms of radiance based on the ray law as in Equation 11 (BARANOSKI; KRISHNASWAMY, 2010).

$$\underbrace{L(x,\psi,\lambda)}_{\text{total}} = \underbrace{L_{\mathrm{e}}(x,\psi,\lambda)}_{\text{emitted}} + \underbrace{L_{\mathrm{p}}(x,\psi,\lambda)}_{\text{propagated}} \tag{11}$$

where x represents a point on a surface, ψ represents the direction, λ is the wavelength and L represents the radiance.

The equation is a theoretical base from which most of the light transport algorithms are developed. However, the rendering equation does not have a closed solution. For simple cases, a series of expansions can be employed, but the equation is too complex to be solved analytically for ample use (AYOUB, 2020). Therefore, light transport algorithms based on ray tracing provide an approximated solution, with accuracy coupled to the number of rays traced.

In that sense, ray tracing algorithms need a mathematical way to describe the trajectory of the rays. There are several techniques for this task from the first trigonometric

methods to more modern algebraic methods (KIDGER, 2002). Gross (2005) details the procedures of paraxial γ-u, paraxial s-h, meridional S-U and meridional Q-U methods to position the rays in the space. The method used has correlation to the software architecture and impacts simulation speed.

Ray tracing algorithms can also be classified as forward, when rays follow the natural ray direction, from source to view plane; and backward, when light is traced from viewer to surfaces (AYOUB, 2020). Ray tracing software can be sequential or non-sequential. In sequential ray tracing, rays reach optical surfaces sequentially in a pre-defined order (OKUMURA et al., 2011). In non-sequential ray tracing, the rays can reach the surfaces in any order and at any number of times with automatic ray splitting (STEVENSON, 2006). Since several ray processes are computed at the same time, a probabilistic Monte Carlo method is of particular usefulness for non-sequential algorithms. This probabilistic method will determine the ray path with random numbers according to the corresponding probabilities of an event (GROSS, 2005).

Although ray tracing algorithms require several computational techniques to achieve a viable code implementation, the core of the technique is based on simple laws of geometrical optics. These physical principles are briefly summed in the following sections.

2.3 NATURE OF LIGHT

The nature of light is yet not completely understood by the scientific community. Many models and mental concepts have been used throughout the years in order to improve our understanding of its nature and properties. Recent developments define light as a specific range of electromagnetic energy (FEYNMAN, 2006; VANDERGRIFF, 2008). The term "photon", that comes from the Greek word for light, has a long history that was reshaped in many occasions as described by Hentschel (2018). He also enumerates in detail the history and main contributions of several of the conceptual models of the light quantum, as follows:

1. corpuscular model: interprets light as a stream of very small spherical corpuscles;
2. singularity model: associates electromagnetic fields with singular points of denser centers in the field;
3. binary model: considers structures with two components where oscillations and rotation degrees of freedom have impact in the generation of wave characteristics;
4. wave packet: considers that light quanta, similar to matter waves, is a localized phenomenon constricted to small region of the space-time;

5. semiclassical model: attempts to combine classical electromagnetic waves and quantized matter concepts;

6. QED - Quantum Electrodynamics: in this case the photon is a massless, exchange 'particle' that bounces back and fourth at electromagnetic interactions.

Almost all light related phenomena can be described using the quantum electrodynamics theory, also known as quantum optics, the most recent theory developed. Excluding the phenomena that are intrinsically of quantum mechanics nature, it is encountered what is called classical optics. The electromagnetic optics theory provides the most complete description of light phenomena in the classical domain. There are, however, more simplistic theories, such as wave optics, that can describe most of the optical phenomena through scalar wave functions and ray optics that employs geometrical rules to account for the propagation of light through objects that have dimensions significantly higher than the wavelength of the light. The theories were chronologically developed with the increase in completeness and complexity, as illustrated in Figure 11 (SALEH; TEICH, 2019).

Figure 11 – Optical theories in proposition and complexity order, from the simplest ray optics to the most complete quantum optics.

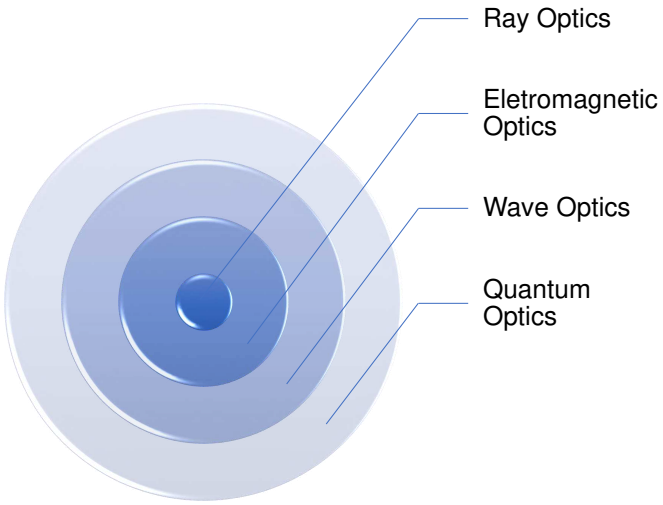

Source: adapted from Saleh and Teich (2019).

It is well established that electromagnetic radiation has similar wavelike properties, that in turn are function of the wavelength (VANDERGRIFF, 2008). Figure 12 shows the electromagnetic wave spectrum, ranging from the short gamma rays to the longer radio waves. In photocatalysis, it is of particular interest the ultraviolet (UV) range, since it is the wavelength that activate the catalytic properties of TiO_2. Also, there is a series of works

focused in the achievement of TiO_2 doped materials that have catalytic properties activated in the presence of visible light (ETACHERI et al., 2015).

Figure 12 – Electromagnetic spectrum.

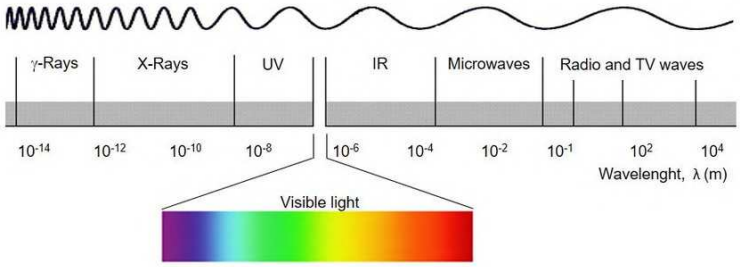

Source: Casimiro et al. (2019).

2.4 OVERVIEW OF BASIC RAY OPTICS CONCEPTS

As mentioned previously, ray optics is the simplest and oldest of the optical formulations. Some of its principles and laws were already discussed in ancient times by Greek mathematicians (GIUSFREDI, 2019; WYROWSKI et al., 2015; VOHNSEN, 2004). In this case, light is described by rays that travel through distinct media obeying a set of geometrical rules, and for that, is also referred to as geometrical optics (SALEH; TEICH, 2019). Ray optics theory was developed on its own, however, it can be related to Maxwell's equations inside the electromagnetism's theory. Therefore, with a set of approximations, is possible to go from Maxwell's equations to geometrical optics (MOLESINI, 2005).

According to Mahajan (2014) the rays of light propagate following three laws; i) rectilinear propagation; ii) refraction; and iii) reflection. The rays are not physical entities, they are a useful way to represent the propagation of light. Rays are lines perpendicular to wave fronts that specify the direction of energy flow in a wave (PEDROTTI, 2008).

Geometrical optics addresses the locations and directions of light rays, allowing rays to be traced through an optical system and establish the optical energy that crosses a specific area (SALEH; TEICH, 2019). Therefore, ray optics constitutes an interesting option to calculate the amounts of energy that a light source can provide for the illumination of a catalytic surface area. The next topics summarize the most relevant principle of the ray optics formulation.

2.4.1 Reflection of light

At an interface between materials, ray optics account for four possibilities: i) light is partly or totally reflected; ii) can be scattered in random directions; iii) can be partly

refracted (transmitted) and enter the second medium; or iv) it can be partly absorbed by any of the medium (PEDROTTI, 2008).

The law of reflection, for plane surfaces, states that the angle of reflection is identical to the angle of incidence (BHATTACHARJEE, 2005). The same affirmation is valid for curved surfaces. The difference is the drawn of a surface plane tangent to the point of incidence (PEDROTTI, 2008).

Basically, three types of reflection can be found when light reaches the interface of a material. As Figure 13 illustrates, the three possibilities for reflection are: a) specular; b) spread and c) diffuse. The specular reflection, common behavior for mirror and polished surfaces, presupposes that a ray of light will be reflected with the same angle that it reached the surface. A rough and uneven surface will not be capable to reproduce this effect, and will reflect light with several angles that are approximately the same of the incident one. This behavior is called spread reflection. For surfaces rough or matte surfaces, light will be reflected in several directions at once, with many distinct angles. This diffuse reflection is usually called scattering or lambertian scattering (TAYLOR, 2000).

Figure 13 – Types of reflection.

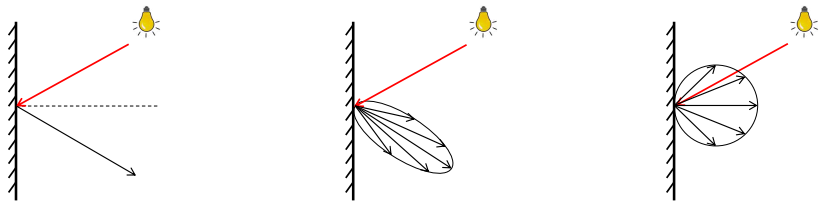

a) Specular b) Spread c) Diffuse

Source: elaborated by the author (2022).

2.4.2 Refraction of light

When light reaches an interface, it can be partially reflected and partially transmitted to the next medium. Therefore, the need of characterization of each medium is necessary. This characterization is done via an index, denominated index of refraction.

2.4.2.1 Index of refraction

In a vacuum, light travels at a constant speed of $2.99 \cdot 10^8$ m/s. However, at different media the speed is altered; for example, light traveling through clear air is about 0.03% slower than light traveling through vacuum. Through glass media the light traveling velocity can be around 30% slower (VANDERGRIFF, 2008).

In vacuum, all light waves travel at the same speed. In other media, the travel speed differs according to the light wave. The velocity at any medium is determined as the product of the frequency (that is independent of the media) by the wavelength (Equation (12)):

$$v = f\lambda \tag{12}$$

The index of refraction (*n*) relates the light speed in vacuum (c) with the light speed registered in other media (v_m), as expressed in Equation (13). For air and most gases, the index of refraction is very close to 1, and therefore is usually the employed value (PEDROTTI, 2008).

$$n = \frac{c}{v_m} \tag{13}$$

2.4.2.2 Snell's law (law of refraction)

Snell's law (Figure 14) is the basis of ray tracing technique. It determines the change in the direction of a ray at materials interfaces.

Figure 14 – Snell's law of refraction.

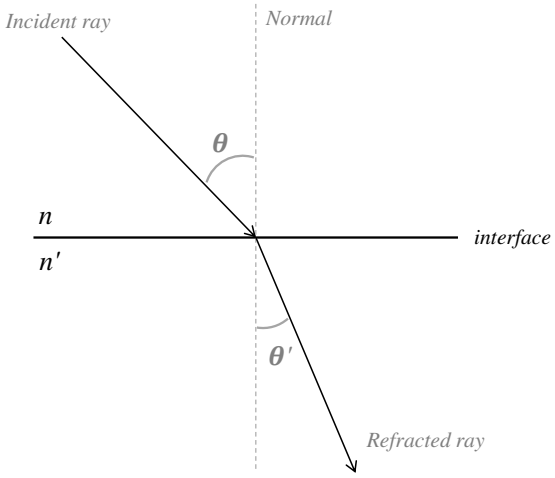

Source: elaborated by the author (2022).

This law correlates the index of refraction of two media with the incident and refracted angles, according to Equation (14). Also, Snell's law can be used for reflection, reversing the sign of the incident material index (BENTLEY; OLSON, 2012).

$$n\ sin\ \theta = n'\ sin\ \theta' \tag{14}$$

where n is the index in the incident medium, θ is the angle of incidence, n' is the index in the refracting medium and θ' is the angle of refraction.

2.4.2.3 Critical angle and total internal reflection

When the direction of light goes from a medium of higher index to one of lower index of refraction a ray can face four outcomes as described by Pedrotti (2008):

Figure 15 – Critical angle and internal reflection: a) ray normal to the interface; b) incident angle smaller than the critical one; c) critical angle; and d) incident angle greater than critical value, leading to internal reflection.

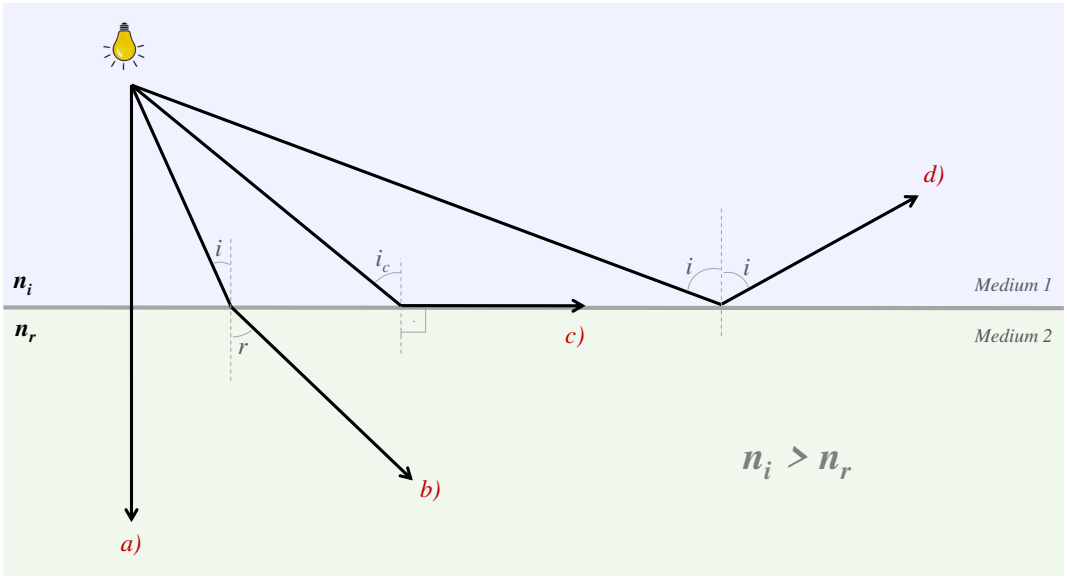

Source: elaborated by the author (2022).

1. if the angle of incidence is normal to the interface, the ray will keep traveling with the same direction into the next medium, and will gain speed due to the change in index and will suffer no bending (ray *a)* in Figure 15);

2. if the ray reaches the interface with a smaller angle than the critical, light will bend and keep traveling into the next medium (ray *b)* - Figure 15);

3. if the ray reaches the interface at a specific critical angle, it will bend in order to be parallel to the interface, and will keep traveling at the interface plane (ray *c)* - Figure 15);

4. the last possibility is the ray reaching the interface with an angle greater than the critical one. In this case the ray will follow the law of reflection and will be reflected into the same medium that it came from (ray *d)* - Figure 15).

The fourth possibility is particularly interesting for fiber optics and is also observed in the simulations of this thesis for the FSI disposition of the catalyst. In these simulations, after light is emitted from a source, it travels through an air medium until it reaches a glass slab, and afterwards it must travel through the reactor flow. This flow constitutes basically of contaminated air, that has a lesser index than the glass. Therefore, some of the rays will keep being reflected internally on the glass window.

The critical angle (i_c) is determined through Snell's law (Equation (14)) with the refracting angle equivalent to 90·. Therefore, the critical angle can be determined with Equation (15).

$$i_c = \sin^{-1}\left(\frac{n'}{n}\right) \tag{15}$$

2.4.3 Absorption of light

The absorption of light within a medium can be described by the Beer-Lambert law of absorption (Equation (16)), which states that an equal thickness of a given homogeneous material absorbs the same fraction of light (TAYLOR, 2000). This gives an exponential relationship between the amount of incident light and the path of the traveling light. For example, an $'x'$ length of a certain material absorbs 50% of the electromagnetic energy that is incident at this material. A length of $2'x'$ would then absorb 75% of the incident light.

$$I = I_0 e^{-\beta c x} \tag{16}$$

where I is the intensity of transmitted light, I_0 is the intensity of light entering the material (excluding the fraction of light that is reflected), β is the absorption per concentration coefficient, c is the concentration of the absorbing material and x is the path length in which light will travel.

2.4.4 Radiometric quantities

Radiometry refers to the physical measurement of electromagnetic radiation. The radiometric quantities commonly employed to light transport simulations are the radiant power, radiant intensity, radiance and radiant exitance (Table 2). These quantities describe

measurements integrated over all wavelengths, and the term spectral is added to characterize the measurement for a specific wavelength (BARANOSKI; KRISHNASWAMY, 2010). The main radiometric quantities are defined below.

Radiant energy (Q) [J]: express the energy of a packet of rays.

Radiant power (Φ) [W]: is the most fundamental radiometric quantity, also denominated as flux. It expresses how much energy flows across a surface over time.

Irradiance (E) [W/m^2]: is the incident radiant power on a surface per unit of area (Equation (17)).

$$E = \frac{d\phi}{dA} \tag{17}$$

Radiance (L) [W/srm^2]: quantifies the emission of particles as a flux per unit of projected area per solid angle. It represents the amount of energy that arrives or leaves a point on a surface per unit of solid angle and per unit of projected area. Radiance varies with position and direction vector (Equation (18)) (DUTRÉ; BALA; BEKAERT, 2006).

$$L = \frac{d^2\Phi}{d\omega dA^{\perp}} \tag{18}$$

where L is radiance, Φ is the radiant power, $d\omega$ is a differential direction (or solid angle), $dA^{\perp}$ is a hypothetical differential area perpendicular to the direction.

Table 2 – Radiometric and photometric quantities.

Quantity	Formula	Radiometric term	Unity	Photometric term	Unity
Energy	Q	Energy	W · s = J	Luminous Energy	Lm · s
Power Radiation Flux	Φ		W	Luminous Flux	Lm
Power per Area and Solid Angle	$L = \frac{d^2\Phi}{\cos\theta d\Omega dA}$	Radiance	W/sr/m^2	Luminance	cd/m^2
Power per Solid Angle	$I = \frac{d\Phi}{d\Omega} = \int L dA_{\perp}$	Radiant intensity	W/sr	Luminous Intensity	Lm/sr, cd
Emitted Power per Area	$E = \frac{d\Phi}{dA} = \int L \cdot \cos\theta d\Omega$	Radiant exitance	W/m^2	Luminous excitance	Lm/m^2
Incident Power per Area	$E = \frac{d\Phi}{dA} = \int L \cdot \cos\theta d\Omega$	Irradiance	W/m^2	Illuminance	Lx = Lm/m^2
Time Integral of the Power per Area	$H = \int E dt$	Radiant exposure	W · s/m^2 = J/m^2	Light exposure	Lx · s

Source: Gross (2005).

2.5 MODELING AND SIMULATION OF PHOTOCATALYTIC REACTORS: STATE OF THE ART

The potential of photocatalysis in areas of green energy conversion and environment purification is remarkable. However, the commercialization and popularization of the technique seems to be limited by the difficulties of scaling up the process. It is mainly in this sense that computer simulations can help improve the technology, being a key tool for photoreactor's optimization (JANCZAREK; KOWALSKA, 2021).

The modeling of photocatalytic reactors has three key elements: radiation model, kinetic model and fluid dynamic model. Computational fluid dynamics (CFD) is one of the most precise methods to simulate the species transport within air flows (NAKAHARA et al., 2020) and has been extensively employed for photocatalytic reactors simulation and optimization. CFD employs the mass and momentum conservation equations to describe the fluid flow. This method presents a superior precision in comparison to simplified models such as plug flow and eliminates the necessity of several correlations when the reactor's geometry is complex (TAGHIPOUR; MOHSENI, 2005).

The kinetic mechanism and reaction rate model are crucial to the performance of photocatalytic reactor simulations. The reaction rate model does not always reconstruct the group of reaction mechanisms (OLLIS, 2018). Anyhow, a rate model that fits experimental data, desirably with intrinsic parameters, is fundamental to the description of a specific or a group of pollutants degradation. For photocatalytic processes this reaction rate model is usually expressed in some form of Langmuir-Hinshelwood or power law equations (MUESES et al., 2021).

Nakahara et al. (2017) employed CFD simulations using Ansys Fluent® to evaluate the photocatalytic oxidation of toluene at ceramic building materials coated with TiO_2 using the CFD simulations as a tool for kinetic parameters definition. Verbruggen, Lenaerts, and Denys (2015) compared the obtained Langmuir-Hinshelwood parameters via analytic and CFD approaches for pollutant degradation in a slit photocatalytic reactor. Brito Lira et al. (2019) evaluated the abatement of NO_x from gas streams at a slit reactor using CFD, and latter Lira et al. (2020) combined CFD with surface response analysis to optimize the photocatalytic reactor.

One of the main challenges in photocatalytic reactors simulations is related to light modeling, since fluid-dynamics is already a consolidate field and the kinetic models based on empirical data can represent the global reactions. There are several methods to solve radiation transport, those can be stochastic or deterministic methods.

Salvadó-Estivill, Hargreaves, and Li Puma (2007) coupled the kinetic model of trichloroethylene degradation with radiation field data. Authors used a flat plate reactor illuminated with 1, 3 or 5 blacklight blue florescent lamps. The linear source spherical emission model (LSSE) was used to represent lamps emission. The model considers the cylindrical lamp to be a line source, in which each point emits radiation in every direction isotropically.

Zimeng et al. (2012) evaluated the dimethyl sulfide (DMS) oxidation in a photocatalytic plate reactor. Similarly to the model used by Salvadó-Estivill, Hargreaves, and Li Puma (2007), Zimeng et al. (2012) developed a method to simulate the 17 LEDs used to illuminate the plate reactor. Authors found that the proximity of the LEDs to the photo-

catalyst has great impact in the radiation intensity and uniformity. Increasing the distance of LEDs to catalyst improves the uniformity at the expense of radiation intensity.

Zazueta, Destaillats, and Li Puma (2013) used an in-house code of a Monte Carlo method to simulate and optimize the radiation field in a modular multi-plate photocatalytic reactor (MPPR) for air or water purification. The reactor is composed by a series of parallel plates where the catalyst is deposited. These plates are perforated to accommodate cylindrical UV lamps that are orthogonal to the plates. Authors tested illumination systems with 1, 4 and 5 lamps. Dimensionless parameters, that account for geometrical location of lamps, were evaluated to optimize the illumination system efficiency, considering photon absorption and field uniformity.

Roegiers, Walsem, and Denys (2018) developed a multiphysics model for a gas phase photocatalytic reactor applied in the oxidation of acetaldehyde. The reactor is composed by a glass tube (d = 29 mm) with seven smaller (d = 7 mm) tubes in its interior. The interior tubes are coated with TiO_2 and the reactor is illuminated by two external cylindrical lamps. Irradiance and emission spectrum of the lamps were measured by a spectrometer. Irradiance was measured at different points of the reactor. The radiation field was simulated using a ray optics module contained in COMSOL Multiphysics. Simulations were validated via experimental data and the irradiance simulated was latter coupled to CFD and kinetic modeling.

Moreno, Casado, and Marugán (2019) implemented a new DOM module in OpenFOAM, aiming the simulation capability of both diffuse and specular phenomena for surfaces and volumetric conditions. The adaptive quadrature implemented in the DOM was validated with experimental data and the code verified against other DOM already implemented and available to simulations. The main improvement proposed by the authors regards the emission surfaces, in order to better represent LEDs and achieve an accuracy similar to ray tracing techniques. In another paper (MORENO-SANSEGUNDO; CASADO; MARUGÁN, 2020), the authors employed the improved DOM for the radiative transfer simulation of an annular photoreactor (isotropic emission), a CPC solar photoreactor (parallel light emission) and a tubular LED cone reactor (cone-shaped and power-cosine emission). The results were successfully compared to the same method being solved in Ansys Fluent®.

Muñoz et al. (2019) evaluated the radiation incidence over a ceramic plate coated with catalyst for NO_x degradation. The Ansys Fluent® DOM method was employed with an angular discretization value (15 x 15) optimized to have accurate results with time reasonable cost. Cilindrical lamps were used in experiments and were modeled as isotropic emitting surfaces. The catalyst to lamp height was varied in order to obtain a high radiation uniformity in the catalyst area. The irradiance value was then averaged and introduced in

the kinetic model as a constant.

Passalía et al. (2020a) simulated the radiation field in the NETmix photocatalytic reactor employing the DOM implemented in Ansys Fluent®. Two configurations of the photocatalyst were simulated for an illumination system composed of 18 LEDs. The geometry was discretized with about $1.7{\cdot}10^6$ elements and the simulation time registered by the authors is of around 50 min. The performance of the photoreactor was evaluated according to an efficiency in series method considering three efficiencies: i) outer geometrical; ii) inner geometrical; and iii) reaction photonic efficiency for the aqueous phase degradation of As(III) (trivalent arsenite) into As(V) (pentavalent arsenite).

2.6 CHAPTER'S CONCLUDING REMARKS

Photocatalysis is a versatile process with applications ranging from energy production to environmental remediation purposes. It is one of many techniques available to remove pollutants from air streams. Photocatalytic oxidation processes have two limitation issues: photon transfer and mass transfer. Therefore, literature is abundant on reactors configurations for both illumination system and reaction chamber configurations. The distinct geometrical characteristics of the reactor are proposed to improve catalyst surface to reactor volume ratio and improve catalyst illumination.

Numerical simulations of heterogeneous photo-oxidation processes consist of two main parts: light transport simulation and fluid dynamics simulation. In general terms, fluid dynamics is already a widely explored area, and the main challenge for heterogeneous photocatalysis is the implementation of a good kinetic model for the reaction in question. The base of this reaction rate models is dependent of experimental analysis.

Light transport simulation is a bit more challenging. Although several algorithms have been proposed and are implemented in a number of commercial software, few studies consider the simulation of light transport, and propose alterations in the illumination systems in order to improve irradiance distribution and reactor's efficiency. Besides that, researchers commonly employ averaged irradiance values, obtained through separate simulations of light, into fluid dynamics simulations; therefore, do not take into consideration the irradiance distribution in the catalyst area.

Based on these statements, the current work aims to evaluate the irradiance profile captured at the surface of the catalyst though ray tracing simulations. In addition to the investigation on the impact of LEDs-to-catalyst distance like most of the available literature, this work also investigates the impact of the LEDs-to-LEDs distance and the number of employed LEDs. The irradiance values are evaluated along with the absorption efficiency and the light homogeneity over the catalyst surface. Also, to investigate the relevance of

the field homogeneity, light transport simulations are coupled with fluid dynamics. Again, differently than most literature works, instead of the implementation of an averaged irradiance value, the irradiance profile is coupled with the CFD simulations in this work, meaning that for each point of the catalyst surface a irradiance value, according to the ray tracing simulations, is employed for the calculation of the reaction rate. This procedure generates insight into the influence of the LEDs position over the photocatalytic efficiency of a system.

3 RADIATION FIELD MODELING OF THE NETMIX MILLI-PHOTOCATALYTIC REACTOR: EFFECT OF LEDS POSITION OVER THE REACTOR WINDOW

This chapter is based on the paper entitled “Radiation Field Modeling of the NETmix Milli-Photocatalytic Reactor: Effect of LEDs Position over the Reactor Window” (Chemical Engineering Journal, doi.org/10.1016/j.cej.2021.131670), by Tatiana Matiazzo, Kishor Ramaswamy, Vítor J.P. Vilar, Natan Padoin and Cíntia Soares. Abstract, keywords, acknowledgments and references were omitted.

3.1 INTRODUCTION

Since the first studies conducted by Fujishima and Honda (1972) on water splitting into hydrogen and oxygen in the presence of light and a semiconductor material, photocatalysis gained visibility and is the topic of several studies with a variety of applications (BOYJOO et al., 2017), such as liquid and gas streams decontamination, synthesis of high value products (IBHADON; FITZPATRICK, 2013; DAGHRIR; DROGUI; ROBERT, 2013) and many others.

The design of a photocatalytic reactor has two main challenges: mass transfer and photon transfer. Mass transfer can be influenced by operational parameters and by catalyst properties. However, mass transfer limitations can have lesser impact concerning gaseous streams (VAN GERVEN et al., 2007; DINGWANG; LI; RAY, 2001). The photon transfer is influenced by the illumination mechanism, by the catalyst thickness and also by the light source type and geometrical arrangement over the reaction zone (PADOIN; SOARES, 2017; ZAZUETA; DESTAILLATS; LI PUMA, 2013). The literature shows that the distance between light sources and the photocatalytic reactor has great influence over the radiation field registered on the catalyst. It has been shown that the increase in this distance improves the uniformity of the field at the expense of radiation intensity (ZIMENG et al., 2012; MUÑOZ et al., 2019). This work aims to explore the impact of LEDs-to-LEDs distance besides the evaluation of LEDs-to-reactor distance.

Recently, light emitting diodes (LEDs) gained attention and boosted photocatalytic applications, since this light source has less limitations related to sustainability and environment matters in comparison to the traditional light sources (ZIMENG et al., 2012). For example, mercury vapor lamps, besides containing a hazardous heavy metal, demand high energy consumption and need a cooling system. In the use of solar light, for instance, there is a demand for large areas, which results in high installation costs and there are limitations on the operational time (JO; TAYADE, 2014). Therefore, LEDs are presented as a more viable alternative for photocatalysis, offering several advantages, such as: i) low energy consumption; ii) high lifetime; iii) narrow emission spectrum, resulting in a pseudo-

monochromatic emission, closer to the photocatalyst band-gap, and iv) small dimension, ideal for light source miniaturization (BOYJOO et al., 2017; HOU; KU, 2013; CHEN; LOEB; KIM, 2017).

To simulate the photon transfer, researchers have been using light transport algorithms that are finite element or Monte Carlo (MC) based (AYOUB, 2020). An example of finite element-based algorithm is the discrete ordinate model (DOM), one of the most widespread models for the solution of the radiative transport equation (RTE) (JENSEN et al., 2007; MODEST, 2003a). Nonetheless, finite element techniques can run into difficulties if radiative properties vary with direction and in the presence of scattering and reflecting walls, which might implicate in slow convergence (MODEST, 2003a,b).

Monte Carlo based algorithms are then an alternative capable of dealing with complex geometries without excessive computational demands. MC has a probabilistic core that will be employed to trace the probable path of the photons being emitted from a light source and its interactions with the materials that compose the reactor (AKACH; KABUBA; OCHIENG, 2020; ASADOLLAHFARDI et al., 2018; ZAZUETA; DESTAILLATS; LI PUMA, 2013).

Zimeng et al. (2012) used 27 LEDs to illuminate a photocatalytic reactor for the dimethyl sulfide degradation in a gas stream. The radiation field was evaluated based on a linear source spherical emission model (LSSE). The authors compared distinct distances between the reactor and the LEDs plate and verified that this distance presents a strong influence over the radiation intensity. Zazueta, Destaillats, and Li Puma (2013) implemented a Monte Carlo algorithm to simulate the radiation field of cylindrical lamps crossing TiO_2 catalytic plates. They varied the number of lamps and optimized the distance between lamps, evaluating the impact on the light absorption efficiency and the uniformity of light distribution over the catalyst surface. It was assumed that no band-gap photons could be transmitted through the photocatalytic film, and that absorbance and reflectance were independent of light incident angle. Passalía et al. (2020b) simulated an arrangement of 18 LEDs to illuminate a meso-scale reactor known as NETmix employing a DOM method. Two illumination mechanisms were compared. A concept of efficiencies in series was proposed and associated with the oxidation of trivalent arsenate to pentavalent arsenate in aqueous solutions.

In the current work, a non-sequential ray tracing, based on Monte Carlo, was employed for the evaluation of the NETmix reactor illumination system. In this technique rays can hit the same surface multiple times without any predefined order with ray scattering (NÉMETH; VERES; NAGY, 2012). Therefore, the rays can interact with the system materials as it would in real life. The main advantage lays on the capacity to simulate complex geometries in the presence of diffuse surfaces with high accuracy. This allows the repre-

sentation of the TiO_2-P25 catalyst, employed in this work, as a mixture of specular and lambertian reflections that vary with the light incident angle. The irradiance values were validated with experimental data and afterwards the geometrical arrangement of the 18 LEDs towards the reaction zone is investigated. Twenty-seven arrangements of the 18 LEDs were proposed and the incident radiation flux over the catalyst surface was obtained for the front side and back side illumination mechanisms, where the catalyst is immobilized in the channels and chambers of a back stainless steel slab or in one side of the front borosilicate glass slab (the “window”-radiance entrance to the reactor), respectively. An ideal arrangement can then be appointed through the analysis of the absorption efficiency, variation coefficient and irradiance magnitude.

3.2 REACTOR DESIGN AND EXPERIMENTAL DATA

The photocatalytic reactor employed in this study is known as NETmix. A detailed description of the entire apparatus is given by Da Costa Filho et al. (2019). The reactor is composed of a stainless steel slab (SSS) engraved with a series of cylindrical chambers interconnected by prismatic channels. The SSS is sealed with a high transparency borosilicate glass slab (BGS), resulting in a reactor window of 136 mm $\times$ 76 mm.

The illumination system consists of 18 LEDs units total, arranged in three arrays with 6 LEDs each. The geometrical arrangement of the LEDs located above the reactor window is described in Figure 16. The Seoul Viosys UV Z5 series, CUN66A1B, was the selected LED, with a peak wavelength of 365 nm, a spectrum half width equivalent to 9 nm, radiant power of 900 mW and a view angle of 120 degrees.

Da Costa Filho et al. (2019) employed a 2-nitrobenzaldehyde method to determine via actinometry the radiant power inside the reactor. The method returned a value of 5.3 $\pm$ 0.1 W for an 18 LEDs array disposed according to Figure 16.

Thin TiO_2-P25 films were uniformly immobilized by a spray method in one side of the borosilicate glass slab or in the walls of the channels and chambers of the stainless steel slab. When the catalyst is supported in the BGS, the illumination mechanism is denominated back-side illumination (BSI), (Figure 17). In this case, the light must go through the BGS until it reaches the catalyst film surface that is in direct contact with the reactive flow. In the case where the catalyst is supported in the SSS, the illumination mechanism is known as front-side illumination (FSI). The light must travel across the BGS and then go through the fluid until it reaches the catalyst surface where the reactants are adsorbed.

Figure 16 – LEDs geometrical position.

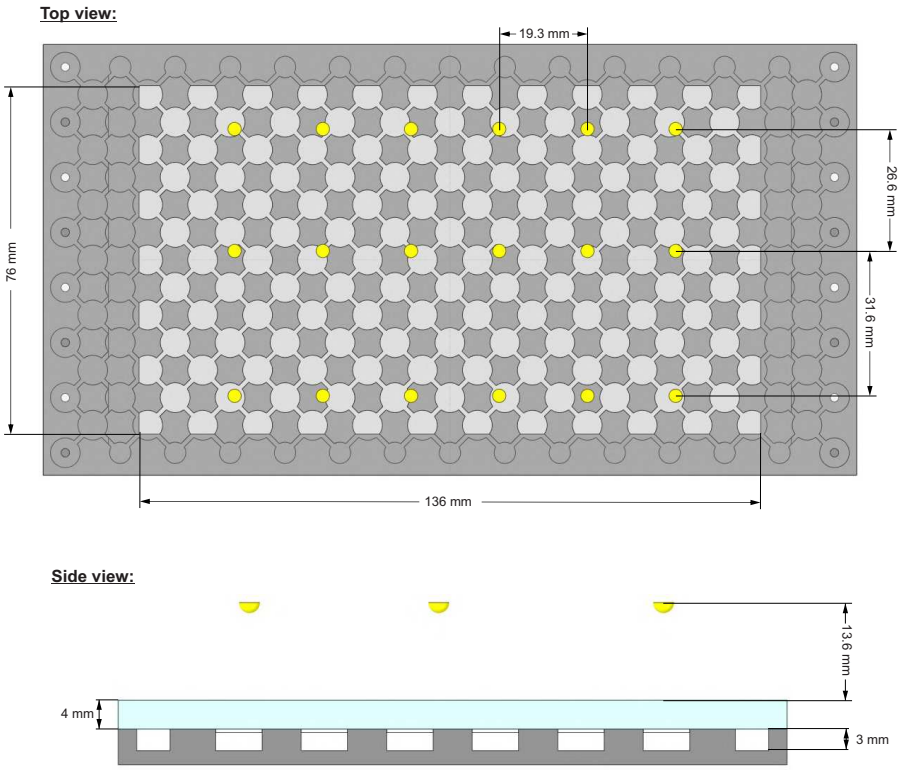

Source: Matiazzo et al. (2022a).

3.3 NUMERICAL METHODOLOGY

To analyze the light intensity that reaches the catalyst surface, the optical software Ansys Speos® was employed. The software uses a non-sequential ray tracing algorithm based on Monte Carlo method that enables the user to simulate the light interactions with distinct materials (NÉMETH; VERES; NAGY, 2012).

3.3.1 Light sources

In order to simulate the photoreactor system, it is necessary to create illumination sources that will represent the LEDs used in experiments. Therefore, 18 surface sources were created with the following information: i) LEDs surface area; ii) power emitted by each LED, which in this case is equivalent to 0.9 W; iii) light spectrum (365 nm peak, 9 nm half width); and, iv) light intensity distribution, which is provided by the manufacturer. The LEDs near-field and far-field intensity distribution is available in the supplementary material (Appendix C).

Figure 17 – NETmix BSI and FSI schemes.

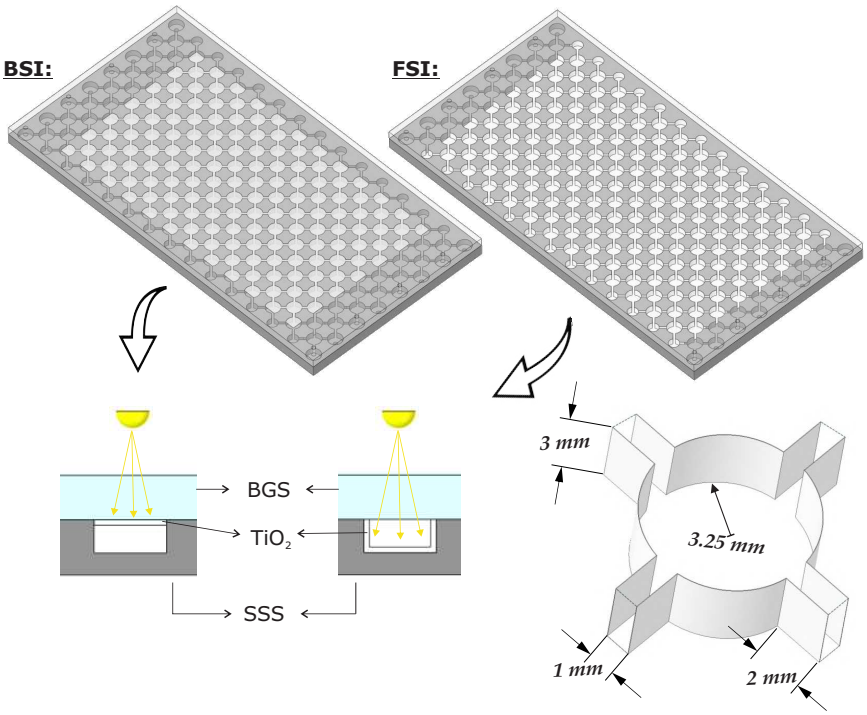

Source: Matiazzo et al. (2022a).

3.3.2 Materials and optical properties

The optical properties of the three materials that affects light distribution (borosilicate glass, TiO_2-P25 catalyst, and stainless steel) inside the reactor must be defined and volume and surface properties are required. The volume properties of the BGS includes the refraction index ($n_{d\ (\lambda=587{,}6\ nm)}$ = 1.47140) and the Abbe number (V_e = 65.41), both values reported by the manufacturer. For the surface properties of the BGS the optical polished type was used, which means that Fresnel equations are employed to calculate the surface interactions. For the SSS, the volume property was set as opaque type, which is employed for non-transparent materials, and the surface property was define as mirror type, used for perfect specular surfaces, with the reflectance adjusted to 90%, in accordance to the work of Nakahara et al. (2017).

The literature shows that the TiO_2 films properties are dependent on immobilization technique, temperature of immobilization, film thickness, besides TiO_2 phase proportions and granulometry (MIKHAILOV et al., 2018; STA et al., 2014; SHEI, 2013). Therefore, there is no consensus regarding optical properties of TiO_2 in the literature. For the volume properties of TiO_2 a refractive index equivalent to $n_{d\ (\lambda=587{,}6\ nm)}$ = 2.61420 and an Abbe number of 9.87 were employed in accordance to DeVore (1951).

Advanced surface properties option was selected to characterize the surface properties of TiO_2, where reflection, absorption and transmittance data according to the incident angle and wavelength must be informed. In this work, the wavelength dependence was kept constant. According to Janecek and Moses (2008b), TiO_2 is a reflector that presents a combination of lambertian and specular reflection, meaning that when light reaches TiO_2 surface, part of it will be reflected with the same angle of the light that reaches its surface (specular reflection), and part of it will be reflected in a broad range of directions (lambertian/diffuse reflection). Janecek and Moses (2008a) measured the proportion of light that is reflected as lambertian against specular according to the incident angle of light.

Therefore, the fraction of light that is transmitted, absorbed and reflected by the TiO_2 catalyst was defined according to a sensibility test. Regarding reflection, lambertian and specular reflection were considered, always maintaining the fractions of each reflection as established in the work of Janecek and Moses (2008a). The values employed in this work to simulate a high porosity ($\sim$50-60%) thin film of TiO_2 are listed in Table 3. The catalyst thickness employed for the BSI and FSI configurations correspond to 5.3 μm and 17.3 μm, respectively.

Table 3 – Optical properties of TiO_2.

Incident Angle (°)	0	10	20	30	40	50	60	70	80	90
Specular (%)	0.7	1.4	2.1	3.5	8.4	18.9	28.0	32.2	33.6	34.3
Lambertian (%)	34.3	33.6	32.9	31.5	26.6	16.1	7.0	2.8	1.4	0.7
Absorption (%)					60.0					
Transmission (%)					5.0					

Source: Matiazzo et al. (2022a).

3.3.3 Simulation and Sensors Properties

The effects of the illumination system over the catalyst surface are analyzed through a radiometric sensor located at its surface. A planar integration, orthogonal to the sensor plane, is employed, taking into account the cosine fall off of the irradiance as a function of the incident angle (Equation (19)), according to Bouguer's law.

$$E = \frac{I\ cos\ \varepsilon}{D^2} \tag{19}$$

where E represents the irradiance in W/m^2, I is the intensity in W/sr, ε is the incident angle and D is the light travel distance.

The sensor requires the creation of a mesh. As a result of an independence test, the created triangular mesh employs a sag value (maximum distance that can exist between

mesh and geometry) and a step value (maximum length of a segment) equivalent to 0.75 mm; and a meshing angle (maximum angle tolerated between the normal of the tangent formed at each segment ends) of 15°. Irradiance values are registered at each vertex of the mesh. This means that for the BSI and FSI mechanisms, respectively, a data set of 15,192 and 103,341 nodes are analyzed.

A Direct Simulation is then conducted, this means that the propagation of rays from sources to sensor is tracked. Double precision was enabled for the ray tracer and the maximum number of surface interactions was kept as 100, which means that a ray can interact 100 times with the geometry before its propagation stops. To end the simulation a criterion must be set, such as, a specific time or a number of processed rays. In this case, simulations were finalized after the processing of $1.8{\cdot}10^7$ rays.

3.3.4 Simulated Cases

In order to evaluate the positioning of the 18 LEDs over the reactor window area, three parameters were created: ω and ℓ that represents the distance between LEDs in the z-axis and x-axis direction, respectively, and h that indicates the distance between the LEDs plate and the reactor window as depicted in Figure18. For each variable, three distinct values were used in simulations. Therefore, a total of 27 simulations were performed according to Table 4.

Both ω and ℓ are dimensionless parameters, based on the distance of LED to LED divided by the usable values of window width and length, respectively.

Table 4 – Simulated cases.

Case	ℓ	ω	$h\ (mm)$	Case	ℓ	ω	$h\ (mm)$
Case 1	0.2	0.2	6	Case 15	0.5	0.6	14
Case 2	0.2	0.4	6	Case 16	0.9	0.2	14
Case 3	0.2	0.6	6	Case 17	0.9	0.4	14
Case 4	0.5	0.2	6	Case 18	0.9	0.6	14
Case 5	0.5	0.4	6	Case 19	0.2	0.2	22
Case 6	0.5	0.6	6	Case 20	0.2	0.4	22
Case 7	0.9	0.2	6	Case 21	0.2	0.6	22
Case 8	0.9	0.4	6	Case 22	0.5	0.2	22
Case 9	0.9	0.6	6	Case 23	0.5	0.4	22
Case 10	0.2	0.2	14	Case 24	0.5	0.6	22
Case 11	0.2	0.4	14	Case 25	0.9	0.2	22
Case 12	0.2	0.6	14	Case 26	0.9	0.4	22
Case 13	0.5	0.2	14	Case 27	0.9	0.6	22
Case 14	0.5	0.4	14				

Source: Matiazzo et al. (2022a).

Figure 18 – LEDs positioning parameters.

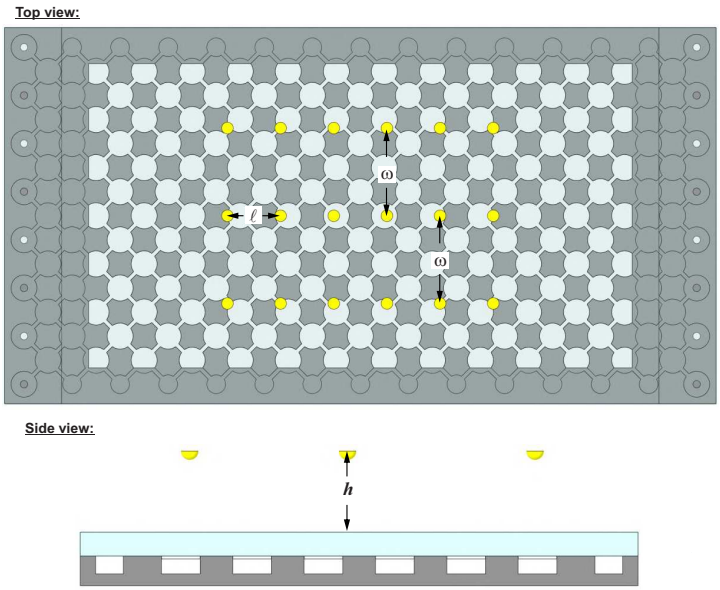

Source: Matiazzo et al. (2022a).

As stated previously, the simulations return a value of irradiance for each meshing node. Therefore, to evaluate the impact of the LEDs positioning the absorption efficiency will be analyzed. This efficiency corresponds to the ratio between the absorbed irradiance by the total emitted irradiance, as expressed in Equation (20).

$$\phi\ (\%) = 100\frac{\Phi_A}{N_L \Phi_E} \tag{20}$$

where ϕ is the absorption efficiency in percentage, Φ_A is the radiant power absorbed by the catalyst, N_L is the number of LEDs and Φ_E is the radiant power emitted by each LED.

To evaluate the uniformity of the irradiance values along the catalyst surface, the ratio between the standard deviation (σ) and the average value of data set (μ), designated as coefficient of variation, C_V (Equation (21)), was calculated. Higher C_V values indicates a more heterogeneous distribution of irradiance over the catalyst surface.

$$C_V\ (\%) = 100\frac{\sigma}{\mu} \tag{21}$$

Figure 19 – Irradiance map of BSI configuration.

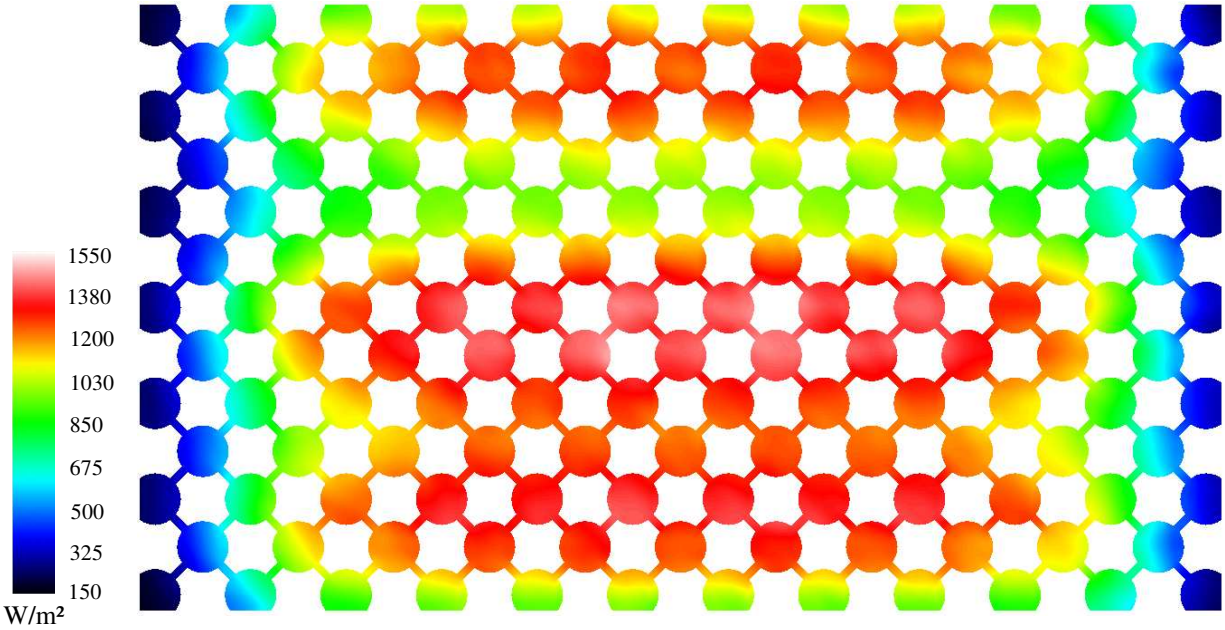

Source: Matiazzo et al. (2022a).

3.4 RESULTS AND DISCUSSION

3.4.1 Validation Case

The first simulations performed aimed at the validation of the optical properties defined for the illumination system and its composing materials. For this, the LEDs positions adopted are the same employed by Da Costa Filho et al. (2019), as described in Figure 16, and the optical properties as described in Section 3.3.2.

Figure 19 shows the irradiation map obtained for the BSI configuration. For the BSI configuration the average irradiation found through simulation is equivalent to approximately 1018 W/m^2, which corresponds to an overestimation of 2.3% in relation to the experimental value of 995 W/m^2 obtained by Da Costa Filho et al. (2019). The absorption efficiency in this case is equivalent to 33.5% and the variation coefficient obtained corresponds to 31.6%. It is possible to observe how the irradiance intensity is greater on the spots located right below the LEDs. The position of the three arrays of 6 LEDs are not evenly spaced (see Figure 16), and therefore a more homogeneous distribution of light on the catalyst surface can be obtained by optimizing the LEDs position. It should also be stated that the intensity profile captured by the sensor can present some uneven

Figure 20 – Irradiance map of FSI configuration.

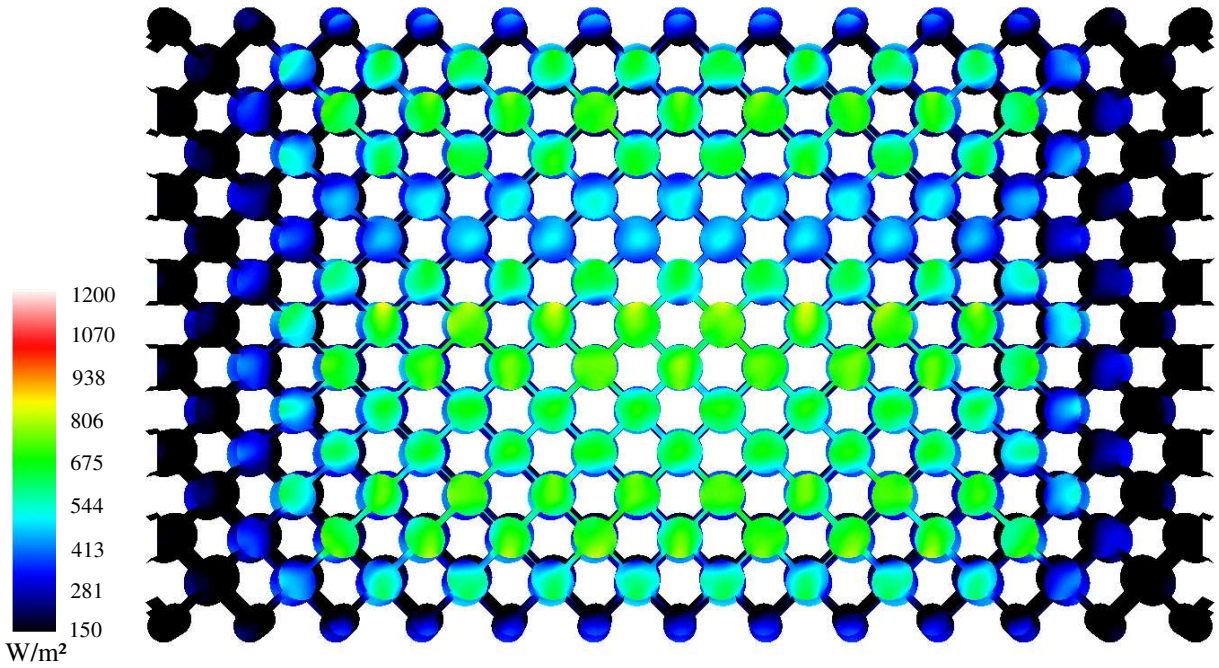

Source: Matiazzo et al. (2022a).

regions due to the ray tracing technique employed that uses a finite number of rays in the simulations (ÁDÁM; ZOLTÁN; GYÖRGY, 2012).

A simulation considering the FSI configuration was also performed, and in this case the average irradiance obtained is equivalent to approximately 285 W/m^2 with an error to the experimental value (266 W/m^2) equivalent to 7.0%. The increase in the relative error, in comparison to the BSI configuration, is due to the fact that differently from the BSI the FSI surface area is not set only in the reactor window area. Its dimensions comprise the entire reactor width. Besides that, the sealing components that are responsible to keep the SSS and the BGS together plus the LEDs support were not represented in the simulation. These structures can be in the path of part of the photons that reached the FSI catalyst in the current simulation. However, an error of about 7% can be considered acceptable.

Figure 20 shows the irradiance map obtained when the catalyst is disposed in all the walls of the network imprinted in SSS. The representation shows that the center of the cylindrical chamber in the region directly below the LEDs is where the highest values of irradiance can be achieved. The same location in the BSI and FSI configurations can receive about 40-50% less light in the FSI disposition due to the increase in distance from the LEDs and shading. It is clear that not all the cylindrical chamber perpendicular

to the LEDs is illuminated homogeneously due to shading effects of the 3D disposition of the catalyst. It is noticeable that the vertical walls of the chambers are also illuminated, however the intensity reached in this case is one order of magnitude lower, even if these walls are positioned right below a LED array, and has an even lesser order of magnitude for the vertical walls of the prismatic channels.

The absorption efficiency is similar to the one of BSI (ϕ = 35%). In contrast, the coefficient of variation is greater in the FSI case, reaching 70.6% due to the lack of homogeneity as discussed previously. In the FSI configuration 2/3 of the catalyst surface corresponds to the vertical walls that are less illuminated. The remaining surface, parallel to the reactor window, corresponds to only a third of the superficial catalyst area. However, it is responsible for the absorption of nearly half of the absorbed light.

3.4.2 LEDs geometrical arrangement - BSI

In order to verify the importance of each LED localization in the illumination system and in order to search for configurations that can provide greater irradiance magnitudes and a more homogeneous distribution of light, the 27 simulations proposed in Table 4 were carried out and their results were compared.

The variation of all three parameters - ω, ℓ and h - was found to generate influence in the irradiance captured at the catalyst surface. The 27 simulations with the parameters already described in Table 4 reached irradiance values ranging from 889 W/m^2 to 1301 W/m^2. This means that between 29.2% and 42.8% of the emitted energy is absorbed by the catalyst. Figure 21a presents the behavior of the absorption efficiency as a function of ω and ℓ, and Figure 21b presents the behavior as a function of h and ℓ.

It is possible to verify that the distance between the LEDs and the reactor, h, has the most significant impact in the irradiance value, as expected. The further the light must travel, the lower will be its intensity, and therefore, the lesser is the absorption efficiency reported. The distance between LEDs, parameters ω and ℓ, are also relevant. As shown in Figure 21a, the absorption efficiency is greater when the LEDs are closer to each other (when ω and ℓ have lower values). However, the proximity between LEDs leads to a high coefficient of variation, as presented in Figure 22a. This means that the irradiance along the catalyst surface is highly heterogeneous, presenting areas of low illuminance and areas with high irradiance values. This behavior is not desirable since the goal is to illuminate the entire catalyst surface in order to optimize the photocatalytic reaction.

Figure 22b shows how the variation coefficient varies with the parameter ℓ and with the distance between reactor and LEDs plate, h, and again it is possible to verify that the parameter h exerts a relevant influence in the homogeneity of the irradiance data set.

Figure 21 – Absorption efficiency - BSI cases.

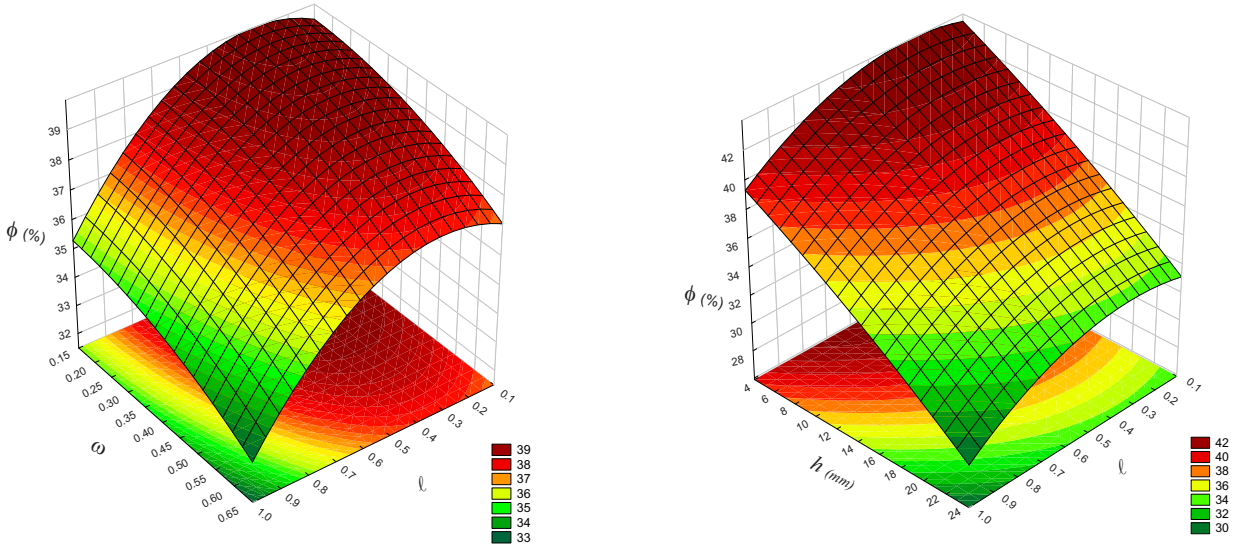

(a) (b)

Source: Matiazzo et al. (2022a).

Figure 22 – Coefficient of variation - BSI cases.

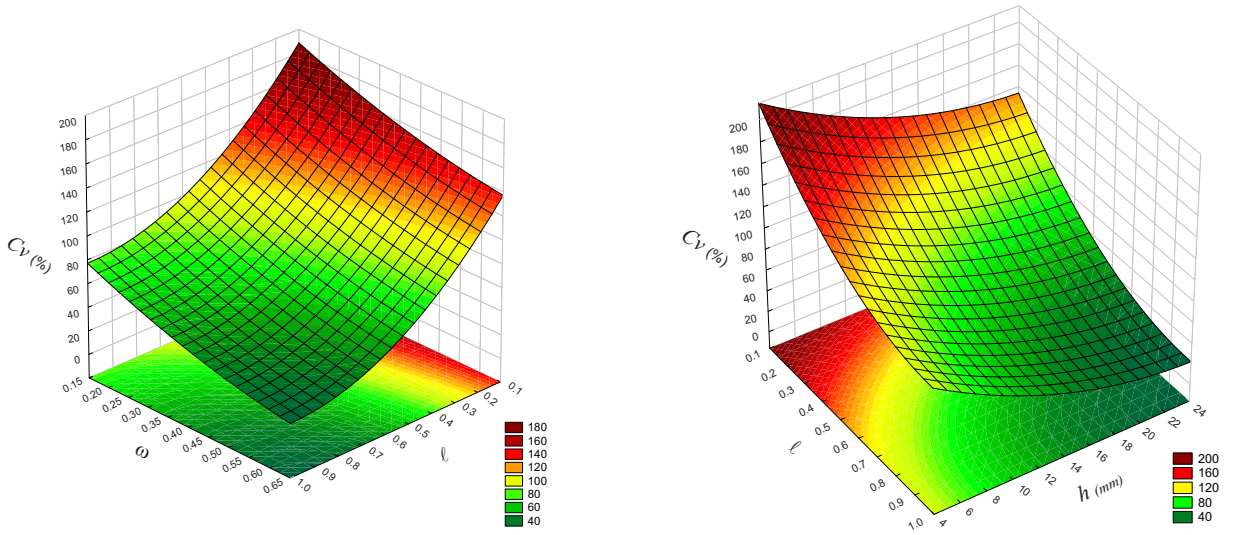

(a) (b)

Source: Matiazzo et al. (2022a).

Figure 23 – Irradiance maps of cases 1 and 27.

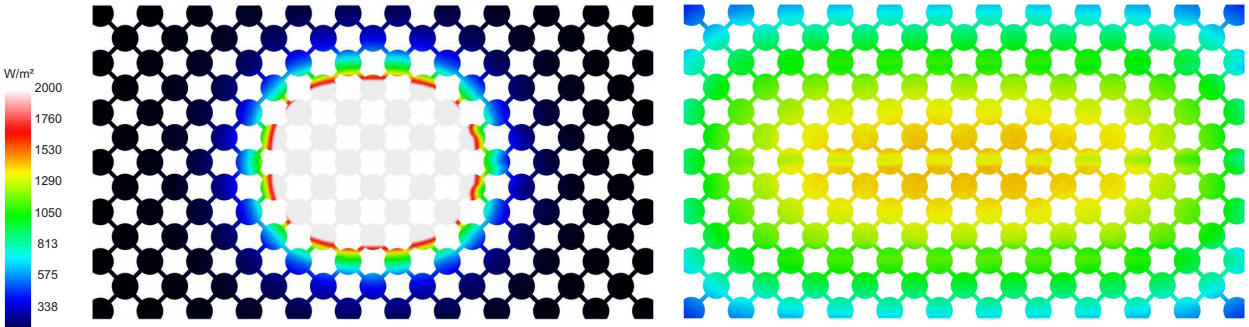

(a) Case 1: $\ell = 0.2$, $\omega = 0.2$ and $h = 6\ mm$ (b) Case 27: $\ell = 0.9$, $\omega = 0.6$ and $h = 22\ mm$

Source: Matiazzo et al. (2022a).

When the LEDs are closer to the reactor, the photons tend to be concentrated in areas right below the LEDs and so the distribution of light intensity is less uniform. When the LEDs plate is positioned further from the reactor, and the LEDs are further apart from each other, light is better distributed leading to a more homogeneous data set. Case 27, where ℓ and ω are, respectively, 0.9 and 0.6, while h is equivalent to 22 mm, shows the example with the higher distance between LEDs, resulting in the lowest variation coefficient (C_V = 24.5%). On the other hand, for case 1, where LEDs are the closest to each other as well as closest to the reactor window, it was obtained the highest value of variation coefficient (C_V = 238.0%), which leads to a lack of uniformity in the irradiance distribution along the catalyst surface. These differences are easily spotted in Figure 23, where the irradiance maps of cases 1 and 27 are depicted. The irradiance maps of all simulated cases are available in the supplementary material (Appendix C). Both cases are also on opposite sides of the absorption efficiency scale. Case 1 is one of the cases that presents the highest absorption efficiency. Case 1 returns an absorption efficiency of 42.3%, whilst case 27 has an efficiency of 29.2%. The light absorption by the catalyst film is mainly dependent on the LEDs-to-reactor distance, since the LEDs-to-LEDs distance has low effect with the decrease in LEDs-to-reactor distance.

3.4.3 LEDs geometrical arrangement - FSI

Cases 1 to 27 were also simulated for the condition where the catalyst is immobilized in the network of chambers and channels imprinted in the stainless steel slab (FSI scheme). The results followed the same pattern; an increase in the parameter: h leads to a decrease in the absorption efficiency, and therefore lower values of irradiance are registered (Figure 24b). The same effect is observed varying ω and ℓ. The proximity between LEDs leads to slight increase in the absorption efficiency (Figure 24a). Similar to the

Figure 24 – Absorption efficiency - FSI cases.

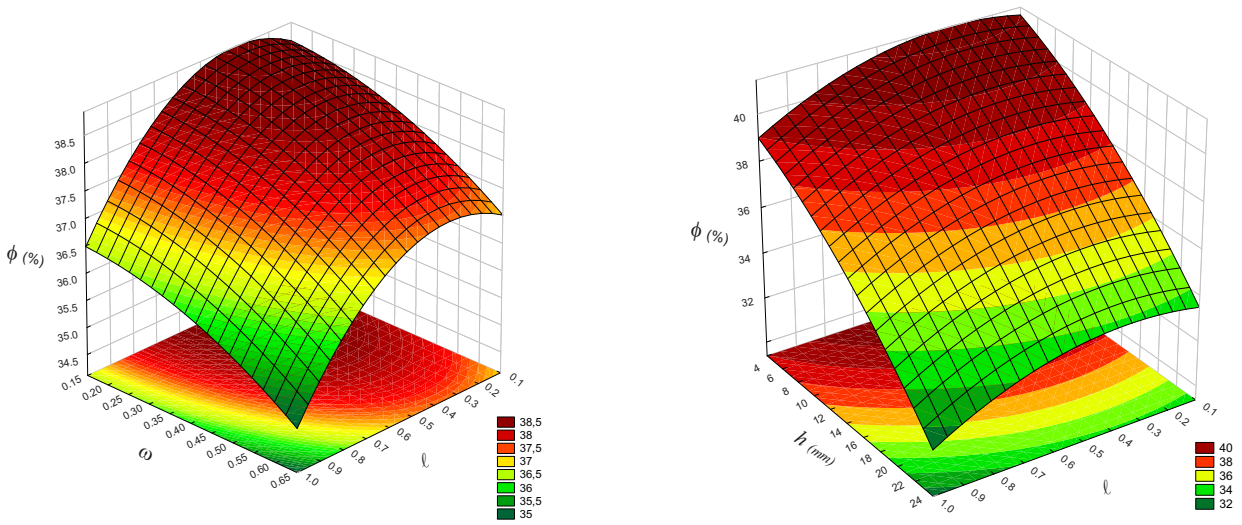

(a) (b)

Source: Matiazzo et al. (2022a).

BSI results, Cases 4 and 27 have the highest and lowest absorption efficiencies, reaching values of 40.3% and 31.3%, respectively. However, the irradiance intensity is lesser in the FSI than in the BSI. While the BSI scheme reaches average values around 1000 W/m^2, in the FSI condition the values range from 255 W/m^2 to 330 W/m^2. Overall, the irradiance values of BSI are almost 4 times greater than the ones of FSI, approximately the same ratio that exists between the FSI to BSI surface areas. Even with lower irradiance values and higher variance coefficient, the higher catalyst area per volume of the FSI configuration still makes this configuration more advantageous than BSI.

The coefficient of variation has also a similar behavior to the BSI, decreasing with the increment of ω, ℓ and h (Figure 25). The main difference between the FSI and the previous results obtained for the BSI is the order of magnitude for the variation coefficient. Cases 1 and 27 are still the ones with the highest and lowest values of C_V, but while the BSI range is between 25% to 238%; for the FSI the coefficient varies from 68% to 306%. This means that the light intensity in the FSI configuration is even less homogeneous than in BSI due to the fact that 1/3 of the FSI area is perpendicular to the light sources, while the other 2/3 are more or less aligned with the travelling direction of the photons.

For both BSI and FSI, the case that presents the highest irradiance value, and consequently, the highest absorption efficiency, is case 4 (ℓ = 0.5, ω = 0.2 and h = 6 mm). However, the variation coefficient registered in this case is elevated ($C_{V,BSI} \simeq$ 151% and $C_{V,FSI} \simeq$ 201%). Therefore, the data suggests that the most advantageous of the simulated

Figure 25 – Coefficient of variation - FSI cases.

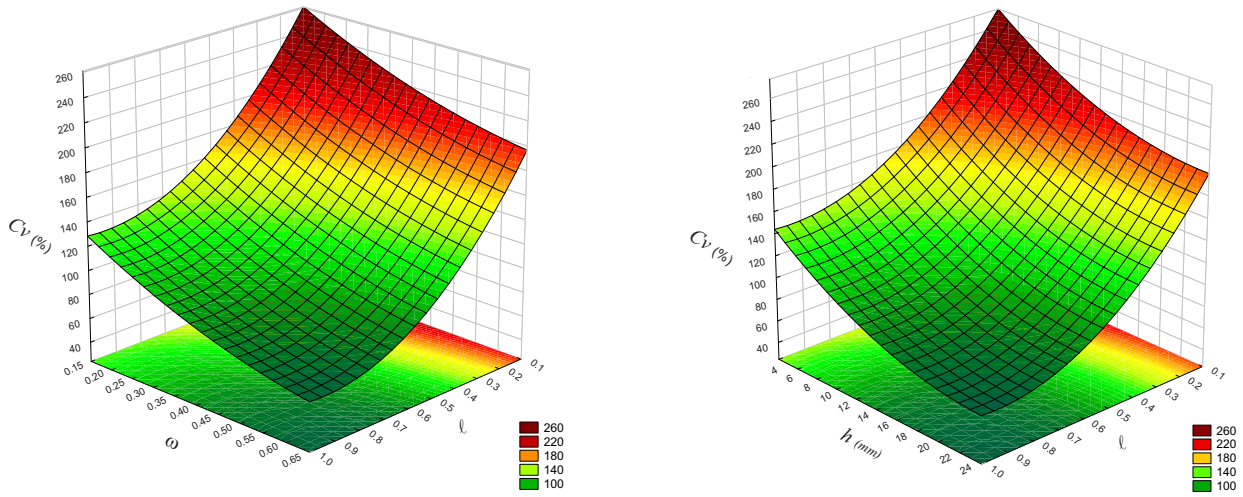

(a) (b)

Source: Matiazzo et al. (2022a).

cases is case 9 (ℓ = 0.9, ω = 0.6 and h = 6 mm), since only a small relative reduction percentage in the irradiance is registered, 6.7% and 2.2% for BSI and FSI respectively, while improving significantly the variation coefficient, leading to a relative reduction of 62.6% and 52.7% in the C_V. This reduction ultimately leads to a more homogeneous intensity along the catalyst surface that is expected to improve the conversion of any photocatalytic reaction conducted in the reactor. Case 9 has the LEDs positioned the furthest apart from each other while having the lowest distance to the reactor window, confirming that the correct positioning of LEDs is significant for the operation of the photocatalytic reactor.

3.5 CONCLUSIONS

The radiation field incident at a TiO_2 catalyst film provided by 18 LEDs was simulated employing a non-sequential ray tracing algorithm for the NETmix milli-photocatalytic reactor.

The catalyst was disposed in two distinct arrangements, back-side illumination (BSI) and front-side illumination (FSI), and for both conditions the simulations were validated, with a relative error to the experimental data of 2.3 and 7.0%, respectively.

The position of the 18 LEDs was evaluated through three created parameters, ω, ℓ and h, that represent the proximity between LEDs and the proximity of the LEDs plate to the photoreactor window. Three values were attributed to each of the parameters and a combination between them was simulated resulting in 27 simulations for each BSI and FSI

schemes in order to verify the best location for each LED.

The results show that the absorption efficiency increases with the proximity of LEDs to each other and to the reactor window, however the homogeneity of the illuminance intensity decreases. The absorption efficiencies range from 29.2% to 42.8% for the BSI and from 31.3% to 40.5% for the FSI. The variation coefficient ranges from 25% to 238% for the BSI cases and from 68% to 306% for the FSI configuration. The case that presents the highest absorption whilst having the lowest variance coefficient, i.e. case 9 (ℓ = 0.9, ω = 0.6 and h = 6 mm), has an approximate absorption efficiency of 40% and a C_V of 57% and 95% for BSI and FSI, respectively.

The results also show that the distinct locations of the catalyst films have significant importance. The FSI cases present similar absorption efficiency to the BSI, even though the FSI configuration has almost 4 times more superficial area than BSI. Also, the FSI cases present higher values of variation coefficient, meaning that the area is less homogeneously illuminated. Ultimately, the simulations allow the selection of a possibly ideal scenario for the LEDs position that permits to maximize the absorption efficiency at the same time increasing the homogeneity of irradiance distribution.

4 CFD AND RADIATION FIELD MODELING OF THE NETMIX MILLI-PHOTOCATALYTIC REACTOR FOR *N*-DECANE OXIDATION AT GAS PHASE: EFFECT OF LEDS NUMBER AND ARRANGEMENT

This chapter is based on the paper entitled “CFD and Radiation Field Modeling of the NETmix Milli-Photocatalytic Reactor for *n*-Decane Oxidation at Gas Phase: Effect of LEDs Number and Arrangement” (Chemical Engineering Journal, doi.org/10.1016/j.cej.2022.136577), by Tatiana Matiazzo, Vítor J.P. Vilar, Humberto Gracher Riella, Natan Padoin and Cíntia Soares. Copyright © 2022 Elsevier B. V. Abstract, keywords, acknowledgments and references were omitted.

4.1 INTRODUCTION

Heterogeneous photocatalysis has been recognized as a powerful technology for air streams decontamination containing Volatile Organic Compounds (VOCs) (COSTA FILHO; VILAR, 2020). Among the reactors designs available for photocatalytic oxidation processes are the flat plate, honeycomb monolith, annular, packed bed, slurry, hollow fiber, milli- and microreactors (SUNDAR; KANMANI, 2020; MALAYERI; HAGHIGHAT; CHANG-SEO, 2019; BOYJOO et al., 2017; TANIMU; JAENICKE; ALHOOSHANI, 2017; VERBRUGGEN; LENAERTS; DENYS, 2015; MO et al., 2009; MATSUSHITA et al., 2008; BIRNIE; RIFFAT; GILLOTT, 2006; JUAN; XUDONG, 2003; HOSSAIN et al., 1999). The capability for the minimization of costs with simultaneous increase in raw material and energy efficiencies makes milli- and microreactors technology an ideal tool for process intensification (ABIEV, 2019; JESSY; HAYNES, 2017). A myriad of designs is available for this class of reactors (SHUKLA et al., 2021; KAYAHAN et al., 2020). Lopes et al. (2005) developed a static continuous flow mesoscale mixer, known as NETmix, composed by a network of cylindrical chambers interconnected by prismatic channels. The NETmix design provides high mixing besides high catalytic surface area and low optical path in heterogeneous photocatalytic reactions (PASSALÍA et al., 2020a). However, due to the internal reactor geometry, the illumination of the entire catalytic surface is a huge challenge, even with the use of UV Light Emitting Diodes (LEDs) (DA COSTA FILHO et al., 2019). An adequate illumination system needs to maximize the illumination efficiency as well as the uniformity of the radiation field over the catalyst surface. At the same time, it should maximize the irradiance levels obtained on the catalyst surface while minimizing the energy consumption of the light sources. In this sense, computational tools are of great assistance to the project and evaluation of photocatalyst systems (ALVARADO-ROLON et al., 2018; ZAZUETA; DESTAILLATS; LI PUMA, 2013).

The photon transfer remains as one the main challenges in this class of reactors

project. To simulate the photon transfer, two types of algorithms have been widely employed: i) stochastic models solved mainly by the Monte Carlo method, and ii) deterministic models, such as finite element methods; also referred to as view-dependent and view-independent methods, respectively (AYOUB, 2020). View-independent algorithms were adapted from radiative heat transport methods and initially forced all surfaces to be lambertian reflectors (JAKICA, 2018; LESEV, 2010). On the other hand, ray tracing algorithms are classified as view-dependent since the photon flux is calculated in specific areas of the domain, emulating the natural illumination mechanism (AYOUB, 2020). In this approach light is represented as rays that travel from light sources to the medium obeying the laws of geometrical optics (LALAU KERALY et al., 2017). This method can simulate the interactions of light with complex geometries, accounting for distinct reflections, absorption and transmission of photons (TSANGRASSOULIS; BOURDAKIS, 2003).

The association of radiation field data or ray tracing with computational fluid dynamics (CFD) simulations is still scarce in the literature, contrasting with view dependent algorithms such as discrete ordinate method (DOM) (PASSALÍA et al., 2020a; MORENO-SANSEGUNDO; CASADO; MARUGÁN, 2020; MORENO; CASADO; MARUGÁN, 2019; MUÑOZ-BATISTA et al., 2019). Salvadó-Estivill, Hargreaves, and Li Puma (2007) coupled the kinetic model of trichloroethylene degradation with radiation field data. Authors used a flat plate reactor illuminated with 1, 3 or 5 blacklight blue florescent lamps. The linear source spherical emission model (LSSE) was used to represent lamps emission. The model considers the cylindrical lamp to be a line source, that in each point emits radiation in every direction isotropically. Similarly, Zimeng et al. (2012) evaluated the dimethyl sulfide (DMS) oxidation in a photocatalytic plate reactor developing a method to simulate the 27 LEDs used to illuminate a plate reactor. Authors found that the proximity of the LEDs to the photocatalyst has great impact in the radiation intensity and uniformity. Increasing the distance of LEDs to catalyst improves the uniformity at the expense of radiation intensity. Zazueta, Destaillats, and Li Puma (2013) used an in-house code of a Monte Carlo method to simulate and optimize the radiation field in a modular multi-plate photocatalytic reactor (MPPR) for air or water purification. The reactor is composed by a series of parallel plates where the catalyst is deposited. These plates are perforated to accommodate cylindrical UV lamps that are orthogonal to the plates. Authors tested illumination systems with 1, 4 and 5 lamps. Dimensionless parameters, that account for the geometrical location of the lamps, were evaluated to optimize the illumination system efficiency, considering photon absorption and field uniformity. Queffeulou et al. (2010) and Queffeulou, Geron, and Schaer (2010) also employed ray tracing to investigate the impact of irradiance in the Langmuir-Hinshelwood kinetics of acetaldehyde oxidation from an air stream, developing a methodology to predict the performance of an air purifier and the evolution in time and

space of the pollutant concentration when the photoreactor is placed in a contaminated room.

In our previous work (MATIAZZO et al., 2022a), an investigation into how the position of the LEDs can alter the radiation field registered over the surface of the TiO_2 catalyst was performed. The radiation field in the meso-scale NETmix photocatalytic reactor was evaluated employing a Monte Carlo-based algorithm using the software Ansys Speos®. A total of 18 inline LEDs were disposed according to 27 variations that alter the LEDs-to-reactor and the LEDs-to-LEDs distances. The distinct geometrical positions of the same LEDs increased the light absorption efficiency up to 13 percentage points. Also, greater LEDs-to-LEDs distances provided more homogeneous radiation fields. The importance of the homogeneity of the field was investigated in the current work, associating the radiation field modeling of illumination systems composed by distinct numbers of LEDs with computational fluid dynamics (CFD) simulations of the oxidation of VOCs.

Therefore, this work presents, not only the radiation field modeling of several illumination systems, but the coupling with computational fluid dynamics to evaluate the impact of photon transfer in the photocatalytic oxidation of an airborne pollutant. Seven illumination systems are proposed, consisting of 5 to 30 LEDs disposed in an inline or staggered configuration, aiming the largest LEDs-to-LEDs distance possible. A non-sequential ray tracing algorithm, based on the Monte Carlo method, was employed to simulate the behavior of light. The radiation field obtained on the TiO_2-P25 catalyst surface, deposited over the walls of the channels and chambers that compose the NETmix milli-photoreactor, were then coupled to CFD simulations to evaluate the photocatalytic degradation of a model VOC, n-decane, contained in an air stream. Light absorption efficiency, irradiance levels, uniformity and overall photonic efficiency of the illumination systems were evaluated and compared against the pollutant conversion in order to appoint an ideal illumination system.

4.2 REACTOR DESIGN AND EXPERIMENTAL DATA

The NETmix milli-photocatalytic reactor was employed in this study. A detailed description of the entire apparatus and its operation is given by Da Costa Filho et al. (2019). The reactor is composed of a stainless-steel slab (SSS) and a borosilicate glass slab (BGS) illuminated by a series of LEDs located at a distance h above the BGS (Figure 26). The reaction compartment is formed when the SSS, engraved with a pattern of cylindrical chambers interconnected by prismatic channels, is sealed with a high transparency BGS. The reactor contains 8 inlets and 8 outlets distributed equally between the SSS and the BGS. The TiO_2-P25 photocatalyst was uniformly immobilized, using a spray method, over the walls of the chambers and channels engraved into the stainless-steel slab, forming a

thin film with a thickness of about 17.3 μm, illuminated according to a front-side illumination (FSI) scheme.

Figure 26 – NETmix photocatalytic reactor.

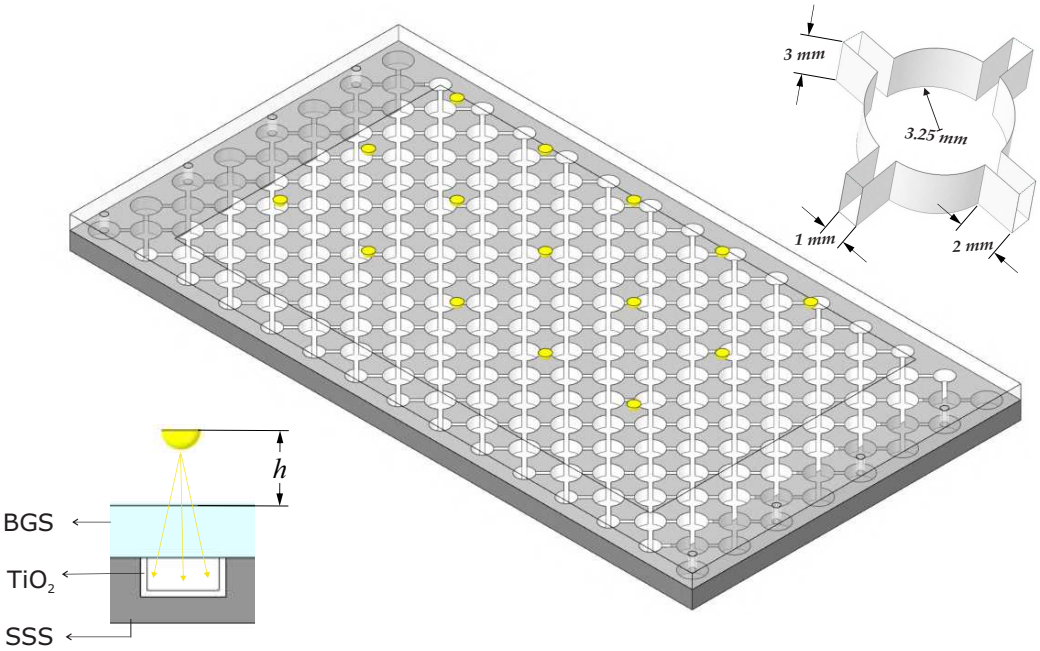

Source: Matiazzo et al. (2022b).

4.3 NUMERICAL METHODOLOGY

4.3.1 Light modeling

The optical software Ansys Speos® was employed to obtain the irradiation field over the catalyst surface. The non-sequential ray tracing algorithm is based on the Monte Carlo method and in the principles of ray optics. To represent each LED that compose the illumination system, a surface source is created at the geometrical position of the LED in the system. Besides the surface area of the LED, the following information are required: i) emitted power (0.9 W); ii) light spectrum (365 nm peak, 9 nm half width); and iii) light intensity distribution, which is provided by the manufacturer.

For the borosilicate glass slab a refraction index $n_{d(\lambda=587.6\ nm)}$ = 1.47140 and an Abbe number equivalent to 65.41 were employed in accordance to the manufacturer data. The surface of the BGS was modeled according to an optical polished type, which means that Fresnel equations are used to calculate surface interactions. The SSS was modeled as an opaque volume, and the surface of the SSS was modeled as a mirror type with 90% reflectance. For the TiO_2 catalyst, a refraction index $n_{d(\lambda=587.6\ nm)}$ = 2.61420 and an Abbe

number equivalent to 9.87 were associated with an advanced surface that reflects light as a mixture of specular and Lambertian reflection depending on the light incident angle. Through a sensibility test it has been determined that 60% of the light is absorbed and 5% is transmitted by the catalyst. Therefore, 35% of the light is reflected by the catalyst surface. The proportion of light that is reflected as specular and Lambertian is based on the work of Janecek and Moses (2008a) and is a function of the incident angle as depicted in Table 5.

Table 5 – Optical properties of TiO_2.

Incident Angle (°)	0	10	20	30	40	50	60	70	80	90
Specular (%)	0.7	1.4	2.1	3.5	8.4	18.9	28.0	32.2	33.6	34.3
Lambertian (%)	34.3	33.6	32.9	31.5	26.6	16.1	7.0	2.8	1.4	0.7
Absorption (%)					60.0					
Transmission (%)					5.0					

Source: Matiazzo et al. (2022b).

A planar integration orthogonal to the sensor plane, created at the surface of the catalyst, is performed taking into account the cosine fall off the irradiance as a function of the incident angle, based on Bouguer's law (Equation (22)).

$$E = \frac{I\ cos\ \varepsilon}{D^2} \tag{22}$$

where E represents the irradiance in W/m^2, I is the intensity in W/sr, ε is the incident angle and D is the light travel distance (m).

The sensor consists of a triangular mesh, created with a total of 103,341 nodes, where the values of irradiance are registered for posterior analysis. A direct simulation is then conducted, where rays are traced from the light sources to the sensor. The simulations were performed with double precision enabled, the maximum number of interactions was set to 100 and the minimum energy percentage for a ray to keep being traced was set to 0.5% of its initial energy. The stop criterion of the simulation is the number of traced rays.

The number of traced rays will also define the precision of the results. Therefore, a test to determine the ideal number of traced rays was performed. The time required to complete the simulation along with the standard deviation of the irradiance data set were compared. Six simulations were performed for a total of 10^5, $6{\cdot}10^5$, 10^6, $6{\cdot}10^6$, 10^7 and $6{\cdot}10^7$ traced rays.

Figure 27 shows that the increase in the number of processed rays leads to an exponential increase of the simulation time demand. The opposite can be stated for the standard deviation. As the number of processed rays increase the deviation tends to stabilize at a value near 200 W/m^2. Therefore, in order to balance the time demand with

Figure 27 – Definition of simulated rays number.

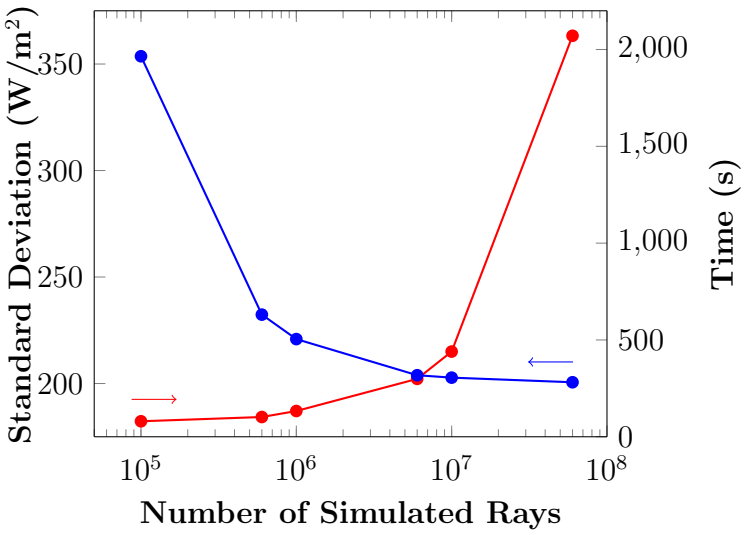

Source: Matiazzo et al. (2022b).

the accuracy of the results, a threshold of $6{\cdot}10^6$ rays was employed as a stop criterion in the ray tracing simulations performed in this research.

4.3.2 CFD modeling

The software Ansys Fluent® was employed to model the fluid dynamics inside the reactor. The heterogeneous reacting system was simulated under isothermal and steady state conditions. The polluted air stream was considered a Newtonian incompressible fluid flowing in a laminar regime. The mathematical modeling of the system was then expressed though the solution of the mass, momentum and species conservation equations (Equations (23)-(25)).

$$\nabla \cdot (\rho \boldsymbol{\nu}) = 0 \tag{23}$$

$$\nabla \cdot (\rho \nu \boldsymbol{\nu}) = -\nabla P + \nabla \cdot (\boldsymbol{\tau}) \tag{24}$$

$$\nabla \cdot (\rho \boldsymbol{\nu} C_i) = -\nabla \cdot \boldsymbol{J}_i \tag{25}$$

where ρ (kg/m^3) represents the density, $\boldsymbol{\nu}$ (m/s) is the velocity, P represents pressure (Pa), $\boldsymbol{\tau}$ (Pa) is the stress tensor, C_i (kmol/m^3) is the species concentration and $\boldsymbol{J}_i$ (kmol/m^2·s) represents the diffusion flux of species i.

4.3.2.1 Boundary conditions

The reactor's walls were set as stationary walls with no slip boundary condition. The heterogeneous reaction rate was introduced in the modeling as a boundary condition. For the catalytic walls, the diffusive molar flux of the pollutant must be equal to the heterogeneous reaction rate (Equation (26)), while for the non-catalytic walls a zero molar flux was employed for all species (Equation (27)).

$$\boldsymbol{n} \cdot \boldsymbol{N}_{dec}|_{A_{cat}} = \boldsymbol{n} \cdot (-D_{dec,m} \nabla C_{dec})|_{A_{cat}} = r_{dec} \tag{26}$$

$$\boldsymbol{n} \cdot \boldsymbol{N}_{dec}|_{A_{non-cat}} = 0 \tag{27}$$

The reaction rate (r_{dec}) was imposed to the CFD solver via a user defined function (UDF). To describe the photocatalytic oxidation of *n*-decane in the NETmix reactor, a power law rate equation (Equation (28)) was obtained from the experimental data of Da Costa Filho et al. (2017).

$$r_{dec} = 3.09 \cdot 10^{-8}\ E\ C_{dec}^{0.43}\ C_{w}^{0.18} \tag{28}$$

where r_{dec} represents the reaction rate in kmol/m^2·s, 3.09·10^{-8} represents the reaction rate constant in kmol W^{-1} s^{-1} (kmol m^{-3})$^{-0.61}$, E represents the irradiance in W/m^2, and C_{dec} and C_w (kmol/m^3) represents the concentration of *n*-decane and water vapor, respectively.

The irradiance field (E) obtained in the ray tracing simulations was introduced into the CFD solver through a user defined scalar (UDS). For the reactor inlet the velocity was prescribed, and the molar fractions of *n*-decane and water vapor were informed. At the reactor outlet, the gauge pressure was set as zero.

The convergence criteria of the steady-state simulations was set as 10^{-3} for the momentum, 10^{-5} for continuity and water vapor species, and 10^{-6} for energy and for *n*-decane species. The structured mesh employed consists of a total of 10,785,298 hexahedron elements. This mesh was selected after an uncertainty assessment was performed based on the method proposed by Roache (1994). Simulations were performed in a 64-bit Windows Server 2019 Datacenter equipped with Intel Xeon Gold 6126 CPU operating at 2.6 GHz, with access to 50 GB RAM memory. The CFD simulations were performed with 8 parallel solver processes and demanded 4 h - 5 h to completion

4.3.3 Simulated cases

In this work, the number of LEDs was varied from 5 to 30. The LEDs were distributed according to two arrangements: inline and staggered, as exemplified in Figure 28. For the inline arrangement, three LEDs plates were simulated, containing 6, 15 and 28 LEDs, and for the staggered arrangement four plates were analyzed, each having 5, 12, 18 and 30 LEDs. The seven proposed illumination systems are illustrated in detail in the supplementary material (Appendix D). For all of the investigated systems four distances of LEDs-to-reactor were simulated: 6 mm, 12 mm, 24 mm and 48 mm. Therefore, a total of 28 simulation cases are proposed as indicated in Table 6.

Table 6 – Evaluated cases.

Case	Number of LEDs	Arrangement	h (mm)	Case	Number of LEDs	Arrangement	h (mm)
Case 1-S	5	Staggered	6	Case 15-I	15	Inline	24
Case 2-S	5	Staggered	12	Case 16-I	15	Inline	48
Case 3-S	5	Staggered	24	Case 17-S	18	Staggered	6
Case 4-S	5	Staggered	48	Case 18-S	18	Staggered	12
Case 5-I	6	Inline	6	Case 19-S	18	Staggered	24
Case 6-I	6	Inline	12	Case 20-S	18	Staggered	48
Case 7-I	6	Inline	24	Case 21-I	28	Inline	6
Case 8-I	6	Inline	48	Case 22-I	28	Inline	12
Case 9-S	12	Staggered	6	Case 23-I	28	Inline	24
Case 10-S	12	Staggered	12	Case 24-I	28	Inline	48
Case 11-S	12	Staggered	24	Case 25-S	30	Staggered	6
Case 12-S	12	Staggered	48	Case 26-S	30	Staggered	12
Case 13-I	15	Inline	6	Case 27-S	30	Staggered	24
Case 14-I	15	Inline	12	Case 28-S	30	Staggered	48

Source: Matiazzo et al. (2022b).

The irradiance levels of each illumination system were compared along with the photon absorption efficiency (Equation (29)), uniformity index (Equation (30)) and overall photonic efficiency (Equation (31)):

$$\phi = \frac{E\ A_{cat}}{N_L \Phi_e} \tag{29}$$

$$\gamma = 1 - \frac{\sum_{i=1}^{n} \left[\left(\left| E_i - \bar{E}_{\mathrm{a}} \right| \right) A_i \right]}{2 \left| \bar{E}_{\mathrm{a}} \right| \sum_{i=1}^{n} A_i} \tag{30}$$

$$\eta = \phi\gamma \tag{31}$$

where E represents the irradiance value in W/m^2, A_{cat} (m^2) is the catalyst area, N_L is the number of LEDs in the system, Φ_e (W) represents the power emitted by each LED, i is the

Figure 28 – Proposed illumination systems.

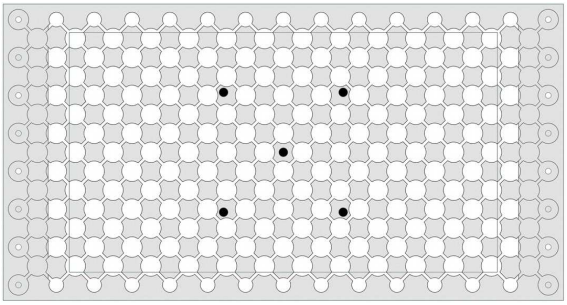

(a) 5 staggered LEDs

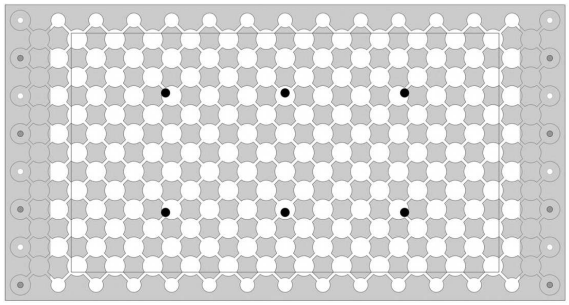

(b) 6 inline LEDs

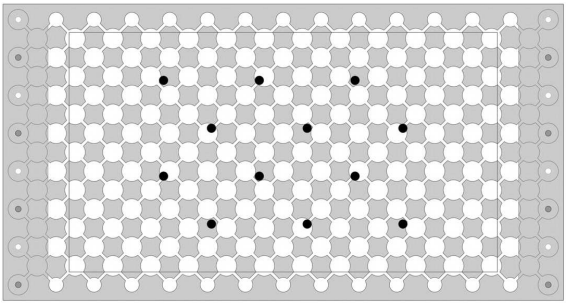

(c) 12 staggered LEDs

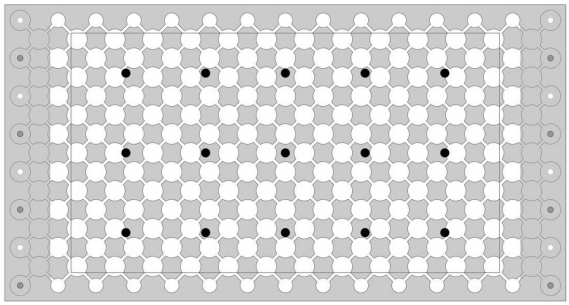

(d) 15 inline LEDs

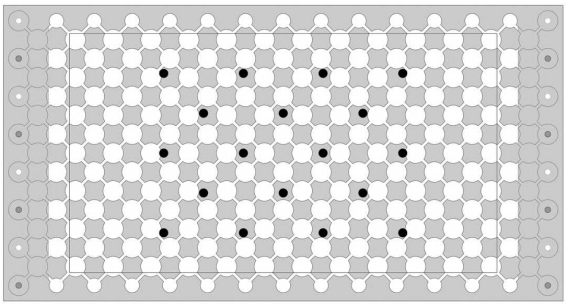

(e) 18 staggered LEDs

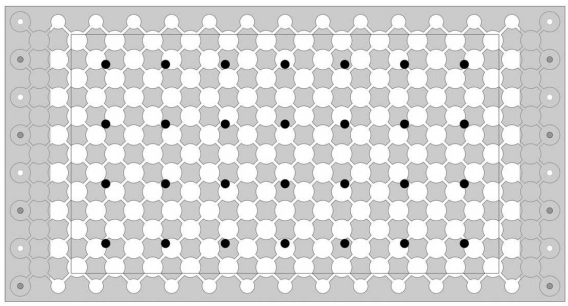

(f) 28 inline LEDs

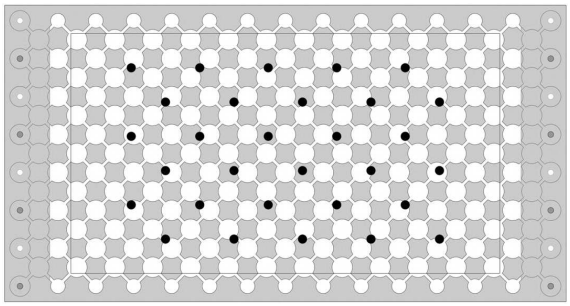

(g) 30 staggered LEDs

Source: Matiazzo et al. (2022b).

facet index of a surface with *n* facets, and $\bar{E}_{\mathrm{a}}$ (W/m^2) is the average value of the irradiance over the surface.

Both the absorption efficiency and uniformity index are equally significant to determine the performance of the illumination system. The first expresses the number of photons that became available for the photodegradation, and the latter relates the geometrical availability of these photons on the catalyst surface. Consequently, the most efficient system results from the maximization of both parameters. Therefore, an overall photonic efficiency parameter (η) can be obtained as the product of ϕ and γ.

Afterwards, the radiation profiles obtained through the 28 ray tracing simulations were employed in CFD simulations to evaluate how the intensity and homogeneity of the produced radiation field impacts the degradation of *n*-decane. Therefore, 28 CFD simulations were performed according to the conditions indicated in Table 7.

Table 7 – Boundary conditions of the CFD tests.

Velocity inlet:	0.5 m/s
Molar fraction of *n*-decane:	$7{\cdot}10^{-4}$
Molar fraction of water vapor:	10^{-2}
Pressure outlet:	Atmospheric
Walls:	No slip
Reactive walls:	$r_{dec} = 3.09 \cdot 10^{-8}\ E\ C_{dec}^{0.43}\ C_{w}^{0.18}$

Source: Matiazzo et al. (2022b).

4.4 RESULTS AND DISCUSSION

4.4.1 Model validation

The model validation was performed against the experimental data of Da Costa Filho et al. (2019). The radiation field modeling validation is presented in detail in our previous publication (Matiazzo et al. (2022a)), where a relative error of about 7% was found for the radiation field obtained at the surface of an FSI catalyst in the NETmix illuminated by 18 inline LEDs.

Subsequently, the radiation field of the 18 inline LEDs was coupled with CFD, and the obtained degradation of the pollutant was compared to the experimental data, as shown in Table 8. Two simulation cases were conducted in CFD simulations varying the inlet velocity and the pollutant initial concentration. However, the experimental conversion is virtually indistinguishable for both cases. The relative error between simulations and experimental data obtained was equivalent to 4.1% and 3.1%.

Table 8 – Computational fluid dynamics set-up and validation.

Catalyst disposition:	FSI	FSI
Velocity inlet (m/s):	0.43	0.54
Inlet molar fraction of *n*-decane	$1.7 \cdot 10^{-4}$	$2.5 \cdot 10^{-4}$
Inlet molar fraction of water vapor	10^{-2}	10^{-2}
X_{Exp} (%) :	96.00	96.00
X_{CFD} (%) :	99.97	99.00
Relative error (%):	4.1	3.1

Source: Matiazzo et al. (2022b).

4.4.2 Radiation field

To verify the impact that the disposition and the number of LEDs that compose the illumination system have over the radiation field registered at the surface of the photocatalyst, 28 ray tracing simulations were conducted in accordance with Table 6.

The number of LEDs that compose the illumination system ranged from a total of 5 to 30 LEDs, arranged in two manners: staggered or inline. Altogether, the 7 LEDs plates proposed had their plate-to-reactor distance varied between 6 mm and 48 mm (Table 6). The systems analyzed reached irradiance values ranging from 57 W/m^2 to 589 W/m^2, meaning that 22% to 44% of the emitted light is absorbed by the catalyst.

Figure 29 – Irradiance values obtained through ray tracing. St. – 6 mm (staggered cases 1, 9, 17 and 25); St. – 12 mm (staggered cases 2, 10, 18 and 26); St. – 24 mm (staggered cases 3, 11, 19 and 27); St. – 48 mm (staggered cases 4, 12, 20 and 28); In. – 6 mm (inline cases 5, 13 and 21); In. – 12 mm (inline cases 6, 14 and 22); In. – 24 mm (inline cases 7, 15 and 23); In. – 48 mm (inline cases 8, 16 and 24).

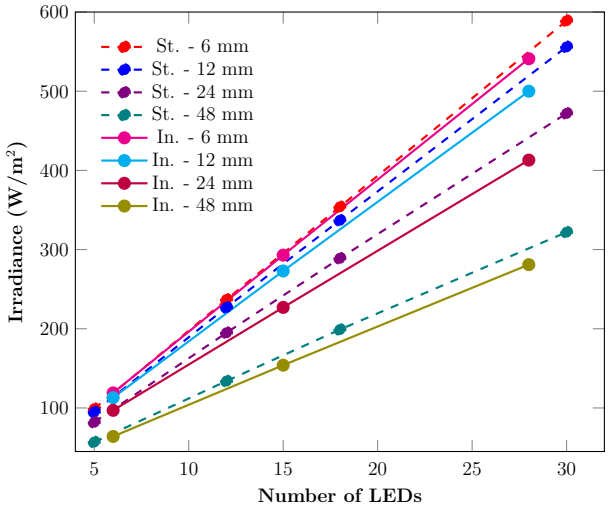

Source: Matiazzo et al. (2022b).

Figure 29 shows the irradiance obtained at the surface of the catalyst inside the NETmix photoreactor for each of the proposed illumination systems. In Figure 29 each line shows the irradiance behavior for one of the arrangements at each of the LEDs-to-reactor heights simulated (6 mm, 12 mm, 24 mm and 48 mm). The dotted lines show the behavior for the staggered systems and the full lines represent the inline systems. The irradiance values grow linearly with the increase of LEDs for each of the proposed arrangements, and it is noticeable that the staggered systems yield slightly higher irradiance values. This increment in the irradiance is particularly noticeable for greater LEDs-to-reactor distances.

In Figure 30 the absorption efficiency is plotted against the number of LEDs in the system. Each line of the graph represents one LEDs-to-reactor distance and again the dotted lines represent the staggered systems. Analogous to the irradiance, the absorption efficiency is a bit lower for the inline systems (around 1-2 percentage points). Once more, the greater the LEDs-to-reactor distance, the higher is the influence of the chosen alignment. The absorption efficiency is a clear function of the LEDs-to-reactor distance, and ranges from around 20% for distances equivalent to 48 mm to above 40% for LEDs-to-reactor distances of 6 mm and 12 mm.

Figure 30 – Light absorption efficiency of simulated cases. St. – 6 mm (staggered cases 1, 9, 17 and 25); St. – 12 mm (staggered cases 2, 10, 18 and 26); St. – 24 mm (staggered cases 3, 11, 19 and 27); St. – 48 mm (staggered cases 4, 12, 20 and 28); In. – 6 mm (inline cases 5, 13 and 21); In. – 12 mm (inline cases 6, 14 and 22); In. – 24 mm (inline cases 7, 15 and 23); In. – 48 mm (inline cases 8, 16 and 24).

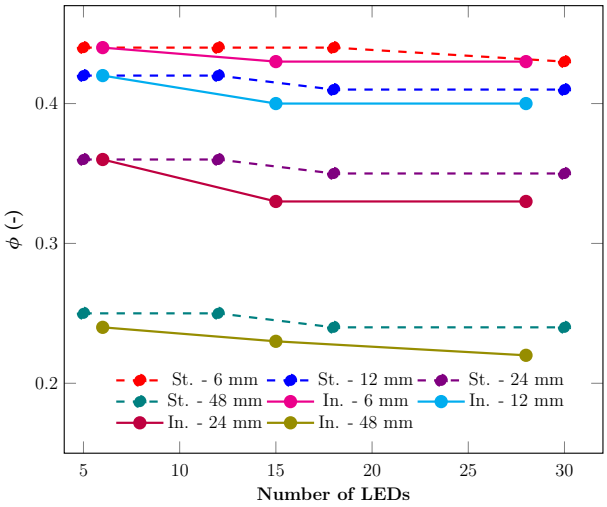

Source: Matiazzo et al. (2022b).

The uniformity of the radiation field is also of interest. Therefore, the uniformity index (Equation (30)) weighted by the area of the catalyst is analyzed. Figure 31 shows the uniformity index obtained for each illumination system. It is noticeable that when ob-

serving the same arrangement type, a larger number of LEDs results in greater uniformity indexes. Also, the inline arrangement produces higher radiation fields with significantly higher uniformity.

Figure 31 – Irradiance field uniformity index. Dashed lines represent the staggered systems and full lines show the behavior of inline arrangement.

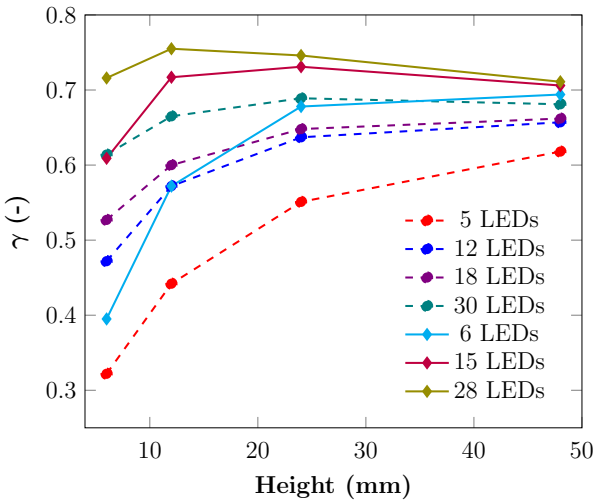

Source: Matiazzo et al. (2022b).

Figure 32 shows the calculated overall photonic efficiency. The obtained values range from 14% to a maximum of 31% efficiency. It is noticeable that even with absorption efficiencies slightly lower but presenting higher uniformity, the inline systems have overall efficiencies higher than the staggered arrangement. For example, 15 LEDs arranged inline present an overall photonic efficiency higher than 25% at LEDs-to-reactor distances inferior to 20 mm. In the staggered arrangement, only the system with 30 LEDs is able to surpass the 25% threshold. Also, the increase in the LEDs-to-reactor distance tend to take all the systems to the same overall photonic efficiency of about 16%. For almost all the systems a peak of efficiency is obtained at a LEDs-to-reactor distance equivalent to 12 mm, which is also one of the distances that preserve high values of irradiance. This behavior is related to the inverse square law, that states that the illumination intensity is proportional to the inverse square of the distance from the light sources. Therefore, the irradiance values decrease with the augment of LEDs-to-reactor distance, whilst the homogeneity increases. The overall photonic efficiency overlaps both properties The overall photonic efficiency overlaps both irradiance values and homogeneity and allows the identification of the ideal LEDs-to-reactor distance, in this case 12 mm, in which the irradiance is kept high, and the homogeneity is maximized. This ideal distance is characteristic of the employed LEDs view angle, intensity distribution and power.

Figure 32 – Overall photonic efficiency. Dashed lines represent the staggered systems and full lines show the behavior of inline arrangement.

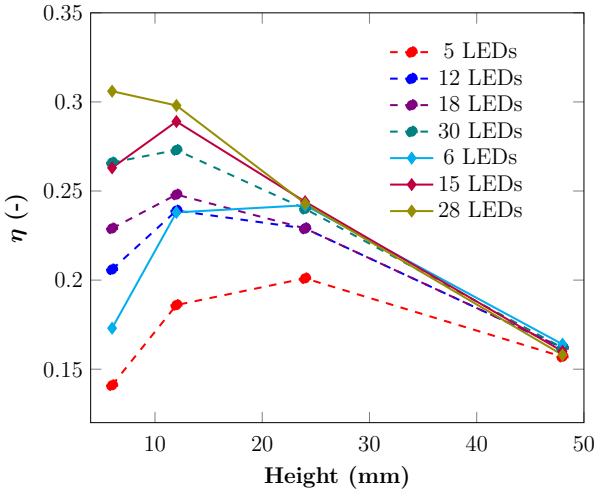

Source: Matiazzo et al. (2022b).

Figure 33 – Irradiation maps cases with lowest and highest overall photonic efficiency.

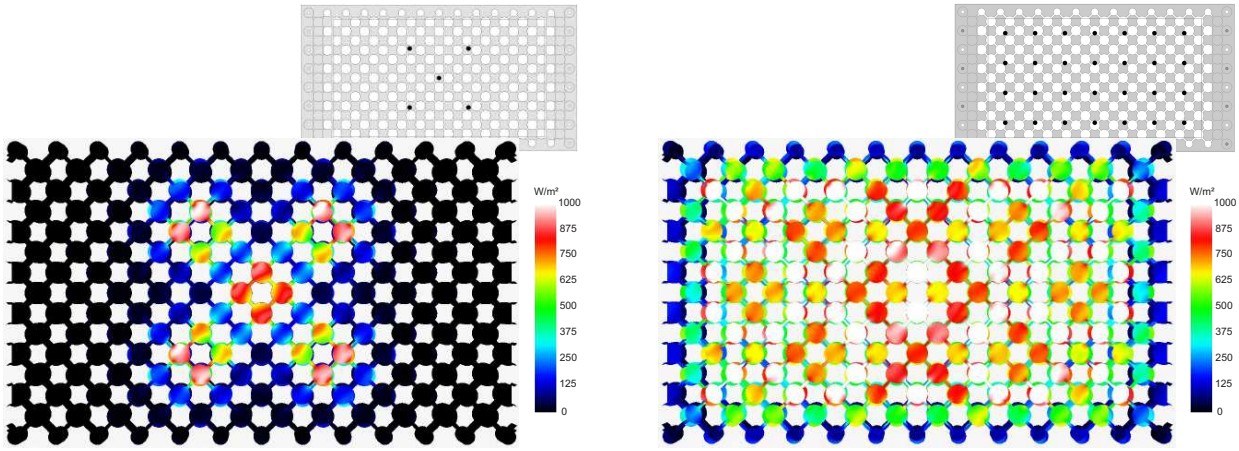

(a) Case 1-S: 5 Staggered LEDs, h = 6 mm (b) Case 21-I: 28 Inline LEDs, h = 6 mm

Source: Matiazzo et al. (2022b).

Figure 33 shows the irradiance map obtained for case 1-S (5 Staggered LEDs, h = 6 mm) that presents the lowest overall photonic efficiency (η = 14%) and case 21-I (28 Inline LEDs, h = 6 mm), that presents the highest overall photonic efficiency achieved (η = 31%). Irradiance maps of all simulated cases are available in the supplementary material (Appendix D).

Figure 34 – Velocity flow inside the NETmix milli-photoreactor: a) isometric view of velocity streamlines; b) top view of vector velocity for a plane in the center of the reactor; c) vector velocity inside a reactor channel; d) top view of vector velocity inside a reactor channel; e) top view of the velocity field inside a cylindrical chamber.

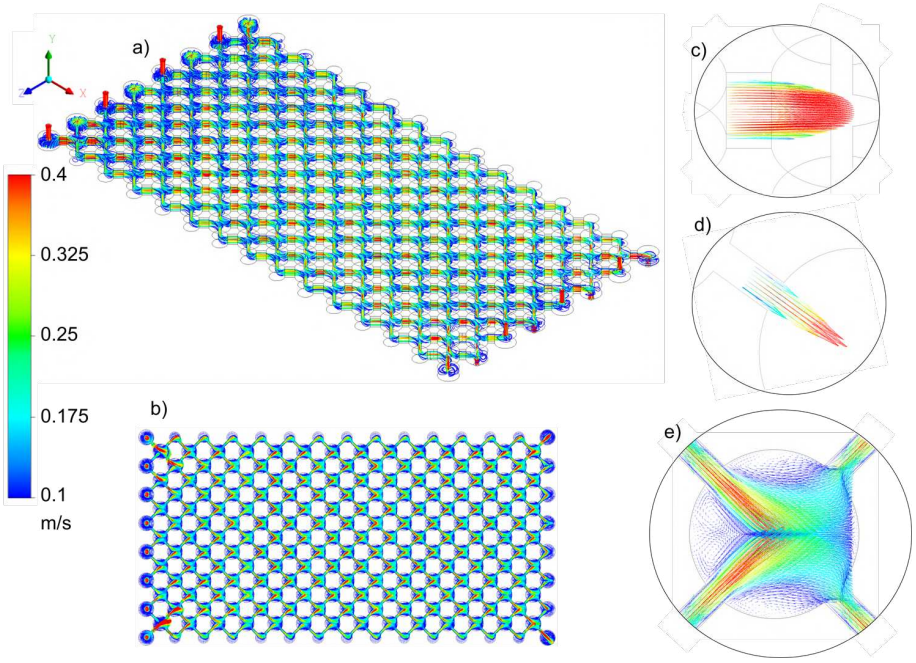

Source: Matiazzo et al. (2022b).

4.4.3 Degradation dynamics

To evaluate how the distinct illumination systems affect the pollutant degradation inside the NETmix milli-photoreactor, fluid dynamics simulations were performed linking the radiation fields obtained in each illumination system with the degradation of *n*-decane. The 28 CFD simulations were set with the same conditions (Table 7), except for the radiation field. The flow inside the reactor is laminar, with an average Reynolds number equivalent to 27 inside the prismatic channels. As shown in Figure 34, the flow is accelerated inside the prismatic channels resulting in recirculation zones inside the cylindrical chambers.

Under the analyzed conditions, 31% to 99% of the pollutant was degraded in the photoreactor. The degradation rate varied from $5.0{\cdot}10^{-9}$ to $1.6{\cdot}10^{-8}$ kmol/m^2·s. In Figure 35, the patterns of degradation rate and pollutant fraction over the catalyst for the cases with lowest and highest conversions are presented. It is clear that the light intensity distribution has great effect in the pollutant degradation rate. The chambers that receive more illumination register higher irradiance values that in turn contribute to greater pollutant local removal. The maps for pollutant fraction and degradation rate of all simulated cases are also available in the supplementary material (Appendix D).

Figure 36 shows the fractional conversion obtained with each of the illumination

Figure 35 – Pollutant degradation of selected cases.

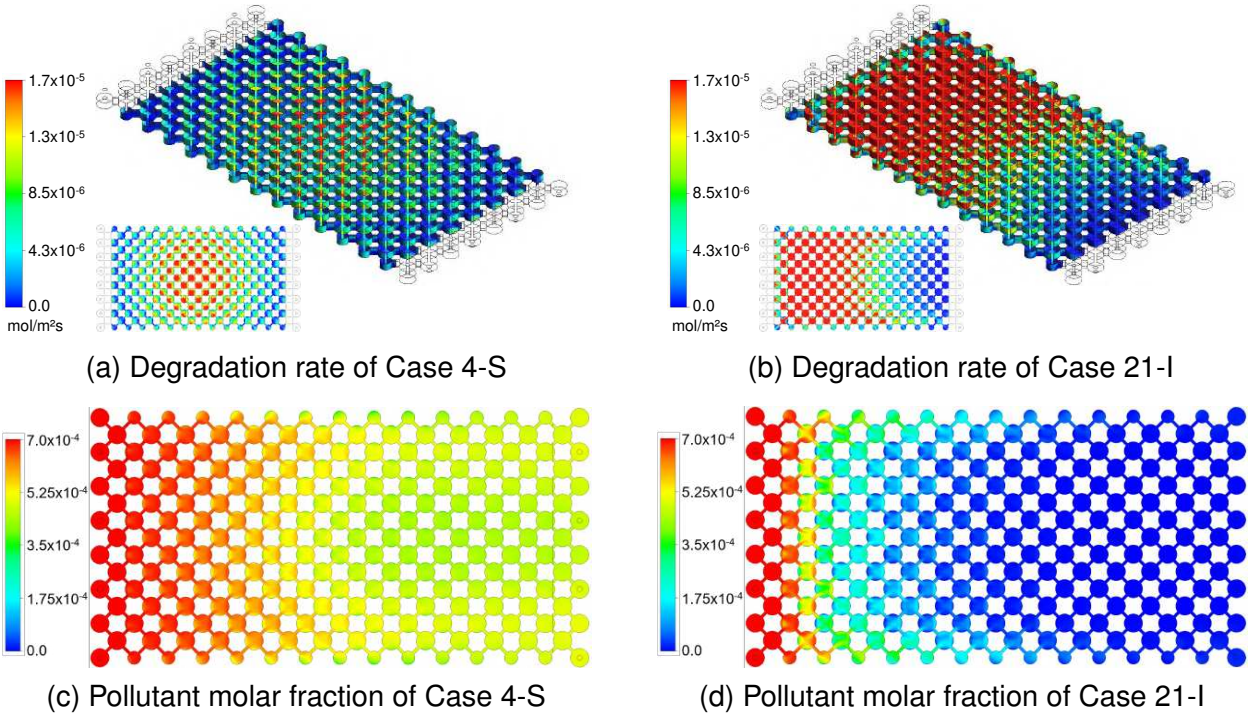

(a) Degradation rate of Case 4-S

(b) Degradation rate of Case 21-I

(c) Pollutant molar fraction of Case 4-S

(d) Pollutant molar fraction of Case 21-I

Source: Matiazzo et al. (2022b).

systems for the degradation of *n*-decane according to the conditions expressed in Table 7. Each line shows the behavior of a system with the variation of the LEDs-to-reactor distance. It is noticeable that the pollutant conversion increases with the number of LEDs, which is expected since more LEDs in the system leads to higher irradiance values. Although irradiance values also increase with the decrease in LEDs-to-reactor distance, the conversion does not follow this pattern and presents a peak of conversion at a distance equivalent to 12 mm. This is related to the overall photonic efficiency (Figure 32) and shows that the illumination system must be designed to provide the sufficient radiative energy levels associated with a good uniformity in the radiation field. It is important to mention here that the irradiance levels and uniformity index are not the only parameters that influence the reaction performance. The velocity field and the amount of pollutant in the feed flow are also determinant factors for the reactor's performance. The mass transfer, for instance can be appointed as the limiting factor in the cases with high irradiance values (28 and 30 LEDs). However, the focus of the current discussion is the photon transfer, for which was verified that the LEDs-to-reactor distance plays a key role. Regarding the photon transfer, independently of the LEDs arrangement and number, an ideal LEDs-to-reactor distance was identified, as 12 mm, where both overall photonic efficiency and pollutant conversion are maximized.

Figure 36 – Fractional pollutant conversion. Dashed lines represent the staggered systems and full lines show the behavior of inline arrangement.

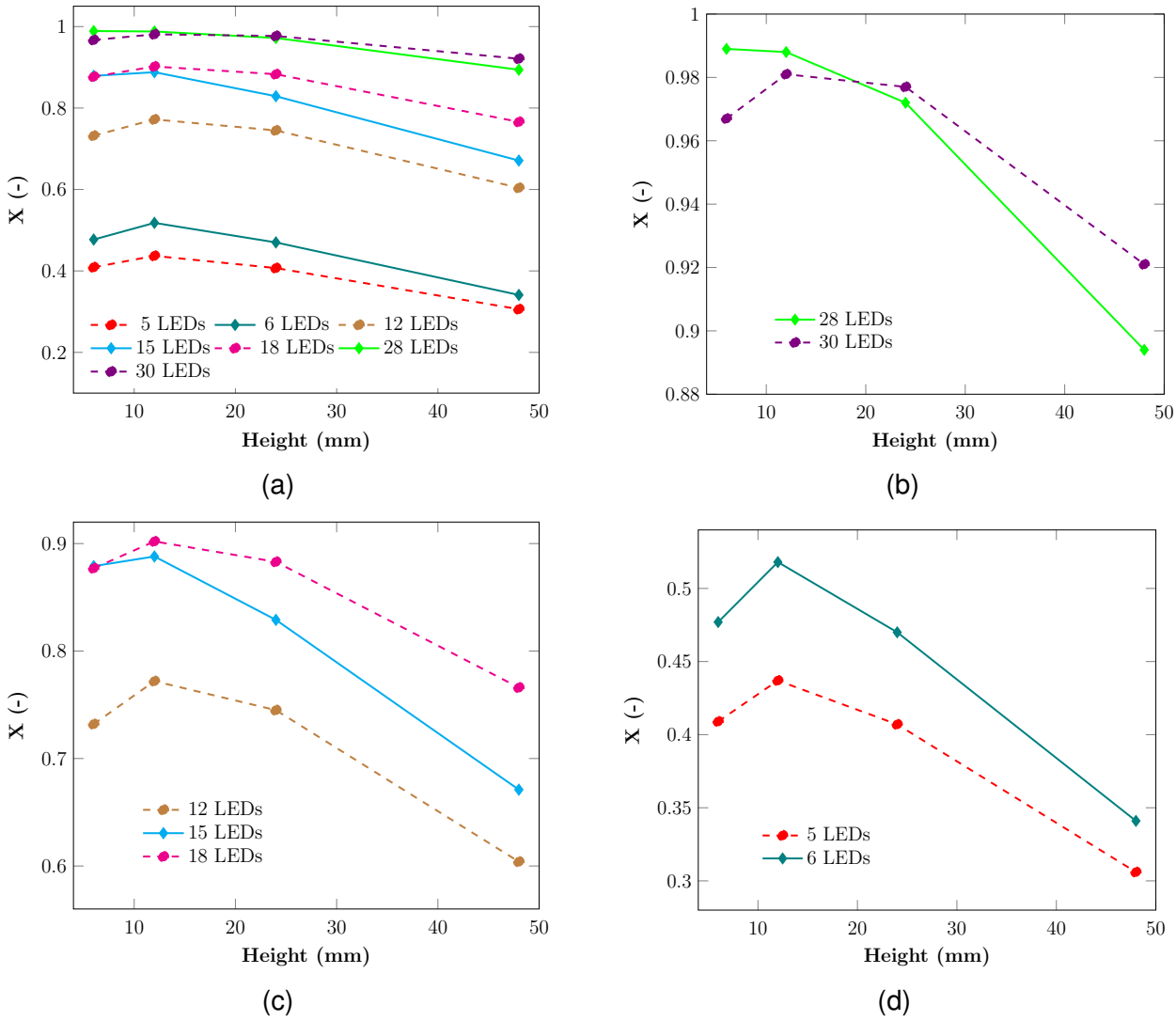

Source: Matiazzo et al. (2022b).

Figure 37 – Pollutant conversion against irradiance levels.

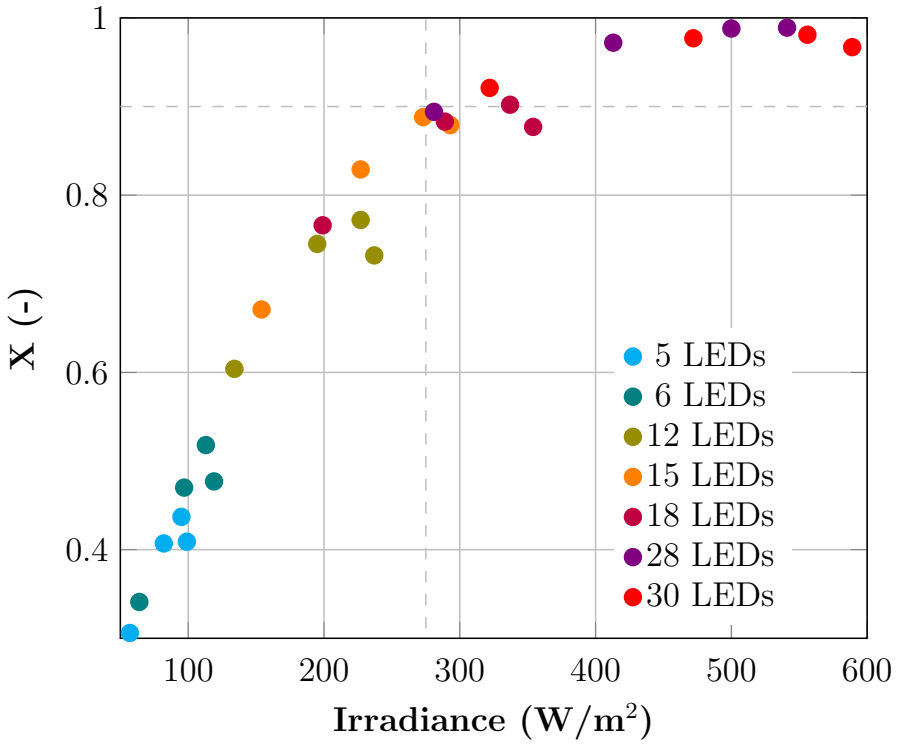

Source: Matiazzo et al. (2022b).

Figure 37 shows the pollutant conversion as a function of the irradiance values. Conversions above 95% were obtained for irradiance values above 400 W/m^2, corresponding to systems composed of 28 and 30 LEDs. However, systems that provide about 275 W/m^2 result in conversions a little under 90%. The cases that provide such illumination are case 13-I, 14-I, 19-S and 24-I (Table 6). These cases are composed of 15, 18 or 28 LEDs. Therefore, a system composed of 15 inline LEDs can be appointed as an ideal illumination system for the degradation of *n*-decane in the studied conditions, since correctly choosing the LEDs-to-reactor distance of a 15 LEDs plate can give similar results of an 18 LEDs plate or even a 28 LEDs plate that has a greater LEDs-to-reactor distance. This demonstrates that evaluating the irradiance levels along with the overall photonic efficiency and homogeneity of the field can lead to improvements on the illumination system, translating into better implantation and operational costs.

4.5 CONCLUSIONS

The radiation field incident on a TiO_2 film disposed in a FSI configuration in the NETmix milli-photoreactor was successfully evaluated through a non-sequential ray tracing technique. The use of 5, 12, 18 and 30 LEDs disposed in a staggered configuration were

compared to 6, 15 and 28 LEDs disposed in an inline arrangement over the reactor's window.

The LEDs-to-reactor distance was varied for all the illumination systems proposed and the resulting irradiance levels, absorption efficiency, uniformity of the radiation field and overall photonic efficiency were compared. An ideal distance equal to 12 mm was identified. With this LEDs-to-reactor distance, it is possible to achieve high irradiance levels while improving the uniformity of the irradiance distribution across the catalyst surface.

The proposed systems provided irradiance levels ranging from 57 W/m^2 to 589 W/m^2, with absorption efficiencies reaching 44% and uniformity indexes of up to 76%. Therefore, the systems presented overall photonic efficiencies between 14% and 31%.

The radiation field results were incorporated into CFD simulations. The degradation of *n*-decane was simulated for all of the 7 illumination systems with 4 LEDs-to-reactor distances, which gives a total of 28 cases. Irradiance levels between 400 W/m^2 and 600 W/m^2 resulted in conversions superior to 95%, while irradiance levels around 275 W/m^2 can convert near 90% of the inlet pollutant employing basically half of the LEDs.

Therefore, the combination of ray tracing and CFD simulations allows the identification of an ideal illumination system composed of 15 inline LEDs with a LEDs-to-reactor distance equivalent to 12 mm. This configuration was able to balance the number of required LEDs with high overall photonic efficiency, allowing the degradation of 89% of the pollutant in the feed.

5 COMPARISON OF CFD EMPLOYING AVERAGED IRRADIANCE VALUES AND CFD COUPLED WITH RADIATION FIELD MODELING DATA

As stated previously, many of the works available in the literature employ averaged values of irradiance into CFD simulations of photocatalytic oxidation, even if these values were obtained through radiation field analysis. To quantify the relevance of coupling the radiation field data with CFD, two cases from Chapter 4 were compared with CFD simulations employing the averaged value of irradiance in the reaction rate instead of reading the radiation field data.

Cases 1-S and 22-I (Table 6) presented the lowest and highest homogeneity index (γ) among the cases evaluated in Chapter 4. Case 1-S (Figure 38a) consisted of 5 LEDs disposed in a staggered alignment with a LEDs-to-reactor distance equivalent to 6 mm. This case provides an average irradiance equivalent to 99 W/m^2 with a homogeneity index of 32%. Case 22-I (Figure 38b) is composed by 28 LEDs arranged inline with a LEDs-to-reactor distance of 12 mm, such illumination system provides an average irradiation of 500 W/m^2 with a homogeneity index of 76%. Chapter 4 describes the CFD and radiation field coupling of these cases and the obtained pollutant degradation found for cases 1-S and 22-I was 40.9% and 98.8%, respectively.

Two CFD simulations were conducted for the same conditions (Table 7) of cases 1-S and 22-I but instead of reading the radiation field profile the irradiance was implemented in the user defined function (UDF) as a constant equivalent to 99 W/m^2 or 500 W/m^2, according to each case; therefore, in every point of the catalyst surface the irradiance assumes the same value.

Figure 38 – Reaction rate on the catalyst surface.

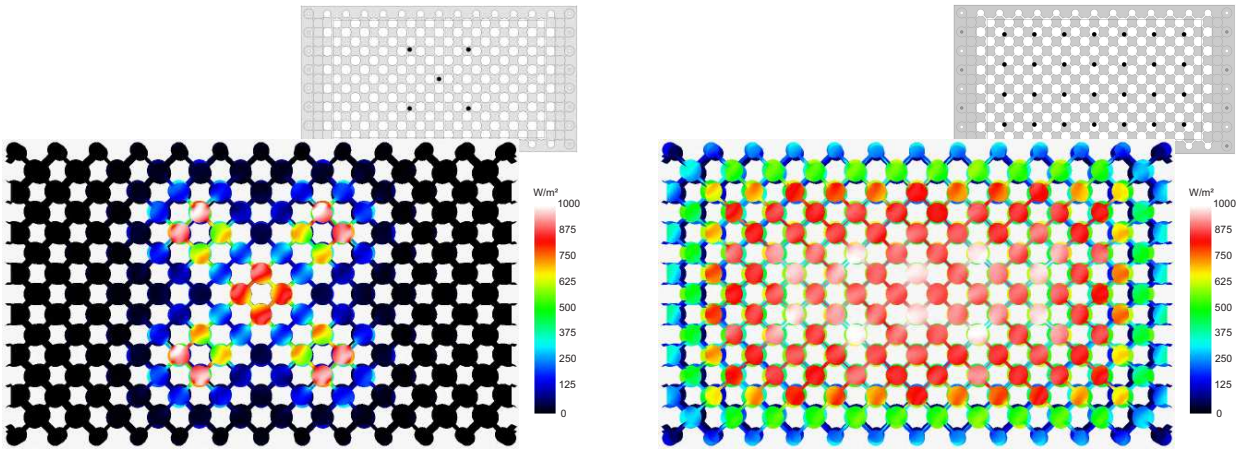

(a) Case 1-S: 5 LEDs, h = 6=mm, $E_{avg} = 99\ W/m^2, \gamma = 32\%$

(b) Case 22-I: 28 LEDs, h = 12=mm, $E_{avg} = 500\ W/m^2, \gamma = 76\%$

Source: elaborated by the author (2022).

Figure 39 – Reaction rate on the catalyst surface.

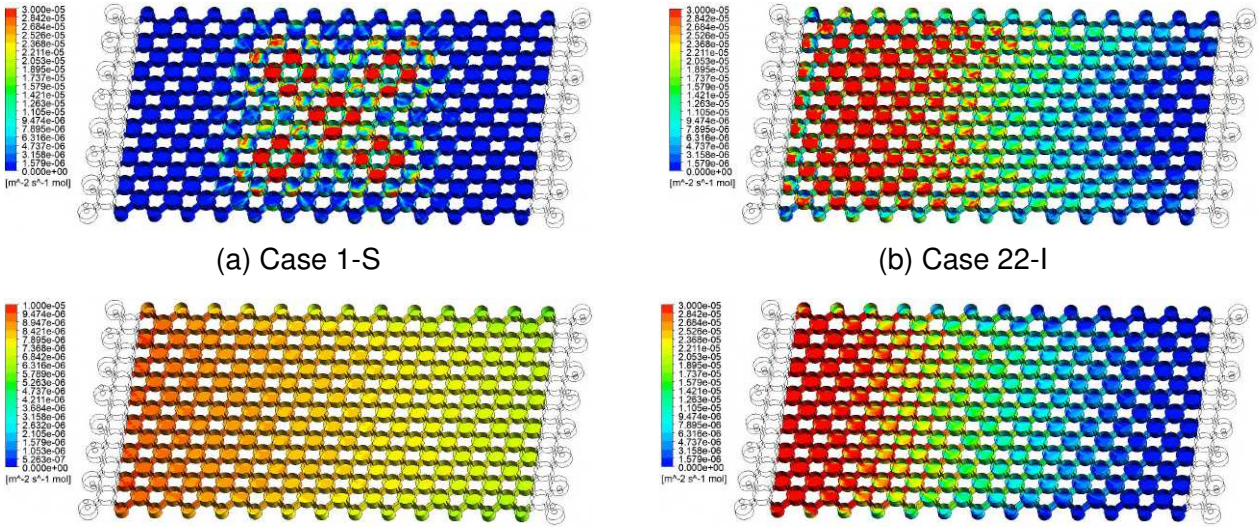

(a) Case 1-S

(b) Case 22-I

(c) E_{avg}=99 W/m^2 - Case 1

(d) E_{avg}=500 W/m^2 - Case 22

Source: elaborated by the author (2022).

Figure 39 displays the reaction rate obtained at the catalyst surface for both cases using the radiation profile and cases using an averaged value of irradiance. It is noticeable that the patterns of the reaction rate differ from employing profile data and averaged values. For case 1, that employs only 5 LEDs and has a lower homogeneity, the differences are easier to spot. In Figure 39a the reaction rate is clearly faster in the chambers closer to the position of the 5 LEDs, in the center of the reactor, that is expected since those chambers are better illuminated due to their geometrical positions. Employing the averaged value of irradiance does not reach the same reaction pattern, as seen in Figure 39c. In this case it is assumed that every point of the catalyst receives the same amount of illumination and therefore, the rate of reaction decreases, almost homogeneously, with the length of the reactor as the pollutant becomes scarcer.

For case 22-I (Figure 39b) and its equivalent case with average values (Figure 39d) the similar behavior was registered, however, with less intensity. These considerations are reaffirmed analyzing the progression of the pollutant conversion along the length of the reactor, Figure 40. Case 22-I and the simulation employing an average irradiance of 500 W/m^2 have similar behavior and similar pollutant conversion values. Therefore, both cases produce very similar pollutants conversion and kinetic rates. This is related to the fact that when 28 LEDs were employed in the current disposition a high level of irradiance is registered, and the radiation field obtained has a high homogeneity index (76%). In this way, the relative error of using an averaged value of irradiance was approximately only 1%.

On the other hand, the case employing only 5 LEDs (γ = 32%) did not present

Figure 40 – Pollutant conversion along the length of the reactor.

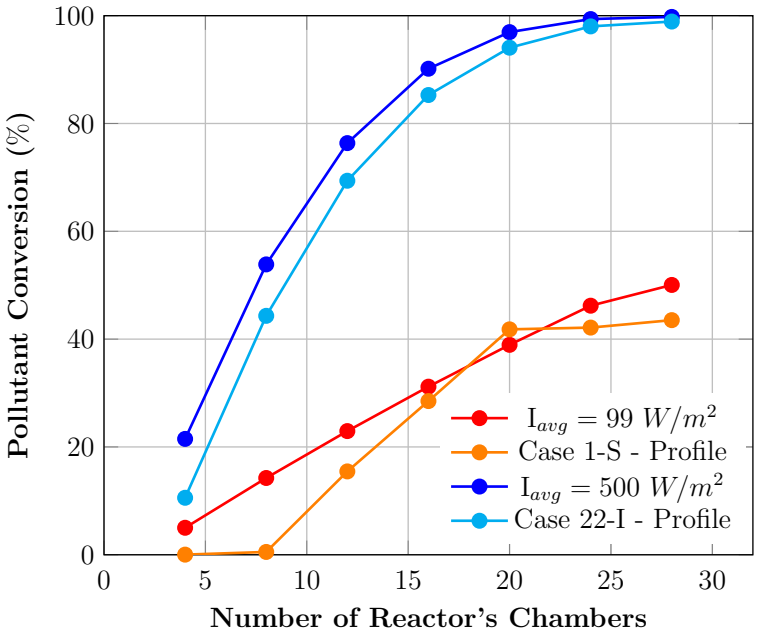

Source: elaborated by the author (2022).

the same level of similarity. As shown in Figure 40, in the case employing an average value of 99 W/m^2 for irradiance the conversion of the pollutant has an approximate linear progression through the length of the reactor. In case 1-S, using the radiation profile, the pollutant conversion starts around the eighth chamber row and progress linearly until it reaches the twentieth chamber row, and then the conversion stabilizes from this point forwards. This is justified by the position of LEDs in the illumination system. Virtually no light reaches the firsts and lasts chambers of the reactor. Therefore, the relative error of employing averaged values of irradiance in this case can be as high as 24%, as specified in Table 9. Consequently, it can be concluded that using average values of irradiance in CFD simulations can only provide accurate results if the radiation field of the case presents a high homogeneity index.

Table 9 – Comparison of results obtained for CFD simulations employing radiation field data and averaged values.

Variable	Number of LEDs	Radiation Profile Data	Averaged Values	Relative Error
Pollutant Conversion	5	40.9%	50.8%	24.0%
	28	98.8%	99.8%	1.0%
Degradation Rate (kmol/m^2· s)	5	$6.80{\cdot}10^{-9}$	$8.05{\cdot}10^{-9}$	18.4%
	28	$1.57{\cdot}10^{-8}$	$1.58{\cdot}10^{-8}$	0.8%

Source: elaborated by the author (2022).

6 PERFORMANCE EVALUATION OF THE MILLI-PHOTOCATALYTIC REACTOR NETMIX OPERATING UNDER DISTINCT REYNOLDS NUMBERS

In this chapter, the performance of the NETmix milli-photoreactor is evaluated according to dimensionless numbers and to a number of transfer units method (NTUm). The usefulness of the methodology and the adaptation from heat exchangers evaluations to PCO was first presented by Yinping, Yang, and Zhao (2003). The method uses three dimensionless fractional variables to evaluate the performance of the photocatalytic oxidation. The variables are the fractional conversion (ϵ), the number of transfer units (NTUm) and the reaction effectiveness parameter (η).

6.1 METHODOLOGY

The photocatalytic process investigated here was simulated under isothermal steady state conditions with the Newtonian fluid being incompressible with constant variables. The conservation of mass, momentum and species are summarized in Equations (32) to (38). The realizable $k-\varepsilon$ was employed to account for turbulence in the system as indicated in Equations (39) to (44).

$$\nabla \cdot (\rho \boldsymbol{\nu}) = 0 \tag{32}$$

$$\nabla \cdot (\rho \boldsymbol{\nu}\boldsymbol{\nu} + \rho \boldsymbol{\nu'}\boldsymbol{\nu'}) = -\nabla P - \nabla \cdot \boldsymbol{\tau} \tag{33}$$

$$\nabla \cdot (\rho \boldsymbol{\nu}\boldsymbol{\nu}) = -\nabla \mathbf{P} - \nabla \cdot \boldsymbol{\tau}^{\boldsymbol{eff}} \tag{34}$$

$$\boldsymbol{\tau}^{\boldsymbol{eff}} = \boldsymbol{\tau} + \boldsymbol{\tau_t} \tag{35}$$

$$\boldsymbol{\tau} = \mu \left(\nabla \boldsymbol{\nu} + \nabla \boldsymbol{\nu}^T \right) - \frac{2}{3} \mu \nabla \cdot \boldsymbol{\nu} I \tag{36}$$

$$\boldsymbol{\tau_t} = \rho \boldsymbol{\nu'}\boldsymbol{\nu'} \tag{37}$$

$$\nabla \cdot (\rho \boldsymbol{\nu} \boldsymbol{x_i} + \rho \boldsymbol{\nu'} \boldsymbol{x_i'}) = -\nabla \boldsymbol{J_i} \tag{38}$$

$$\tau_{\mathrm{t}} = \mu_{\mathrm{t}} \left(\nabla \nu + \nabla \nu^{\mathrm{T}} \right) - \frac{2}{3} \mathrm{I} \left(\mu_{\mathrm{t}} \nabla \cdot \nu + \rho k \right) \tag{39}$$

$$\mu_{\mathrm{t}} = C_{\mu} \rho \frac{k^2}{\varepsilon} \tag{40}$$

$$C_{\mu} = \frac{1}{4.04 + A_{\mathrm{s}} U^* \frac{k}{\varepsilon}} \tag{41}$$

$$\nabla \cdot (\rho \nu k) = \nabla \cdot \left[\left(\mu + \frac{\mu_{\mathrm{t}}}{\sigma_k} \right) \nabla k \right] + \mathrm{P}_k - \rho \varepsilon \tag{42}$$

$$\nabla \cdot (\rho \nu \varepsilon) = \nabla \cdot \left[\left(\mu + \frac{\mu_{\mathrm{t}}}{\sigma_{\varepsilon}} \right) \nabla \varepsilon \right] + C_1 \rho S_{\varepsilon} + C_{1\varepsilon} \frac{\varepsilon}{k} \mathrm{P}_k - C_2 \rho \frac{\varepsilon^2}{k + \sqrt{\nu \varepsilon}} \tag{43}$$

$$\mathrm{P}_k = \mu_{\mathrm{t}} \left[\nabla \nu + (\nabla \nu)^{\mathrm{T}} \right] : \nabla \nu \tag{44}$$

where $\sigma_{\varepsilon} = 1.2$, $C_2 = 1.9$, $C_1 = \max |0.43, \quad \eta/(\eta + 5)|$ (with $\eta = kS/\varepsilon$), and $C_{\mu} = 1/\left(4.04 + A_{\mathrm{S}} k U^*/\varepsilon\right)$, where $A_{\mathrm{S}} = 6^{1/2} \cos \Phi, \Phi = \left(\cos^{-1} 6^{1/2} W\right)/3$, $W = \bar{S}_{ij} \bar{S}_{jk} \bar{S}_{ki} / \breve{S}^3 \breve{S} = \sqrt{2 S_{ij} S_{ij}}, \quad U^* = \sqrt{\bar{S}_{ij} \bar{S}_{ij} + \bar{\Omega}_{ij} \bar{\Omega}_{ij}} \quad \bar{S}_{ij} = \frac{1}{2} \left(\frac{\partial u_i}{\partial x_j} + \frac{\partial u_j}{\partial x_i} \right) - \frac{1}{3} \frac{\partial u_k}{\partial x_k} \delta_{ij}$ and $\bar{\Omega}_{ij} = \frac{1}{2} \left(\frac{\partial u_i}{\partial x_j} - \frac{\partial u_j}{\partial x_i} \right)$.

Firstly, simulations of air and water flow were conducted for various Reynolds numbers without any reaction rate. Following, the oxidation of *n*-decane from an air stream was conducted for distinct pollutant concentrations and inlet velocities (Table 10) for the evaluation of the reactor performance according to number of mass transfer units (NTUm).

6.2 PRESSURE DROP AND FRICTION FACTOR BEHAVIOR

To evaluate the pressure drop and the friction factor simulations for the flow of air and water were conducted for a variety of Reynolds numbers. Figure 41 depicts how the

Table 10 – Boundary conditions of CFD cases for NTUm evaluation.

Velocity inlet:	0.01, 0.025, 0.05, 0.075, 0.1, 0.25, 0.5, 0.75, 1.0, 1.5, 2.0, 3.0, 5.0, 10.0 m/s
Molar fraction of *n*-decane:	$7{\cdot}10^{-4}$, $1.4{\cdot}10^{-3}$
Molar fraction of water vapor:	10^{-2}
Pressure outlet:	Atmospheric
Walls:	No slip
Reactive walls:	$r_{dec} = 3.09 \cdot 10^{-8}\ E\ C_{dec}^{0.43}\ C_{w}^{0.18}$

Source: elaborated by the author (2022).

pressure drop increases in the NETmix reactor with the augment of Reynolds number. The Reynolds number inside the channels of the reactor was varied from 0.2 to around 3,500 in numerical simulations. The pressure drop registered for an air stream varied from 0.05 Pa to approximately 35,000 Pa. For a water stream the pressure drop ranged from 0.2 Pa to about 122,000 Pa. For laminar flows, the dependency of ΔP with the Reynolds number is linear due to the Hagen-Poiseuille equation, but in the presence of vortex structures this dependency becomes a square law (KHAYDAROV; BOROVINSKAYA; RESCHETILOWSKI, 2018). For Reynolds numbers lower than 10 this linear dependency was verified and the pressure drop can be expressed as ΔP = 0.3 Re for the air flow and ΔP = 1.1 Re for water flow. Covering a wider range of Reynolds numbers a square law can describe the pressure drop in the reactor as ΔP = 0.0028 Re^2 + 0.5563 Re and ΔP = 0.0108 Re^2 + 1.6644 Re for air and water, respectively.

Figure 41 – Pressure drop for distinct Reynolds numbers.

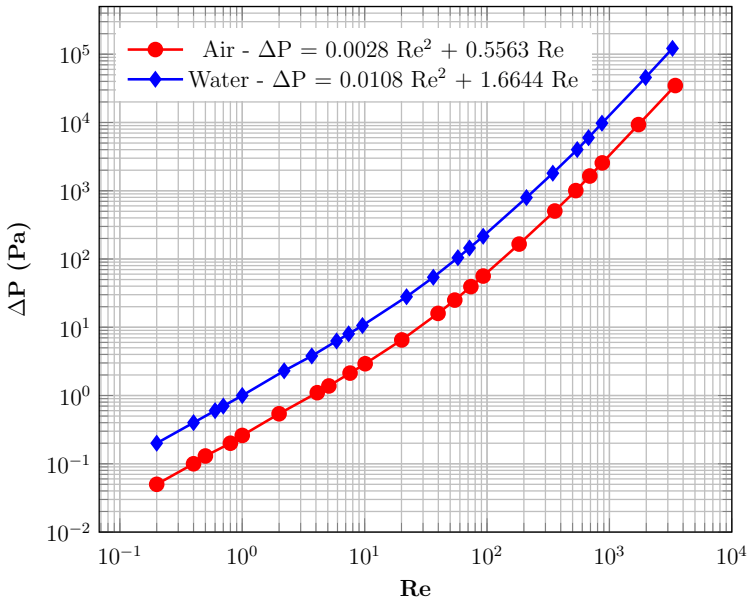

Source: elaborated by the author (2022).

The Darcy friction factor (Equation (45)) normalizes the pressure drop based on inertial scales and it is a dimensionless form to evaluate the flow resistance (NGUYEN; ABOUEZZI; RISTROPH, 2021). In Figure 42 the friction factor calculated at each Reynolds number is displayed for both air and water flows. For comparison an f_D = 32/Re is plotted alongside the results. For low Reynolds numbers the friction factor was approximately equivalent to 32/Re. For Reynolds numbers between 10 and 100 the friction factor gradually increases from 32/Re to 64/Re, which is still compatible with laminar flow. For Reynolds numbers above 100 the friction factor increases potentially with the augment of Reynolds number and tends to reach and stabilize at a value of around 0.5.

$$f_D = \frac{2}{\nu^2}\frac{d_h}{l}\frac{\Delta P}{\rho} \tag{45}$$

where ΔP (Pa) is the pressure drop, l (m) is the length of the reactor, ρ (kg/m^3) is the density of the fluid, v (m/s) is the velocity and d_h (m) is the hydraulic diameter.

Figure 42 – Friction factor calculated at distinct Reynolds numbers.

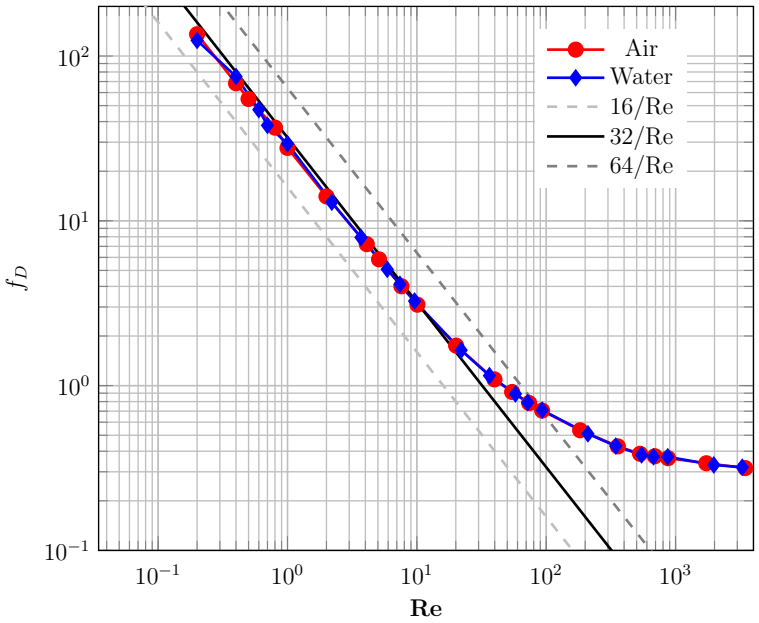

Source: elaborated by the author (2022).

6.3 NUMBER OF MASS TRANSFER UNITS (NTU$_m$) ANALYSIS

Analogously to the number of transfer units (NTU) employed in the project of heat exchangers, the number of mass transfer units (NTUm) for photocatalytic reactors can be defined as in Equation (46).

$$NTUm = \frac{K_t A}{G} \tag{46}$$

where K_t (m/s) is the total removing factor (Equation (47)) based on the mass transfer coefficient (h_{mass}) and apparent rate constant (k_{app}), A (m^2) is the catalytic area and G (m^3/s) is the flow rate through the reactor.

$$K_t = \frac{1}{\frac{1}{h_{mass}} + \frac{1}{k_{app}}} \tag{47}$$

The removal of VOCs can be measured through the use of Equation (48) that represents the fractional conversion.

$$\epsilon = \frac{C_{dec.inlet} - C_{dec.outlet}}{C_{dec.inlet}} = 1 - e^{-NTUm} \tag{48}$$

The effectiveness of the reaction is accessed through the ideal number of mass transfer units, $NTUm_{ideal}$ (Equation (49)). Under ideal photocatalytic reaction conditions the system is completely controlled by mass transfer; therefore $k_{app} \rightarrow \infty$ and then K_t becomes h_{mass} (Equation (47)). Accordingly, $NTUm_{ideal}$, ϵ_{ideal}, and η can be expressed as in Equations (49)-(51).

$$NTUm_{ideal} = \frac{h_{mass} A}{G} \tag{49}$$

$$\epsilon_{ideal} = 1 - e^{-NTUm_{ideal}} \tag{50}$$

$$\eta = \frac{\epsilon}{\epsilon_{ideal}} \tag{51}$$

As state by Walsem et al. (2018), the analysis of the reaction effectiveness parameter (η) express if the system is mass transfer or reaction controlled. When $k_{app} \gg h_{mass}$, η approaches 1 and therefore the system is controlled by the mass transfer. Alterations in the reactor's geometry can be utilized to overcome such transfers limitations, for example. On the other hand, if η approaches 0 ($h_{mass} \gg k_{app}$) the system is limited by the photocatalytic reaction, and enhancements in the illumination system can be proved beneficial to the reactor's performance.

To determine the reaction effectiveness, the mass transfer coefficient must be determined in order to calculate the NTUm$_{ideal}$ (Equation (49)). The h_{mass} can be determined through the determination of the Sherwood number, employing Equations (52) to (55).

$$Sh = \frac{h_{mass} d_h}{D_{dec,m}} \tag{52}$$

$$Sh = Sh_{\infty} \left(1 + 0.095 \frac{d_h}{l} Pe\right)^{0.45} \tag{53}$$

$$Sh_{\infty} = 2.8932 + 4.6482 \exp(-4.4754 \frac{H}{W}) \tag{54}$$

$$Pe = Re\ Sc = \frac{\rho\ v\ d_h}{\mu}\ \frac{\mu}{\rho\ D_{dec,m}} = \frac{v d_h}{D_{dec,m}} \tag{55}$$

where Sh is the dimensionless Sherwood number, h_{mass} (m^2/s) is the mass transfer coefficient, d_h (m^2) is the hydraulic diameter, $D_{dec,m}$ (m^2/s) is the diffusion coefficient of the VOC in the air mixture, Sh$_{\infty}$ is the asymptotic value of Sherwood, Pe is the dimensionless Péclet number, l (m) is the reactor's length, H (m) is height of the channel, W (m) is the channel's width, v (m/s) is the flow velocity, and Re and Sc represent the dimensionless numbers of Reynolds and Schmidt, respectively.

Figure 43a shows the progression of the Péclet number (Equation (55)) with the increase of Reynolds number. The evaluated flows have Reynolds numbers in the reactor's channels ranging from 0.5 to 530, consequently, the Péclet varies from 2 to 1980. The obtained Péclet number was then introduced in Kashid, Renken, and Kiwi-Minsker (2015) correlation of Sherwood number (Equation (53)). The resulted Sherwood number (Figure 43b) was used to calculate the mass transfer coefficient as in Equation (52). The calculated coefficients varied from $7.5{\cdot}10^{-3}$ m^2/s to $1.1{\cdot}10^{-2}$ m^2/s (Figure 43c).

Figure 44 shows the number of mass transfer units calculated with the fractional conversion (Equation (48)) and the NTUm$_{ideal}$ calculated considering the system under ideal photocatalytic conditions (Equation (49)). For Reynolds numbers under five a pollutant conversion of 100% is achieved and the NTUm is identical to NTUm$_{ideal}$. This means that for these conditions the system is completely controlled by the mass transfer. As the Reynolds number progress, the relative error between NTUm and NTUm$_{ideal}$ reaches up to 94%.

In Figure 45 the fractional conversion obtained in the simulations as well as the ideal fractional conversion calculated are compared for two inlet pollutant concentrations.

Figure 43 – Numbers of Péclet, Sherwood and mass transfer coefficients obtained at different Reynolds numbers.

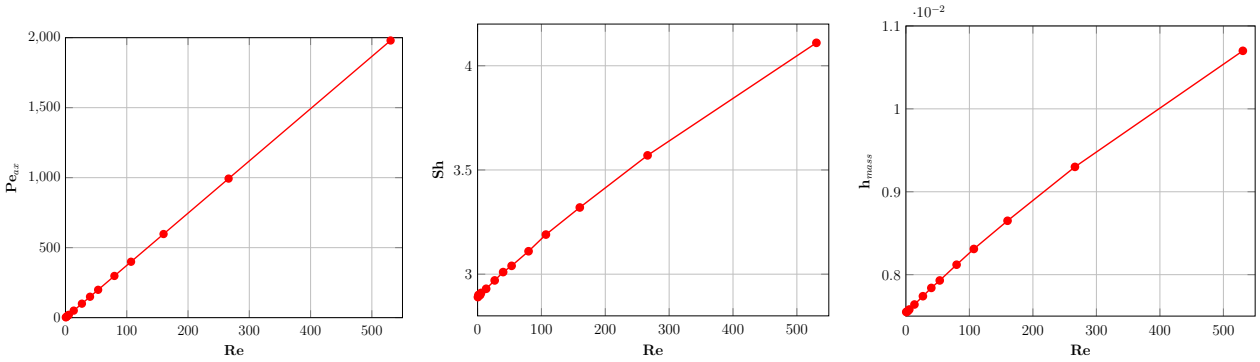

(a) Péclet Number (b) Sherwood Number (c) Mass transfer coefficient

Source: elaborated by the author (2022).

Figure 44 – NTUm comparison.

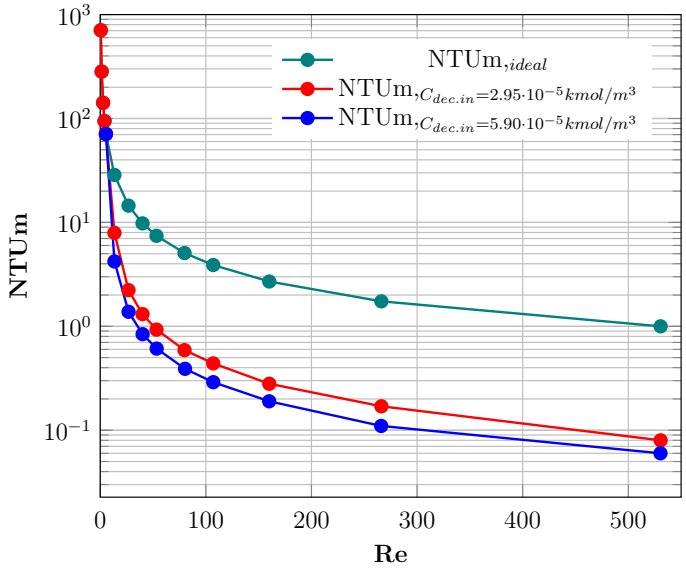

Source: elaborated by the author (2022).

Figure 45 also expresses the progression of reaction effectiveness for the distinct Reynolds numbers analyzed. For Reynolds numbers lower than 10, the reaction effectiveness was equivalent to 1. This means that the system operation under such conditions is controlled by the mass transfer. For higher Reynolds numbers the reaction effectiveness factor decreases gradually to 0.13 and 0.09 for an initial pollutant concentration equivalent to $2.95{\cdot}10^{-5}$ kmol/m^3 and $5.90{\cdot}10^{-5}$ kmol/m^3, respectively. Therefore, when higher Reynolds numbers are employed $\eta \to 0$ and the system becomes reaction controlled.

Figure 45 – Fractional conversion and reaction effectiveness parameter.

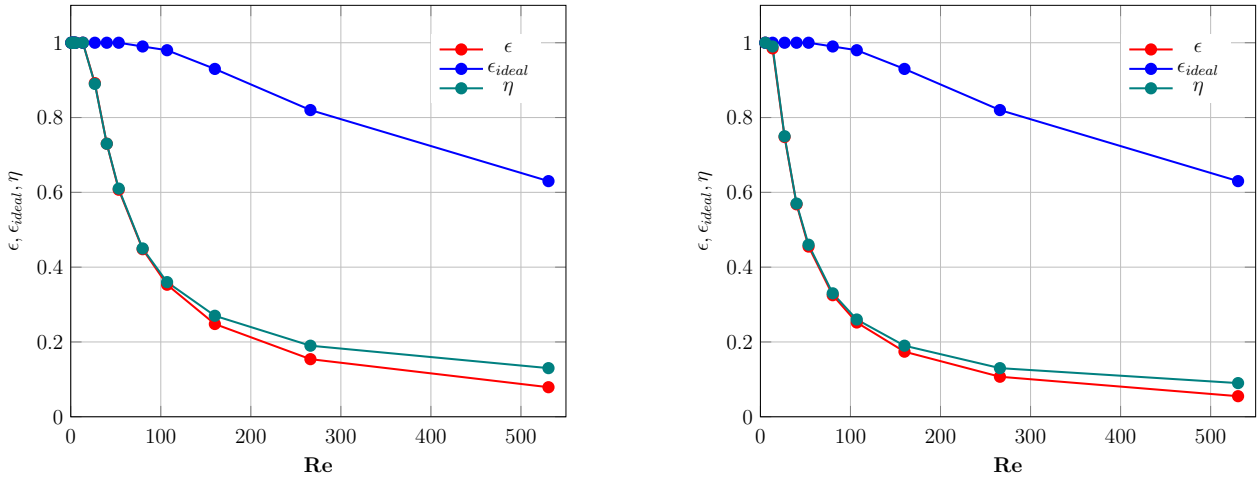

(a) $C_{dec,in}$ = 2.95·10^{-5} kmol/m^3 (b) $C_{dec,in}$ = 5.90·10^{-5} kmol/m^3

Source: elaborated by the author (2022).

7 CONCLUDING REMARKS

Air quality in the workplace and inside households is a matter of growing concern, since many building materials employed in construction sites, along with paints and furniture items can exhale volatile organic compounds. Photocatalytic reactors are a promising alternative for the treatment of air streams containing volatile organic compounds (VOCs), resulting in the oxidation of those toxic compounds into inert species. The emergence of LED technology facilitates the use of photocatalytic reactors and the miniaturization of such systems, besides contributing to its lower costs of implantation and operation. Therefore, in this work the aid of computational tools in the project of photocatalytic reactors was explored.

A computational fluid dynamics (CFD) and a ray tracing model were coupled to simulate the reactive flow and light transport in the NETmix milli-photocatalytic reactor used in the removal of VOCs from air streams. For the model development, the optical properties of the TiO_2 catalyst were investigated, as well as the reaction rate of a model VOC pollutant, *n*-decane. Both, CFD and ray tracing simulations were validated successfully against experimental data. The model was then used to investigate the relevance of the geometrical position, the arrangement and the number of the LEDs that compose the reactor's illumination system, as well as the impact that irradiance field levels and homogeneity have over the pollutants oxidation. A number of transfer units model (NTUm) was also employed to verify the system bottleneck limitations. The main finds of the current thesis are summarized as follows:

- the illumination system of the NETmix milli-photocatalytic reactor was evaluated considering two catalyst deposition schemes, back-side illumination (BSI) and front-side illumination (FSI). The radiation field incident at a TiO_2 catalyst film was simulated employing a non-sequential ray tracing algorithm and were validated against experimental data. The validation of ray tracing simulations presented a relative error of 2.3% and 7.0% for the BSI and FSI schemes, respectively;

- the geometrical position of an illumination system composed of 18 LEDs was evaluated considering three parameters, ω, ℓ and h, that represent the proximity between LEDs and the proximity of the LEDs plate to the photoreactor window. In total, 27 simulation points were generated for the 18 LEDs set. Simulations were conducted for both BSI and FSI. The light absorption efficiency and the homogeneity of the radiation film was evaluated. The pattern of the absorption efficiency was similar for both BSI and FSI, however the homogeneity of the field in the FSI catalyst was inferior. The results also show that the absorption efficiency increase with the proximity of

LEDs to each other and to the reactor window, however in the same conditions the homogeneity of the irradiation field decreases;

- the use of 5, 12, 18 and 30 LEDs disposed in a staggered arrangement were compared to 6, 15 and 28 LEDs disposed in an inline arrangement over the reactor's window. For each system the LEDs-to-reactor distance was varied and the radiation field incident in a FSI TiO_2 catalyst thin film was evaluated. The irradiance levels, absorption efficiency, uniformity and global efficiency provided by each LEDs set was compared and latter coupled to CFD simulations for the *n*-decane removal from an air stream;

- variations in the number of LEDs in the illumination system resulted in irradiance levels ranging from 57 W/m^2 to 589 W/m^2, with absorption efficiencies reaching 44% and uniformity indexes of up to 76%. Overall illumination efficiencies ranged from 14% to 31%. When the radiation fields were incorporated to CFD simulations, a pattern for the ideal LEDs-to-reactor distance emerged. Independently of the number of LEDs used in the system the best pollutant conversion was reached for an LEDs-to-reactor distance equivalent to 12 mm. At such distance was possible to maintain high irradiance levels with high field homogeneity;

- irradiance levels between 400 W/m^2 and 600 W/m^2 resulted in conversions superior to 95%, while irradiance levels around 275 W/m^2 can convert near 90% of the inlet pollutant employing basically half of the LEDs. Therefore, the combination of ray tracing and CFD simulations allow the identification of an ideal illumination system, balancing absorption and homogeneity;

- a number of mass transfer units method (NTUm) was employed to evaluate which phenomena controls the system, either reaction rate or mass transfer, under Reynolds numbers ranging from 0.5 to 530. The method demonstrates that under low Reynolds numbers the performance of the photocatalytic reactor was controlled by the mass transfer whilst for higher Reynolds numbers the bottleneck of the system was the reaction rate.

Overall, CFD and ray tracing simulations are invaluable tools in the project design and performance evaluation of photoreactors. Both techniques are of great assistance in the modeling of mass and light transport. Also, it has been shown that the coupling of radiation field data with CFD is of great importance for the accuracy of reaction rate simulations above all for systems that provide radiation fields with low homogeneity. For cases where the radiation field has high homogeneity indexes, employing an average

irradiance value in the CFD simulations can be a reasonable simplification; however, the same cannot be stated for radiation fields that lack homogeneity. With a homogeneity index of only 32% a relative error as high as 24% has been registered in the pollutant conversion. That said, the light transport is a defining phenomenon in the project and performance of photocatalytic reactors and ray tracing techniques can be of great assistance to the optimization of light transport in photocatalytic reactors.

REFERENCES

ABDULLAH, N.; KAMARUDIN, S.K. Titanium dioxide in fuel cell technology: An overview. **Journal of Power Sources**, v. 278, p. 109–118, Mar. 2015. ISSN 03787753.

ABIEV, Rufat S. Process intensification in chemical engineering: general trends and Russian contribution. **Reviews in Chemical Engineering**, Mar. 2019. ISSN 2191-0235.

ÁDÁM, Veres; ZOLTÁN, Németh; GYÖRGY, Ábrahám. Calculations and Simulations for the Usability of Polyhedron Shaped Integrating Photometers. In: XIV INTERNATIONAL PhD WORKSHOP OWD. Wisła: Conference Archives PTETiS, 2012. v. 31. P. 229–234.

AKACH, John; KABUBA, John; OCHIENG, Aoyi. Simulation of the Light Distribution in a Solar Photocatalytic Bubble Column Reactor Using the Monte Carlo Method. **Industrial & Engineering Chemistry Research**, v. 59, n. 40, p. 17708–17719, Oct. 2020. ISSN 0888-5885.

AKERDI, Abdollah Gholami; BAHRAMI, S. Hajir. Application of heterogeneous nano-semiconductors for photocatalytic advanced oxidation of organic compounds: A review. **Journal of Environmental Chemical Engineering**, v. 7, n. 5, p. 103283, Oct. 2019. ISSN 22133437.

ALVARADO-ROLON, O.; NATIVIDAD, R.; ROMERO, R.; HURTADO, L.; RAMÍREZ-SERRANO, A. Modelling and Simulation of the Radiant Field in an Annular Heterogeneous Photoreactor Using a Four-Flux Model. **International Journal of Photoenergy**, v. 2018, 2018. ISSN 1110-662X.

ASADOLLAHFARDI, G.; NOORI, M.; ASADI, M.; TAHERIOUN, M. The comparison of discrete ordinate and Monte Carlo methods in solving of the radiation transfer equations in a heterogenous reactor. **Journal of Water Supply: Research and Technology - Aqua**, v. 67, n. 1, p. 109–118, Feb. 2018. ISSN 0003-7214.

AYOUB, Mohammed. A review on light transport algorithms and simulation tools to model daylighting inside buildings. **Solar Energy**, v. 198, p. 623–642, Mar. 2020. ISSN 0038092X.

BARANOSKI, Gladimir V. G.; KRISHNASWAMY, Aravind. **Light & Skin Interactions. Simulations for Computer Graphics Applications**. Burlington: Morgan Kaufmann Publishers - Elsevier, 2010.

BENTLEY, Julie; OLSON, Craig. Snell's Law and Ray Tracing. In: FIELD Guide to Lens Design. [S.l.]: SPIE, 2012.

BERENJIAN, Aydin; CHAN, Natalie; MALMIRI, Hoda Jafarizadeh. VOLATILE ORGANIC COMPOUNDS REMOVAL METHODS: A REVIEW. **American Journal of Biochemistry and Biotechnology**, v. 8, n. 4, p. 220–229, Apr. 2012. ISSN 1553-3468.

BHATTACHARJEE, Pramode Ranjan. The generalized vectorial laws of reflection and refraction. **European Journal of Physics**, v. 26, n. 5, Sept. 2005. ISSN 0143-0807.

BIRNIE, M.; RIFFAT, S.; GILLOTT, M. Photocatalytic reactors: design for effective air purification. **International Journal of Low-Carbon Technologies**, v. 1, n. 1, p. 47–58, Jan. 2006. ISSN 1748-1317.

BOYJOO, Yash; SUN, Hongqi; LIU, Jian; PAREEK, Vishnu K.; WANG, Shaobin. A review on photocatalysis for air treatment: From catalyst development to reactor design. **Chemical Engineering Journal**, v. 310, p. 537–559, Feb. 2017. ISSN 13858947.

BRITO LIRA, Jéssica Oliveira de; PADOIN, Natan; VILAR, Vítor J. P.; SOARES, Cíntia. Photocatalytic NOx abatement: Mathematical modeling, CFD validation and reactor analysis. **Journal of Hazardous Materials**, v. 372, p. 145–153, 2019. SI: Photocatalysis:Future Trend. ISSN 0304-3894.

CASIMIRO, Maria Helena; FERREIRA, Luis Mota; LEAL, João Paulo; PEREIRA, Claudia Cristina Lage; MONTEIRO, Bernardo. Ionizing Radiation for Preparation and Functionalization of Membranes and Their Biomedical and Environmental Applications. **Membranes**, v. 9, n. 12, Dec. 2019. ISSN 2077-0375.

CELIK, Ismail B.; GHIA, Urmila; ROACHE, Patrick J.; FREITAS, Christopher J.; COLEMAN, Hugh; RAAD, Peter E. Procedure for Estimation and Reporting of Uncertainty Due to Discretization in CFD Applications. **Journal of Fluids Engineering**, v. 130, n. 7, p. 078001, 2008. ISSN 00982202.

CHEEK, Emily; GUERCIO, Valentina; SHRUBSOLE, Clive; DIMITROULOPOULOU, Sani. Portable air purification: Review of impacts on indoor air quality and health. **Science of The Total Environment**, v. 766, Apr. 2021. ISSN 00489697.

CHEN, Jian; LOEB, Stephanie; KIM, Jae-Hong. LED revolution: fundamentals and prospects for UV disinfection applications. **Environmental Science: Water Research & Technology**, v. 3, n. 2, 2017. ISSN 2053-1400.

CHONG, Meng Nan; JIN, Bo; CHOW, Christopher W.K.; SAINT, Chris. Recent developments in photocatalytic water treatment technology: A review. **Water Research**, v. 44, n. 10, p. 2997–3027, May 2010. ISSN 00431354.

CINCINELLI, Alessandra; MARTELLINI, Tania. Indoor Air Quality and Health. **International Journal of Environmental Research and Public Health**, v. 14, n. 11, 2017. ISSN 1660-4601.

COSTA FILHO, Batuira M. da; VILAR, Vítor J.P. Strategies for the intensification of photocatalytic oxidation processes towards air streams decontamination: A review. **Chemical Engineering Journal**, v. 391, p. 123531, July 2020. ISSN 13858947.

DA COSTA FILHO, Batuira M; ARAUJO, Ana L.P.; PADRÃO, Stefan P.; BOAVENTURA, Rui A.R.; DIAS, Madalena M.; LOPES, José Carlos B.; VILAR, Vítor J.P. Effect of catalyst coated surface, illumination mechanism and light source in heterogeneous TiO2 photocatalysis using a mili-photoreactor for n-decane oxidation at gas phase. **Chemical Engineering Journal**, v. 366, p. 560–568, June 2019. ISSN 13858947.

DA COSTA FILHO, Batuira M; ARAUJO, Ana L.P.; SILVA, Gabriela V.; BOAVENTURA, Rui A.R.; DIAS, Madalena M.; LOPES, José C.B.; VILAR, Vítor J.P. Intensification of heterogeneous TiO 2 photocatalysis using an innovative micro-meso-structured-photoreactor for n -decane oxidation at gas phase. **Chemical Engineering Journal**, v. 310, p. 331–341, Feb. 2017. ISSN 13858947.

DAGHRIR, Rimeh; DROGUI, Patrick; ROBERT, Didier. Modified TiO2 For Environmental Photocatalytic Applications: A Review. **Industrial & Engineering Chemistry Research**, v. 52, n. 10, p. 3581–3599, Mar. 2013. ISSN 0888-5885.

DEVORE, J. R. Refractive Indices of Rutile and Sphalerite. **Journal of the Optical Society of America**, v. 41, n. 6, p. 416, June 1951. ISSN 0030-3941.

DHANJAI; SINHA, Ankita; ZHAO, Huimin; CHEN, Jiping; MUGO, Samuel M. Determination of Chemical Oxygen Demand: An Analytical Approach. In: REFERENCE Module in Chemistry, Molecular Sciences and Chemical Engineering. [S.l.]: Elsevier, 2018.

DINGWANG, Chen; LI, Fengmei; RAY, Ajay K. External and internal mass transfer effect on photocatalytic degradation. **Catalysis Today**, Elsevier BV, v. 66, n. 2-4, p. 475–485, Mar. 2001.

DURAN, J. Esteban; TAGHIPOUR, Fariborz; MOHSENI, Madjid. Irradiance modeling in annular photoreactors using the finite-volume method. **Journal of Photochemistry and Photobiology A: Chemistry**, v. 215, n. 1, p. 81–89, Sept. 2010. ISSN 10106030.

DUTRÉ, Philip; BALA, Kavita; BEKAERT, Philippe. **Advanced Global Illumination**. Second Edition. Wellesley: A K Peters, Ltd., 2006.

ETACHERI, Vinodkumar; DI VALENTIN, Cristiana; SCHNEIDER, Jenny; BAHNEMANN, Detlef; PILLAI, Suresh C. Visible-light activation of TiO2 photocatalysts: Advances in theory and experiments. **Journal of Photochemistry and Photobiology C: Photochemistry Reviews**, v. 25, Dec. 2015. ISSN 13895567.

FEYNMAN, Richard Phillips. **QED: The strange theory of light and matter**. New Jersey: Princeton University Press, 2006. v. 90, p. 1–153.

FUJISHIMA, Akira; HONDA, Kenichi. Electrochemical Photolysis of Water at a Semiconductor Electrode. **Nature**, v. 238, n. 5358, p. 37–38, July 1972. ISSN 0028-0836.

FUJISHIMA, Akira; RAO, Tata N.; TRYK, Donald A. Titanium dioxide photocatalysis. **Journal of Photochemistry and Photobiology C: Photochemistry Reviews**, v. 1, n. 1, p. 1–21, June 2000. ISSN 13895567.

GAMAGE, Joanne; ZHANG, Zisheng. Applications of Photocatalytic Disinfection. **International Journal of Photoenergy**, v. 2010, 2010. ISSN 1110-662X.

GAYA, Umar Ibrahim. Origin of the Activity of Semiconductor Photocatalysts. In: HETEROGENEOUS Photocatalysis Using Inorganic Semiconductor Solids. Dordrecht: Springer Netherlands, 2014. P. 91–135.

GAYA, Umar Ibrahim. Perspectives and Advances in Photocatalysis. In: HETEROGENEOUS Photocatalysis Using Inorganic Semiconductor Solids. Dordrecht: Springer Netherlands, 2014. P. 137–186.

GENNARO, Gianluigi de; DAMBRUOSO, Paolo Rosario; LOIOTILE, Annamaria Demarinis; DI GILIO, Alessia; GIUNGATO, Pasquale; TUTINO, Maria; MARZOCCA, Annalisa; MAZZONE, Antonio; PALMISANI, Jolanda; PORCELLI, Francesca. Indoor air quality in schools. **Environmental Chemistry Letters**, v. 12, n. 4, Dec. 2014. ISSN 1610-3653.

GIUSFREDI, Giovanni. Geometrical Optics. In: [s.l.: s.n.], 2019.

GONZÁLEZ-MARTÍN, Javier; KRAAKMAN, Norbertus Johannes Richardus; PÉREZ, Cristina; LEBRERO, Raquel; MUÑOZ, Raúl. A state–of–the-art review on indoor air pollution and strategies for indoor air pollution control. **Chemosphere**, v. 262, Jan. 2021. ISSN 00456535.

GORGES, Roger; MEYER, Susann; KREISEL, Günter. Photocatalysis in microreactors. **Journal of Photochemistry and Photobiology A: Chemistry**, v. 167, n. 2-3, Oct. 2004. ISSN 10106030.

GROSS, Herbert. **Handbook of Optical Systems**. Ed. by Herbert Gross. Weinheim, Germany: Wiley-VCH Verlag GmbH & Co. KGaA, Jan. 2005. v. 1. ISBN 9783527699223.

GUIEYSSE, Benoit; HORT, Cecile; PLATEL, Vincent; MUNOZ, Raul; ONDARTS, Michel; REVAH, Sergio. Biological treatment of indoor air for VOC removal: Potential and challenges. **Biotechnology Advances**, v. 26, n. 5, Sept. 2008. ISSN 07349750.

HABIBI-YANGJEH, Aziz; ASADZADEH-KHANEGHAH, Soheila; FEIZPOOR, Solmaz; ROUHI, Afsar. Review on heterogeneous photocatalytic disinfection of waterborne, airborne, and foodborne viruses: Can we win against pathogenic viruses? **Journal of Colloid and Interface Science**, v. 580, Nov. 2020. ISSN 00219797.

HAJAGHAZADEH, Mohammad; VAIANO, Vincenzo; SANNINO, Diana; KAKOOEI, Hossein; SOTUDEH-GHAREBAGH, Rahmat; CIAMBELLI, Paolo. Heterogeneous photocatalytic oxidation of methyl ethyl ketone under UV-A light in an LED-fluidized bed reactor. **Catalysis Today**, v. 230, July 2014. ISSN 09205861.

HASHIMOTO, Kazuhito; IRIE, Hiroshi; FUJISHIMA, Akira. TiO 2 Photocatalysis: A Historical Overview and Future Prospects. **Japanese Journal of Applied Physics**, v. 44, n. 12, p. 8269–8285, Dec. 2005. ISSN 0021-4922.

HAY, Stephen; OBEE, Timothy; LUO, Zhu; JIANG, Ting; MENG, Yongtao; HE, Junkai; MURPHY, Steven; SUIB, Steven. The Viability of Photocatalysis for Air Purification. **Molecules**, v. 20, n. 1, Jan. 2015. ISSN 1420-3049.

HE, Chi; CHENG, Jie; ZHANG, Xin; DOUTHWAITE, Mark; PATTISSON, Samuel; HAO, Zhengping. Recent Advances in the Catalytic Oxidation of Volatile Organic Compounds: A Review Based on Pollutant Sorts and Sources. **Chemical Reviews**, v. 119, n. 7, p. 4471–4568, Apr. 2019. ISSN 0009-2665.

HENTSCHEL, Klaus. **Photons - The History and Mental Models of Light Quanta**. Cham: Springer International Publishing, 2018. ISBN 978-3-319-95251-2.

HORTELANO, Carlos; LUIS DE LA FUENTE, José. Chapter 9 - New Developments in Composite Propellants Catalysis: From Nanoparticles to Metallo-Polyurethanes. In: YAN, Qi-Long; HE, Guo-Qiang; LIU, Pei-Jin; GOZIN, Michael (Eds.). **Nanomaterials in Rocket Propulsion Systems**. [S.l.]: Elsevier, 2019. P. 363–388.

HOSSAIN, Md. Moazzem; RAUPP, Gregory B.; HAY, Steven O.; OBEE, Timothy N. Three-dimensional developing flow model for photocatalytic monolith reactors. **AIChE Journal**, v. 45, n. 6, June 1999. ISSN 00011541.

HOU, Wei-Ming; KU, Young. Photocatalytic decomposition of gaseous isopropanol in a tubular optical fiber reactor under periodic UV-LED illumination. **Journal of Molecular Catalysis A: Chemical**, v. 374-375, p. 7–11, Aug. 2013. ISSN 13811169.

IBHADON, Alex; FITZPATRICK, Paul. Heterogeneous Photocatalysis: Recent Advances and Applications. **Catalysts**, v. 3, n. 1, p. 189–218, Mar. 2013. ISSN 2073-4344.

JAKICA, Nebojsa. State-of-the-art review of solar design tools and methods for assessing daylighting and solar potential for building-integrated photovoltaics. **Renewable and Sustainable Energy Reviews**, v. 81, Jan. 2018. ISSN 13640321.

JANCZAREK, Marcin; KOWALSKA, Ewa. Computer Simulations of Photocatalytic Reactors. **Catalysts**, v. 11, n. 2, Feb. 2021. ISSN 2073-4344.

JANECEK, Martin; MOSES, William W. Measuring Light Reflectance of BGO Crystal Surfaces. **IEEE Transactions on Nuclear Science**, v. 55, n. 5, p. 2443–2449, Oct. 2008. ISSN 0018-9499.

JANECEK, Martin; MOSES, William W. Optical Reflectance Measurements for Commonly Used Reflectors. **IEEE Transactions on Nuclear Science**, v. 55, n. 4, p. 2432–2437, Aug. 2008. ISSN 0018-9499.

JENSEN, K; RIPOLL, J; WRAY, A; JOSEPH, D; ELHAFI, M. On various modeling approaches to radiative heat transfer in pool fires. **Combustion and Flame**, v. 148, n. 4, p. 263–279, Mar. 2007. ISSN 00102180.

JEONGHYUN, Kim; JANG, Jaesung. Inactivation of airborne viruses using vacuum ultraviolet photocatalysis for a flow-through indoor air purifier with short irradiation time. **Aerosol Science and Technology**, v. 52, n. 5, May 2018. ISSN 0278-6826.

JESSY, J.L. Lee; HAYNES, Brian S. Process intensification writ large with microchannel absorption in nitric acid production. **Chemical Engineering Science**, Elsevier BV, v. 169, p. 140–150, Sept. 2017.

JING, Li; HAO, Yufang; SIMAYI, Maimaiti; SHI, Yuqi; XI, Ziyan; XIE, Shaodong. Verification of anthropogenic VOC emission inventory through ambient measurements and satellite retrievals. **Atmospheric Chemistry and Physics**, Copernicus GmbH, v. 19, n. 9, p. 5905–5921, May 2019.

JO, Wan-Kuen; TAYADE, Rajesh J. New Generation Energy-Efficient Light Source for Photocatalysis: LEDs for Environmental Applications. **Industrial & Engineering Chemistry Research**, v. 53, n. 6, p. 2073–2084, Feb. 2014. ISSN 0888-5885.

JUAN, Zhao; XUDONG, Yang. Photocatalytic oxidation for indoor air purification: a literature review. **Building and Environment**, v. 38, n. 5, p. 645–654, May 2003. ISSN 03601323.

JÚNIOR, João Lameu da Silva. An Introduction to Computational Fluid Dynamics and Its Application in Microfluidics. In: [s.l.: s.n.], 2019. P. 50–78.

KASHID, Madhvanand N.; RENKEN, Albert; KIWI-MINSKER, Lioubov. **Microstructured Devices for Chemical Processing**. Weinheim: Wiley-VCH, 2015. P. 1–384.

KAYAHAN, Emine; JACOBS, Mathias; BRAEKEN, Leen; THOMASSEN, Leen CJ; KUHN, Simon; GERVEN, Tom van; LEBLEBICI, M Enis. Dawn of a new era in industrial photochemistry: the scale-up of micro- and mesostructured photoreactors. **Beilstein Journal of Organic Chemistry**, v. 16, p. 2484–2504, Oct. 2020. ISSN 1860-5397.

KELLY, Frank J.; FUSSELL, Julia C. Improving indoor air quality, health and performance within environments where people live, travel, learn and work. **Atmospheric Environment**, v. 200, p. 90–109, Mar. 2019. ISSN 13522310.

KHAYDAROV, Valentin; BOROVINSKAYA, Ekaterina; RESCHETILOWSKI, Wladimir. Numerical and Experimental Investigations of a Micromixer with Chicane Mixing Geometry. **Applied Sciences**, v. 8, n. 12, p. 2458, Dec. 2018. ISSN 2076-3417.

KIDGER, Michael J. **Fundamental Optical Design**. [S.l.]: SPIE, 2002.

KJÆRGAARD, Søren; MØLHAVE, Lars; PEDERSEN, Ole Find. Human reactions to indoor air pollutants: N-decane. **Environment International**, v. 15, n. 1-6, p. 473–482, Jan. 1989. ISSN 01604120.

KONSTANTINOU, Ioannis K; ALBANIS, Triantafyllos A. TiO2-assisted photocatalytic degradation of azo dyes in aqueous solution: kinetic and mechanistic investigations. **Applied Catalysis B: Environmental**, v. 49, n. 1, p. 1–14, Apr. 2004. ISSN 09263373.

KOTAKE, Kei; IWAKAMI, Wakana; OHNISHI, Naofumi; YAMADA, Shoichi. Ray-Tracing Analysis of Anisotropic Neutrino Radiation for Estimating Gravitational Waves in Core-Collapse Supernovae. **The Astrophysical Journal**, v. 704, n. 2, Oct. 2009. ISSN 0004-637X.

LALAU KERALY, C.; KURITZKY, L.; COCHET, M.; WEISBUCH, Claude. Ray Tracing for Light Extraction Efficiency (LEE) Modeling in Nitride LEDs. In: SEONG, Tae-Yeon; HAN, Jung; AMANO, Hiroshi; MORKOÇ, Hadis (Eds.). **III-Nitride Based Light Emitting Diodes and Applications**. 2. ed. Singapore: Springer Nature, 2017. v. 133. P. 301–340.

LE BAHERS, Tangui; TAKANABE, Kazuhiro. Combined theoretical and experimental characterizations of semiconductors for photoelectrocatalytic applications. **Journal of Photochemistry and Photobiology C: Photochemistry Reviews**, v. 40, p. 212–233, Sept. 2019. ISSN 13895567.

LESEV, Hristo Iliyanov. Classification of Global Illumination Algorithms. In: ANNIVERSARY International Conference REMIA2010. Plovdiv: University of Plovdiv, Dec. 2010. P. 271–278.

LIANG, Hui; SIT, Jason; CHANG, Jian; ZHANG, Jian Jun. Computer animation data management: Review of evolution phases and emerging issues. **International Journal of Information Management**, v. 36, n. 6, Dec. 2016. ISSN 02684012.

LINSEBIGLER, Amy L.; LU, Guangquan.; YATES, John T. Photocatalysis on TiO2 Surfaces: Principles, Mechanisms, and Selected Results. **Chemical Reviews**, v. 95, n. 3, p. 735–758, May 1995. ISSN 0009-2665.

LIRA, Jéssica O.B.; RIELLA, Humberto G.; PADOIN, Natan; SOARES, Cíntia. CFD + DoE optimization of a flat plate photocatalytic reactor applied to NOx abatement. **Chemical Engineering and Processing - Process Intensification**, v. 154, p. 107998, 2020. ISSN 0255-2701.

LIU, Zongyuan; LIU, Sheng; WANG, Kai; LUO, Xiaobing. Optical Analysis of Color Distribution in White LEDs With Various Packaging Methods. **IEEE Photonics Technology Letters**, Institute of Electrical and Electronics Engineers (IEEE), v. 20, n. 24, p. 2027–2029, Dec. 2008.

LOPES, José Carlos Brito; LARANJEIRA, Paulo Eduardo Miranda Dos Santos Da Costa; DIAS, Madalena Maria Gomes Queiroz; MARTINS, Antonio Augusto Areosa. **Network mixer and related mixing process**. [S.l.: s.n.], 2005.

LUENGAS, Angela; BARONA, Astrid; HORT, Cecile; GALLASTEGUI, Gorka; PLATEL, Vincent; ELIAS, Ana. A review of indoor air treatment technologies. **Reviews in Environmental Science and Bio/Technology**, v. 14, n. 3, Sept. 2015. ISSN 1569-1705.

MAHAJAN, Virendra N. **Fundamentals of Geometrical Optics**. [S.l.]: SPIE, June 2014. ISBN 9780819499998.

MAK, Cheuk Ming; ZHEN, Wang. Recent advances in building acoustics: An overview of prediction methods and their applications. **Building and Environment**, v. 91, Sept. 2015. ISSN 03601323.

MALAYERI, Mojtaba; HAGHIGHAT, Fariborz; CHANG-SEO, Lee. Modeling of volatile organic compounds degradation by photocatalytic oxidation reactor in indoor air: A review. **Building and Environment**, v. 154, May 2019. ISSN 03601323.

MATIAZZO, Tatiana; RAMASWAMY, Kishor; VILAR, Vítor J.P.; PADOIN, Natan; SOARES, Cíntia. Radiation field modeling of the NETmix milli-photocatalytic reactor: Effect of LEDs position over the reactor window. **Chemical Engineering Journal**, v. 429, Feb. 2022. ISSN 13858947.

MATIAZZO, Tatiana; VILAR, Vítor J.P.; RIELLA, Humberto Gracher; PADOIN, Natan; SOARES, Cíntia. CFD and Radiation Field Modeling of the NETmix Milli-Photocatalytic Reactor for n-Decane Oxidation at Gas Phase: Effect of LEDs Number and Arrangement. **Chemical Engineering Journal**, 2022. ISSN 1385-8947.

MATSUSHITA, Y; OHBA, N; KUMADA, S; SAKEDA, K; SUZUKI, T; ICHIMURA, T. Photocatalytic reactions in microreactors. **Chemical Engineering Journal**, v. 135, Jan. 2008. ISSN 13858947.

MENDIVE, Cecilia B.; CURTI, Mariano; BAHNEMANN, Detlef. CHAPTER 3. Current Issues Concerning the Mechanism of Pristine TiO2 Photocatalysis and the Effects on Photonic Crystal Nanostructures. In: PHOTOCATALYSIS: Fundamentals and Perspectives. [S.l.]: The Royal Society of Chemistry, 2016. P. 51–79.

MIKHAILOV, Mikhail M.; NESHCHIMENKO, Vitaly V.; YURYEV, Semyon A.; SOKOLOVSKIY, Alexey N. Investigation of Optical Properties and Radiation Stability of TiO2 Powders before and after Modification by Nanopowders of Various Oxides. In: TITANIUM Dioxide - Material for a Sustainable Environment. [S.l.]: InTech, June 2018.

MO, Jinhan; ZHANG, Yinping; XU, Qiujian; LAMSON, Jennifer Joaquin; ZHAO, Rongyi. Photocatalytic purification of volatile organic compounds in indoor air: A literature review. **Atmospheric Environment**, v. 43, n. 14, p. 2229–2246, May 2009. ISSN 13522310.

MODEST, Michael F. THE METHOD OF DISCRETE ORDINATES (SN-APPROXIMATION). In: RADIATIVE Heat Transfer. [S.l.]: Elsevier, 2003.

MODEST, Michael F. THE MONTE CARLO METHOD FOR THERMAL RADIATION. In: RADIATIVE Heat Transfer. [S.l.]: Elsevier, 2003.

MOLESINI, G. Geometrical Optics. In: ENCYCLOPEDIA of Condensed Matter Physics. [S.l.]: Elsevier, 2005.

MORENO, José; CASADO, Cintia; MARUGÁN, Javier. Improved discrete ordinate method for accurate simulation radiation transport using solar and LED light sources. **Chemical Engineering Science**, v. 205, Sept. 2019. ISSN 00092509.

MORENO-SANSEGUNDO, José; CASADO, Cintia; MARUGÁN, Javier. Enhanced numerical simulation of photocatalytic reactors with an improved solver for the radiative transfer equation. **Chemical Engineering Journal**, v. 388, May 2020. ISSN 13858947.

MOZIA, Sylwia. Photocatalytic membrane reactors (PMRs) in water and wastewater treatment. A review. **Separation and Purification Technology**, v. 73, n. 2, p. 71–91, June 2010. ISSN 13835866.

MUDLIAR, Sandeep; GIRI, Balendu; PADOLEY, Kiran; SATPUTE, Dewanand; DIXIT, Rashmi; BHATT, Praveena; PANDEY, Ram; JUWARKAR, Asha; VAIDYA, Atul. Bioreactors for treatment of VOCs and odours – A review. **Journal of Environmental Management**, v. 91, n. 5, May 2010. ISSN 03014797.

MUESES, Miguel Angel; COLINA-MÁRQUEZ, José; MACHUCA-MARTÍNEZ, Fiderman; LI PUMA, Gianluca. Recent advances on modeling of solar heterogeneous photocatalytic reactors applied for degradation of pharmaceuticals and emerging organic contaminants in water. **Current Opinion in Green and Sustainable Chemistry**, Mar. 2021. ISSN 24522236.

MUÑOZ, Vanesa; CASADO, Cintia; SUÁREZ, Silvia; SÁNCHEZ, Benigno; MARUGÁN, Javier. Photocatalytic NOx removal: Rigorous kinetic modelling and ISO standard reactor simulation. **Catalysis Today**, v. 326, Apr. 2019. ISSN 09205861.

MUÑOZ-BATISTA, Mario J.; BALLARI, María M.; KUBACKA, Anna; ALFANO, Orlando M.; FERNÁNDEZ-GARCÍA, Marcos. Braiding kinetics and spectroscopy in photo-catalysis: the spectro-kinetic approach. **Chemical Society Reviews**, v. 48, n. 2, p. 637–682, 2019. ISSN 0306-0012.

NAKAHARA, Koki; MUTTAKIN, Mahbubul; YAMAMOTO, Kiyoshi; ITO, Kazuhide. Computational fluid dynamics modelling of the visible light photocatalytic oxidation process of toluene for indoor building materials with locally doped titanium dioxide. **Indoor and Built Environment**, v. 29, n. 2, Feb. 2020. ISSN 1420-326X.

NAKAHARA, Koki; YAMAGUCHI, Takahiro; LIM, Eunsu; ITO, Kazuhide. Computational fluid dynamics modeling and parameterization of the visible light photocatalytic oxidation process of toluene for indoor building material. **Sustainable Cities and Society**, v. 35, p. 298–308, Nov. 2017. ISSN 22106707.

NÉMETH, Zoltán; VERES, Ádám; NAGY, Balázs Vince. Simulations for optical design and analysis. In: MECHANISMENTECHNIK in Ilmenau. Ilmenau: Universitätsverlag Ilmenau, 2012. P. 135–144.

NGUYEN, Quynh M.; ABOUEZZI, Joanna; RISTROPH, Leif. Early turbulence and pulsatile flows enhance diodicity of Tesla's macrofluidic valve. **Nature Communications**, v. 12, n. 1, p. 2884, Dec. 2021. ISSN 2041-1723.

OBENDORF, S.K. Improving the functionality of clothing through novel pesticide protection. In: FUNCTIONAL Textiles for Improved Performance, Protection and Health. [S.l.]: Elsevier, 2011.

OHTANI, B. Photocatalysis by inorganic solid materials. In: [s.l.: s.n.], 2011. P. 395–430.

OKUMURA, Akira; HAYASHIDA, Masaaki; KATAGIRI, Hideaki; SAITO, Takayuki; VASSILIEV, Vladimir. Development of Non-sequential Ray-tracing Software for Cosmic-ray Telescopes. In: 32ND International Cosmic Ray Conference. Beijing: [s.n.], 2011.

OLLIS, David F. Kinetics of Photocatalyzed Reactions: Five Lessons Learned. **Frontiers in Chemistry**, v. 6, Aug. 2018. ISSN 2296-2646.

PADOIN, Natan; SOARES, Cíntia. An explicit correlation for optimal TiO 2 film thickness in immobilized photocatalytic reaction systems. **Chemical Engineering Journal**, v. 310, p. 381–388, Feb. 2017. ISSN 13858947.

PASSALÍA, Claudio; FLORES, Marina; SANTOS, Sara G.S.; PAULISTA, Larissa O.; LABAS, Marisol D.; VILAR, Vítor J.P.; BRANDI, Rodolfo J. Radiation modelling in the NETmix photocatalytic reactor: The concept of efficiencies in series. **Journal of Environmental Chemical Engineering**, v. 8, n. 6, p. 104464, Dec. 2020. ISSN 22133437.

PASSALÍA, Claudio; FLORES, Marina; SANTOS, Sara G.S.; PAULISTA, Larissa O.; LABAS, Marisol D.; VILAR, Vítor J.P.; BRANDI, Rodolfo J. Radiation modelling in the NETmix photocatalytic reactor: The concept of efficiencies in series. **Journal of Environmental Chemical Engineering**, v. 8, n. 6, Dec. 2020. ISSN 22133437.

PEDROTTI, Leno. Basic Geometrical Optics. In: FUNDAMENTALS of Photonics. 1000 20th Street, Bellingham, WA 98227-0010 USA: SPIE, 2008. P. 73–116.

PETER, Laurence M. CHAPTER 1. Photoelectrochemistry: From Basic Principles to Photocatalysis. In: PHOTOCATALYSIS: Fundamentals and Perspectives. [S.l.]: The Royal Society of Chemistry, 2016. P. 1–28. ISBN 978-1-78262-041-9. Available from: <http://ebook.rsc.org/?DOI=10.1039/9781782622338-00001>.

QIAN, Zhi; QI, Chen; GROSSMANN, Ignacio E. Optimal synthesis of rotating packed bed and packed bed: a case illustrating the integration of PI and PSE. In: [s.l.: s.n.], 2018. P. 2377–2382.

QUEFFEULOU, Amélie; GERON, Laurent; ARCHAMBEAU, Catherine; GALL, Hervé Le; MARQUAIRE, Paul-Marie; ZAHRAA, Orfan. Kinetic Study of Acetaldehyde Photocatalytic Oxidation with a Thin Film of TiO ₂ Coated on Stainless Steel and CFD Modeling Approach. **Industrial Engineering Chemistry Research**, v. 49, p. 6890–6897, 15 Aug. 2010. ISSN 0888-5885.

QUEFFEULOU, Amélie; GERON, Laurent; SCHAER, Eric. Prediction of photocatalytic air purifier apparatus performances with a CFD approach using experimentally determined kinetic parameters. **Chemical Engineering Science**, v. 65, p. 5067–5074, 18 Sept. 2010. ISSN 00092509.

RAMSHAW, C. The incentive for process intensification. In: LIMITED, BHR Group (Ed.). **International Conference on Process Intensification for the Chemical Industry**. Antwerp, Belgium: [s.n.], 1995.

REILLY, Kevin; FANG, Baizeng; TAGHIPOUR, Fariborz; WILKINSON, David P. Enhanced photocatalytic hydrogen production in a UV-irradiated fluidized bed reactor. **Journal of Catalysis**, v. 353, Sept. 2017. ISSN 00219517.

ROACHE, P. J. Perspective: A Method for Uniform Reporting of Grid Refinement Studies. **Journal of Fluids Engineering**, v. 116, n. 3, p. 405–413, Sept. 1994. ISSN 0098-2202.

ROACHE, P. J. QUANTIFICATION OF UNCERTAINTY IN COMPUTATIONAL FLUID DYNAMICS. **Annual Review of Fluid Mechanics**, v. 29, n. 1, p. 123–160, Jan. 1997. ISSN 0066-4189.

ROEGIERS, Jelle; WALSEM, Jeroen van; DENYS, Siegfried. CFD- and radiation field modeling of a gas phase photocatalytic multi-tube reactor. **Chemical Engineering Journal**, v. 338, Apr. 2018. ISSN 13858947.

ROIBU, Anca; MORTHALA, Rishi Bharadwaj; LEBLEBICI, M. Enis; KOZIEJ, Dorota; VAN GERVEN, Tom; KUHN, Simon. Design and characterization of visible-light LED sources for microstructured photoreactors. **Reaction Chemistry & Engineering**, v. 3, n. 6, 2018. ISSN 2058-9883.

RYBARCZYK, Piotr; SZULCZYŃSKI, Bartosz; GBICKI, Jacek; HUPKA, Jan. Treatment of malodorous air in biotrickling filters: A review. **Biochemical Engineering Journal**, v. 141, Jan. 2019. ISSN 1369703X.

SALEH, Bahaa E. A.; TEICH, Malvin Carl. **Fundamentals of Photonics**. Ed. by G. Boreman. Third Edition. New York, USA: John Wiley & Sons, Inc., 2019. ISBN 0471839655.

SALVADÓ-ESTIVILL, Ignasi; HARGREAVES, David M.; LI PUMA, Gianluca. Evaluation of the Intrinsic Photocatalytic Oxidation Kinetics of Indoor Air Pollutants. **Environmental Science & Technology**, v. 41, n. 6, Mar. 2007. ISSN 0013-936X.

SANTANA, Harrson S.; LOPES, Mariana G. M.; SILVA, João L.; TARANTO, Osvaldir P. Application of Microfluidics in Process Intensification. **International Journal of Chemical Reactor Engineering**, v. 16, n. 12, Dec. 2018. ISSN 1542-6580.

SANTANA, Harrson S.; SILVA, Adriano G.P. da; LOPES, Mariana G.M.; RODRIGUES, Alan C.; TARANTO, Osvaldir P.; LAMEU SILVA, João. Computational methodology for the development of microdevices and microreactors with ANSYS CFX. **MethodsX**, v. 7, p. 100765, 2020. ISSN 22150161.

SANTOS, Sara G.S.; PAULISTA, Larissa O.; SILVA, Tânia F.C.V.; DIAS, Madalena M.; LOPES, José Carlos B.; BOAVENTURA, Rui A.R.; VILAR, Vítor J.P. Intensifying heterogeneous TiO2 photocatalysis for bromate reduction using the NETmix photoreactor. **Science of The Total Environment**, v. 664, p. 805–816, May 2019. ISSN 00489697.

SCHIAVON, Marco; TORRETTA, Vincenzo; CASAZZA, Andrea; RAGAZZI, Marco. Non-thermal Plasma as an Innovative Option for the Abatement of Volatile Organic Compounds: a Review. **Water, Air, & Soil Pollution**, v. 228, n. 10, Oct. 2017. ISSN 0049-6979.

SCHRAUFNAGEL, Dean E.; BALMES, John R.; COWL, Clayton T.; DE MATTEIS, Sara; JUNG, Soon-Hee; MORTIMER, Kevin; PEREZ-PADILLA, Rogelio; RICE, Mary B.; RIOJAS-RODRIGUEZ, Horacio; SOOD, Akshay; THURSTON, George D.; TO, Teresa; VANKER, Anessa; WUEBBLES, Donald J. Air Pollution and Noncommunicable Diseases. **Chest**, v. 155, n. 2, p. 417–426, Feb. 2019. ISSN 00123692.

SEGUEL, Joseph M.; MERRILL, Richard; SEGUEL, Dana; CAMPAGNA, Anthony C. Indoor Air Quality. **American Journal of Lifestyle Medicine**, v. 11, n. 4, July 2017. ISSN 1559-8276.

SHAYEGAN, Zahra; LEE, Chang-Seo; HAGHIGHAT, Fariborz. TiO2 photocatalyst for removal of volatile organic compounds in gas phase – A review. **Chemical Engineering Journal**, Elsevier BV, v. 334, p. 2408–2439, Feb. 2018.

SHEI, Shih-Chang. Optical and Structural Properties of Titanium Dioxide Films from and Starting Materials Annealed at Various Temperatures. **Advances in Materials Science and Engineering**, v. 2013, p. 1–7, 2013. ISSN 1687-8434.

SHIN, Jiyong; HWANG, Inha; KIM, Dongpil; MOON, Taewon; KIM, Jaewoo; KANG, Woo Hyun; SON, Jung Eek. Evaluation of the light profile and carbon assimilation of tomato plants in greenhouses with respect to film diffuseness and regional solar radiation using ray-tracing simulation. **Agricultural and Forest Meteorology**, v. 296, Jan. 2021. ISSN 01681923.

SHUKLA, Komal; AGARWALLA, Sushama; DURAISWAMY, Suhanya; GUPTA, Raju Kumar. Recent advances in heterogeneous micro-photoreactors for wastewater treatment application. **Chemical Engineering Science**, v. 235, p. 116511, May 2021. ISSN 00092509.

SOREANU, Gabriela; DIXON, Michael; DARLINGTON, Alan. Botanical biofiltration of indoor gaseous pollutants – A mini-review. **Chemical Engineering Journal**, v. 229, Aug. 2013. ISSN 13858947.

STA, I.; JLASSI, M.; HAJJI, M.; BOUJMIL, M. F.; JERBI, R.; KANDYLA, M.; KOMPITSAS, M.; EZZAOUIA, H. Structural and optical properties of TiO2 thin films prepared by spin coating. **Journal of Sol-Gel Science and Technology**, v. 72, n. 2, p. 421–427, Nov. 2014. ISSN 0928-0707.

STAFFORD, Tess M. Indoor air quality and academic performance. **Journal of Environmental Economics and Management**, v. 70, Mar. 2015. ISSN 00950696.

STEVENSON, Michael. **Optical software: which program is right for me?** [S.l.]: Institute of Physics and IOP Publishing Ltd, 2006.

SUNDAR, Kaviya Piriyah; KANMANI, S. Progression of Photocatalytic reactors and it's comparison: A Review. **Chemical Engineering Research and Design**, v. 154, p. 135–150, Feb. 2020. ISSN 02638762.

TAGHIPOUR, Fariborz; MOHSENI, Madjid. CFD simulation of UV photocatalytic reactors for air treatment. **AIChE Journal**, v. 51, n. 11, Nov. 2005. ISSN 0001-1541.

TANIMU, Abdulkadir; JAENICKE, Stephan; ALHOOSHANI, Khalid. Heterogeneous catalysis in continuous flow microreactors: A review of methods and applications. **Chemical Engineering Journal**, v. 327, Nov. 2017. ISSN 13858947.

TAYLOR, Alma E. F. **Illumination Fundamentals**. [S.l.]: Rensselaer Polytechnic Institute, 2000.

TRI. **Summary of Data for Chemical Selection: Decane 124-18-5**. [S.l.], 2003. P. 24.

TSANGRASSOULIS, Aris; BOURDAKIS, Vassilis. Comparison of radiosity and ray-tracing techniques with a practical design procedure for the prediction of daylight levels in atria. **Renewable Energy**, v. 28, n. 13, Oct. 2003. ISSN 09601481.

VAN GERVEN, Tom; MUL, Guido; MOULIJN, Jacob; STANKIEWICZ, Andrzej. A review of intensification of photocatalytic processes. **Chemical Engineering and Processing: Process Intensification**, v. 46, n. 9, Sept. 2007. ISSN 02552701.

VANDERGRIFF, Linda. Nature and Properties of Light. In: FUNDAMENTALS of Photonics. 1000 20th Street, Bellingham, WA 98227-0010 USA: SPIE, 2008.

VANKAYALA, Bhanu Kiran; LÖB, Patrick; HESSEL, Volker; MENGES, Gabriele; HOFMANN, Christian; METZKE, Daniel; KRTSCHIL, Ulrich; KOST, Hans-Joachim. Scale-up of Process Intensifying Falling Film Microreactors to Pilot Production Scale. **International Journal of Chemical Reactor Engineering**, v. 5, n. 1, Oct. 2007. ISSN 1542-6580.

VEACH, Eric. **Robust Monte Carlo Methods for Light Transport Simulation**. 1997. S. 1–406. PhD thesis – Stanford University.

VERBRUGGEN, Sammy W.; LENAERTS, Silvia; DENYS, Siegfried. Analytic versus CFD approach for kinetic modeling of gas phase photocatalysis. **Chemical Engineering Journal**, v. 262, Feb. 2015. ISSN 13858947.

VISAN, Aura; OMMEN, J. Ruud van; KREUTZER, Michiel T.; LAMMERTINK, Rob G. H. Photocatalytic Reactor Design: Guidelines for Kinetic Investigation. **Industrial & Engineering Chemistry Research**, v. 58, n. 14, p. 5349–5357, Apr. 2019. ISSN 0888-5885.

VOHNSEN, Brian. A Short History of Optics. **Physica Scripta**, T109, 2004. ISSN 0031-8949.

WALSEM, Jeroen van; ROEGIERS, Jelle; MODDE, Bart; LENAERTS, Silvia; DENYS, Siegfried. Determination of intrinsic kinetic parameters in photocatalytic multi-tube reactors by combining the NTUm-method with radiation field modelling. **Chemical Engineering Journal**, v. 354, p. 1042–1049, Dec. 2018. ISSN 13858947.

WANG, Chuan-yi; PAGEL, Ronald; DOHRMANN, Jürgen K.; BAHNEMANN, Detlef W. Antenna mechanism and deaggregation concept: novel mechanistic principles for photocatalysis. **Comptes Rendus Chimie**, v. 9, n. 5-6, p. 761–773, May 2006. ISSN 16310748.

WEIGL, M.; FÜRHAPPER, C.; NIEDERMAYER, S.; HABLA, E.; NOHAVA, M.; NAGL, S.; POLLERES, S. VOC emissions from building materials: results from lab and model room trials. **International Wood Products Journal**, v. 5, n. 3, Aug. 2014. ISSN 2042-6445.

WYROWSKI, Frank; ZHONG, Huiying; ZHANG, Site; HELLMANN, Christian. Approximate solution of Maxwell's equations by geometrical optics. In: SMITH, Daniel G.; WYROWSKI, Frank; ERDMANN, Andreas (Eds.).

XU, Yuxing; LIU, Taifeng; YIN, Heng; YAO, Tingting; WANG, Xiuli; HAN, Hongxian; LI, Can. Simultaneous two-electron transfer from photoirradiated semiconductor to molecular catalyst. **Journal of Photochemistry and Photobiology A: Chemistry**, v. 355, p. 332–337, Mar. 2018. ISSN 10106030.

YANGYANG, Zhang. **Modeling and Design of Photocatalytic reactors for Air Purification**. 2013. S. 167. PhD thesis – College of Engineering University of South Florida.

YINPING, Zhang; YANG, Rui; ZHAO, Rongyi. A model for analyzing the performance of photocatalytic air cleaner in removing volatile organic compounds. **Atmospheric Environment**, Elsevier BV, v. 37, n. 24, p. 3395–3399, Aug. 2003.

YUEHAO, Li. **Applications of CFD Simulations on MicrofluidicSystems for Nanoparticle Synthesis**. 2012. S. 81. PhD thesis – Louisiana State University.

ZAZUETA, Ana Luisa Loo; DESTAILLATS, Hugo; LI PUMA, Gianluca. Radiation field modeling and optimization of a compact and modular multi-plate photocatalytic reactor (MPPR) for air/water purification by Monte Carlo method. **Chemical Engineering Journal**, v. 217, p. 475–485, Feb. 2013. ISSN 13858947.

ZHONG, Lexuan; HAGHIGHAT, Fariborz. Photocatalytic air cleaners and materials technologies – Abilities and limitations. **Building and Environment**, v. 91, Sept. 2015. ISSN 03601323.

ZHONG, Lexuan; HAGHIGHAT, Fariborz; BLONDEAU, Partice; KOZINSKI, Janusz. Modeling and physical interpretation of photocatalytic oxidation efficiency in indoor air applications. **Building and Environment**, v. 45, n. 12, p. 2689–2697, Dec. 2010. ISSN 03601323.

ZHU, Jinyuan; FANG, Hanxian. Research on the disturbance of ballistic missile to ionosphere by using 3D ray tracing method. **Advances in Space Research**, v. 65, n. 3, Feb. 2020. ISSN 02731177.

ZIMENG, Wang; LIU, Jing; DAI, Yuancan; DONG, Weiyang; ZHANG, Shicheng; CHEN, Jianmin. CFD modeling of a UV-LED photocatalytic odor abatement process in a continuous reactor. **Journal of Hazardous Materials**, v. 215-216, p. 25–31, May 2012. ISSN 03043894.

APPENDIX A – POLLUTANT DEGRADATION RATE

To propose a kinetic rate law for the degradation of *n*-decane, the experimental data already published in Da Costa Filho et al. (2017) was considered. The NETmix was operated using a back side illumination (BSI) mode, illuminated by a sunlight simulator.

A total of 36 experiments were analyzed, varying the illumination intensity, pollutant concentration, relative humidity and feed flow. In Table (11), the specifications of cases 1 to 15 are disposed. In this, the relative humidity and the feed flow are maintained constants, while the pollutant concentration and light intensities are varied.

The final pollutant conversion is also expressed in Table (11). This conversion values will be latter compared to the simulations results, in order to evaluate the adequacy of the proposed rate law.

Table 11 – Experimental data - analysis of pollutant concentration.

$Case$	$E\ (W/m^2)$	$Q_{feed}\ (cm^2/min)$	$RH\ (\%)$	$C_{dec,feed}\ (mol/m^3)$	$Conversion\ (\%)$
1	18.9	140	30	$3.23 \cdot 10^{-3}$	63.70
2	18.9	140	30	$6.50 \cdot 10^{-3}$	38.33
3	18.9	140	30	$1.00 \cdot 10^{-2}$	24.34
4	18.9	140	30	$1.31 \cdot 10^{-2}$	31.16
5	18.9	140	30	$1.64 \cdot 10^{-2}$	24.54
6	29.1	140	30	$3.23 \cdot 10^{-3}$	79.97
7	29.1	140	30	$6.50 \cdot 10^{-3}$	45.46
8	29.1	140	30	$1.00 \cdot 10^{-2}$	36.09
9	29.1	140	30	$1.31 \cdot 10^{-2}$	36.56
10	29.1	140	30	$1.64 \cdot 10^{-2}$	28.06
11	38.4	140	30	$3.23 \cdot 10^{-3}$	82.59
12	38.4	140	30	$6.50 \cdot 10^{-3}$	55.72
13	38.4	140	30	$1.00 \cdot 10^{-2}$	47.96
14	38.4	140	30	$1.31 \cdot 10^{-2}$	41.69
15	38.4	140	30	$1.64 \cdot 10^{-2}$	31.40

Source: adapted from Da Costa Filho et al. (2017).

Cases represented in Table (12) evaluate the influence of the feed flow rate under a constant *n*-decane concentration. The cases 16 to 19 are repeated with distinct illumination intensities.

Lastly, cases 29 to 36, depicted in Table (13), investigate the influence of the relative humidity on the degradation rate.

A.1 POWER LAW

First, a power law equation, that is a function of both *n*-decane and water vapor concentration is considered, as expressed in Equation (56):

$$r_{dec} = kC_{dec}^{n}C_{H_2O}^{m} \tag{56}$$

Table 12 – Experimental data - analysis of feed flow.

$Case$	$E\ (W/m^2)$	$Q_{feed}\ (cm^2/min)$	$RH\ (\%)$	$C_{dec,feed}\ (mol/m^3)$	$Conversion\ (\%)$
16	18.9	70	30	$1.31 \cdot 10^{-2}$	42.23
17	18.9	140	30	$1.31 \cdot 10^{-2}$	22.81
18	18.9	220	30	$1.31 \cdot 10^{-2}$	13.66
19	18.9	300	30	$1.31 \cdot 10^{-2}$	5.94
20	29.1	70	30	$1.31 \cdot 10^{-2}$	56.30
21	29.1	140	30	$1.31 \cdot 10^{-2}$	30.82
22	29.1	220	30	$1.31 \cdot 10^{-2}$	22.29
23	29.1	300	30	$1.31 \cdot 10^{-2}$	11.87
24	38.4	70	30	$1.31 \cdot 10^{-2}$	66.09
25	38.4	140	30	$1.31 \cdot 10^{-2}$	33.91
26	38.4	220	30	$1.31 \cdot 10^{-2}$	28.30
27	38.4	300	30	$1.31 \cdot 10^{-2}$	17.43

Source: adapted from Da Costa Filho et al. (2017).

Table 13 – Experimental data - analysis of relative humidity.

$Case$	$E\ (W/m^2)$	$Q_{feed}\ (cm^2/min)$	$RH\ (\%)$	$C_{dec,feed}\ (mol/m^3)$	$Conversion\ (\%)$
28	18.9	220	2	$1.31 \cdot 10^{-2}$	9.89
29	18.9	220	15	$1.31 \cdot 10^{-2}$	16.51
30	18.9	220	30	$1.31 \cdot 10^{-2}$	13.70
31	29.1	220	2	$1.31 \cdot 10^{-2}$	13.17
32	29.1	220	15	$1.31 \cdot 10^{-2}$	21.50
33	29.1	220	30	$1.31 \cdot 10^{-2}$	22.32
34	38.4	220	2	$1.31 \cdot 10^{-2}$	19.12
35	38.4	220	15	$1.31 \cdot 10^{-2}$	24.94
36	38.4	220	30	$1.31 \cdot 10^{-2}$	28.23

Source: adapted from Da Costa Filho et al. (2017).

To fit the experimental data to Equation (56), first the data from cases 1 to 15 are taken into consideration (same flow and relative humidity). Equation (57) is then considered and linearized to became Equation (59). With the plot of the natural logarithm of $r_{dec}\ vs.$ the natural logarithm of the *n*-decane feed concentration, the parameters k^* and n can be determined.

$$r_{dec} = k^* C_{dec}^n \tag{57}$$

where,

$$k^* = k C_{H_2O}^m \tag{58}$$

$$ln(r_{dec}) = ln\left(k^* C_{dec}^n\right) = ln\left(k^*\right) + n ln\left(C_{dec}\right) \tag{59}$$

In Figure (46a), the plot of $ln(r_{dec})\ vs.\ ln(C_{dec,feed})$ permits to find an average parameter n equivalent to 0.43, and a k^* for each illuminance intensity.

Figure 46 – Power law fit of experimental data.

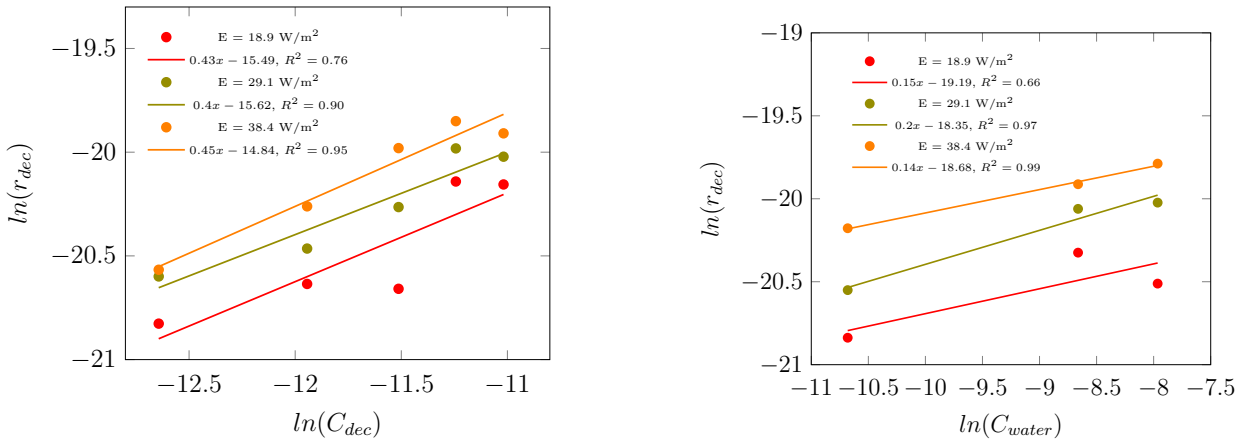

(a) Fit of experiments 1 to 15.

(b) Fit of experiments 28 to 36.

Source: elaborated by the author (2022).

Similarly, with Equations (60) to (62), and the plot of Figure (46b), an average parameter m can be defined as 0.18, and a k' is found for each illuminance intensity.

$$r_{dec} = k' C_{H_2O}^{m} \tag{60}$$

$$k' = k C_{dec}^{n} \tag{61}$$

$$ln(r_{dec}) = ln\left(k' C_{H_2O}^{m}\right) = ln\left(k'\right) + m ln\left(C_{H_2O}\right) \tag{62}$$

Both Equations (58) and (61) can be used to find the value of the constant k, present in Equation (57). For each illuminance intensity, one value of k was determined. In Figure (47) the value of k was plotted against the irradiance power, and therefore, the Equation (63) is proposed to describe the degradation of *n*-decane.

$$r_{dec} = 3.09 \cdot 10^{-8} E C_{dec}^{0.43} C_{H_2O}^{0.18} \tag{63}$$

To evaluate the adequacy of Equation (63), cases 1 to 36 were simulated, and the results of the pollutant conversion simulated were compared with the experimental data. The relative error between simulation and experiments is expressed in Table (14).

The majority of cases presented a relative error inferior to 8%. The average of the relative error is inferior of 10% for the irradiance values of 29.1 and $38.4\ W/m^2$. A greater averaged error was found for the lesser irradiance, with almost 18% of error.

Figure 47 – Power law fit of constant k.

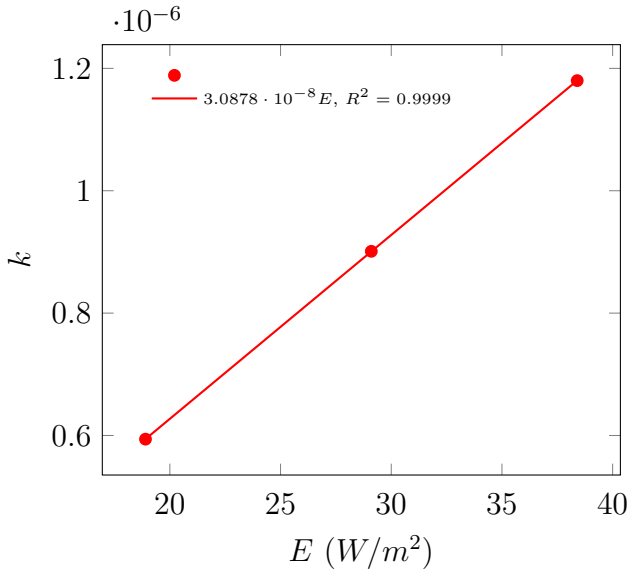

Source: elaborated by the author (2022).

Table 14 – Relative error between experimental data and simulation results employing a power law kinetic rate.

Case	*Experimental Conversion* (%)	*Simulated Conversion* (%)	*Relative Error* (%)	*Case*	*Experimental Conversion* (%)	*Simulated Conversion* (%)	*Relative Error* (%)
01	63.70	45.62	28.38	19	5.94	10.76	81.28
02	38.33	32.28	15.79	20	56.30	60.15	6.84
03	24.34	25.80	6.01	21	30.82	33.12	7.48
04	31.16	22.36	28.26	22	22.29	21.79	2.26
05	24.54	19.82	19.22	23	11.87	16.22	36.69
06	79.97	64.04	19.92	24	66.09	75.69	14.52
07	45.46	46.85	3.06	25	33.91	43.68	28.83
08	36.09	37.96	5.19	26	28.30	29.13	2.94
09	36.56	33.12	9.39	27	17.43	21.82	25.22
10	28.06	29.50	5.16	28	9.89	9.39	5.05
11	82.59	78.97	4.39	29	16.51	13.07	20.83
12	55.72	60.30	8.23	30	13.70	14.53	6.08
13	47.96	49.68	3.58	31	13.17	14.18	7.68
14	41.69	43.68	4.78	32	21.50	19.64	8.64
15	31.40	39.12	24.60	33	22.32	21.79	2.39
16	42.23	42.13	0.22	34	19.12	19.12	0.00
17	22.81	22.36	1.97	35	24.94	26.29	5.41
18	13.66	14.53	6.42	36	28.23	29.13	3.18

Source: elaborated by the author (2022).

A.2 MONOMOLECULAR LANGMUIR-HINSHELWOOD

Employing a monomolecular LH rate law, as in Equation (64), the kinetic parameters can be obtained graphically when considering the linearization of Equation (64), as Equations (65) and (66) bellow:

$$r_{dec} = \frac{kC_{dec}}{1 + K_{dec}C_{dec} + K_wC_w} \tag{64}$$

$$\frac{1}{r_{dec}} = \frac{1}{k}\frac{1}{C_{dec}} + \frac{K_{dec}}{k} \tag{65}$$

$$\frac{1}{r_{dec}} = \frac{1}{k}\frac{1}{C_{dec}} + \frac{K_{dec}}{k} + \frac{K_w}{kC_{dec}}C_w \tag{66}$$

The constants k and K_{voc} are obtained with the plot of $\frac{1}{r_{dec}}$ versus $\frac{1}{C_{dec}}$ (Figure 48a). On the other hand, the constant K_w is achieved with the plot of $\frac{1}{r_{dec}}$ versus C_w (Figure 48b). The parameters were obtained for each light intensity, as showed in Table (15).

Figure 48 – Monomolecular L-H fit of experimental data.

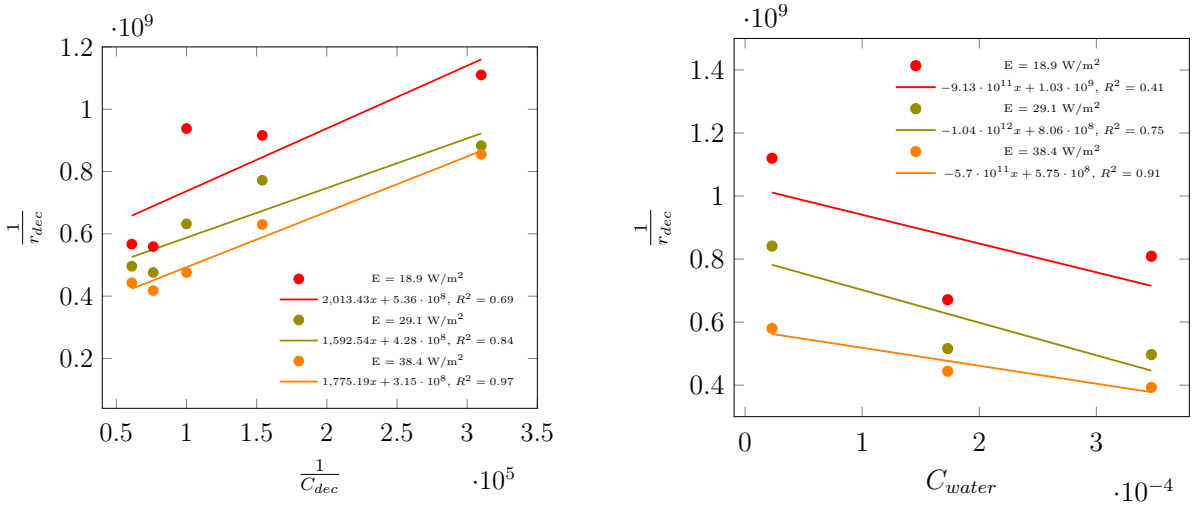

(a) Fit of constants k and K_{dec}.

(b) Fit of constant K_w.

Source: elaborated by the author (2022).

If the parameters of Table (15) are divided by the light intensity (E), creating the new parameters k', K'_{dec} and K'_w, these new parameters can be expressed as linear functions of E. Figure (49) shows these new parameters as functions of light intensity.

Table 15 – Monomolecular L-H parameters.

$E\ (W/m^2)$	k	K_{dec}	K_w
18.9	$4.97 \cdot 10^{-4}$	265935.78	-5949.64
29.1	$6.27 \cdot 10^{-4}$	268386.07	-8512.94
38.4	$5.62 \cdot 10^{-4}$	176989.70	-4186.52

Source: elaborated by the author (2022).

Figure 49 – Kinetic parameters as functions of light intensity.

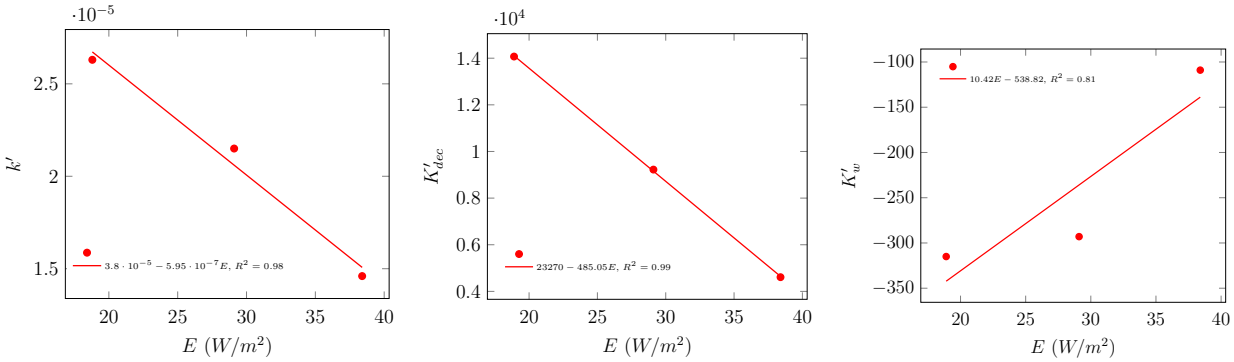

(a) (b) (c)

Source: elaborated by the author (2022).

Therefore, the monomolecular LH model proposed is the one expressed by Equation (67):

$$r_{dec} = \frac{k' E C_{dec}}{1 + K'_{dec} E C_{dec} + K'_w E C_w} \tag{67}$$

where,

$$k' = 3.80 \cdot 10^{-5} - 5.95 \cdot 10^{-7} E \tag{68}$$

$$K'_{dec} = 23270.30 - 485.05E \tag{69}$$

$$K'_w = 10.42E - 538.82 \tag{70}$$

The proposed model was simulated and its results were compared to the experimental data, as shown in Table (16). However, it did not present a good fit to the experimental

data. An averaged relative error of 156.34% was found, and for some points the error was well superior than 200%. This lack of fit was already expected since the linearization of the kinetic model does not represent a very well established linear fit, as already observed in Figures (48a) and (48b).

Table 16 – Relative error between experimental data and simulation results employing a L-H monomolecular kinetic rate.

Case	*Experimental Conversion* (%)	*Simulated Conversion* (%)	*Relative Error* (%)	*Case*	*Experimental Conversion* (%)	*Simulated Conversion* (%)	*Relative Error* (%)
1	63.70	67.31	5.67	19	5.94	39.81	570.37
2	38.33	67.05	74.93	20	56.30	92.21	63.78
3	24.34	66.72	174.16	21	30.82	72.08	133.90
4	31.16	66.43	113.15	22	22.29	55.59	149.41
5	24.54	66.11	169.40	23	11.87	44.88	278.22
6	79.97	72.57	9.25	24	66.09	91.29	38.13
7	45.46	72.44	59.35	25	33.91	70.61	108.25
8	36.09	72.25	100.19	26	28.30	54.19	91.51
9	36.56	72.08	97.18	27	17.43	43.65	150.51
10	28.06	71.90	156.29	28	9.89	48.58	391.35
11	82.59	70.82	14.26	29	16.51	49.24	198.27
12	55.72	70.78	27.03	30	13.70	49.98	264.84
13	47.96	70.69	47.40	31	13.17	54.56	314.20
14	41.69	70.61	69.37	32	21.50	55.05	156.10
15	31.40	70.52	124.61	33	22.32	55.59	149.09
16	42.23	88.85	110.42	34	19.12	53.58	180.18
17	22.81	66.43	191.26	35	24.94	53.87	116.05
18	13.66	49.98	266.01	36	28.23	54.19	91.95

Source: elaborated by the author (2022).

A.3 BIMOLECULAR LANGMUIR-HINSHELWOOD

Considering a bimolecular Langmuir-Hinshelwood rate law, as in Equation (71), the constant parameters of the model can be determined with the linearization of the equation.

$$r_{dec} = \frac{kK_{dec}K_wC_{dec}C_w}{(1 + K_{dec}C_{dec} + K_wC_w)^2} \tag{71}$$

Using experiments run 1 to 15, where the water vapor concentration is maintained constant, the linearization can be written as Equation (72). Meanwhile, when experiments 28 to 36 are taken into consideration, Equation (73) can be used.

$$\frac{1}{\sqrt{k_{voc}}} + \frac{K_{dec}}{\sqrt{k_{voc}}}C_{dec} = \sqrt{\frac{C_{dec}}{r_{dec}}} \tag{72}$$

$$\frac{1}{\sqrt{k_w}} + \frac{K_w}{\sqrt{k_w}} C_w = \sqrt{\frac{C_w}{r_{dec}}} \tag{73}$$

Therefore, the plot of the square root of the ratio of the *n*-decane concentration by the experimental reaction rate versus the *n*-decane concentration, Figure (50a), permits to determine the parameters k and K_{dec} for each light intensity, as listed in Table (17). Analogously, when the pollutant concentration is replaced by the water vapor concentration, Figure (50b), the parameter K_w can be determined for each light intensity (Table (17)).

Figure 50 – Bimolecular L-H fit of experimental data.

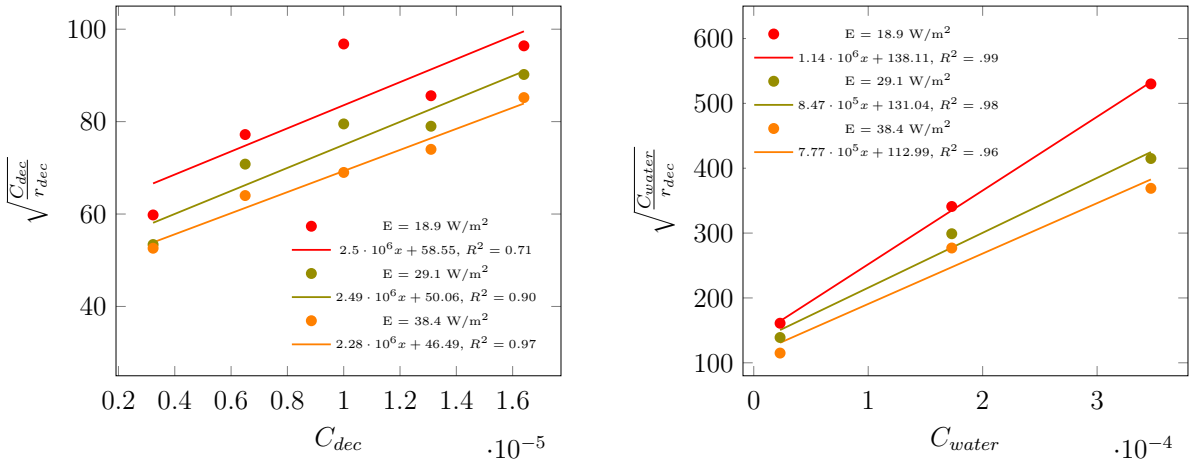

(a) Fit of constants k and K_{dec}. (b) Fit of constant K_w.

Source: elaborated by the author (2022).

Table 17 – Bimolecular LH parameters.

$E\ (W/m^2)$	k	K_{dec}	K_w
18.9	$6.83 \cdot 10^{-9}$	$42663,10$	8263.43
29.1	$8.03 \cdot 10^{-9}$	49635.14	6463.75
38.4	$9.42 \cdot 10^{-9}$	49248.44	6834.50

Source: elaborated by the author (2022).

In an attempt to generalize the kinetic constants, the parameter k was plotted against the light intensity, Figure (51a), obtaining a linear fit.

A linear fit was also obtained when K_{dec}/E is plotted against the light intensity (Figure (51b)). Similarly, when K_w/E is plotted against E, but in this case an exponential fit is obtained (Figure (51c)).

Therefore, the generalized model based on the bimolecular Langmuir-Hinshelwood kinetic rate is expressed in Equation (74):

Figure 51 – Generalization of constant bimolecular L-H kinetic constants.

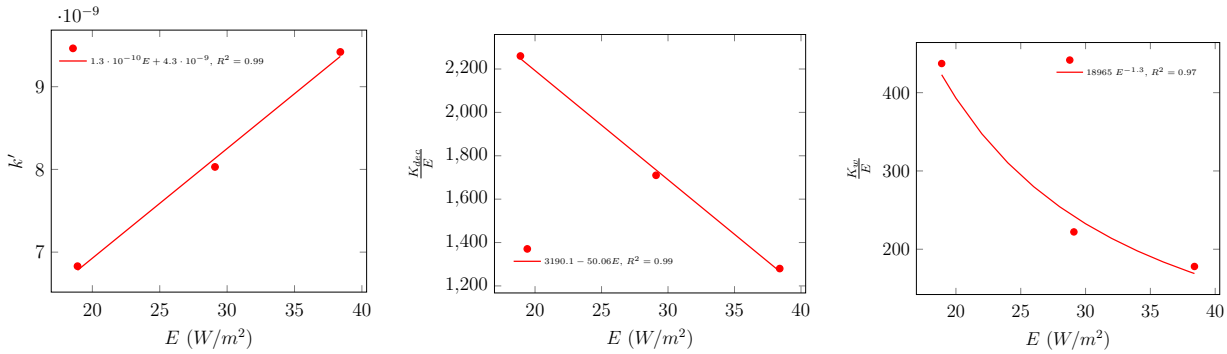

(a) (b) (c)

Source: elaborated by the author (2022).

$$r_{dec} = \frac{k' K'_{dec} K'_w C_{dec} C_w E^2}{\left(1 + E K'_{dec} C_{dec} + E K'_w C_w\right)^2} \tag{74}$$

where,

$$k' = 1.32 \cdot 10^{-10} E + 4.28 \cdot 10^{-9} \tag{75}$$

$$K'_{dec} = 3190.09 - 50.05E \tag{76}$$

$$K'_w = 18965.45 E^{-1.29} \tag{77}$$

Cases 1 to 36 were then simulated employing the bimolecular LH model and the pollutant conversions obtained are listed in Table (18). The relative error between simulations and experimental data, however, is unsatisfactory. Most of the simulations return an error greater than 50%. The global average error is 41%, which is superior than the average error of the power law kinetic rate.

A.4 COMPARISON BETWEEN KINETIC MODELS

Figures (52) to (54) show the conversions obtained with each of the three kinetic equations proposed. They are plotted and compared to the experimental data. In Figure (52), the conversion of cases 1 to 15 is plotted. For these cases the varied parameter is

Table 18 – Relative error between experimental data and simulation results employing a bimolecular Langmuir-Hinshelwood kinetic rate.

Case	*Experimental Conversion* (%)	*Simulated Conversion* (%)	*Relative Error* (%)	*Case*	*Experimental Conversion* (%)	*Simulated Conversion* (%)	*Relative Error* (%)
1	63.70	38.04	40.29	19	5.94	18.62	213.49
2	38.33	37.36	2.53	20	56.30	69.93	24.22
3	24.34	36.58	50.31	21	30.82	44.44	44.21
4	31.16	35.92	15.21	22	22.29	30.97	38.95
5	24.54	35.21	43.46	23	11.87	23.72	99.85
6	79.97	47.33	40.82	24	66.09	72.79	10.14
7	45.46	46.39	2.06	25	33.91	47.07	38.81
8	36.09	45.35	25.66	26	28.30	33.03	16.72
9	36.56	44.44	21.58	27	17.43	25.38	45.62
10	28.06	43.50	55.04	28	9.89	4.71	52.39
11	82.59	49.99	39.47	29	16.51	18.98	14.95
12	55.72	49.05	11.97	30	13.70	24.54	79.12
13	47.96	47.99	0.06	31	13.17	5.60	57.50
14	41.69	47.07	12.89	32	21.50	23.61	9.86
15	31.40	46.10	46.82	33	22.32	30.97	38.78
16	42.23	59.46	40.81	34	19.12	5.85	69.42
17	22.81	35.90	57.43	35	24.94	25.04	0.42
18	13.66	24.54	79.69	36	28.23	33.03	16.99

Source: elaborated by the author (2022).

Figure 52 – Kinetic comparison - Cases 1 to 15.

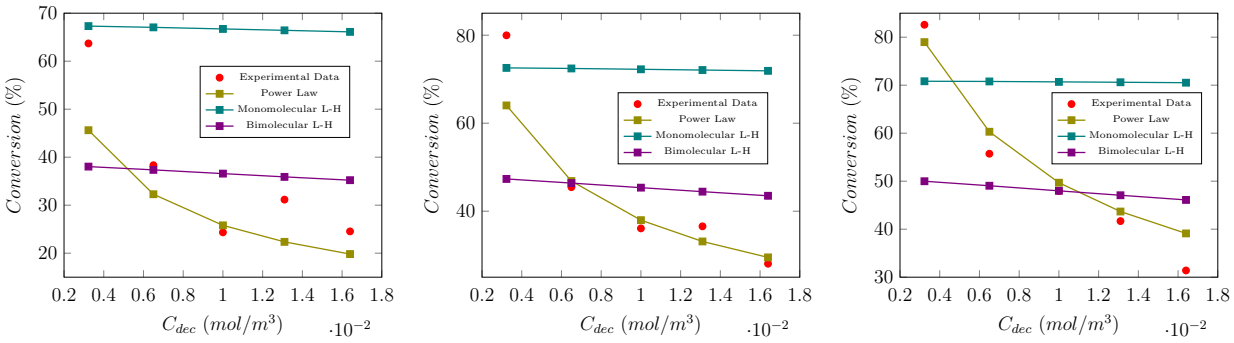

(a) E = 18.9 W/m^2. (b) E = 29.1 W/m^2. (c) E = 38.4 W/m^2.

Source: elaborated by the author (2022).

the initial concentration of the pollutant. Figure (52a) employs an average irradiance of $18.9\ W/m^2$, while Figure (52b) uses $29.1\ W/m^2$ and Figure (52c) $38.4\ W/m^2$.

When the models are compared between each other and with the experimental data, it is noticeable the high divergence of the monomolecular Langmuir-Hinshelwood from the other models and from the experimental data.

It is also clear that neither the Langmuir-Hinshelwood based equations are capable to describe the behavior of distinct pollutant inlet concentrations. The power law equa-

tions is the one that best adapts to the experimental data, although a slight distancing is observed at the lesser pollutant concentrations for the two smaller irradiance intensities.

Figure (53) maps the pollutant conversion for different flow rates. Figures (53a) to (53c) show the experimental and simulated data for $E = 18.9\ W/m^2$, $E = 29.1\ W/m^2$ and $E = 38.4\ W/m^2$, respectively.

All the models present similar behavior, that is, conversion decreases with the increase of the inlet flow. The monomolecular L-H model presents a much higher conversion than the experimental data. The power law equation is the one that presented the closest results to the experimental data, mainly for the two lower radiance intensities.

Figure 53 – Kinetic comparison - Cases 16 to 27.

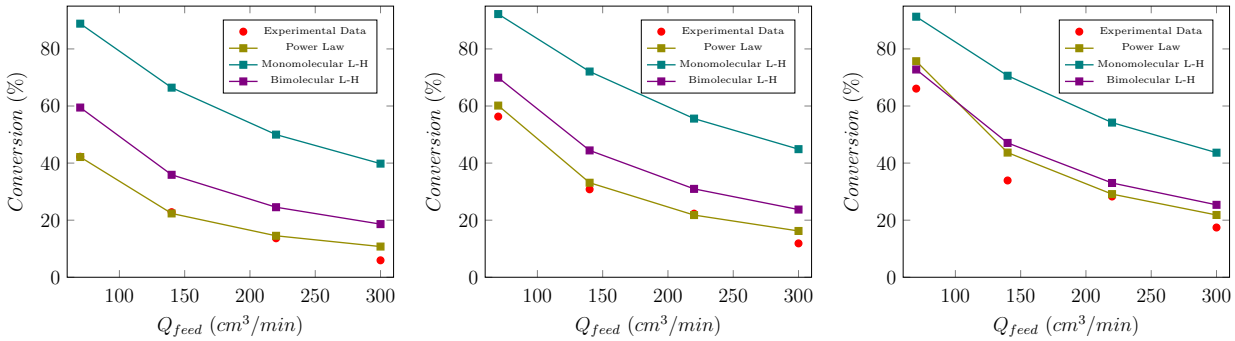

(a) E = 18.9 W/m^2. (b) E = 29.1 W/m^2. (c) E = 38.4 W/m^2.

Source: elaborated by the author (2022).

Lastly, Figure (54) depict the results of conversion for the cases varying the relative humidity of water. Figures (54a) to (54c) show the data employing $E = 18.9\ W/m^2$, $E = 29.1\ W/m^2$ and $E = 38.4\ W/m^2$, respectively.

It is clear, from the figures, that the monomolecular L-H model is once again not capable to describe the behavior of the experimental data. The bimolecular L-H model has a close response when the relative humidity employed is equivalent to 15% ($C_{water} = 1.73 \cdot 10^{-4}\ mol/m^3$). However, for higher or lower concentrations a great distancing from the experimental data is verified. Therefore, from the three models proposed, the one that best fit the experimental data is the power law equation ($r_{dec} = 3.09 \cdot 10^{-8} E C_{dec}^{0.43} C_{H_2O}^{0.18}$); and for that, it is the model implemented in the conducted research.

Figure 54 – Kinetic comparison - Cases 28 to 36.

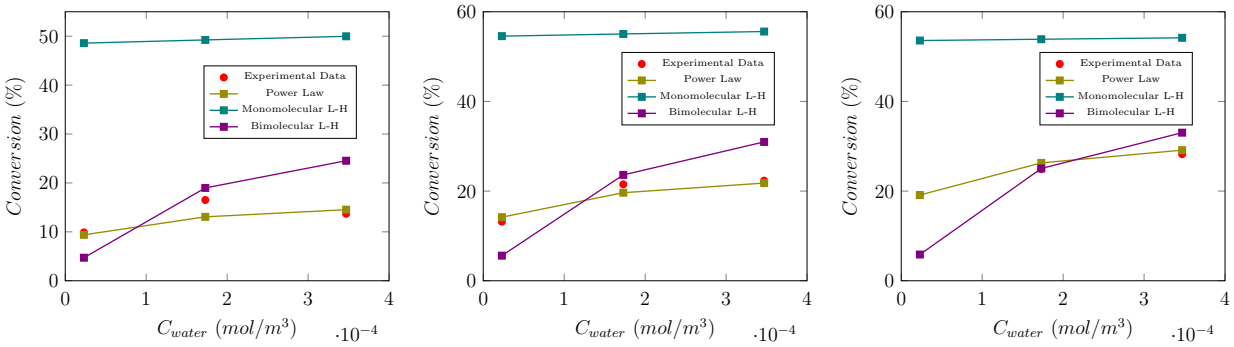

(a) E=18.9 W/m^2. (b) E=29.1 W/m^2. (c) E=38.4 W/m^2.

Source: elaborated by the author (2022).

APPENDIX B – COMPUTATIONAL FLUID DYNAMIC ANALYSIS - GCI AND VALIDATION

For numerical simulations of the reactive flow, the software suite Ansys 2020 was employed. For the reactor's geometry the 3D modeling software SpaceClaim was used, the mesh was generated in Ansys Meshing and the numerical simulations were solved employing the Ansys Fluent solver with parallel processing applying 4 to 8 cores.

As boundary condition, at the inlet of the reactor the velocity-inlet boundary condition was selected, while at the outlet of the reactor the pressure-outlet was selected, where atmospheric pressure was considered (Figure 55). The proposed rate laws for the surface reaction of *n*-decane decomposition was implemented as user-defined functions (UDFs).

Figure 55 – CFD model boundary conditions.

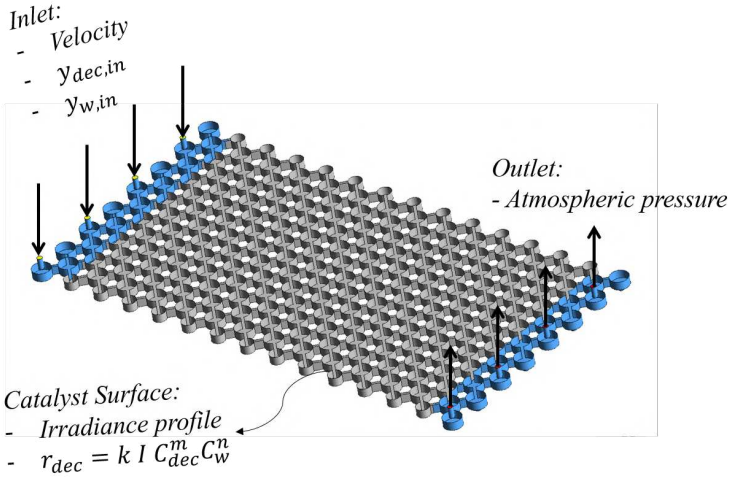

Source: elaborated by the author (2022).

The convergence criteria of the steady-state simulations was set as 10^{-3} for momentum and continuity, 10^{-6} for energy, 10^{-6} for the *n*-decane and 10^{-5} for the water-vapour.

The radiation field was coupled into the CFD simulations through reading a $.csv$ profile containing coordinate and irradiance data and this values were accessed by the user defined function (UDF), that cointain the kinetic rate law, via an user defined scalar (UDS).

B.1 GRID CONVERGENCE INDEX

In order to evaluate the numerical uncertainty due to the construction of the mesh, the Grid Convergence Index (GCI), a method proposed by Roache (1994), was employed. This method estimates the refinement error of the mesh based on the Richardson ex-

trapolation theory and uses three meshes with different levels of refinement (ROACHE, 1997).

Therefore three meshes were created, resulting in meshes with 23,306,450 elements (Grid 1 - Fine), 10,785,298 (Grid 2 - Intermediary) and 5,527,670 elements (Grid 3 - Coarse), which corresponds to a grid refinement factor, r, of approximately 1.3. The configuration of the simulations used in the GCI test are detailed in Table 19.

Table 19 – GCI test settings.

NETmix type:	FSI
Inlet Boundary Condition:	Velocity-Inlet = 0.4263 m/s
$C_{10}H_{22}$ Inlet Mole Fraction:	$1.67 \cdot 10^{-4}$
Relative Humidity:	30%
Temperature:	$298\ K$
Outlet Boundary Condition:	Pressure-Outlet
	- Atmospheric pressure
Wall Boundary Condition:	No-Slip

Source: elaborated by the author (2022).

To calculate the numerical uncertainty, an algorithm was developed in the software Octave 4.0.3 based on the routine described by Celik et al. (2008). The surface reaction rate, the mean *n*-decane concentration in a plane localized in the center of the reactor and the velocity inside a chamber were evaluated. The result of each variable was plotted against the inverse number of elements, as shown in Figure 56. In all cases an asymptotic behavior is observed and for all variables the GCI value calculated is under 2%. Therefore, the intermediary mesh, containing 10,785,298 elements, was selected for further simulations due to the usage of around a third of the simulation time required by the finer grid.

Figure 56 – Grid Convergence Index.

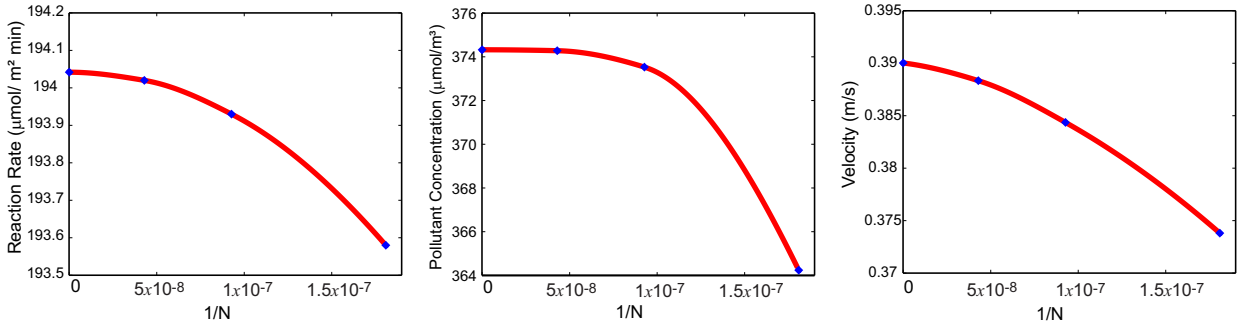

(a) (b) (c)

Source: elaborated by the author (2022).

B.2 COMPUTATIONAL FLUID DYNAMIC VALIDATION

From the experiments of Da Costa Filho et al. (2019), *n*-decane was degraded under three conditions under the 18 LEDs simulated in the previous section. The three reaction points were simulated with the mesh containing 10,785,298 elements. Equation 78 was employed for the kinetic rate.

$$r_{dec} = 3.0878^{-8} EC_{dec}^{0.4263} C_{H_2O}^{0.1652} \tag{78}$$

The simulated cases have distinct catalyst dispositions, inlet velocities and distinct pollutant concentration. All cases were conducted with a relative humidity equivalent to 30% at a temperature of 298 K. The irradiance profile and the power law kinetic equation regressed was capable of representing the experimental data with good agreement. For all of the cases simulated the relative error between experimental data and the pollutant conversion data was bellow 10% (Table 20).

Table 20 – Computational fluid dynamics set-up and validation.

	$Case\ \alpha$	$Case\ \beta$	$Case\ \sigma$
$Catalyst\ disposition$:	BSI	FSI	FSI
$Velocity\ Inlet\ (m/s)$:	0.54	0.43	0.54
$C_{10}H_{22}\ Inlet\ Mole\ Fraction$:	$2.47 \cdot 10^{-4}$	$1.67 \cdot 10^{-4}$	$2.49 \cdot 10^{-4}$
$X_{Exp}\ (\%)$:	90	96	96
$X_{CFD}\ (\%)$:	84.50	99.97	99.00
$Relative\ Error\ (\%)$:	6.1	4.1	3.1

Source: elaborated by the author (2022).

Figure 57 presents the degradation rate registered at the catalyst surface. It is possible to notice that the BSI case (case α) present local kinetic rate values higher than the FSI cases. This is due to the irradiance values, that are of superior intensity in the BSI since the proximity to the LEDs and lack of shadows produced by the reactor's walls contribute to the obtainment of greater irradiance values.

Figure 57 – Reaction rate of validated cases.

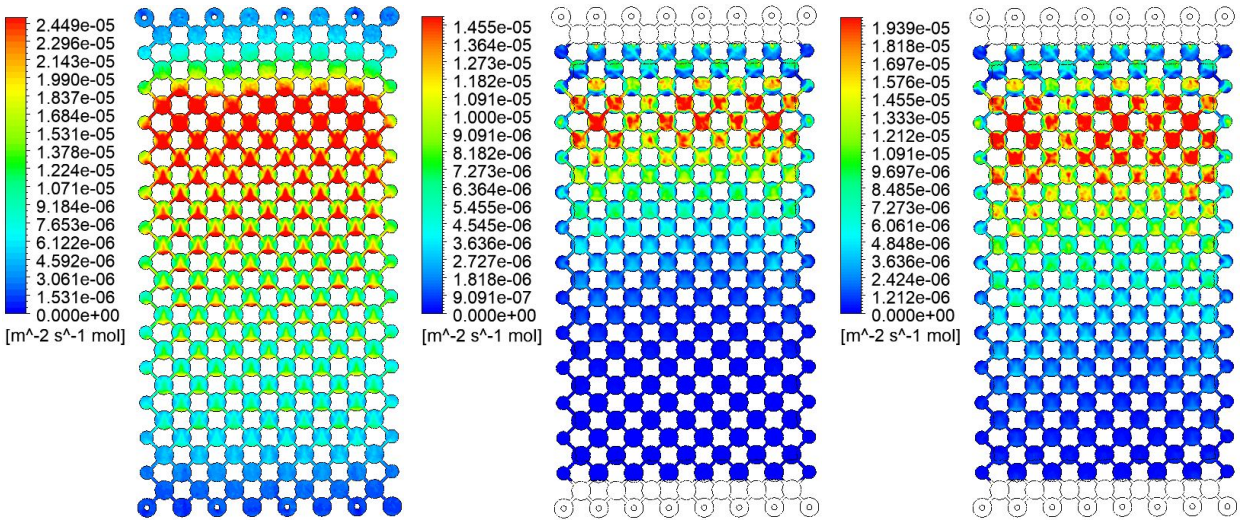

(a) Case α. (b) Case β. (c) Case γ.

Source: elaborated by the author (2022).

APPENDIX C – SUPLEMENTARY MATERIAL - RADIATION FIELD MODELING OF THE NETMIX MILI-PHOTOCATALYTIC REACTOR: EFFECT OF LEDS POSITION OVER THE REACTOR WINDOW

Figure 58 – LEDs positions in each simulation case.

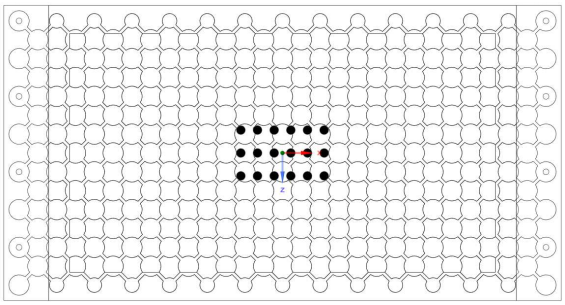

(a) Cases 1, 10 and 19

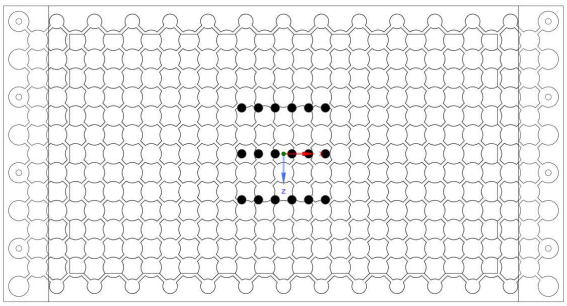

(b) Cases 2, 11 and 20

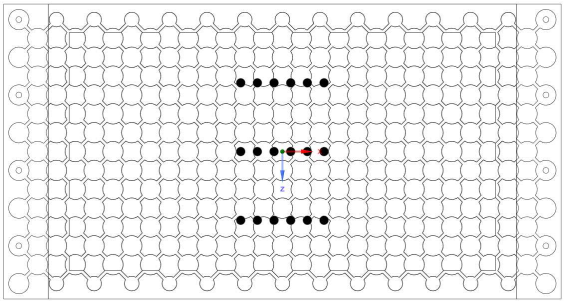

(c) Cases 3, 12 and 21

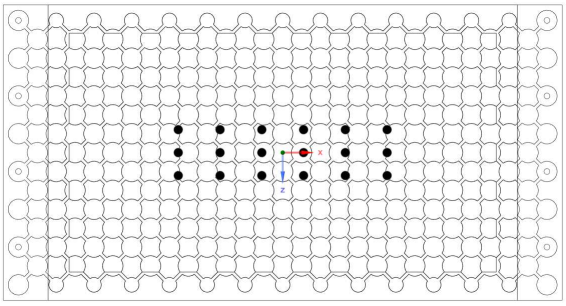

(d) Cases 4, 13 and 22

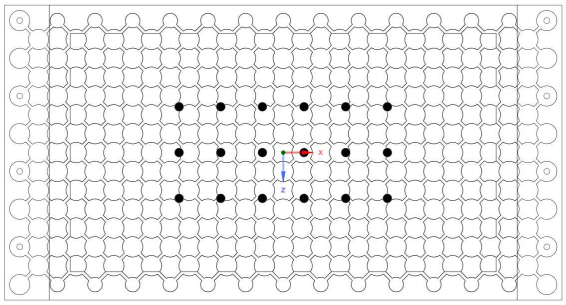

(e) Cases 5, 14 and 23

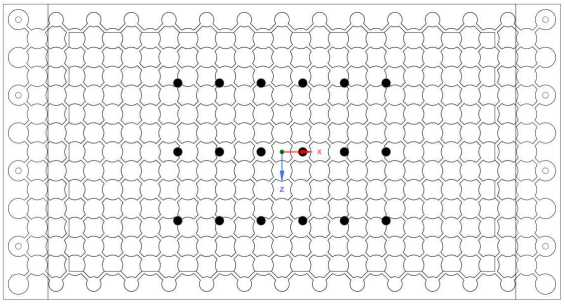

(f) Cases 6, 15 and 24

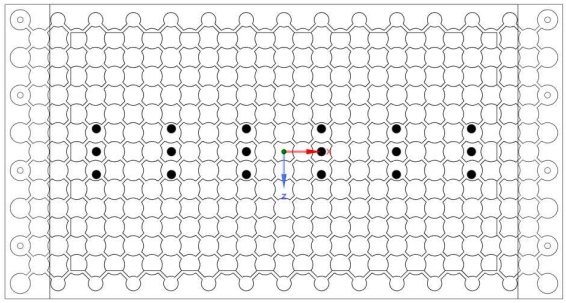

(g) Cases 7, 16 and 25

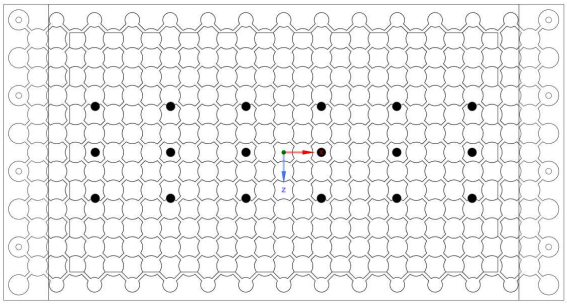

(h) Cases 8, 17 and 26

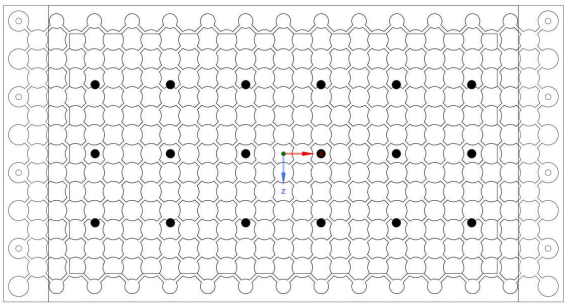

(i) Cases 9, 18 and 27

Source: elaborated by the author (2022).

Figure 59 – Irradiance maps of cases 1 to 27 for BSI and FSI illumination schemes.

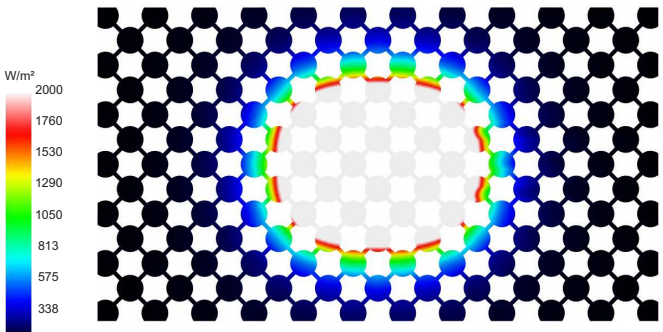

(a) Case 1 - BSI

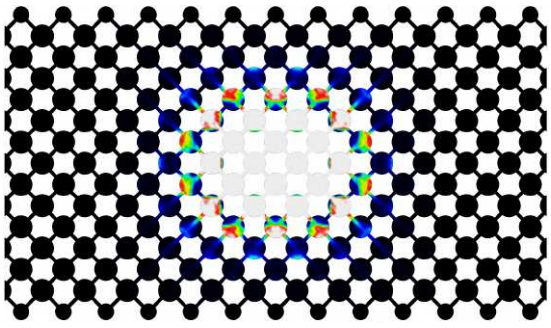

(b) Case 1 - FSI

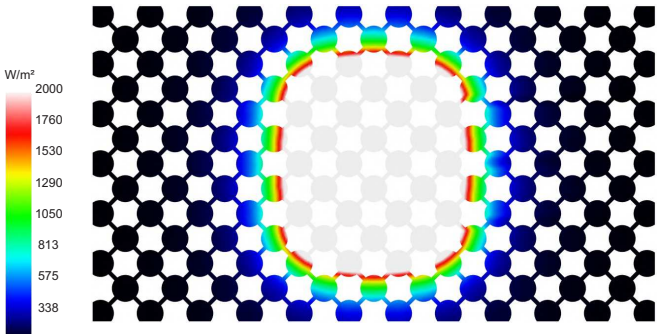

(c) Case 2 - BSI

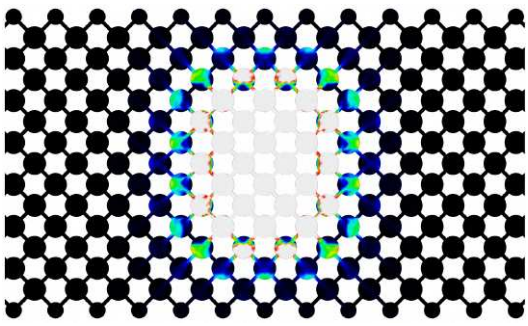

(d) Case 2 - FSI

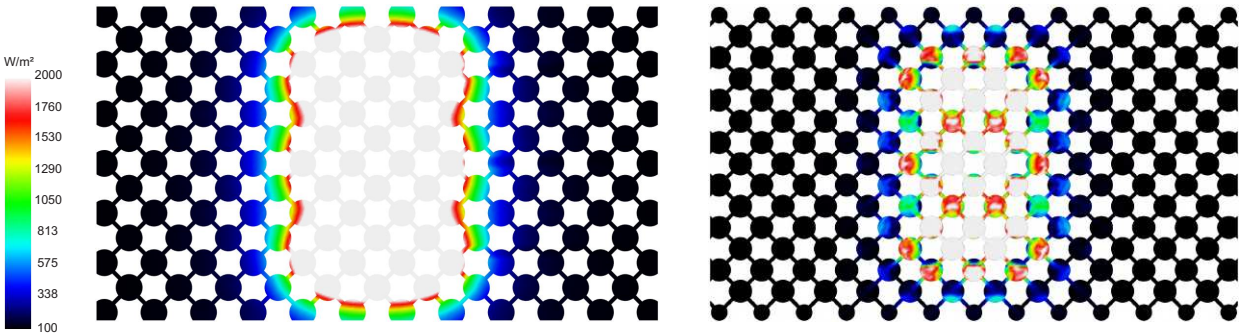

(e) Case 3 - BSI

(f) Case 3 - FSI

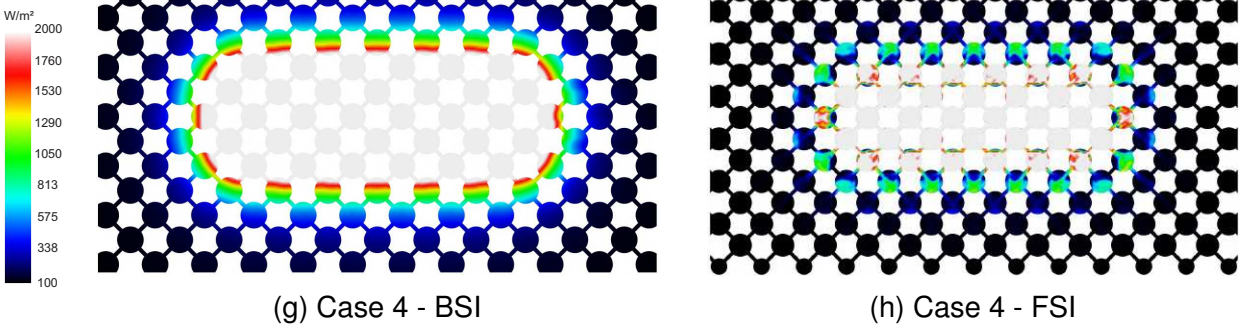

(g) Case 4 - BSI

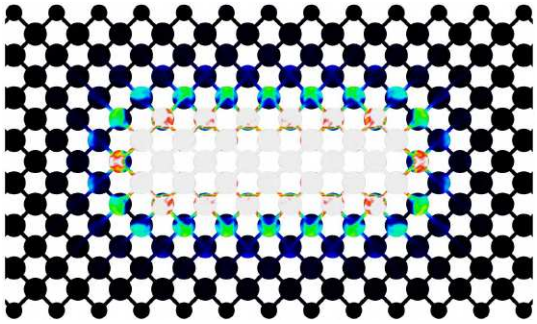

(h) Case 4 - FSI

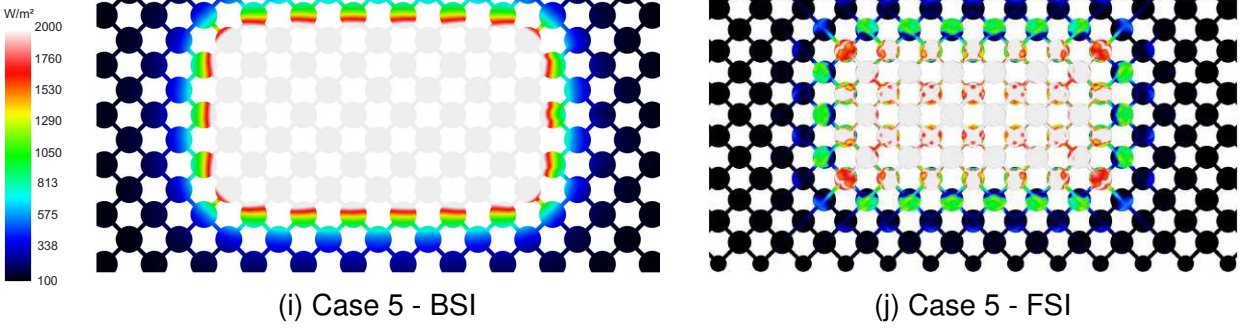

(i) Case 5 - BSI

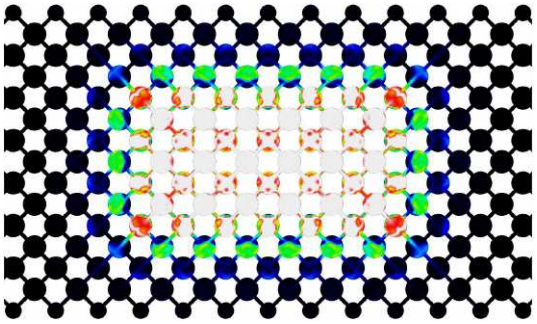

(j) Case 5 - FSI

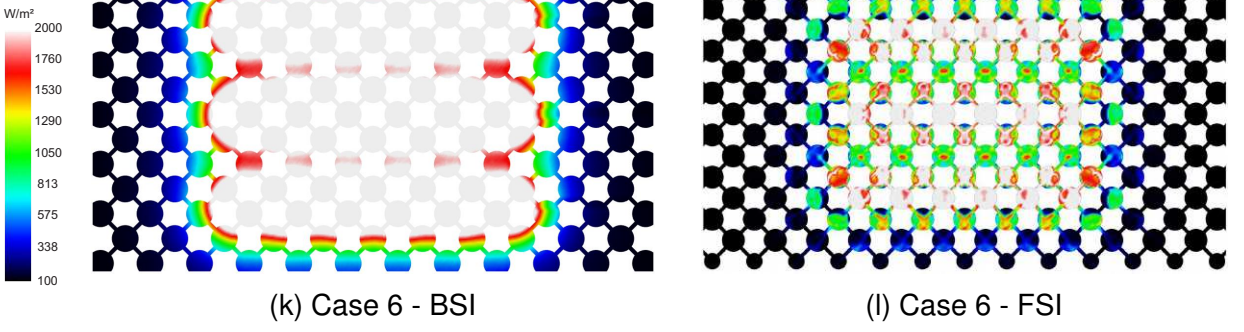

(k) Case 6 - BSI

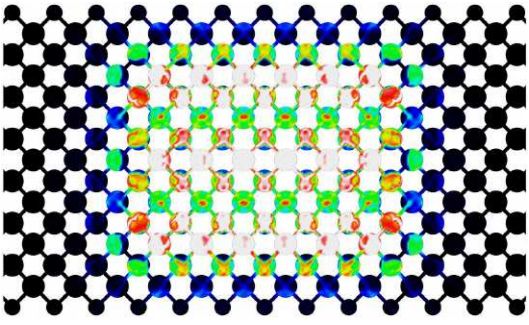

(l) Case 6 - FSI

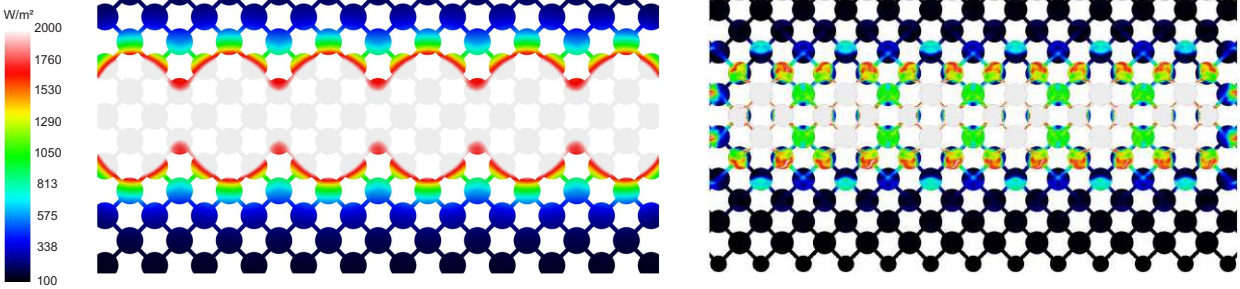

(m) Case 7 - BSI

(n) Case 7 - FSI

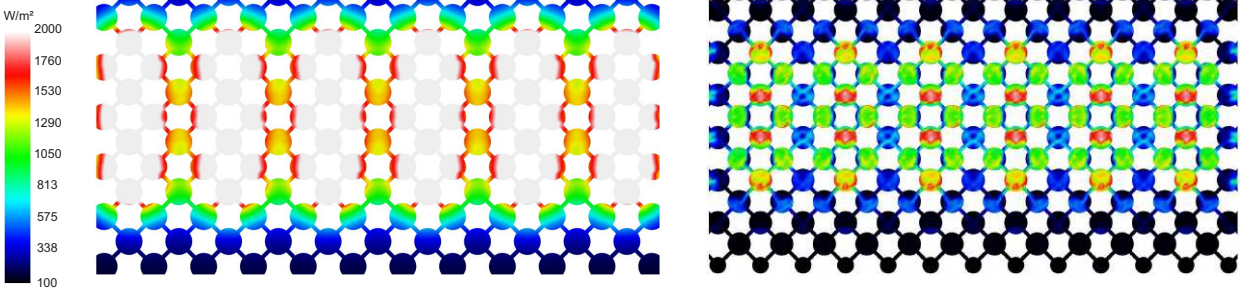

(o) Case 8 - BSI

(p) Case 8 - FSI

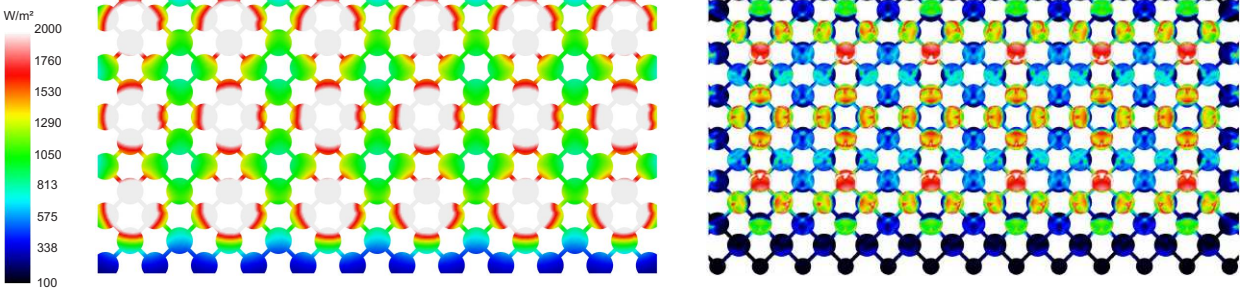

(q) Case 9 - BSI

(r) Case 9 - FSI

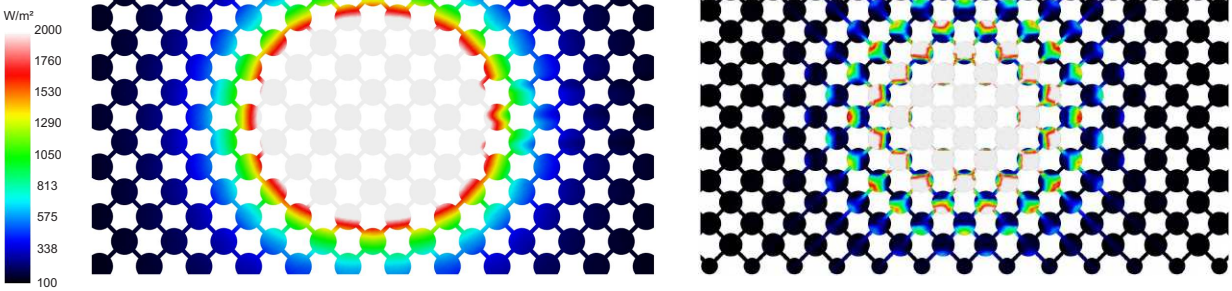

(s) Case 10 - BSI

(t) Case 10 - FSI

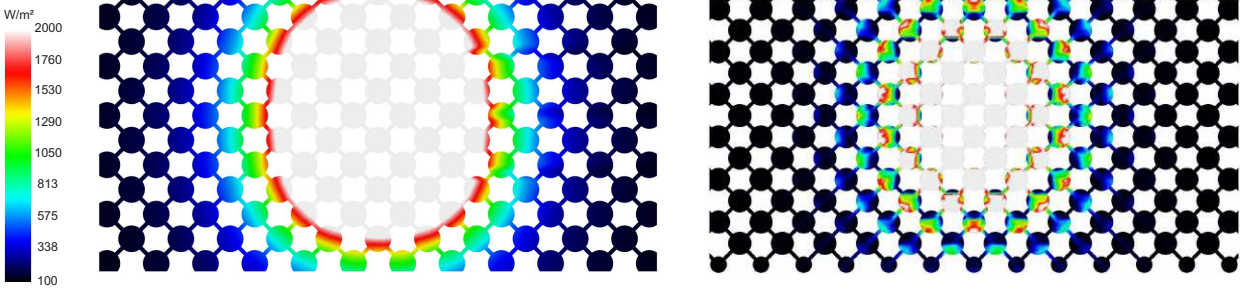

(u) Case 11 - BSI

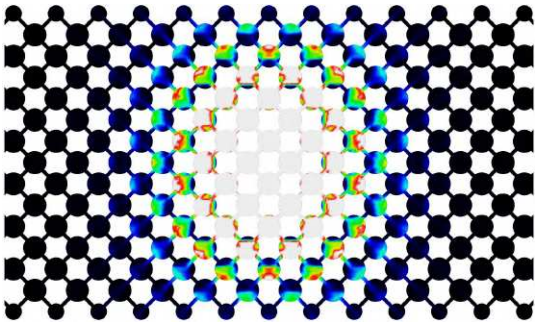

(v) Case 11 - FSI

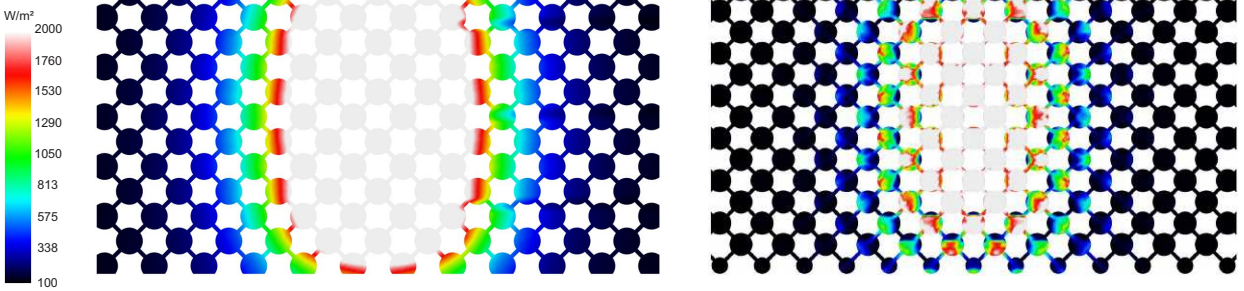

(w) Case 12 - BSI

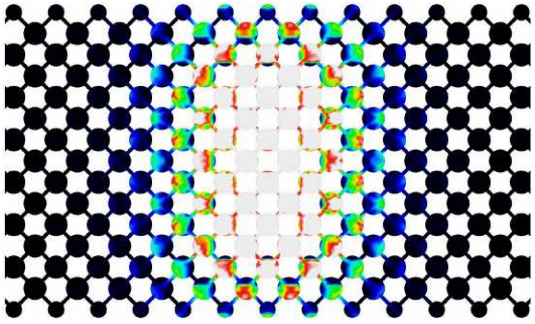

(x) Case 12 - FSI

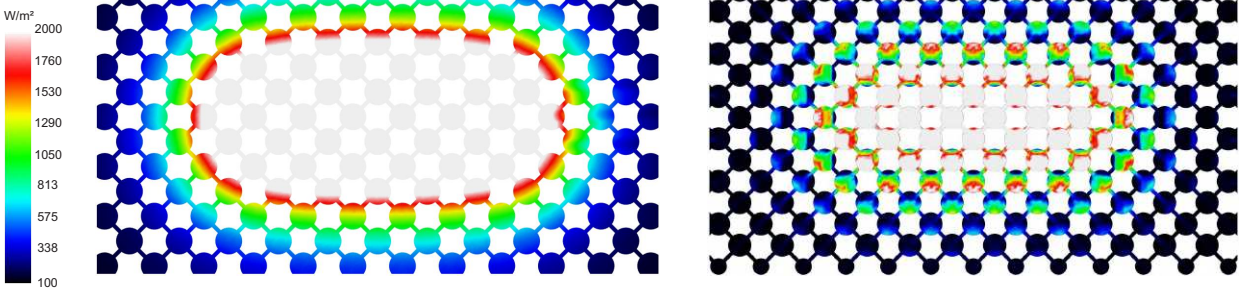

(y) Case 13 - BSI

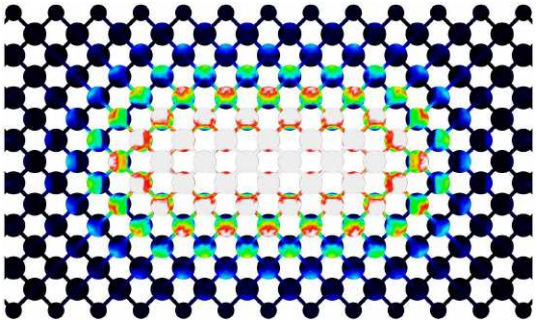

(z) Case 13 - FSI

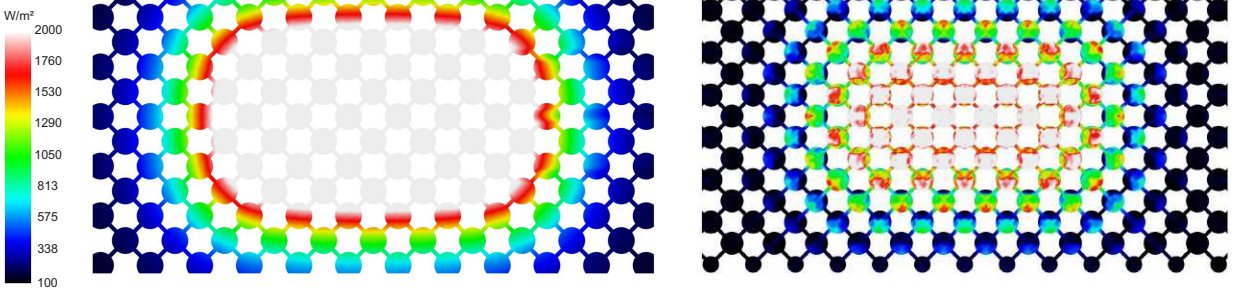

(aa) Case 14 - BSI

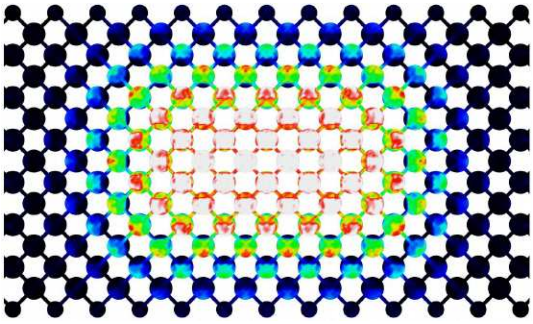

(ab) Case 14 - FSI

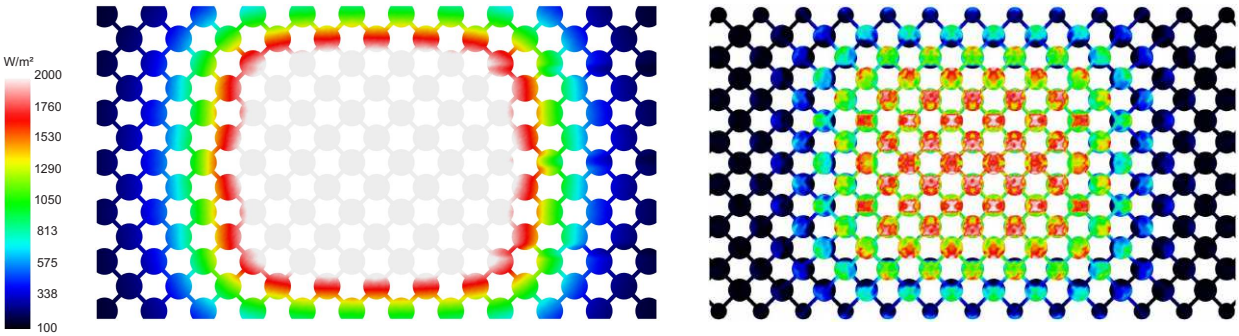

(ac) Case 15 - BSI

(ad) Case 15 - FSI

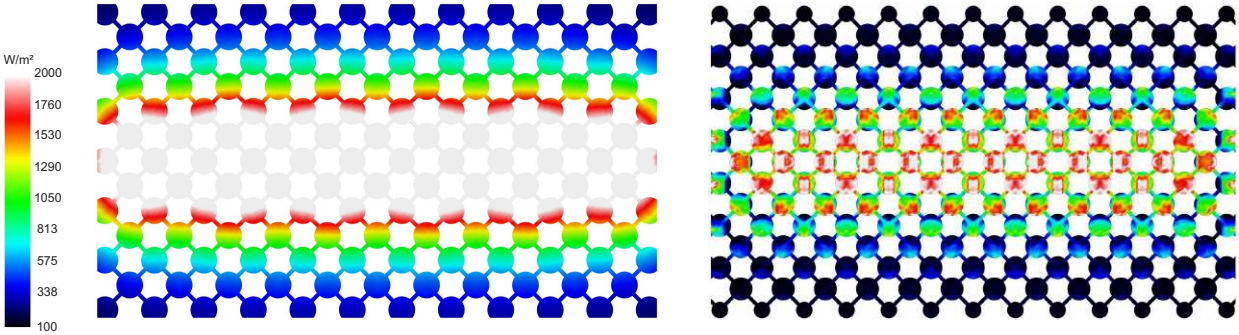

(ae) Case 16 - BSI

(af) Case 16 - FSI

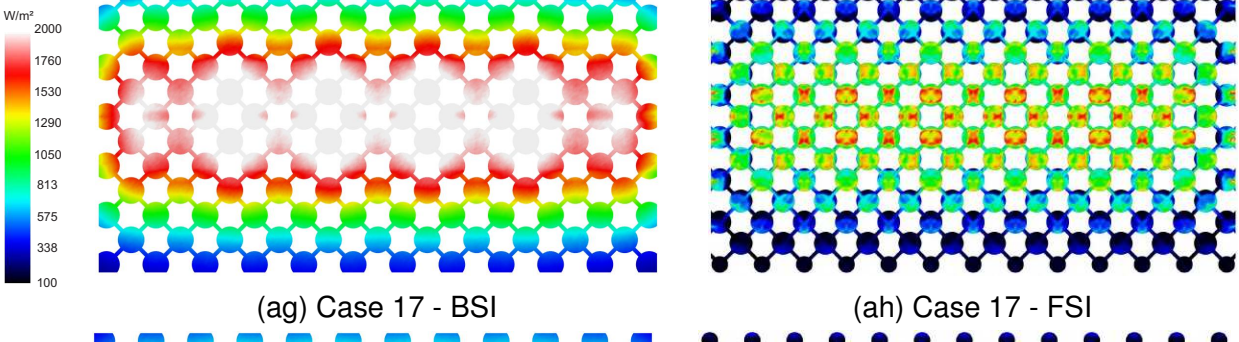

(ag) Case 17 - BSI

(ah) Case 17 - FSI

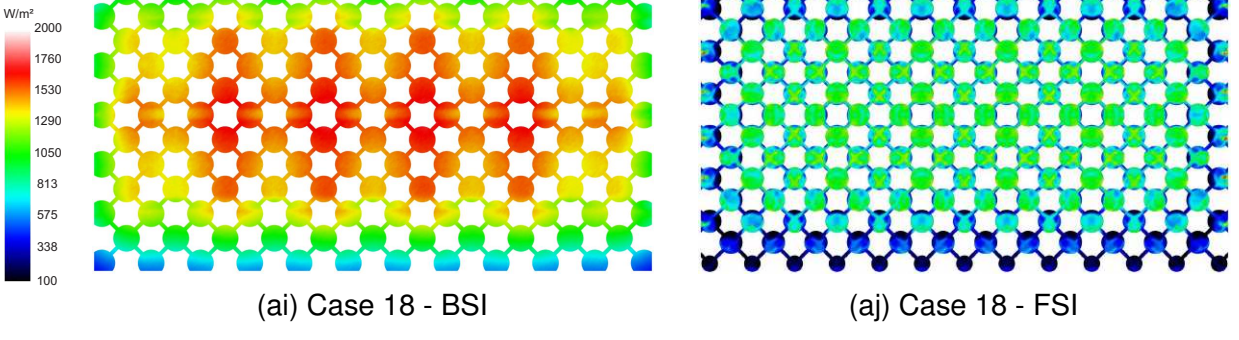

(ai) Case 18 - BSI

(aj) Case 18 - FSI

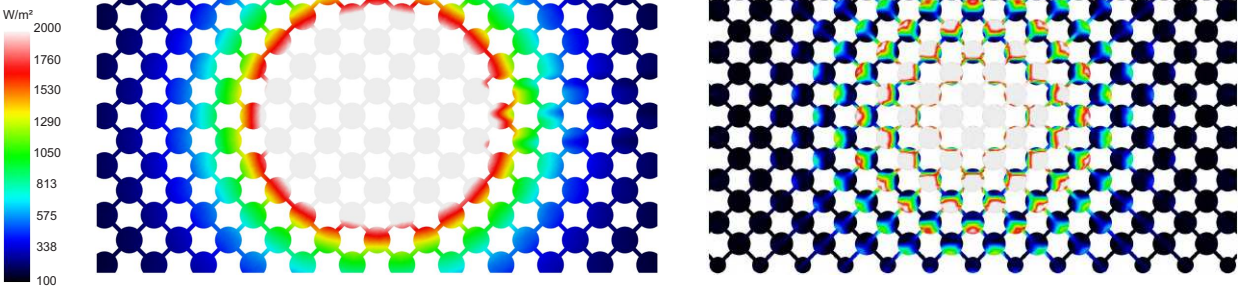

(ak) Case 19 - BSI

(al) Case 19 - FSI

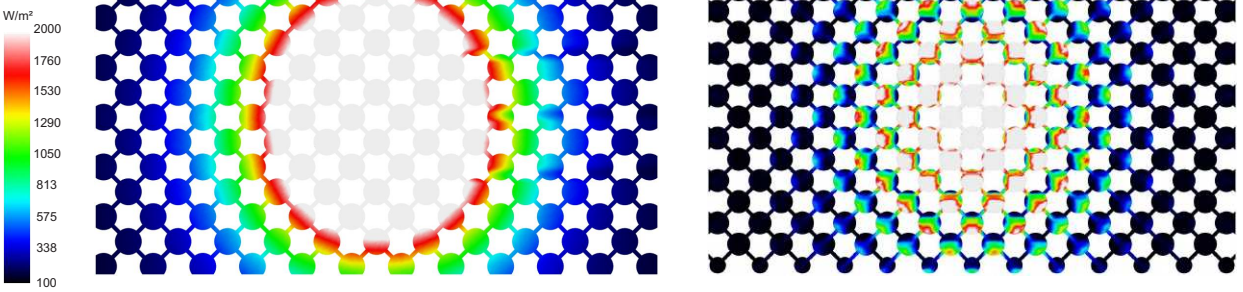

(am) Case 20 - BSI

(an) Case 20 - FSI

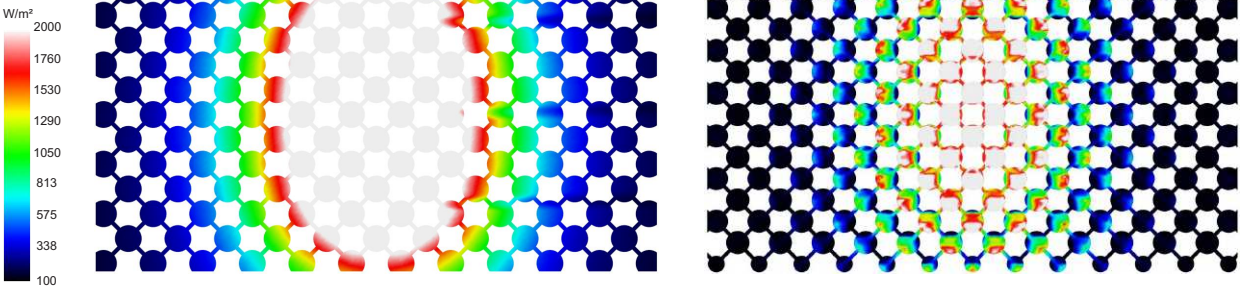

(ao) Case 21 - BSI

(ap) Case 21 - FSI

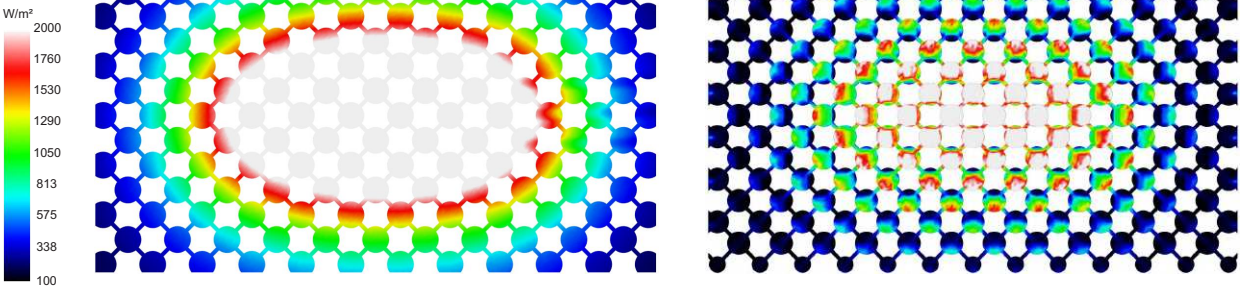

(aq) Case 22 - BSI

(ar) Case 22 - FSI

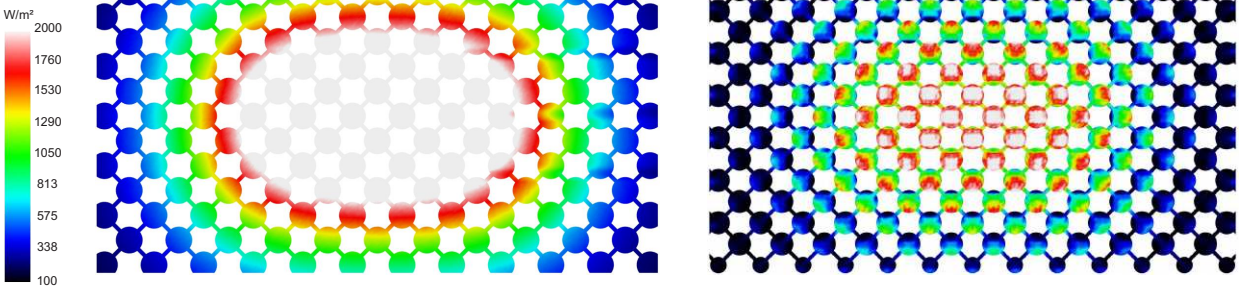

(as) Case 23 - BSI

(at) Case 23 - FSI

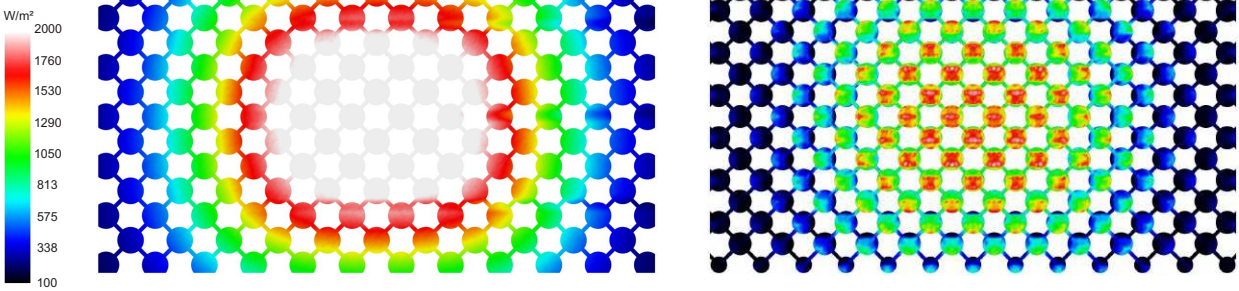

(au) Case 24 - BSI

(av) Case 24 - FSI

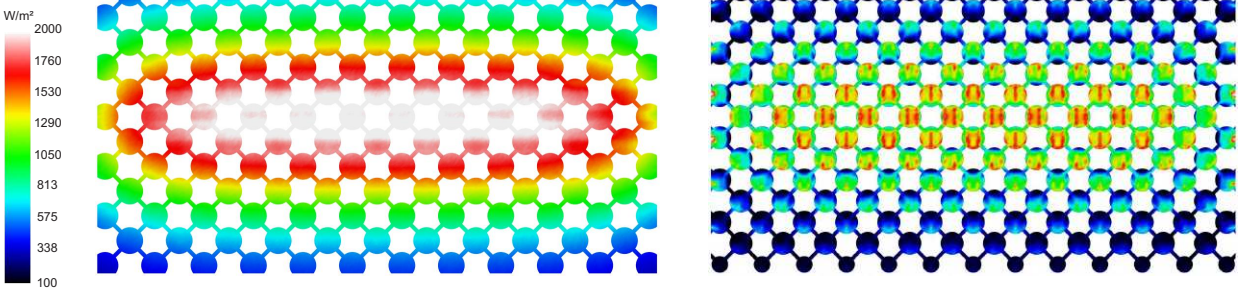

(aw) Case 25 - BSI

(ax) Case 25 - FSI

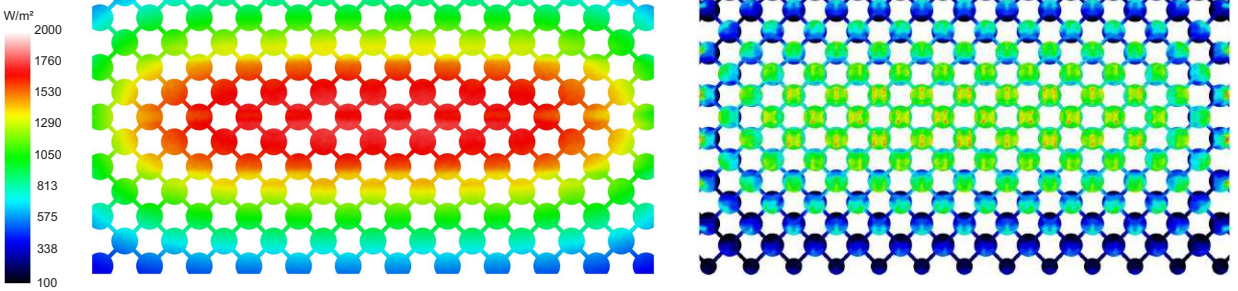

(ay) Case 26 - BSI

(az) Case 26 - FSI

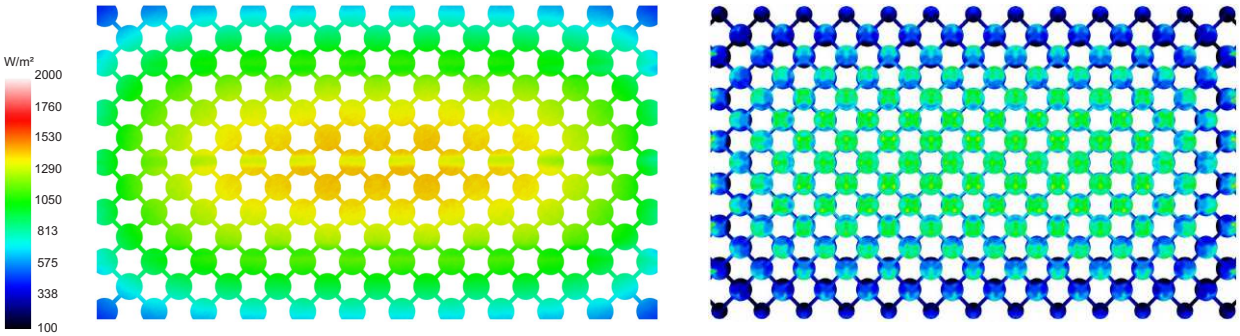

(ba) Case 27 - BSI (bb) Case 27 - FSI

Source: elaborated by the author (2022).

Figure 60 – LEDs far-field angular distribution.

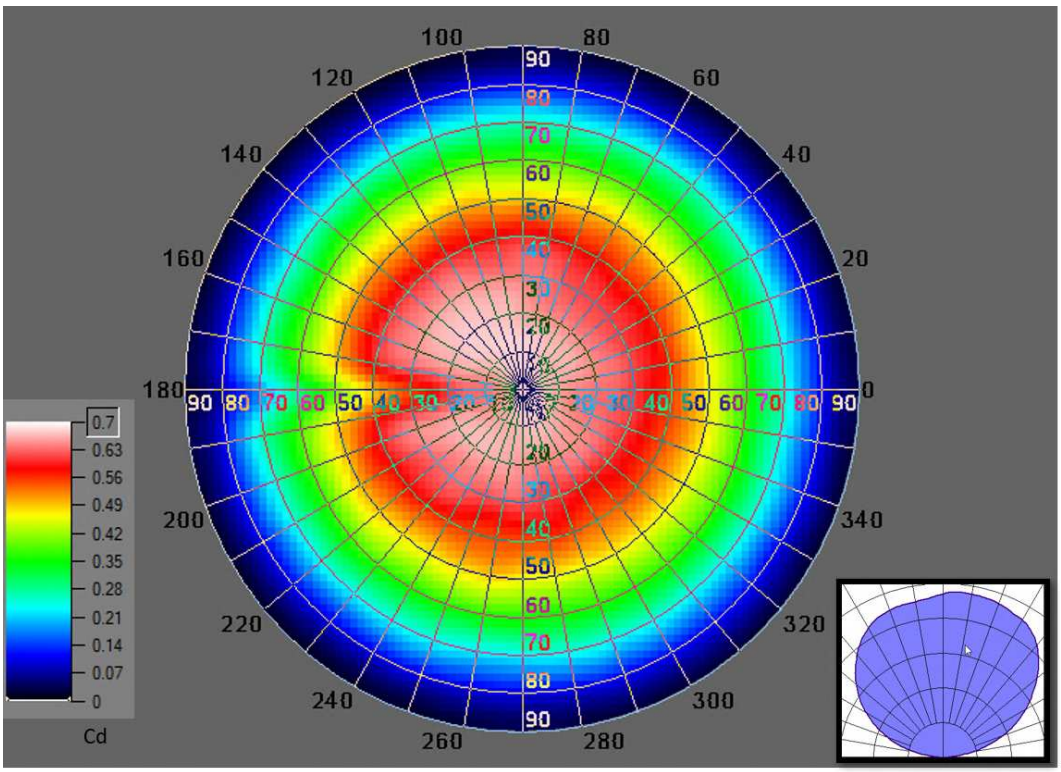

Source: elaborated by the author (2022).

Figure 61 – LEDs near-field distribution.

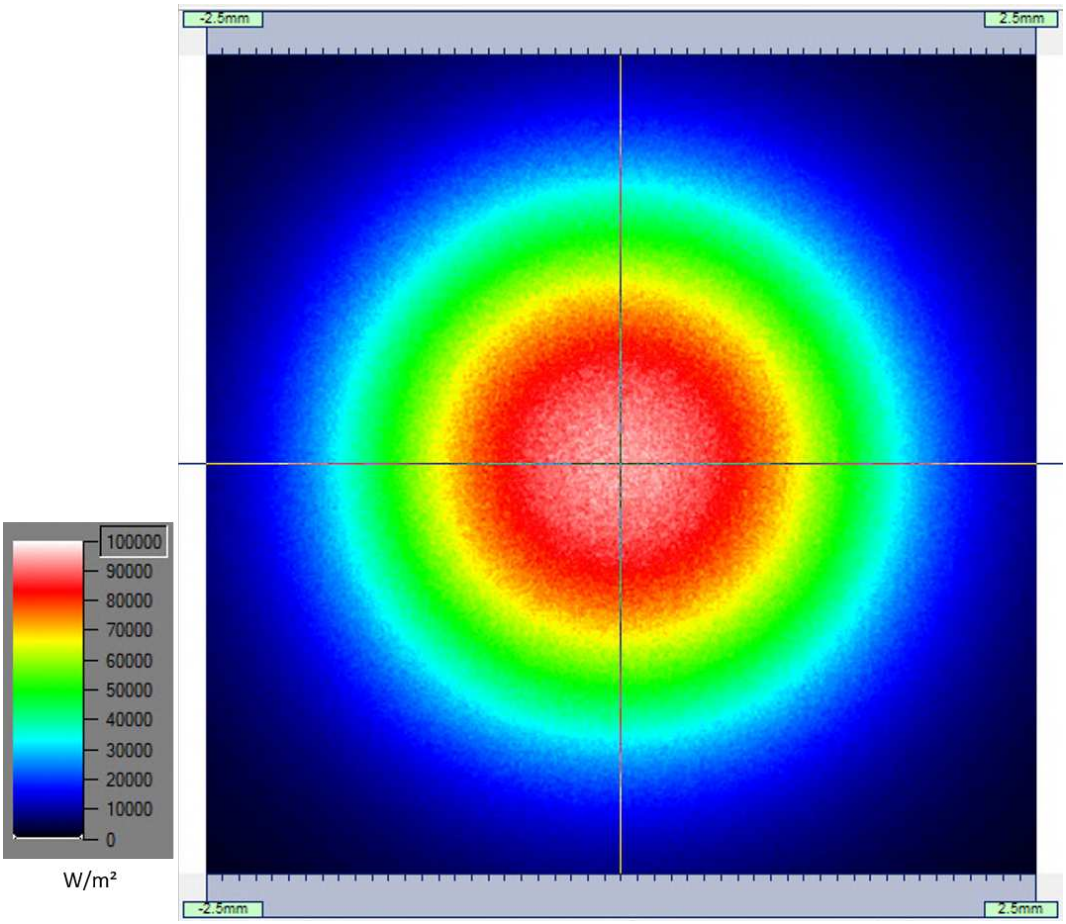

Source: elaborated by the author (2022).

APPENDIX D – SUPLEMENTARY MATERIAL - CFD AND RADIATION FIELD MODELING OF THE NETMIX MILLI-PHOTOCATALYTIC REACTOR FOR *N*-DECANE OXIDATION AT GAS PHASE

Figure 62 – LEDs geometrical position over the reactor window for each LEDs plates proposed.

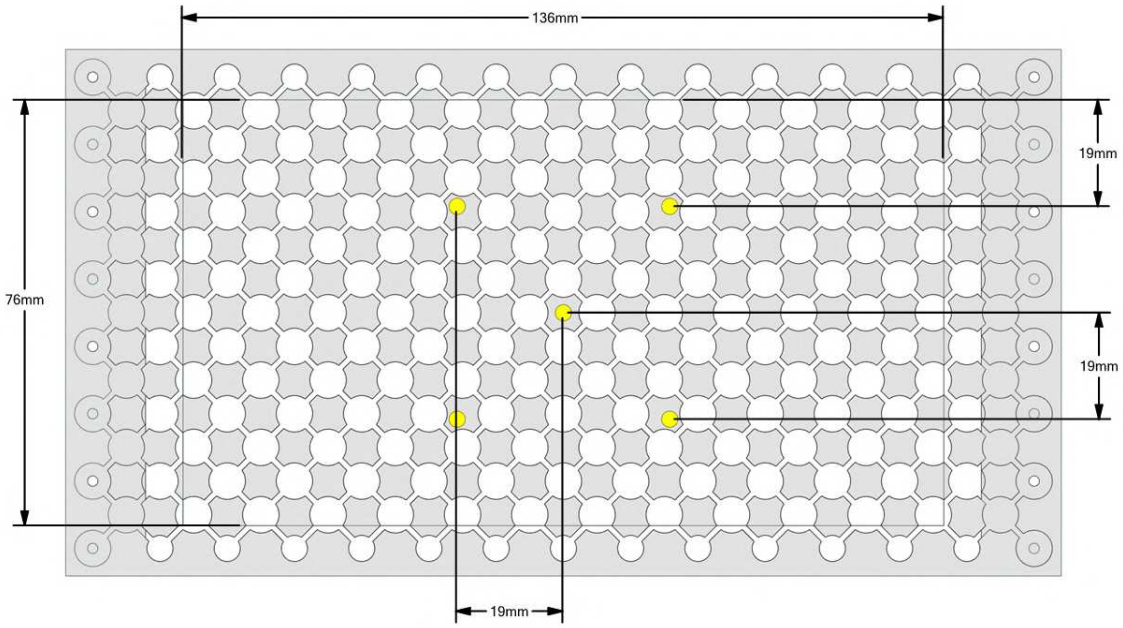

(a) 5 Staggered LEDs - Cases 1 to 4

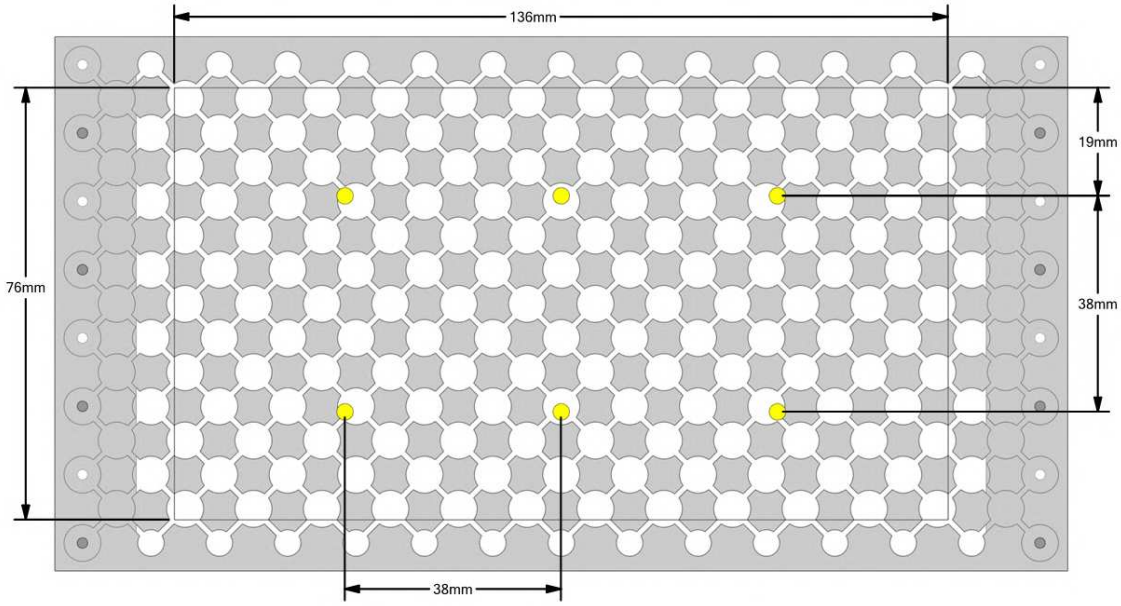

(b) 6 Inline LEDs - Cases 5 to 8

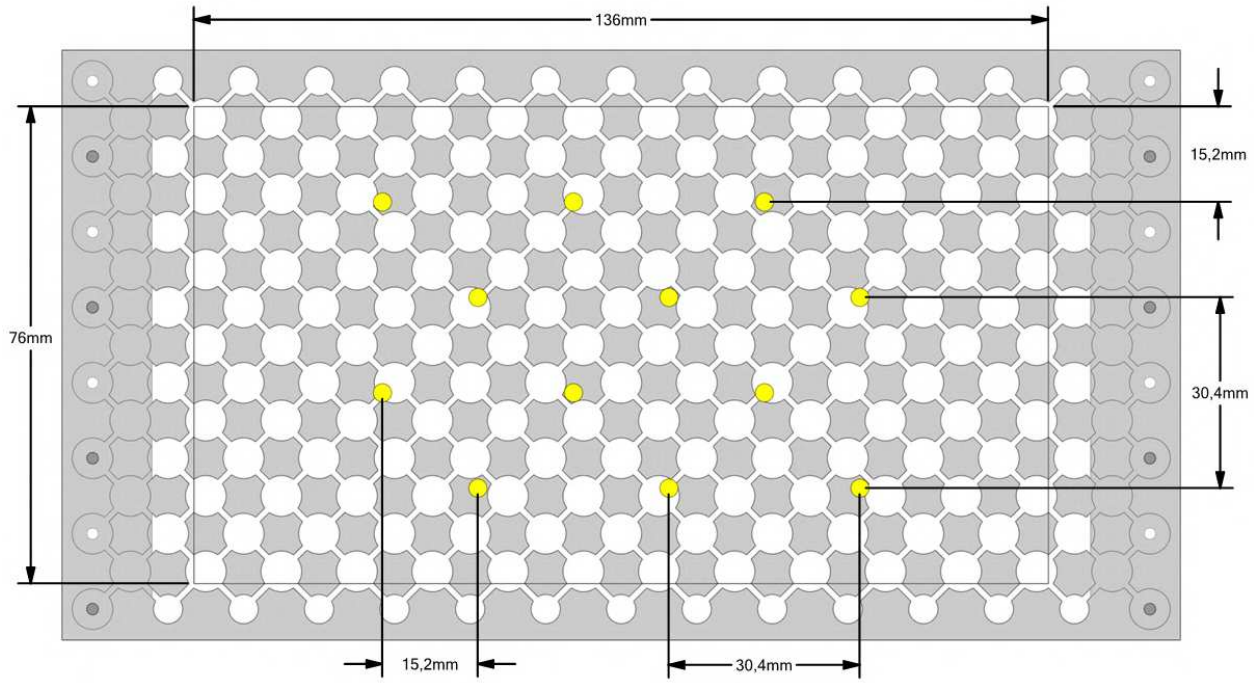

(c) 12 Staggered LEDs - Cases 9 to 12

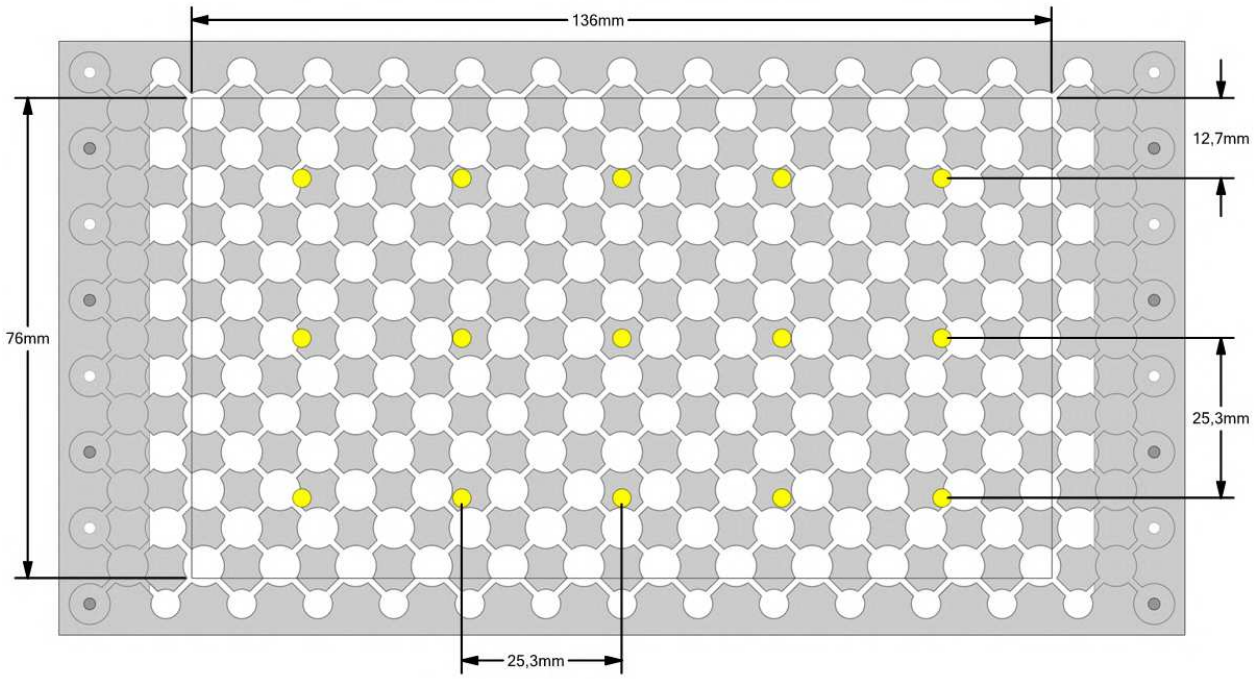

(d) 15 Inline LEDs - Cases 13 to 16

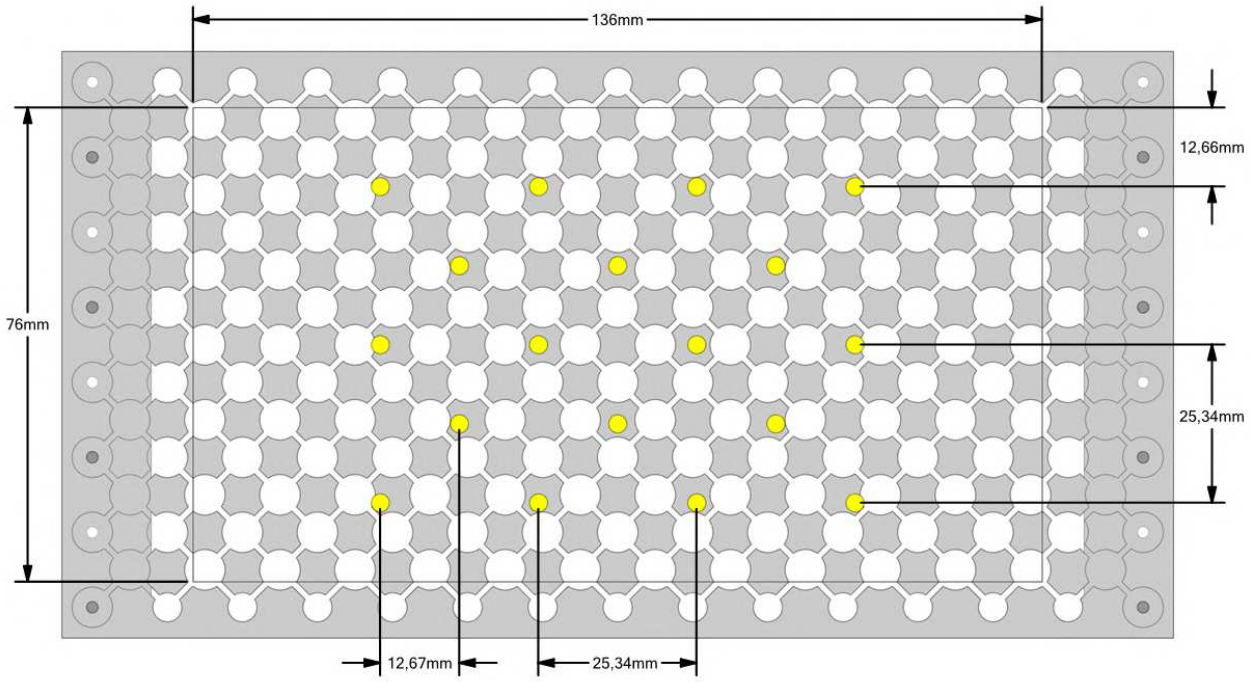

(e) 18 Staggered LEDs - Cases 17 to 20

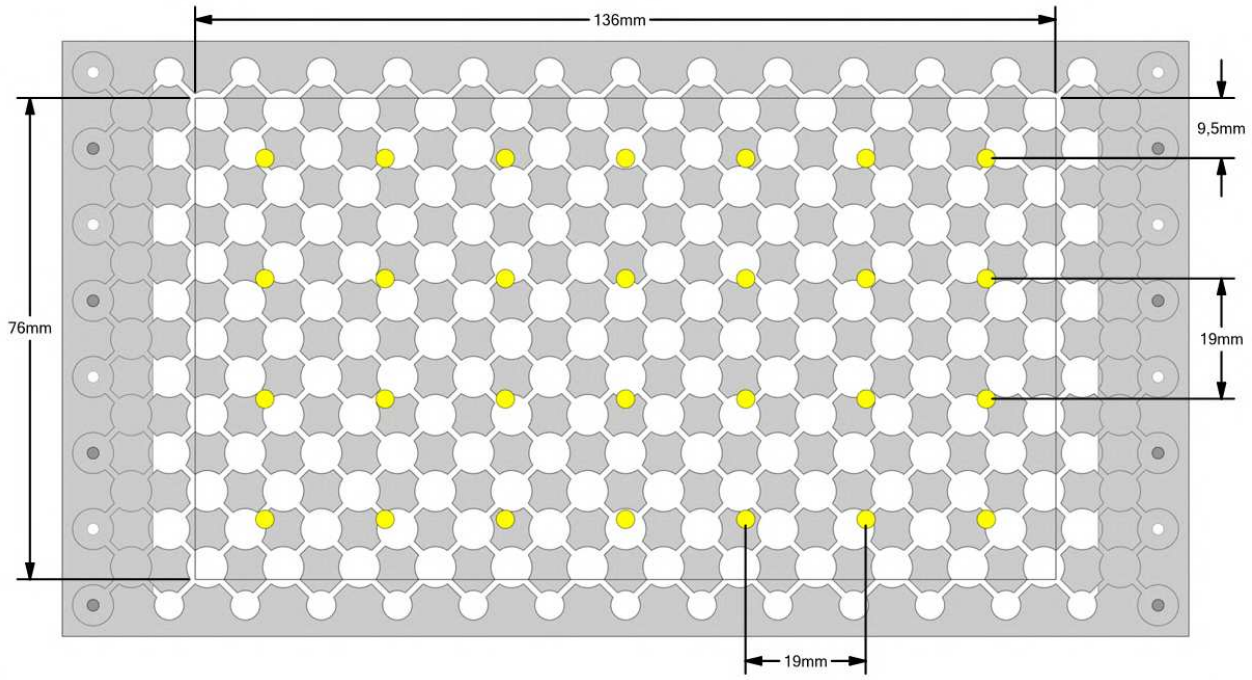

(f) 28 Inline LEDs - Cases 21 to 24

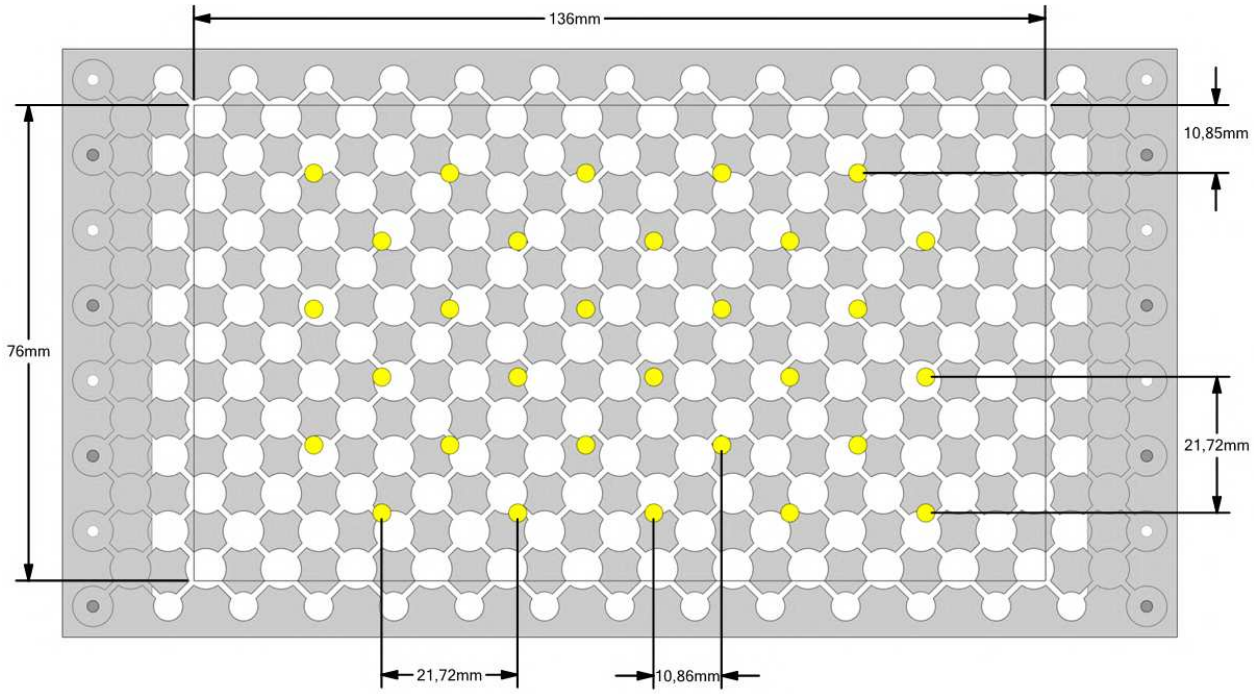

(g) 30 Staggered LEDs - Cases 25 to 28

Source: elaborated by the author (2022).

Figure 63 – Irradiance maps of cases 1 to 28.

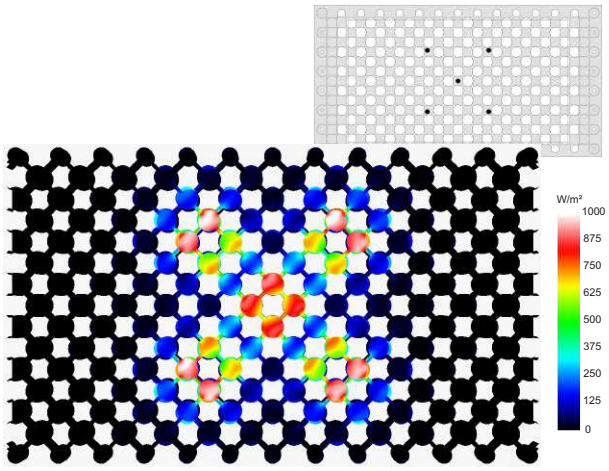

(a) Case 1: 5 LEDs - h = 6 mm

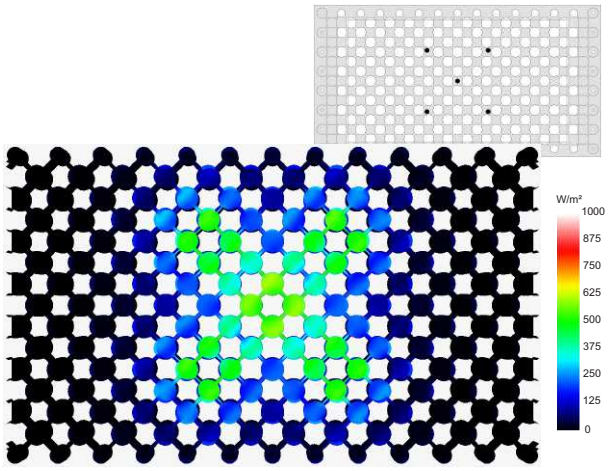

(b) Case 2: 5 LEDs - h = 12 mm

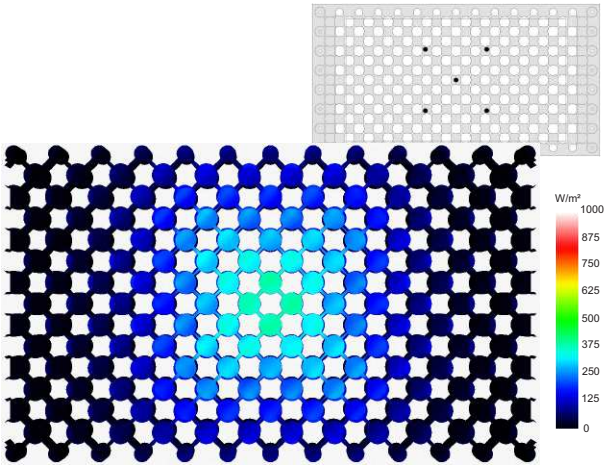

(c) Case 3: 5 LEDs - h = 24 mm

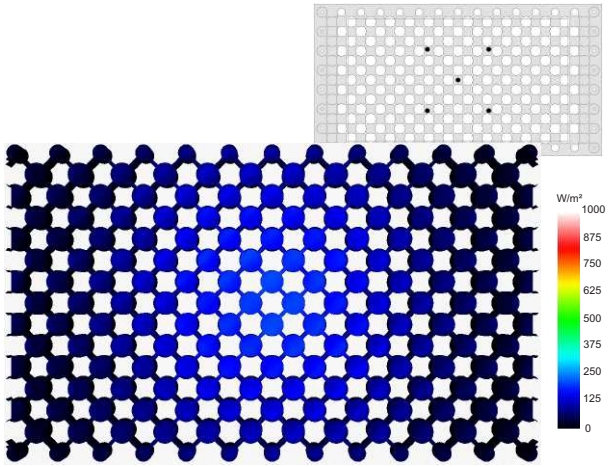

(d) Case 4: 5 LEDs - h = 48 mm

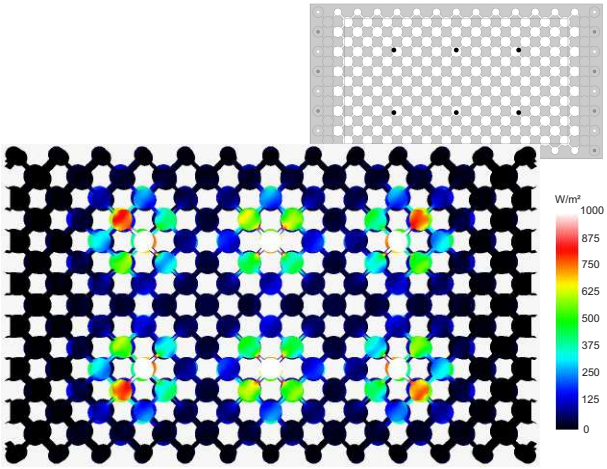

(e) Case 5: 6 LEDs - h = 6 mm

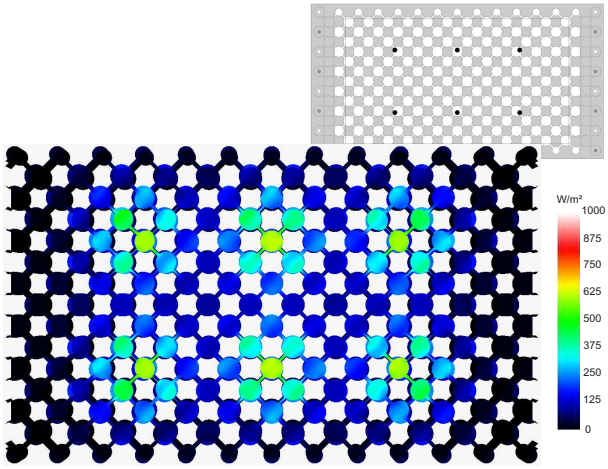

(f) Case 6: 6 LEDs - h = 12 mm

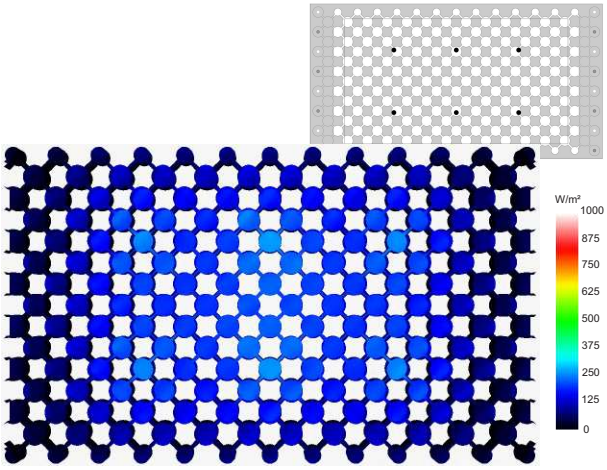

(g) Case 7: 6 LEDs - h = 24 mm

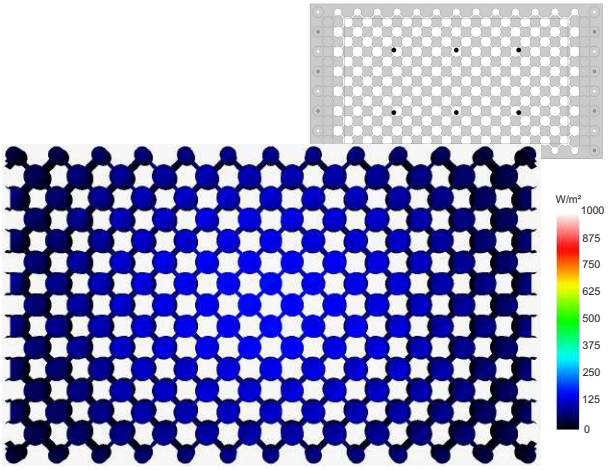

(h) Case 8: 6 LEDs - h = 48 mm

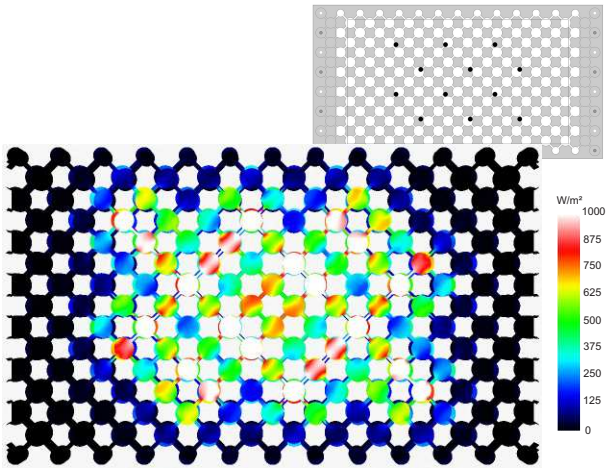

(i) Case 9: 12 LEDs - h = 6 mm

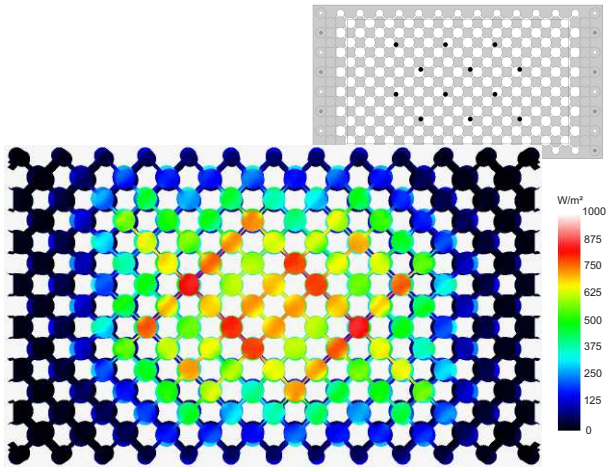

(j) Case 10: 12 LEDs - h = 12 mm

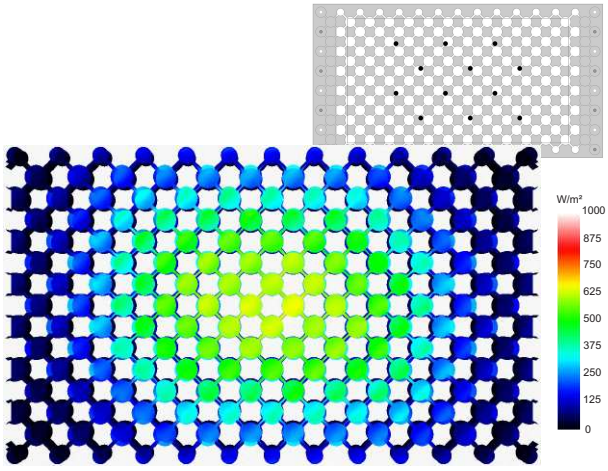

(k) Case 11: 12 LEDs - h = 24 mm

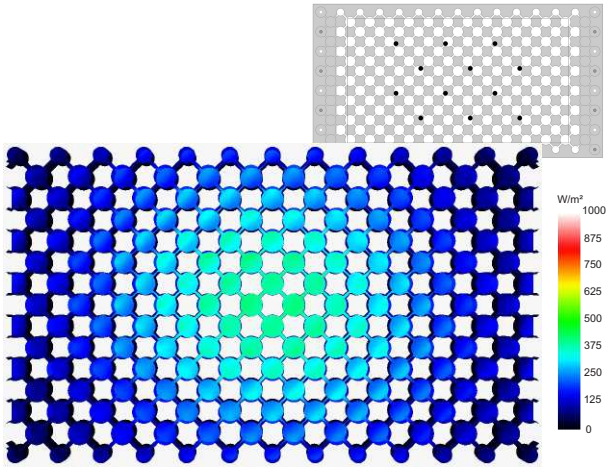

(l) Case 12: 12 LEDs - h = 48 mm

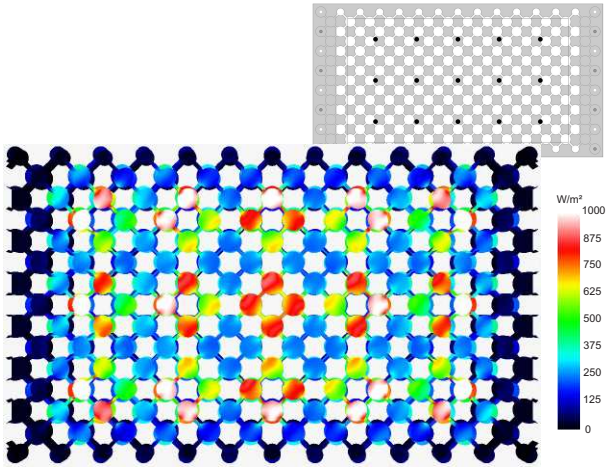

(m) Case 13: 15 LEDs - h = 6 mm

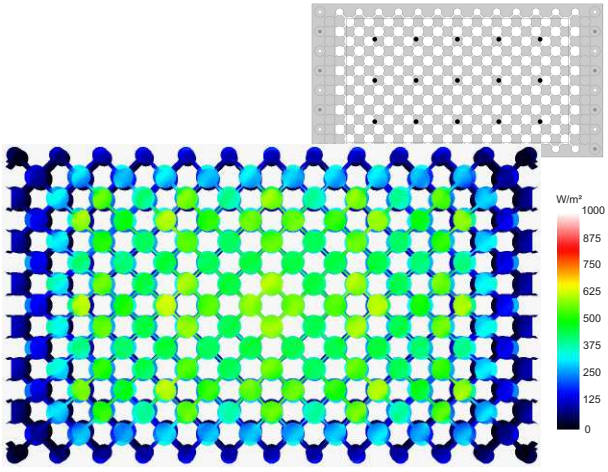

(n) Case 14: 15 LEDs - h = 12 mm

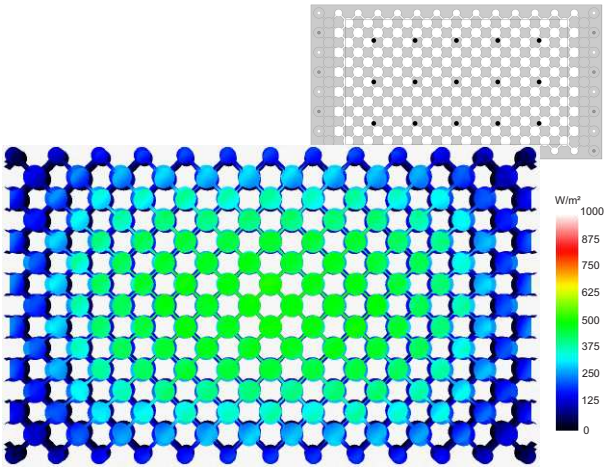

(o) Case 15: 15 LEDs - h = 24 mm

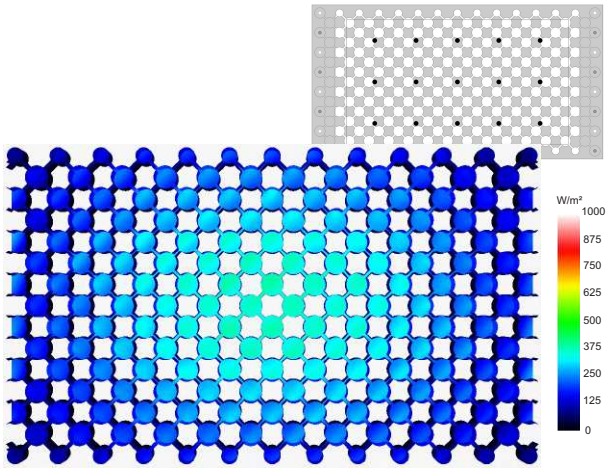

(p) Case 16: 15 LEDs - h = 48 mm

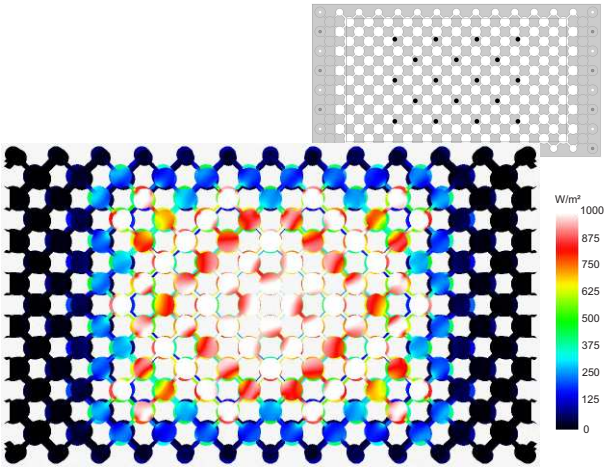

(q) Case 17: 18 LEDs - h = 6 mm

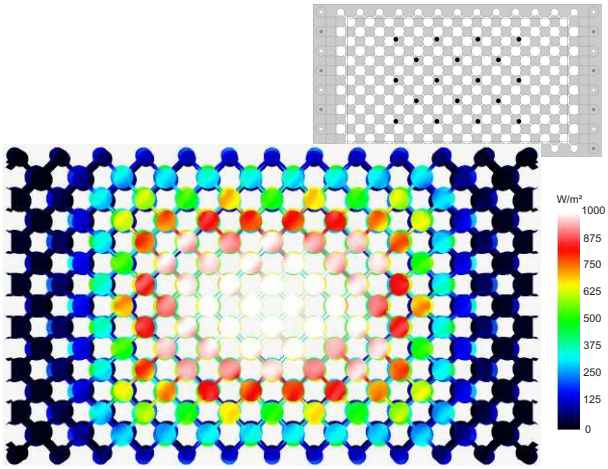

(r) Case 18: 18 LEDs - h = 12 mm

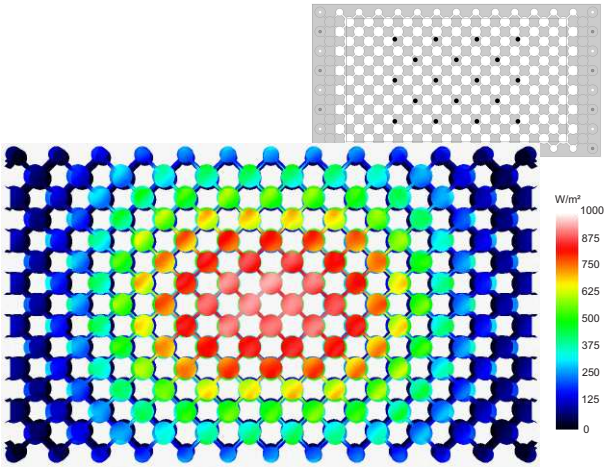

(s) Case 19: 18 LEDs - h = 24 mm

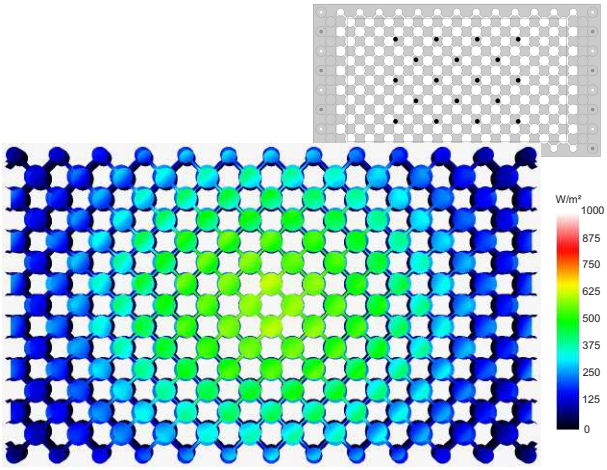

(t) Case 20: 18 LEDs - h = 48 mm

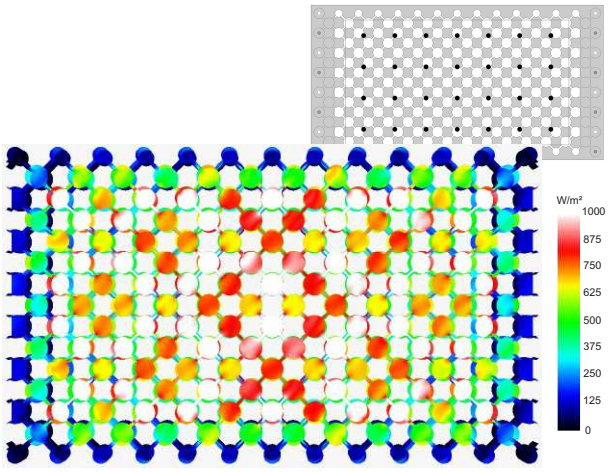

(u) Case 21: 28 LEDs - h = 6 mm

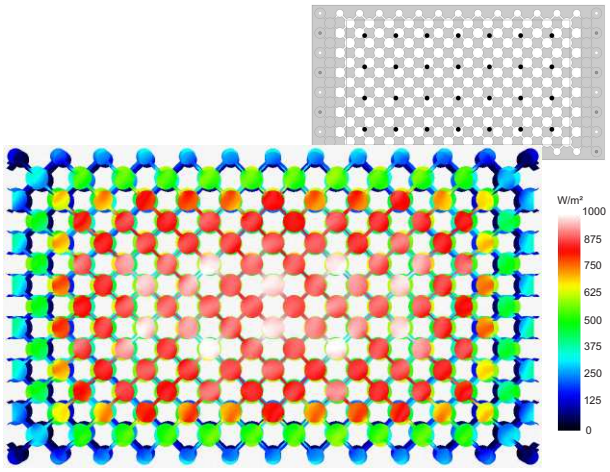

(v) Case 22: 28 LEDs - h = 12 mm

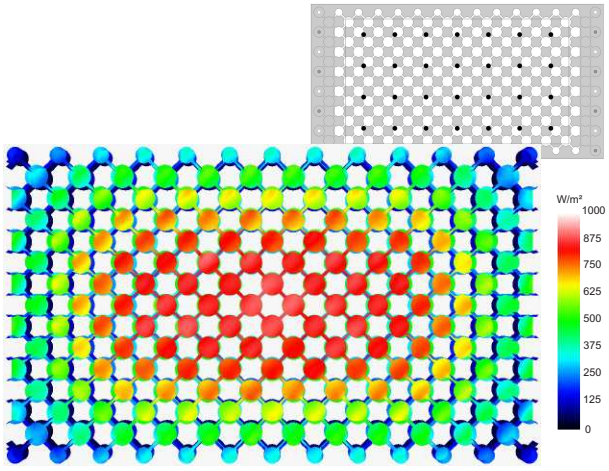

(w) Case 23: 28 LEDs - h = 24 mm

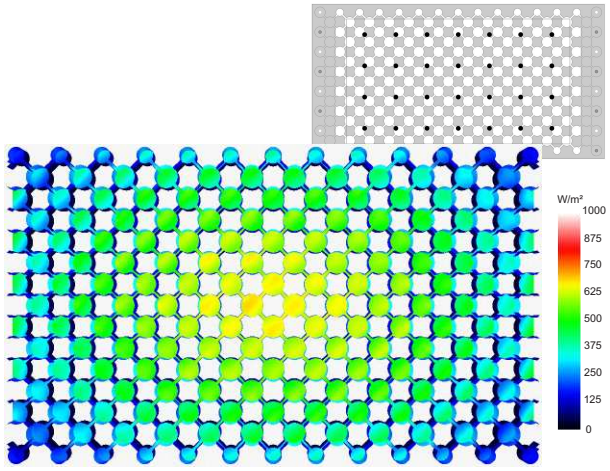

(x) Case 24: 28 LEDs - h = 48 mm

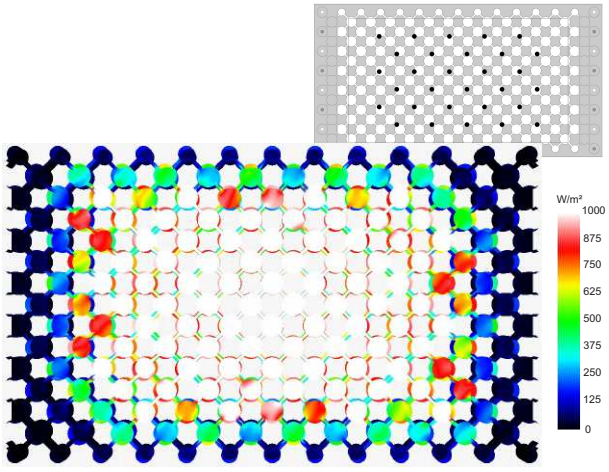

(y) Case 25: 30 LEDs - h = 6 mm

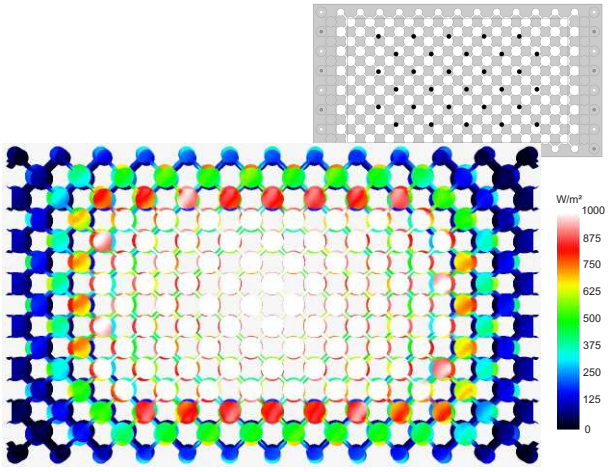

(z) Case 26: 30 LEDs - h = 12 mm

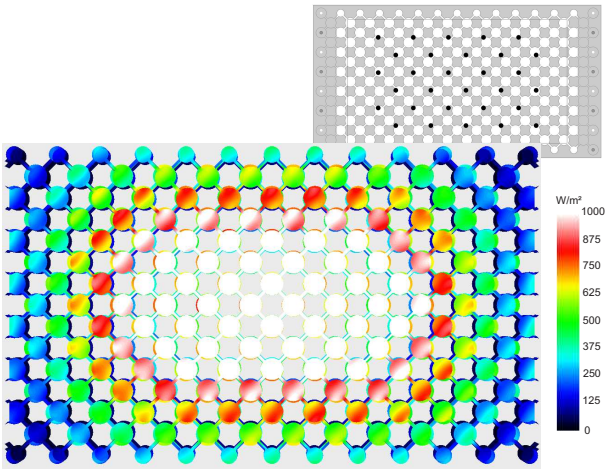

(aa) Case 27: 30 LEDs - h = 24 mm

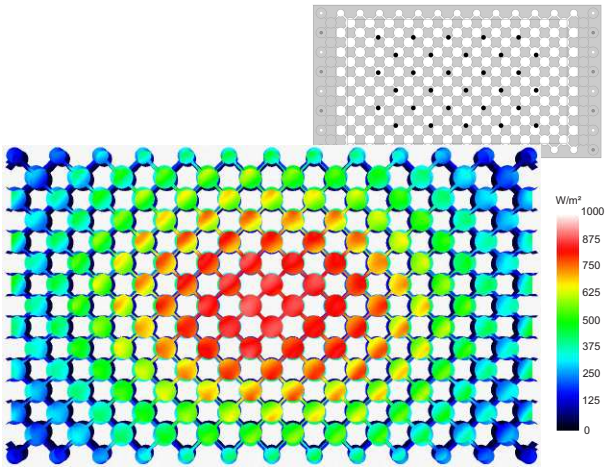

(ab) Case 28: 30 LEDs - h = 48 mm

Source: elaborated by the author (2022).

Figure 64 – Reaction rate of cases 1 to 28.

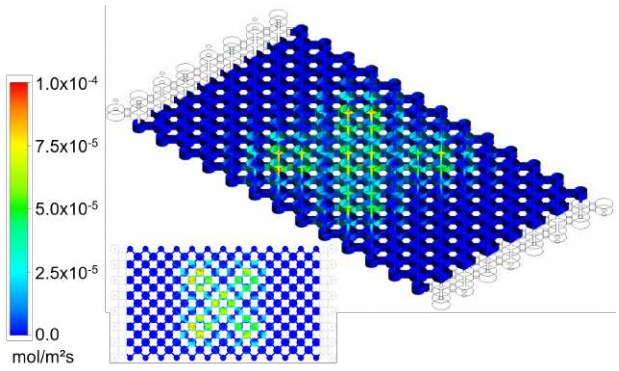

(a) Case 1: 5 LEDs - h = 6 mm

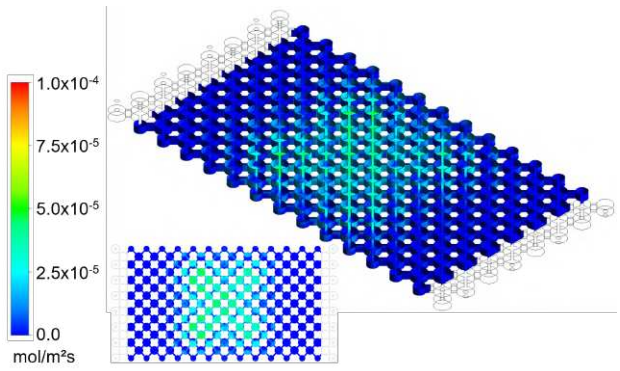

(b) Case 2: 5 LEDs - h = 12 mm

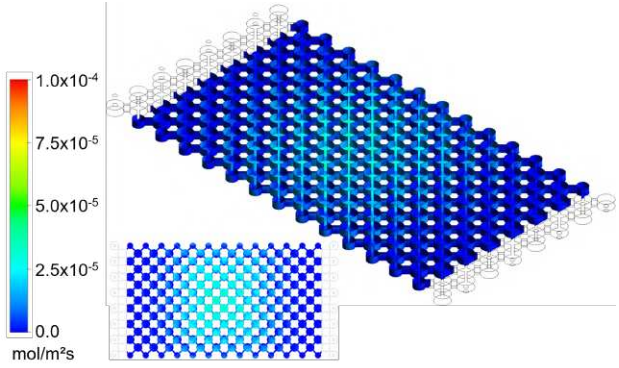

(c) Case 3: 5 LEDs - h = 24 mm

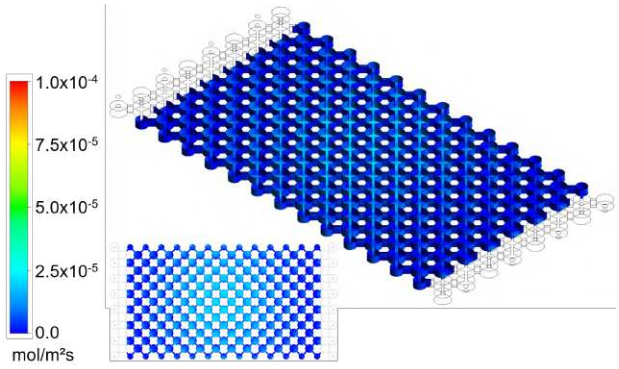

(d) Case 4: 5 LEDs - h = 48 mm

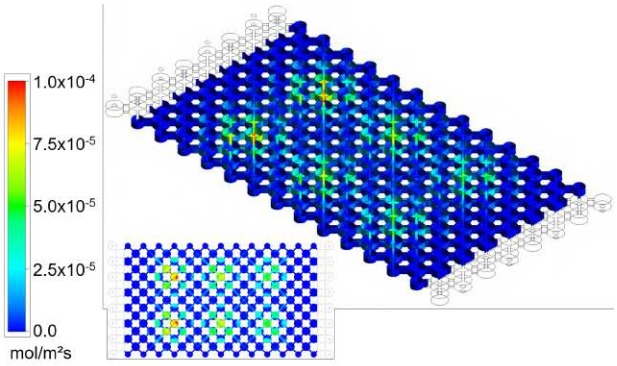

(e) Case 5: 6 LEDs - h = 6 mm

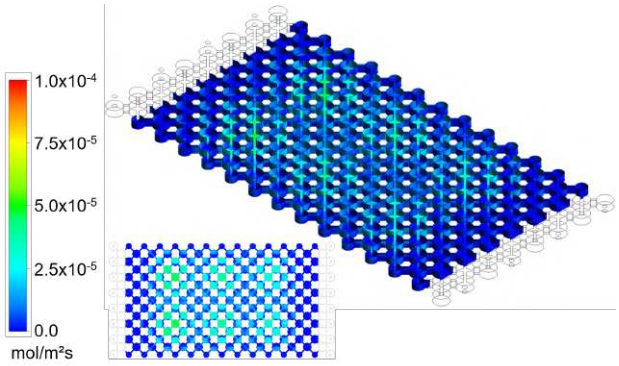

(f) Case 6: 6 LEDs - h = 12 mm

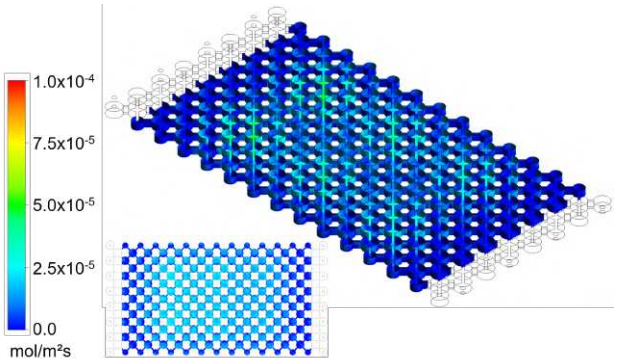

(g) Case 7: 6 LEDs - h = 24 mm

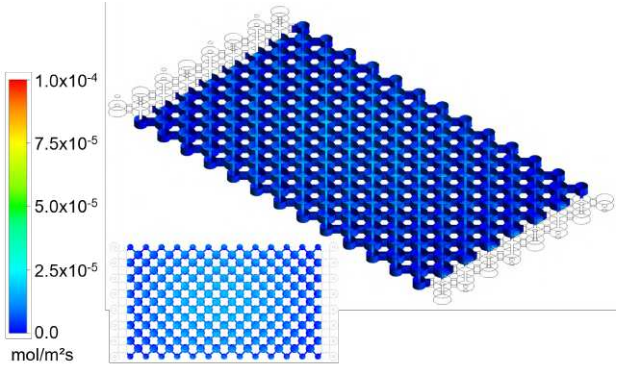

(h) Case 8: 6 LEDs - h = 48 mm

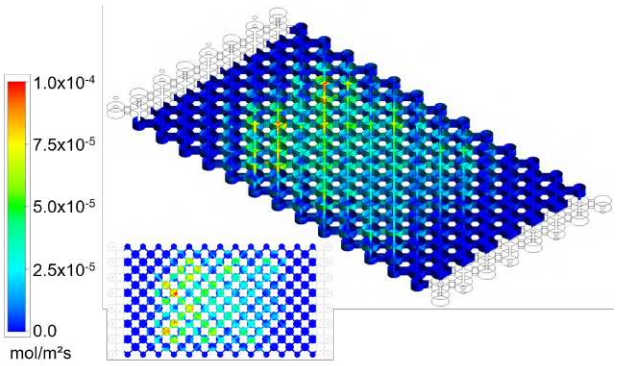

(i) Case 9: 12 LEDs - h = 6 mm

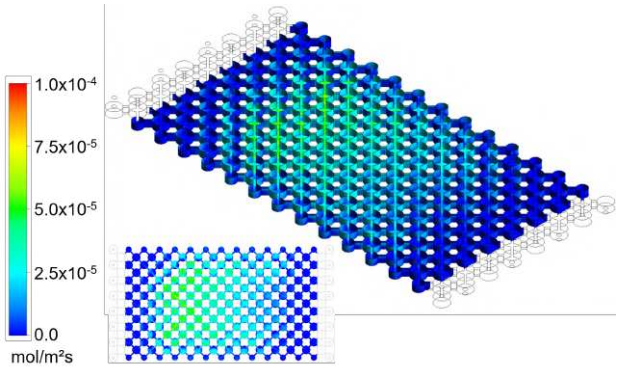

(j) Case 10: 12 LEDs - h = 12 mm

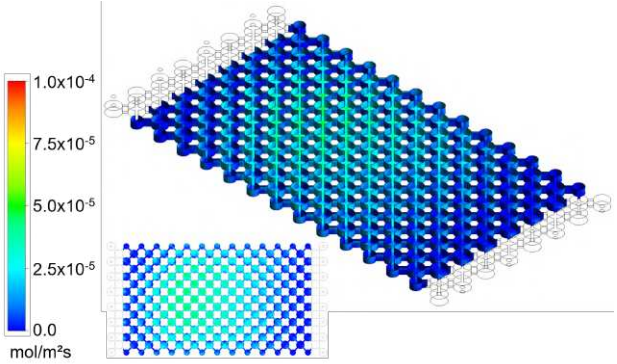

(k) Case 11: 12 LEDs - h = 24 mm

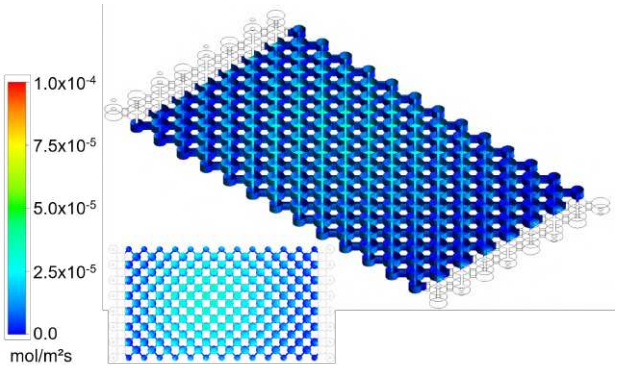

(l) Case 12: 12 LEDs - h = 48 mm

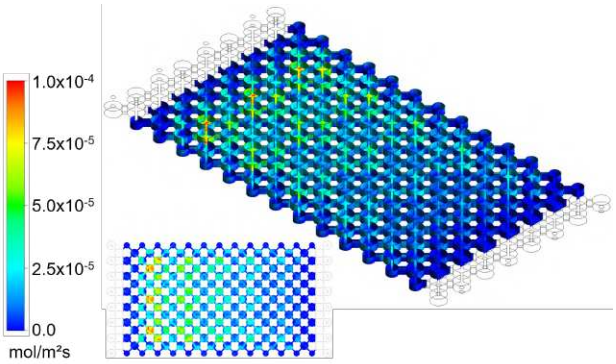

(m) Case 13: 15 LEDs - h = 6 mm

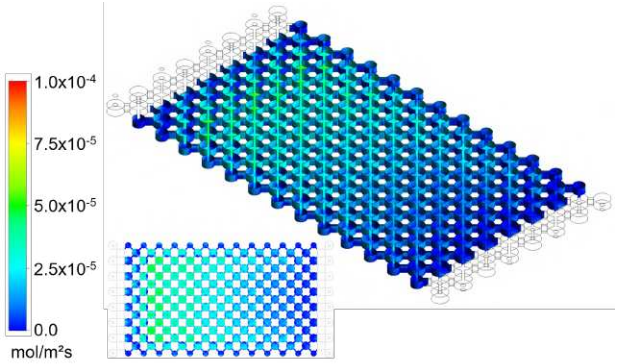

(n) Case 14: 15 LEDs - h = 12 mm

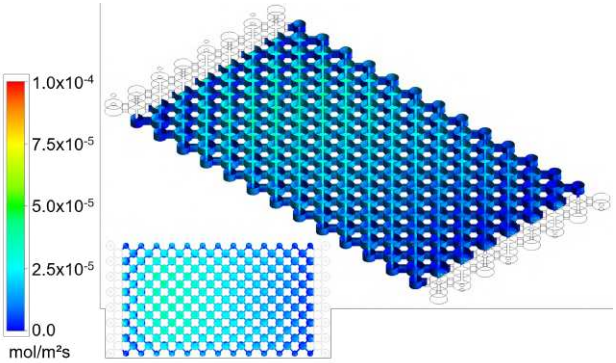

(o) Case 15: 15 LEDs - h = 24 mm

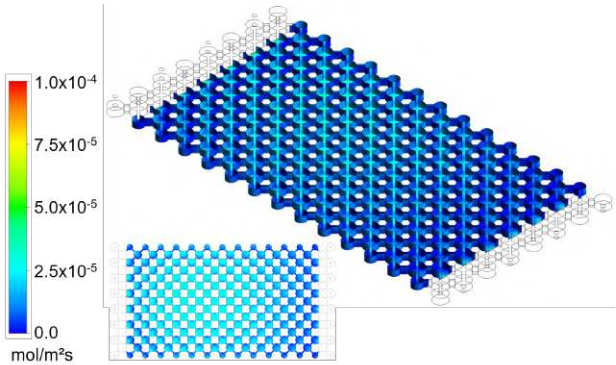

(p) Case 16: 15 LEDs - h = 48 mm

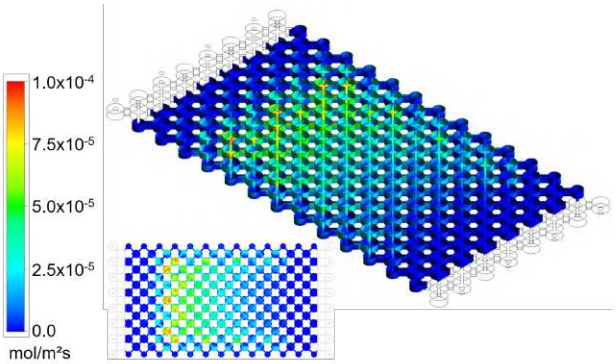

(q) Case 17: 18 LEDs - h = 6 mm

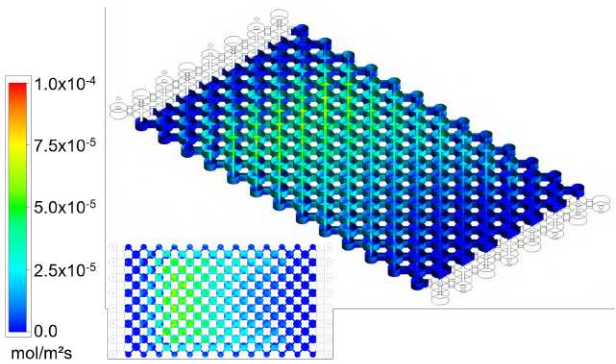

(r) Case 18: 18 LEDs - h = 12 mm

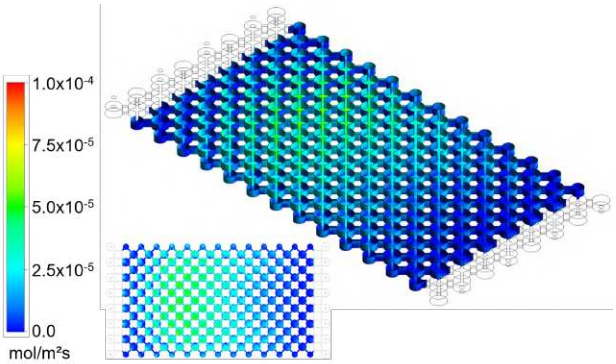

(s) Case 19: 18 LEDs - h = 24 mm

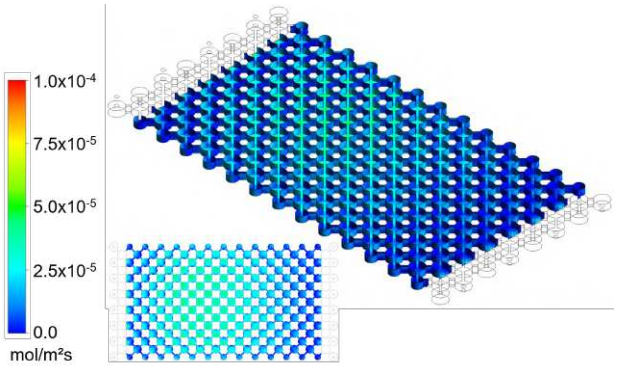

(t) Case 20: 18 LEDs - h = 48 mm

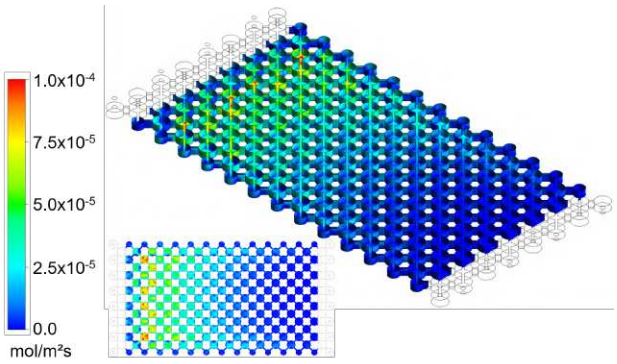

(u) Case 21: 28 LEDs - h = 6 mm

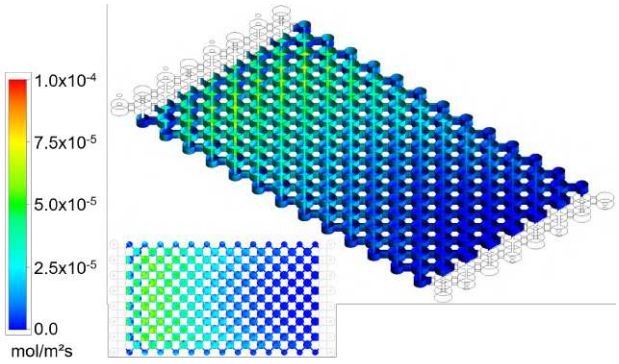

(v) Case 22: 28 LEDs - h = 12 mm

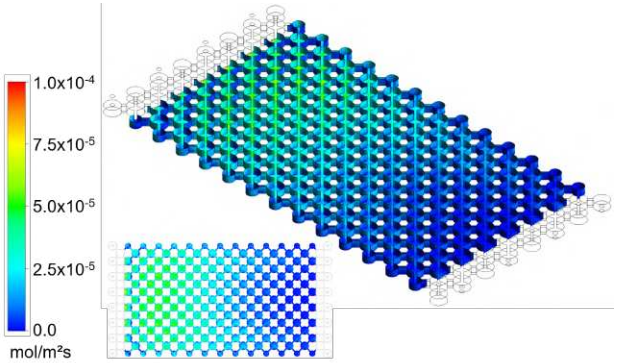

(w) Case 23: 28 LEDs - h = 24 mm

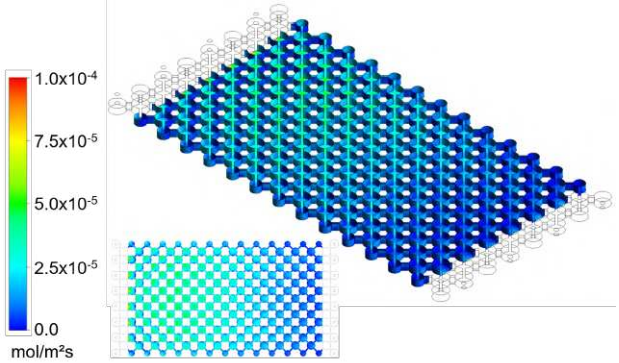

(x) Case 24: 28 LEDs - h = 48 mm

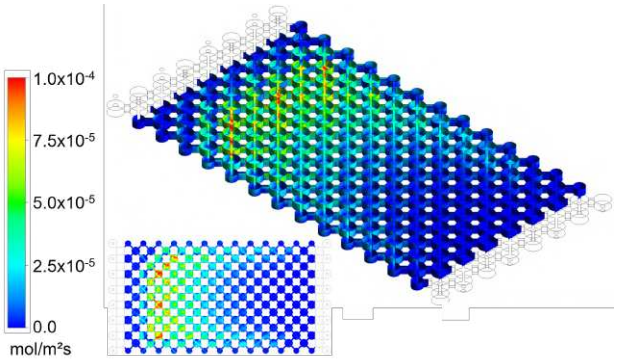

(y) Case 25: 30 LEDs - h = 6 mm

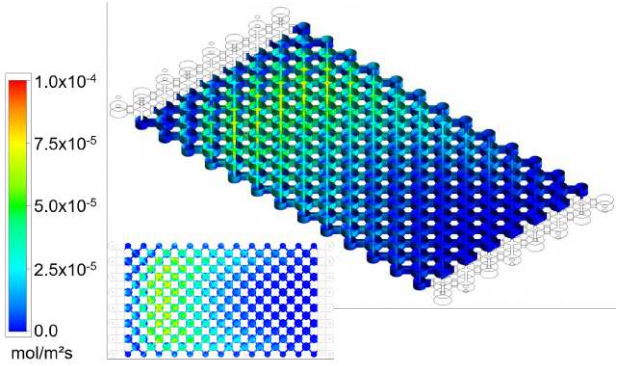

(z) Case 26: 30 LEDs - h = 12 mm

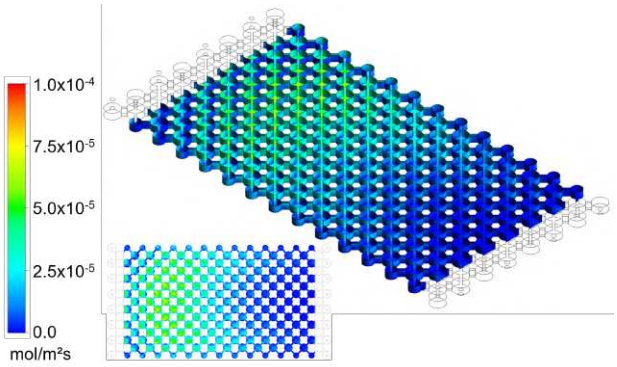

(aa) Case 27: 30 LEDs - h = 24 mm

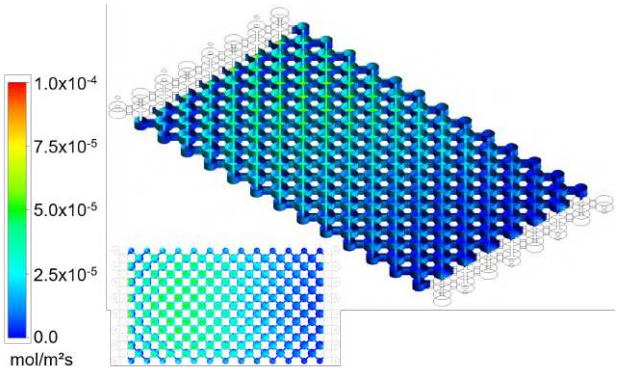

(ab) Case 28: 30 LEDs - h = 48 mm

Source: elaborated by the author (2022).

Figure 65 – Pollutant molar fraction at the bottom of the NETmix reactor for cases 1 to 28.

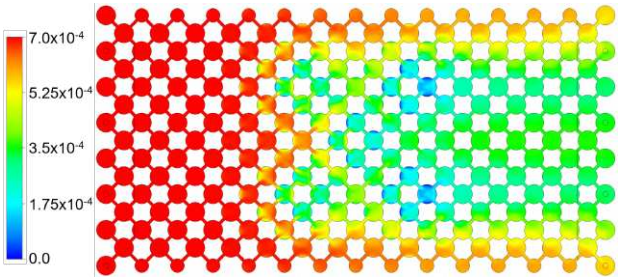

(a) Case 1: 5 LEDs - h = 6 mm

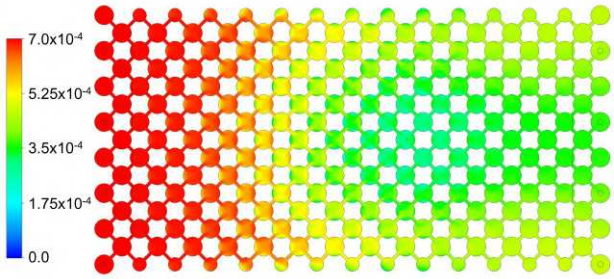

(b) Case 2: 5 LEDs - h = 12 mm

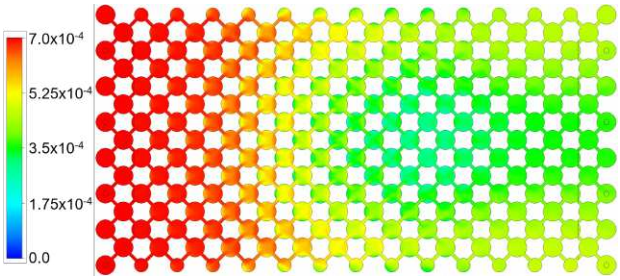

(c) Case 3: 5 LEDs - h = 24 mm

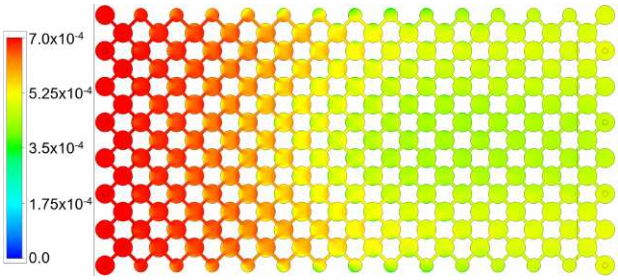

(d) Case 4: 5 LEDs - h = 48 mm

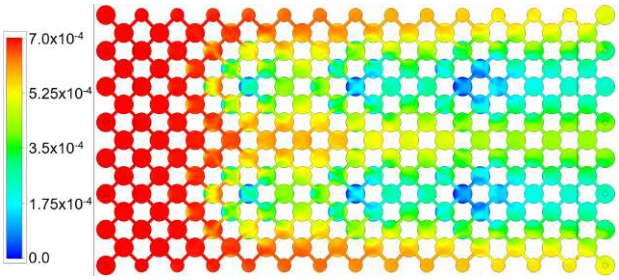

(e) Case 5: 6 LEDs - h = 6 mm

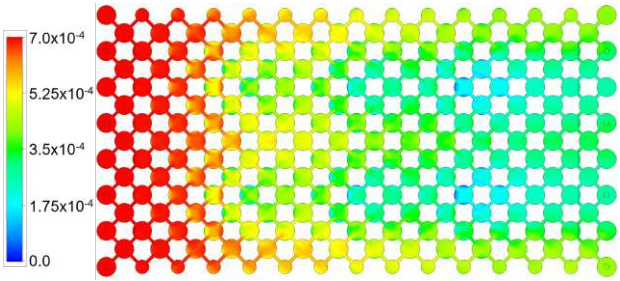

(f) Case 6: 6 LEDs - h = 12 mm

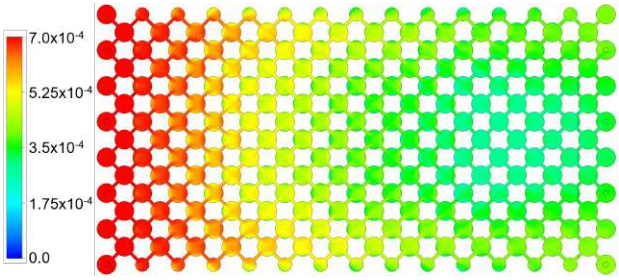

(g) Case 7: 6 LEDs - h = 24 mm

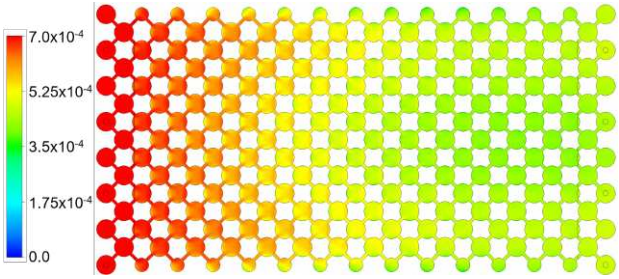

(h) Case 8: 6 LEDs - h = 48 mm

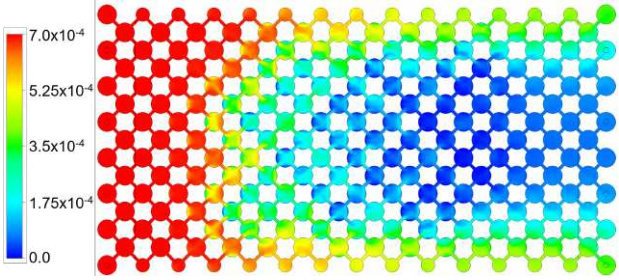

(i) Case 9: 12 LEDs - h = 6 mm

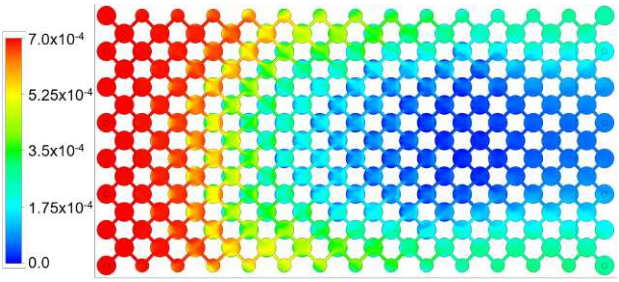

(j) Case 10: 12 LEDs - h = 12 mm

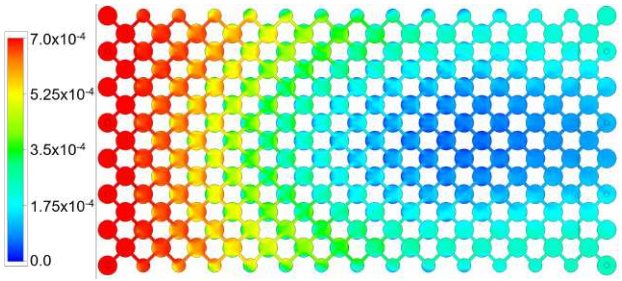

(k) Case 11: 12 LEDs - h = 24 mm

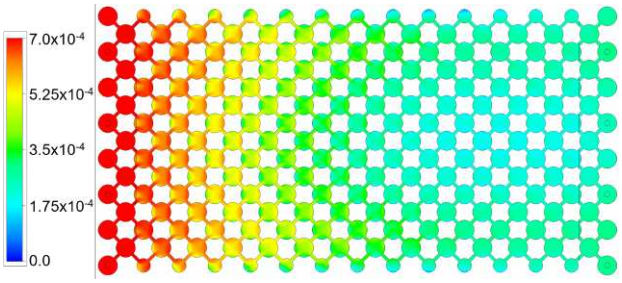

(l) Case 12: 12 LEDs - h = 48 mm

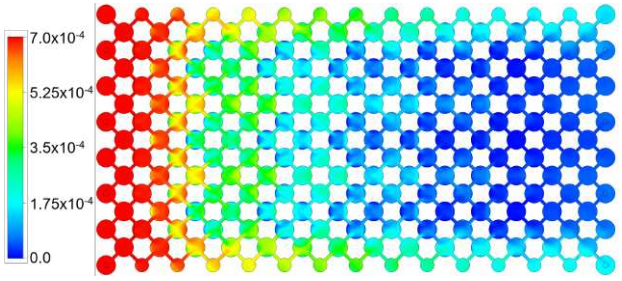

(m) Case 13: 15 LEDs - h = 6 mm

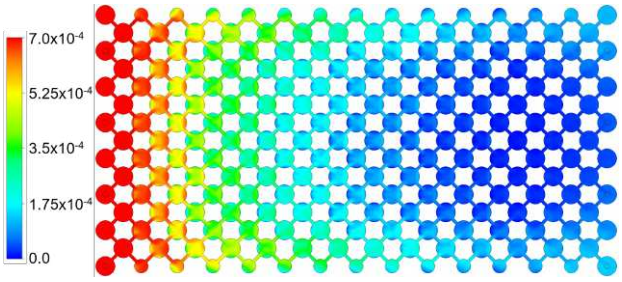

(n) Case 14: 15 LEDs - h = 12 mm

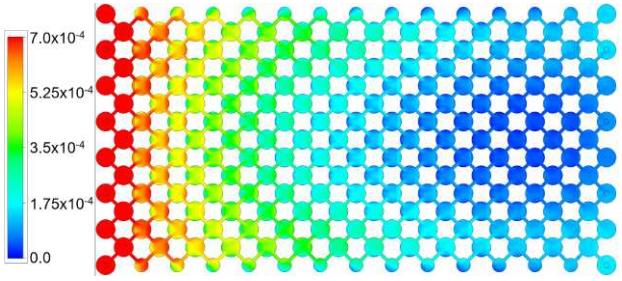

(o) Case 15: 15 LEDs - h = 24 mm

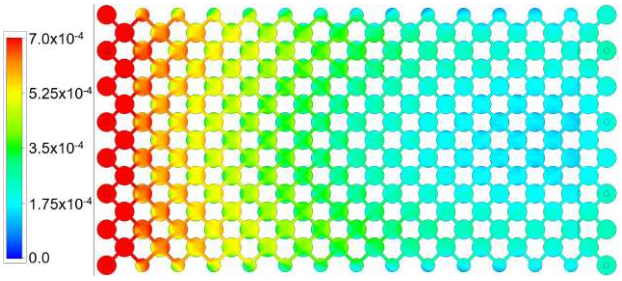

(p) Case 16: 15 LEDs - h = 48 mm

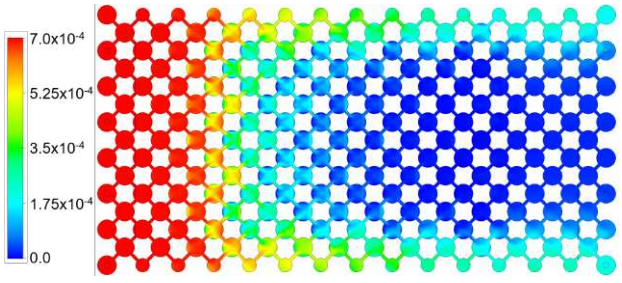

(q) Case 17: 18 LEDs - h = 6 mm

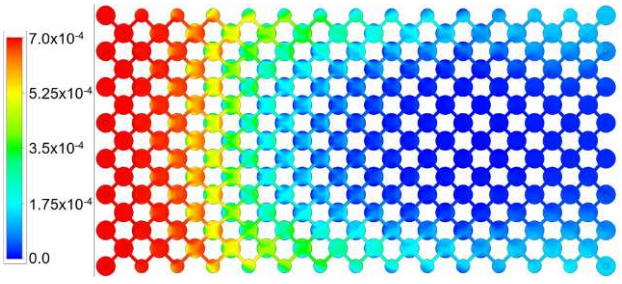

(r) Case 18: 18 LEDs - h = 12 mm

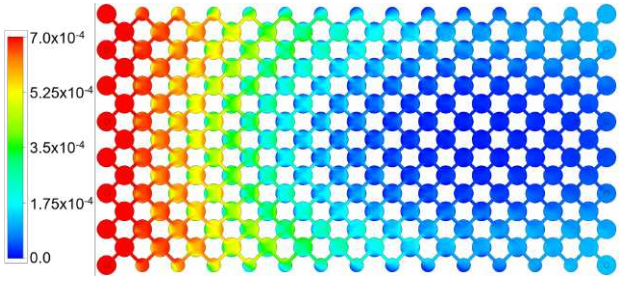

(s) Case 19: 18 LEDs - h = 24 mm

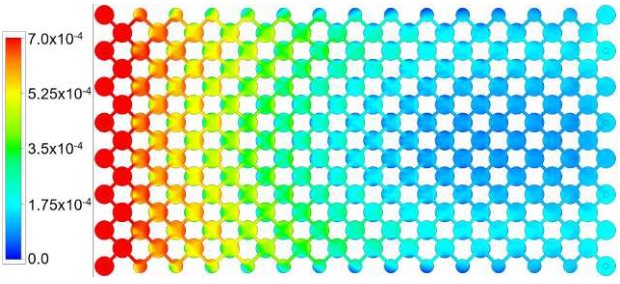

(t) Case 20: 18 LEDs - h = 48 mm

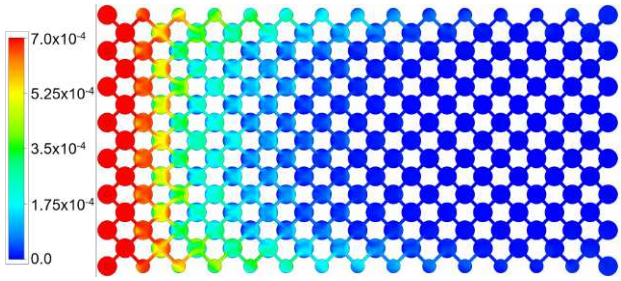

(u) Case 21: 28 LEDs - h = 6 mm

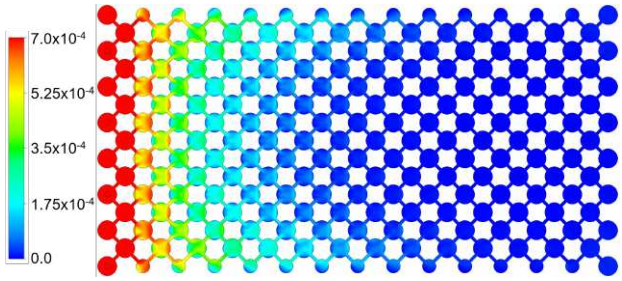

(v) Case 22: 28 LEDs - h = 12 mm

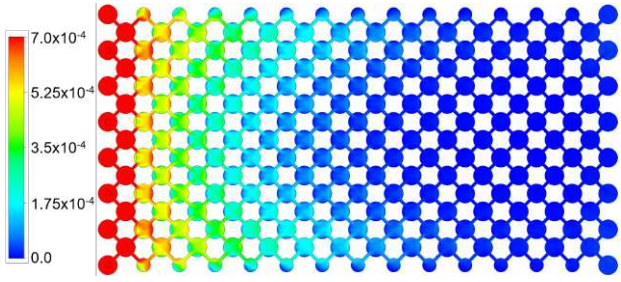

(w) Case 23: 28 LEDs - h = 24 mm

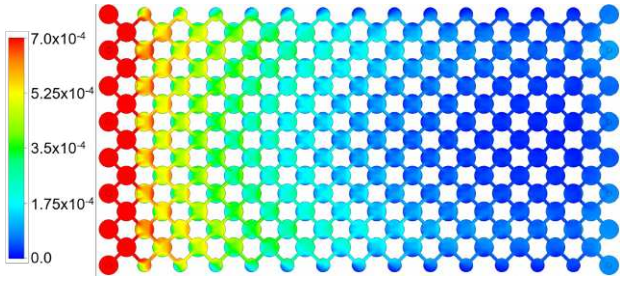

(x) Case 24: 28 LEDs - h = 48 mm

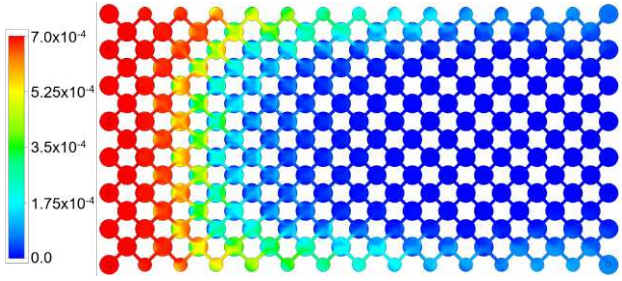

(y) Case 25: 30 LEDs - h = 6 mm

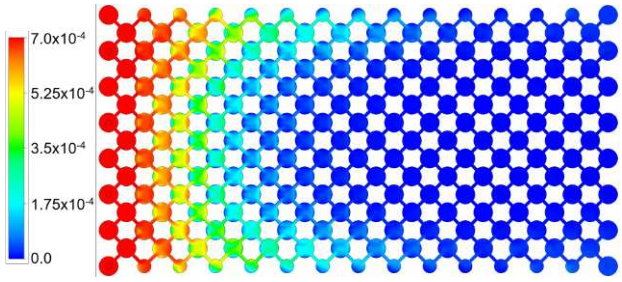

(z) Case 26: 30 LEDs - h = 12 mm

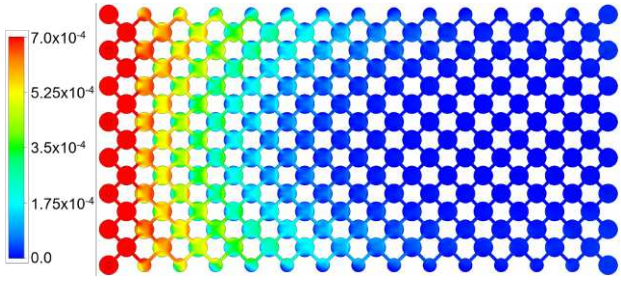

(aa) Case 27: 30 LEDs - h = 24 mm

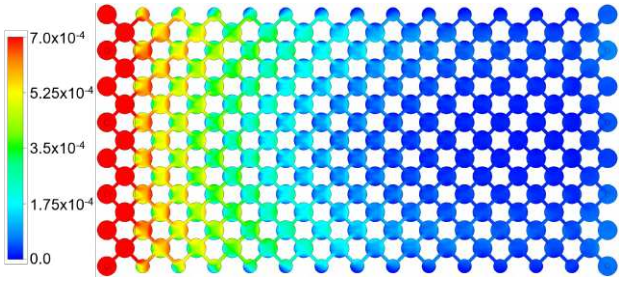

(ab) Case 28: 30 LEDs - h = 48 mm

Source: elaborated by the author (2022).